The Impact of Earthquakes on the Terrestrial Ecosystem Carbon Cycle

Jie Liu

A Thesis submitted for the degree of Doctor of Philosophy

Cardiff University

School of Earth and Environmental Science

October 4 2024

Thesis Summary

Earthquake-induced extensive mass wasting, in particular landslides and debris flows, can severely disturb terrestrial ecosystems by destroying vegetation and eroding soil. These processes lead to large-scale redistribution and export of terrestrial carbon, fundamentally altering the local carbon cycle. There is now compelling evidence that mega earthquakes play a significant role in carbon exchange between rocks and atmosphere on geological time scales (Clark et al. 2017; Hilton and West 2020). However, we have little idea on the fate of terrestrial ecosystem carbon in tectonically active regions.

This thesis investigates the significant impact of mega earthquake, such as the 2008 M_w7.9 Wenchuan earthquake, on terrestrial ecosystem carbon cycle. The research was conducted in three progressive stages. First, preliminary research established the methods and primary research direction, focusing on field sampling to assess the pathways of terrestrial carbon export and redistribution following earthquake triggered landslides (EQTLs) and debris flows. Then, the study expanded by incorporating large-scale sampling, field data from existing literature, and extensive remote sensing datasets. Machine learning techniques were applied to predict the spatial distribution of terrestrial carbon both pre- and post-earthquake, enabling the quantification of hillslope carbon budget following the 2008 M_w7.9 Wenchuan earthquake. This analysis revealed the "capacitor effect", the ability of EQTLs to temporarily store terrestrial organic carbon within mountains and gradually release it over extended periods, much like an electrical capacitor stores and releases energy. Finally, a coupled mass movement and carbon cycle model was developed to analyse how EQTLs affect carbon storage capacity and time scales. By integrating a stochastic earthquake model, the study assessed the long-term impacts of tectonic activity on ecosystem carbon dynamics, demonstrating that earthquakes enhance terrestrial organic carbon storage capacity and promote the long-term increasing of soil organic carbon stock in orogens.

Contents

List of Figures

List of Tables

Acknowledgements

First and foremost, I would like to express my deepest gratitude to my supervisor, Prof. TC. Without your encouragement and support, I would not have been able to complete this PhD thesis. Your guidance in research and your kindness made my one year and ten months in the UK feel like home. Thank you for inviting me to go surfing, BBQs, and for countless lunches and dinners. I am especially grateful for your persistent encouragement and supervision to keep me running regularly—I hope to carry on this great habit and one day fulfil the team tradition by completing a half marathon. I would also like to extend my sincere thanks to my supervisors at Chengdu University of Technology, Prof. Qiang Xu and Prof. Xuanmei Fan. Prof. Xu, you have been a beacon guiding me on my research path, and Prof. Fan, you have been my navigator since the beginning of my scientific journey. I am deeply appreciative of the support and mentorship you have provided throughout my doctoral studies. You have been like family to me, guiding me patiently, and generously offering me support, including the funding to complete my PhD at Cardiff University. My appreciation goes out to my co-supervisor, Dr. Shasta Marrero, for your help and support to my research, your encouragement and guidance in nearly every weekly meeting, along with your warm hugs, and my co-supervisor in Chengdu University of Technology, Prof. Xiaolu Tang, for your guidance in field sampling and constant support. I am also very grateful to Prof. Zhangdong Jin, Prof. Josh West and Prof. Bob Hilton, and Prof. Cees van Western, for offering insightful and thoughtful comments on various chapters of the thesis. Special thanks to Prof. Ernest Chi Fu and Prof. Fiona Clubb for taking time out to review my thesis and provide valuable feedback.

I am deeply indebted to my friends and colleagues who assisted with field data collection and laboratory experiments. Thank you, Bin Xia, Erin, Shikang Liu, Liyang Jiang, Yinshuang Yang, Lan Chen, Tao Wei, and Chengbin Zou, for contributing your time and expertise. I am especially grateful to Chengyong Fang and Lanxin Dai for answering my questions throughout my PhD journey, helping me navigate GIS, process remote sensing

data, and develop new skills step by step. I also want to thank all the PhD and masters in Xuanmei's research team for your help and support.

A special thank you to Erin—I feel incredibly lucky to have met you. Since my arrival in the UK, you took me on unforgettable Cardiff and London city walks, introduced me to your wonderful friends, Ana and Sara, and invited me into your home. I want to extend my gratitude to your parents and sister for their hospitality—the fish and chips was the best I've had in the UK! During my time buried in work, you always checked in on me, and I appreciate that more than words can express. I am also grateful to Kuros for your kindness and support, for inviting me to join your fieldwork—it was a memorable experience walking through the marsh collecting samples.

As my PhD journey has been long, there are many more people to thank. To my dear friends who have been by my side throughout this process—you know who you are, I carry you all in my heart. Thank you to my CDUT friends, Jiajia, Yajie, Daxiao, Huahua, and Duanchaoyi—without our meals and shared frustrations, I'm not sure I would have made it. Special thanks to Xuemin, Xiaoying, and Shunan for being there during every late-night work session. A huge thank you to Shunan for not only helping with our team's work but also taking on extra responsibilities for me while I was in the UK.

I also want to thank my colleagues, Bin Guo, Tiantao Li, Xiufeng Lai, Keren Dai, Xilu Lin, Qi Liu, Chen Rong, Luqing Wang, Yuanyuan Wang, Qian Wang, and Haiyan Wang, for helping to share my administrative duties and for your constant support and concern throughout my PhD journey.

Finally, and most importantly, I want to express my heartfelt gratitude to my family— my parents, my aunt, my cousins Zhaowan, Yingjie, Mengmeng, Meimei, Yunyun, Ruru, my adorable nieces and nephews, and my dear cats Shanshan and Xiaobi. I am incredibly fortunate to have you all in my life. Your unwavering support has made it possible for me to complete this PhD. I cannot thank you enough.

Publications arising from this thesis

Jie Liu, Xuanmei Fan, Xiaolu Tang, Qiang Xu, Erin L. Harvey, Tristram C. Hales, Zhangdong Jin, Ecosystem carbon stock loss after a mega earthquake*, CATENA* 2022; 216. doi: https://doi.org/10.1016/j.catena.2022.106393. (Chapter 4)

Erin L. Harvey, Tristram C. Hales, **Jie Liu**, Daniel E.J. Hobley, Fan Yang, Bing Xia, Xuanmei Fan; Grain-size variability in debris flows of different runout lengths, Wenchuan, China. *GSA Bulletin* 2023; 136 (7-8): 2676–2688. doi: https://doi.org/10.1130/B37027.1 (Chapter 4)

Jie Liu, Xuanmei Fan. Tristram C. Hales, Xiaolu Tang, Erin L. Harvey, Zhangdong Jin, Qiang Xu, Earthquakes Act as a Capacitor for Terrestrial Organic Carbon (Ready for submission, Chapter 5)

Chapter 1

Introduction

Earthquakes have long been considered as an important component of the terrestrial ecosystem carbon cycle via landslides shaping mountain topography and denuding large areas of forest (Garwood et al. 1979a), supposedly leading to enhanced carbon mobilization and declined terrestrial primary productivity. The fate of mobilized carbon might experience burial in massive sediments (Hilton et al. 2008a; Hilton et al. 2011b) and the transfer to hillslope, channel and fluvial systems, and eventual deposition within landscapes or ocean or emission into the atmosphere (Frith et al. 2018; Galy et al. 2007; Galy et al. 2015). Meanwhile, the denuded landslide area with a large extent of mixture of soil and vegetation biomass debris undergoes a series of physicochemical alteration processes and reaccumulates organic carbon for new soil development and vegetation succession (Rasigraf and Wagner 2022). All these processes unravel the geomorphic impacts of earthquakes on the carbon cycle in tectonically active regions.

The immediate landscape response after earthquakes is characterized by the production of large volumes of sediment (Dadson et al. 2004; Fan et al. 2019b; Li et al. 2016; Wang et al. 2015). Earthquake-triggered landslides (EQTLs) initiate a sediment cascade that plays a crucial role in carbon mobilization and transportation. Globally, evidence has indicated the observed positive relationship between suspended sediment discharge and the riverine particulate organic carbon (POC) (Hilton 2017; Hilton et al. 2008a; Wang et al. 2016). Further research highlights the increased export and burial efficiency of ecosystem POC in tectonically active areas through the application of radioactive and stable carbon isotopes to field samples (Galy et al. 2015). In tropical and coastal settings, landslides favour the transport and subsequent deposit of ecosystem organic carbon in fluvial and marine sediments (Clark et al. 2016; Hilton et al. 2008b; Kao et al. 2014b; Ramos Scharrón et al. 2012). The carbon is also protected from oxidation by increased export and burial rates. Overall, landslide carbon will largely contribute to a long-term carbon sink if preserved in stable environments. While in temperate montane ecosystem, landslides act as agents of carbon mobilization, moving carbon from living biomass to hillslope deposits before rarely reaching the fluvial system (Fan et al. 2018; Francis et al. 2022; Li et al. 2014; Märki et al. 2021). This is meanwhile consistent with sediment budget that over 80% of the sediment (up to 3 km^3) produced by 2008 Mw7.9 Wenchuan earthquake remains on hillslope for 10 years (Francis et al. 2022). The persistence of that significant quantities of mobilized ecosystem carbon in landslide deposits may either lead to carbon release through decomposition or oxidation, or carbon sequestration through efficient burial or stabilization, thus influencing terrestrial ecosystem carbon cycle.

EQTLs lead to the redistribution of carbon-rich vegetation biomass and topsoil layers, significantly affecting the recovery of terrestrial carbon. This process is predominantly manifested by soil development and vegetation regrowth (Freund et al. 2021; Rasigraf and Wagner 2022; Schomakers et al. 2017), which are key mechanisms of carbon re-accumulation following landslides. This process, along with the burial of ecosystem carbon, may serve as a significant mechanism for carbon sequestration(Galy et al. 2007; Galy et al. 2015). Most terrestrial carbon cycle models adopt a pool-and-flux framework, using ordinary differential equations (ODEs) to describe the flow of carbon between major carbon pools—such as vegetation, soil, and the atmosphere (Luo and Weng 2011; Luo et al. 2012). However, these models often overlook the critical role of sediment cascading in carbon export, particularly in regions affected by seismic events. Landslides, especially those triggered by mega earthquakes, mobilize significant amounts of ecosystem carbon, which is then redistributed through sediment export. Incorporating sediment erosion into terrestrial carbon cycle models allows for a more comprehensive understanding of carbon movement across landscapes, particularly in response to seismic activity (Booth et al. 2023). This expanded model framework provides insight into how earthquakes related with mass movements influence carbon fluxes, including both the short-term disruption and long-term recovery of carbon storage in terrestrial ecosystems. Moreover, such models are essential for quantifying the broader impact of frequent earthquake events on carbon cycles in mountainous regions.

Despite growing recognition of the connection between sediment erosion and carbon cycling, significant research gaps remain. A key limitation is the lack of empirical data necessary to quantify processes governing carbon dynamics in earthquake affected landscapes. Specifically, there is insufficient field data on spatial and temoral variability of terrestrial carbon storage and flux. This scarcity complicates the task of extrapolating findings from individual case studies to create models applicable at regional or global scales. Additionally, most terrestrial carbon cycle models do not fully account for the impact of large-scale mass movements on carbon fluxes (Doetterl et al. 2016; Yoo et al. 2005, 2006), especially in earthquake-prone areas where EQTLs can rapidly mobilize significant amounts of carbon. The episodic nature of these events, combined with the complexity of sediment transport and carbon burial processes, makes assessing their long-term effects on carbon cycling particularly challenging (Booth et al. 2023). Furthermore, the cumulative impact of frequent seismic events on carbon storage and release in seismically active regions remains poorly understood. This lack of understanding poses a major challenge to evaluating the broader implications of extreme geological events on the global carbon system (Yoo et al. 2005, 2006), particularly as

climate change may increase both the frequency and intensity of such events (Li and Fang 2016).

1.1 Research aims

The overarching aim of this thesis is to explore **the impact of an earthquake (the 2008 Wenchuan earthquake) on the terrestrial carbon cycle**, focusing on how earthquake triggered landslides (EQTLs) influence hillslope carbon and the underlying mechanisms that govern terrestrial carbon storage capacity. This work consists of three main chapters, which together form a systematic research framework. **Chapter 4** focuses on the field plot scale, measuring changes in the concentration of carbon in different pools in earthquake-triggered landslides, debris flows, and unaffected hillslopes. It sets the context how these events affect carbon storage and export through physical transport pathways. **Chapter 5** considers the total carbon storage for all landslides in the earthquake-affected region, quantifying the hillslope carbon mass budget after the Wenchuan earthquake. It reveals the spatial distribution of terrestrial carbon storage and recovery, highlighting the magnitude and timescale of carbon storage for this earthquake and the potential for earthquakes to store terrestrial carbon in mountain ranges. **Chapter 6** develops a coupled carbon cycle and mass movement model that seeks to understand the carbon storage dynamics through time, examining mechanisms controlling carbon storage following a single earthquake and multiple earthquake events.

Research Question 1:

How and where do earthquake-triggered landslides and post-seismic debris flows store and redistribute terrestrial carbon?

In order to understand the fate of terrestrial carbon transfer after earthquake, in-depth preliminary research is conducted on one of the most active catchments with abundant co-seismic landslides and post-seismic debris flows in 2008 Mw7.9 Wenchuan earthquake. An innovative sampling method is devised for the calculation of vegetation biomass and soil organic carbon stock at field, in which the pair-plot design on landslide deposits and adjacent undisturbed forest provides the comparison of terrestrial organic carbon between pre-earthquake and post-earthquake. This research examines catchment-scale change of organic carbon stock following mass movement of EQTLs. It provides a foundational understanding of how carbon is redistributed after earthquake.

Research Question 2:

How much terrestrial carbon can be stored and recovered after a mega earthquake?

To scale up investigation into a regional level, pair-plot field sampling was applied to the area affected by Wenchuan EQTL. I integrated field data and satellite data with machine learning methods to generate a precise predictive model at the regional scale. Machine learning methods considered the complex interactions among topographic, geological, climatic, and ecological covariates on carbon storage. Subsequently, the spatial distribution of ecosystem OC stock before EQTLs and the recovered ecosystem OC stock after EQTLs was predicted. It provides a quantified overview of hillslope carbon mass budget after the 2008 Mw7.9 Wenchuan earthquake, revealing the "capacitor effect" of mountain ranges regulating carbon sequestration and release after earthquakes.

Research Question 3:

How do earthquakes impact the carbon storage capacity across millennia?

This research delves into the mechanisms behind the storage and export of carbon. I generated a carbon cycle model coupled with mass movements following earthquakes. It demonstrates how erosional processes influence carbon flux and carbon pools, specifically examining the impact of landslide proportion and landslide scale on carbon storage capacity and timescale. This chapter aims to uncover the interaction between biochemical processes and erosion that govern the carbon balance observed in tectonically active regions. By considering multiple earthquakes events, the cumulative and long-term effects storage of terrestrial carbon in mountainous landscapes is further investigated.

1.2 Thesis structure

The ultimate goal of this thesis is to investigate the impact of EQTLs on terrestrial ecosystem organic carbon cycle. Each research question will be addressed in each research chapter with respective methodologies. This structure will demonstrate how research questions interconnect to achieve the ultimate aim.

Chapter 2 provides a literature review on the current state of knowledge of carbon cycles in tectonically active regions. It explores the relationship between EQTLs and ecosystem carbon cycle. Emphasis will be placed on ecosystem organic carbon export with the impact of massive sediment cascading. The chapter also summarizes the ecosystem organic carbon mobilized, exported and recovered by EQTLs. This gives a foundational understanding of earthquake impact on carbon dynamics.

Chapter 3 gives a brief background on the Longmenshan region, covering its tectonic, geological and environmental characteristics. I also introduce the 2008 $M_W7.9$ Wenchuan earthquake, detailing the landslide inventory and sediment budget, which is used in Chapter 4. Additionally, this chapter describes the regional and catchment study areas selected for field work and modelling analysis in this thesis.

Chapter 4 focuses on preliminary research at the catchment scale. It details the appropriate field analysis, sampling methods, laboratory work and allometric equations for organic carbon stock and tree biomass, providing the methodology for the upscale study and modelling in Chapter 5. The general pathways of total ecosystem organic carbon are proposed based on sampling results and calculations.

Chapter 5 applies the methodology from Chapter 4 to the 2008 Mw7.9 Wenchuan earthquake affected area. It consists of an extensive dataset from 126 sampling sites, 368 soil profiles and 194 entries within the study area. Combined with 21 covariates from remote sensing data, geographic data and landslide inventory, a prediction model for total terrestrial organic carbon stock is developed after screening 20 machine learning methods. This Chapter provides an overview of spatial distribution of total terrestrial organic carbon stock and recovered carbon after earthquake along hillslope.

Chapter 6 constructs a carbon balance model coupled with mass movement. The sediment budget and carbon mass budget after 2008 Mw7.9 Wenchuan earthquake from Chapter 5 offers the basis for constructing the model structure and initial parameters. This model illustrates the mechanism controlling the capacity of carbon storage in tectonically active region, which further examines the relative effects of landslide proportion, landslide area frequency and erosion rate on carbon balance. Furthermore, a

stochastic earthquake model is integrated to assess carbon dynamics across multiple earthquakes.

Chapter 7 summarizes the main findings of this thesis to frame the research questions set out in introduction. It discusses the potential future research on the carbon cycle in tectonically active region, providing scientific basis and support for post-disaster ecological restoration.

Chapter 2

Literature Review

2.1 Carbon cycle in active mountains

Active mountain regions are critical components of the global carbon cycle, exerting a significant influence on both short-term and long-term carbon dynamics through a variety of complex processes (Hilton and West 2020). The carbon cycle in these regions can be broadly divided into two distinct cycles (Figure 2.1): the short-term carbon cycle, which operates over years to hundreds of years (Luo et al. 2015), and the long-term carbon cycle, which spans thousands to millions of years (France-Lanord and Derry 1997; Maher and Chamberlain 2014). Each cycle is characterized by different mechanisms and timescales, impacting carbon storage and release in unique ways. As shown in Figure 2.1, the flux of organic carbon burial from terrestrial ecosystems serves as a critical link, connecting short-term and long-term processes (Hilton and West 2020).These interconnected processes are vital for understanding how active mountain building influences terrestrial carbon cycling and, ultimately, climate responses and long-term climate stability. This thesis focuses on the short-term carbon cycle, investigating the dynamics of terrestrial carbon fluxes and the role of mass movement in shaping carbon distribution and storage. Furthermore, we explore how these short-term processes may impact the long-term carbon cycle by influencing the rates of carbon sequestration and release associated with geological processes.
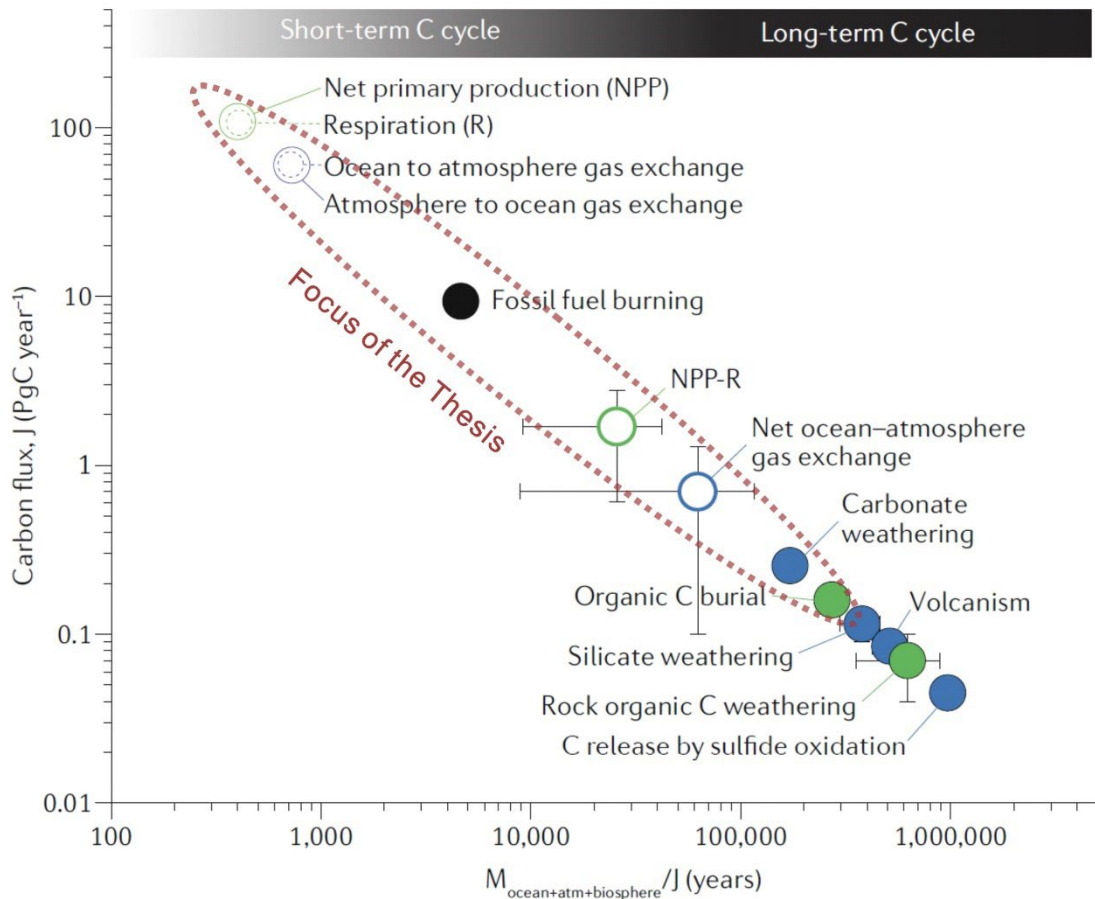
Figure 2.1 Overview of Major Carbon Fluxes and Relevant Timescales in Global Carbon Cycle
Estimated pre-industrial carbon fluxes (Intergovernmental Panel on Climate 2014; Sundquist and Visser 2003) and the timescales required to replace the total carbon mass in Earth's oceans (Hilton and West 2020), atmosphere, and biosphere ($M_{ocean+atm+biosphere}$ = 43,540 ± 550 Petagrams of carbon; PgC) (Sundquist and Visser 2003). Green symbols represent organic carbon processes; blue symbols denote inorganic carbon processes, and black symbols highlight the rapid acceleration of rock organic-carbon oxidation due to fossil-fuel burning. Open circles indicate short-term cycles (<100,000 years), while filled circles indicate long-term cycles (10^5 to 10^6 years). Figure is from Hilton and West (2020)

2.1.1 Long-term carbon cycle and transfers

The long-term carbon cycle involves slower, geological processes that regulate carbon exchange between the atmosphere and the Earth's rock reservoirs over extended timescales. A critical carbon sink in this cycle is silicate weathering, a chemical process in which silicate minerals in rocks break down and react with atmospheric CO_2 to form bicarbonate ions (Chamberlin 1899). These ions are transported to the oceans, where they precipitate as carbonate minerals, effectively removing CO_2 from the atmosphere for millions of years. However, the long-term cycle also includes significant carbon sources, such as the oxidation of sulfide minerals and petrogenic organic carbon (OC_{petro}) (Bouchez et al. 2010b; Torres et al. 2014). Sulfide oxidation generates sulfuric acid, which can react with carbonate rocks to release CO_2 back into the atmosphere, while the

oxidation of OC_{petro}, composed of ancient organic carbon stored in sedimentary rocks, contributes to atmospheric CO_2 release during weathering processes. These long-term processes are primarily driven by geological activities, such as tectonic uplift, erosion, and weathering, which expose fresh rock surfaces to chemical reactions (Calmels et al. 2007; Hilton et al. 2011a). Although the rate of CO_2 degassing from the solid Earth (Wong et al. 2019) may seem minor compared to photosynthesis on shorter timescales (Clark et al. 2017; Galy et al. 2015), it accumulates significantly over millions of years, necessitating counterbalancing geological carbon sinks to maintain long-term climate stability (Hilton 2017; Riebe et al. 2004).

Figure 2.2 shows the emerging view of carbon transfers between rocks and the atmosphere. This geological carbon cycle has been understood as a balance between carbon sources, such as solid-Earth degassing (volcanism) (Wong et al. 2019), and carbon sinks, primarily silicate weathering (Gaillardet et al. 1999; Moon et al. 2014). Solid-Earth degassing contributes approximately 70–100 megatonnes C per year (Mt C yr^{-1}), while silicate weathering is estimated to remove 90–140 Mt C yr^{-1}, from the atmosphere. These processes have been considered the dominant controls on atmospheric CO_2 levels over geological timescales, significantly influencing Earth's long-term climate (Raymo and Ruddiman 1992). However, Hilton and West (2020) emphasize the importance of additional carbon fluxes linked to erosion and weathering processes in mountain regions. These include CO_2 drawdown via terrestrial organic carbon burial (Galy et al. 2007), as well as CO_2 sources from petrogenic organic carbon oxidation (Petsch 2014) and sulfide oxidation coupled to carbonate weathering (Burke et al. 2018; Calmels et al. 2007). Erosion of terrestrial organic carbon and deposition into offshore sediments has been well quantified, representing a sizable and dynamic long-term CO_2 sink if the buried carbon escape subsequent degradation and new plant growth replaces eroded site. The total organic carbon burial flux is approximately 170 Mt C yr^{-1} (Burdige 2007), of which approximately 40-80 Mt C yr^{-1} derived from terrestrial ecosystem is estimated as net carbon sink(Bianchi et al. 2018; Burdige 2005). In contrast, several processes contribute to carbon effluxes between atmosphere and rock, including sulfide oxidation, releasing approximately 40 Mt C yr^{-1}(Burke et al. 2018; Torres et al. 2016) into the atmosphere, and petrogenic organic carbon oxidation, contributing an estimated 40-100 Mt C yr^{-1} (Burdige 2005; Petsch 2014). These carbon effluxes from oxidative weathering are roughly balanced by carbon sinks from terrestrial organic carbon burial. The equilibrium of these fluxes helps maintain a steady-state CO_2 level in atmosphere over long timescales.
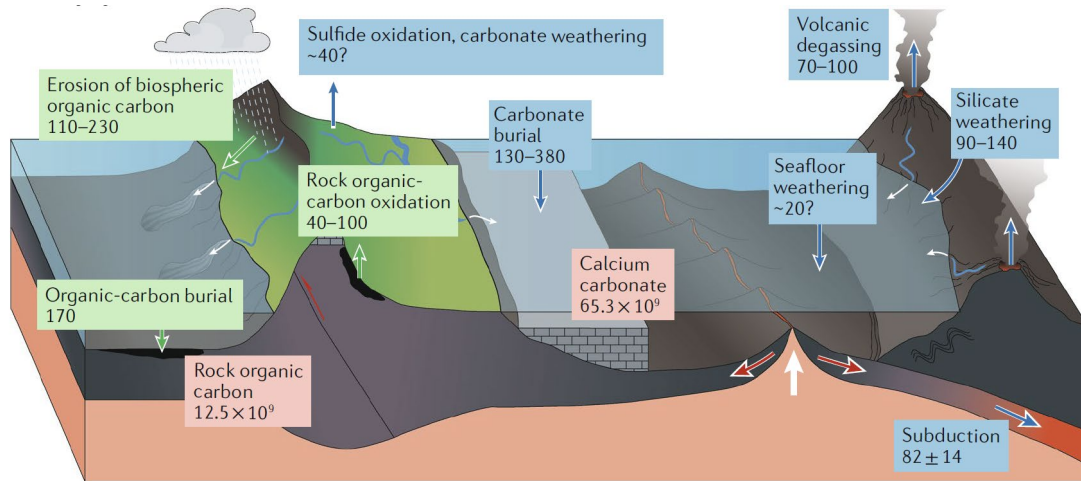
Figure 2.2 Geological Carbon Cycle and transfers of Carbon between Atmosphere and Rocks
The merging view considers the organic-carbon fluxes (shown in green)(Burdige 2007; Galy et al. 2015; Petsch 2014) and inorganic-carbon fluxes (shown in blue)(Burke et al. 2018; Gaillardet et al. 1999; Moon et al. 2014; Torres et al. 2016). The erosion and burial of biospheric organic carbon is studied in this thesis. The carbon stock is in pink with unit of $Mt\ C$. The carbon flux is with unit of $Mt\ C\ yr^{-1}$. Figure is from Hilton and West (2020).

Erosion fundamentally alters carbon fluxes in mountain regions by modifying the rates at which different carbon sinks and sources operate (Clark et al. 2017; Hilton and West 2020). By increasing the exposure of fresh mineral surfaces, erosion enhances silicate weathering (Riebe et al. 2004), thereby increasing the rate of CO_2 drawdown. However, erosion also exposes petrogenic carbon and sulfide minerals (Bouchez et al. 2010a), which, upon oxidation, release carbon back into the atmosphere. This dual effect means that erosion can either function as a net carbon sink or carbon source, depending on the relative rates of these processes. At low erosion rates, silicate weathering is limited by the availability of fresh minerals, resulting in minimal CO_2 removal and reduced burial of terrestrial organic carbon. This leads to a condition known as "supply-limited" weathering (Riebe et al. 2004). Conversely, very high erosion rates can lead to increased exposure of reactive minerals, accelerating both silicate weathering and oxidative weathering of petrogenic carbon and sulfides (Gabet and Mudd 2009; Hilley et al. 2010). However, oxidative weathering processes can surpass silicate weathering, leading to a net release of CO_2. Under this condition, weathering rates are not directly governed by the supply but are instead influenced by other climatic factors. There appears to be an intermediate "sweet spot" of erosion where the CO_2 drawdown is maximized (Edmond and Huh 2003). At these rates, silicate weathering and terrestrial carbon burial are balanced against CO_2 sources from oxidation, potentially making mountain regions a net carbon sink. This balance is influenced by the timing and sequence of mountain building

and erosion, suggesting that different stages of orogenic evolution(Dewey and Horsfield 1970) could lead to shifts in the net carbon balance from a sink to a source or vice versa.

The interplay between erosion rates and carbon fluxes is also strongly modulated by lithology and climate (Hilton and West 2020). Rock types rich in silicates, such as granite and basalt, are more susceptible to silicate weathering (Dessert et al. 2003), a significant CO_2-consuming process, positioning these regions as potential carbon sinks. In contrast, lithologies abundant in sulfide minerals or petrogenic carbon can contribute to CO_2 emissions through oxidative weathering, where sulfuric acid produced from sulfide oxidation reacts with carbonate minerals (Calmels et al. 2007; Emberson et al. 2016), and direct oxidation of petrogenic carbon releases CO_2. Additionally, climatic factors such as precipitation influence both chemical and physical weathering processes and the transport of organic carbon from terrestrial environments to rivers and ocean (Frings 2019). For example, a humid, temperate region with extensive silicate rock formations and high rainfall would likely enhance silicate weathering (Lloret et al. 2013), promoting a net carbon sink. On the other hand, arid regions with carbonate and sulfide-rich lithologies might see limited weathering but significant CO_2 release from oxidative processes (Torres et al. 2014), resulting in a net carbon source.

Hilton and West (2020) have summarized empirical data from various mountain regions to provide support for these arguments. For example, studies in the western Southern Alps of New Zealand, Mackenzie Basin in Canada, Liwu River in Central Taiwan, Zagunao in Longwenshan, China and Narayani river basin in central Himalaya, show that erosion can both enhance the influx of terrestrial organic carbon and oxidation of petrogenic carbon(Gomez et al. 2003; Hilton et al. 2008a; Horan et al. 2019; Jacobson and Blum 2003; Märki et al. 2021; Page et al. 2004; Wang et al. 2016). The observed data indicated that in most cases, the influx of terrestrial organic carbon is higher than the efflux of petrogenic organic carbon. However, exceptions exist, such as catchments in the Southern Alps, where the oxidation rate far surpasses the efficiency of terrestrial carbon burial (Hilton and West 2020), potentially due to the unique topographic, climatic conditions and mountain glaciation (Horan et al. 2017). Thus, the net carbon effect is primarily determined by the inorganic carbon fluxes between silicate weathering and sulfide oxidation, which are closely related to lithology (Kao et al. 2014a). In some cases, sedimentary rocks may lead to either a carbon sink or source depending on their sulfide content. Taking Taiwan as a specific example, the mountainous terrain and active tectonics result in high erosion rates of biospheric organic carbon, potentially approaching global maxima (Hilton et al. 2011a; West et al. 2011). However, comprehensive studies of the Liwu River have shown that high rates of terrestrial carbon

burial are accompanied by significant oxidation of petrogenic organic carbon and sulfide oxidation (Hilton et al. 2008b). This dual process ultimately leads to the Liwu catchment acting as a carbon source (Hilton and West 2020). In contrast, regions dominated by volcanic rocks, such as Guadeloupe (Lloret et al. 2013), favour CO_2 sequestration through enhanced silicate weathering.

The burial of terrestrial organic carbon is considered a significant component in offsetting atmospheric CO_2 emissions, with long-term implications for carbon transfers between rocks and atmosphere. In regions such as the Narayani River basin in the central Himalayas and the Longmenshan region on the eastern edge of the Himalayas (Li et al. 2016; Li et al. 2017a; Märki et al. 2021), erosion rates are lower compared to those in the islands of Oceania and the Bengal fan (Galy et al. 2007; Kao et al. 2014b). In these areas, carbon fluxes may be supply-limited, meaning the rate of terrestrial organic carbon export is controlled by the rate of erosion. Beyond a certain intensity, other factors may also influence carbon export. Additionally, active tectonic activity can trigger substantial mass movements (Fan et al. 2019b), potentially disrupting the storage and export of terrestrial carbon. This transient imbalance in carbon export can lead to short-term perturbations in the terrestrial carbon cycle, which might have long-term impact for carbon storage and climate change.

2.1.2 Short-term carbon cycle and transfers

The short-term carbon cycle is primarily driven by terrestrial carbon processes, involving dynamic interactions among the atmosphere, biosphere, and pedosphere(Schimel 1995). As shown in Figure 2.3, the primary carbon pools in mountainous ecosystems include atmospheric carbon, vegetation carbon, and soil carbon. Vegetation plays a fundamental role in the carbon cycle by absorbing CO_2 from the atmosphere through photosynthesis, converting it into organic compounds, and storing it as biomass (Ciais et al. 2013). This process, known as gross primary productivity (GPP), represents a major contribution of the biosphere to the carbon cycle (Running et al. 2004; Xiao et al. 2019). The organic carbon stored in plants can be released back into the atmosphere through autotrophic respiration of plant roots, contributing to net primary productivity (NPP) (Running et al. 2004). Alternatively, carbon can be transferred to the soil through the decomposition of leaf litter and plant debris. Once in the soil, organic carbon is further decomposed by microbial heterotrophic respiration, releasing CO_2 back to the atmosphere (Keller and Bacon 1998; Schlesinger and Andrews 2000). The size of these carbon pools and the fluxes between them are critical in determining the dynamic equilibrium of local ecosystems. Soils hold more than two-thirds of the carbon stored in terrestrial ecosystems,

making the pedosphere a major part of the global carbon budget. Even small changes in soil carbon can significantly impact atmospheric CO_2 levels.

Additionally, the short-term cycle includes the export of terrestrial carbon through sediment transport processes, where organic carbon is eroded from soils and vegetation, and transported across landscapes (Clark et al. 2017; Lal 2003; Page et al. 2004; Parfitt et al. 2013). This process not only redistributes soil carbon within terrestrial landscapes but also promotes the oxidation or sedimentation of organic carbon (Galy et al. 2007; Yoo et al. 2006). Terrestrial organic carbon burial effectively removes carbon from active circulation and sequesters it in sediments. The balance between carbon sinks and sources in this cycle is influenced by both biological activity and geomorphic processes, which together regulate the amount of carbon stored in and released from terrestrial environments (Doetterl et al. 2016; Doetterl et al. 2012). The intensity of carbon fluxes in the terrestrial carbon cycle is relatively high and can exhibit significant fluctuations in response to disturbances, such as land-use changes or natural events, leading to temporal variations in carbon fluxes on yearly and decadal scales (Kolbe et al. 2016; Smith et al. 1993). Thus, sediment erosion thus plays a crucial role in the terrestrial carbon cycle(Yoo et al. 2006).
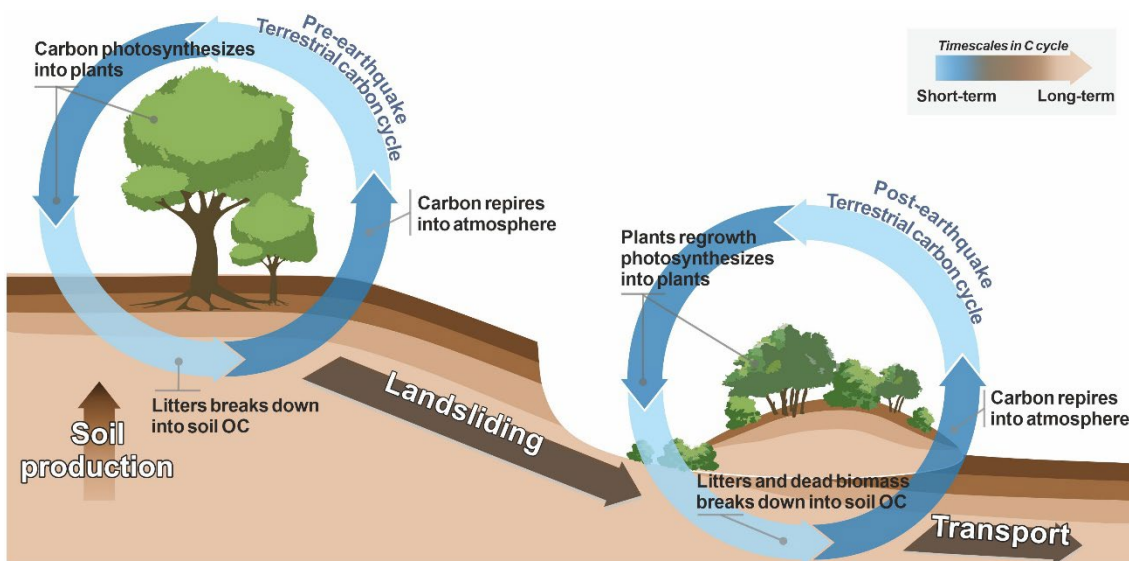
Figure 2.3 Terrestrial Carbon Cycle Pre- and Post-Earthquake
It depicts the continuous flow of carbon through carbon pools of atmosphere, vegetation and soil. It emphasizes the components involved in terrestrial carbon cycle and provides a clearer structure on the carbon transport following earthquake-induced landslides.

In the study of the terrestrial carbon cycle, many land models or ecosystem models are constructed to simulate biochemical process for carbon (Luo et al. 2012; Manzoni and Porporato 2009). These models commonly adopt a pool-and-flux framework (Luo et al. 2015; Luo and Weng 2011), where carbon pools represent different ecosystem components, and fluxes describe the movement of carbon between these pools. Key

processes modelled include carbon input via photosynthesis, distribution among various pools, donor pool-dominated carbon transfer, and the first-order decay of organic matter through respiration and decomposition (Luo et al. 2015). Donor-driven carbon transfer indicates when carbon moves primarily from plant to litter, largely influenced by the carbon stock in the plant pool. Similarly, transfers from litter to soil carbon pools are effectively modelled based on the size of the donor pool rather than the recipient pool. The interaction of these two processes forms the core mechanism driving internal equilibration within the system. Mathematically, these models are expressed through a set of ordinary differential equations (ODEs), which are often condensed into matrix form to facilitate the analysis of carbon dynamics, allowing predictions of carbon pool changes under varying conditions (Luo et al. 2017; Luo and Weng 2011; Sierra and Müller 2015). This structure forms the foundation of most terrestrial carbon models and is integrated into many Earth System Models (ESMs) to simulate carbon cycle processes on a global scale.

In an equilibrium state, carbon inputs to an ecosystem, primarily through processes like photosynthesis, are balanced by outputs such as respiration and decomposition. This balance indicates that carbon stored in various pools—such as vegetation, soil, and litter—remains relatively stable over time. Equilibrium is generally reached when ecosystems remain undisturbed for extended periods, allowing carbon inputs and outputs to stabilize (Luo and Weng 2011). Empirical studies have consistently shown that during forest succession and grassland recovery following disturbances, carbon levels in vegetation and soil pools tend to move toward equilibrium (Matamala et al. 2008; Yang et al. 2011). These systems often return to their pre-disturbance steady states. Consequently, carbon cycle models traditionally assume an equilibrium state before analysing carbon sequestration responses to environmental changes. A non-equilibrium state arises when carbon inputs and outputs become imbalanced, often driven by environmental disturbances or changes, such as fires, earthquakes, storms, land-use change, or climate change (Chambers et al. 2007b; Schuur et al. 2009).

Luo and Weng (2011) introduced the concept of "dynamic disequilibrium" as a framework to quantify carbon sinks and assess their stability in the context of global change. In this framework, at least three aspects of the internal carbon processes are affected by external forces: (i) disturbances alter pool sizes; (ii) equilibrium levels of carbon storage shift due to changes in carbon residence times; and (iii) ecosystem structures transition into different states of the carbon cycle. As shown in Figure 2.4(a), dynamic disequilibrium during a disturbance-recovery phase results in temporal variations in carbon sources and sinks over specific time scales. However, if the

disturbance regime remains unchanged, carbon sequestration will not be significantly impacted for long term. For the ODEs, as long as the equation and parameters remain unchanged, the system will eventually return to its original equilibrium state, regardless of changes in the initial values. Disturbances such as wildfires or extreme events typically lead to rapid carbon loss from vegetation biomass into litter carbon pool, followed by a monotonic recovery phase. Figure 2.4(b) illustrates a scenario where a change in the disturbance regime results in a new equilibrium. This is due to changes in the constant parameters of the ODEs, which reflect altered carbon residence times for each carbon pools. If the coincidence of extreme precipitation following wildfire leads to the increase of turnover rates of soil erosion, it may return to an alternative steady state post-disturbance. This scenarios explains how changes in turnover rates that regulate carbon fluxes, driven by external factors like long-term climate trends. The most complex situation arises when both ecosystem structure and disturbance regimes change, leading to a fundamental alteration of the ODEs. Quantifying these shifts under global change scenarios remains a significant challenge.
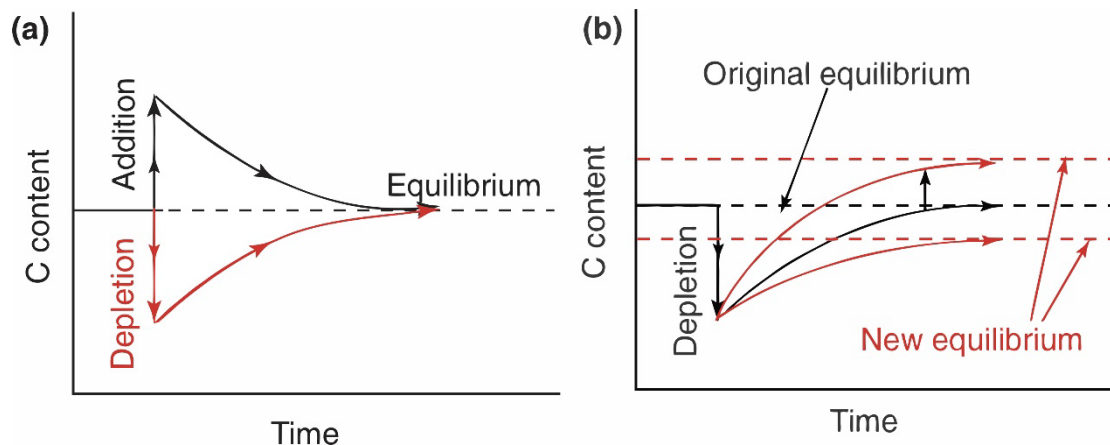
Figure 2.4 Forces Influencing the Dynamic Disequilibrium of Carbon Cycling
(a) Disturbances cause changes in carbon pools by either depleting or adding carbon to plants, litter, and soil, altering photosynthetic capacity, or changing carbon residence times. These disturbances create disequilibrium, but internal processes, like donor pool-dominated transfers, help drive the ecosystem back toward equilibrium; (b) Disturbances, such as global climate change, can alter the carbon cycle's recovery trajectory. Changes in carbon influx and residence times can shift the ecosystem to a new equilibrium, either higher or lower than the original. Figure is from Luo and Weng (2011)

2.2 Carbon export with cascading sediment

Earthquakes significantly influence the geomorphological evolution of active mountain ranges. EQTLs lead to the removal of forest biomass and soil from hillslopes (Garwood et al. 1979b). As illustrated in Figure 2.5, key mechanisms of carbon sequestration,

transport and deposition are closely linked with lateral sediment movement. EQTLs directly disrupt and mobilize terrestrial organic carbon, which has recently been sequestered from atmospheric CO_2 through photosynthesis. This process not only affect the redistribution of carbon in various reservoirs but also facilitate the carbon export within the landscape. As a result, EQTLs may set the disturbance regime in mountain forest ecosystem, influencing their carbon cycle, like productivity and respiration (Restrepo et al. 2009). Moreover, EQTLs have the potential to contribute significantly to the long-term sequestration of organic carbon, playing a crucial role in the carbon balance of mountainous regions.
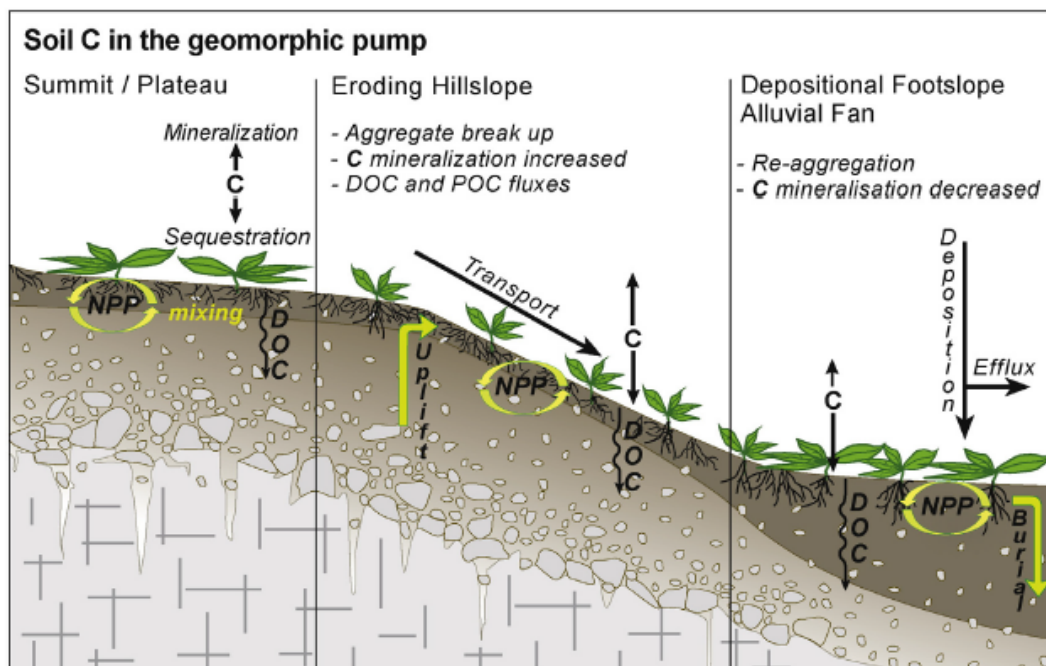
Figure 2.5 Overview on Soil Carbon Cycling in Dynamic Landscapes
The key mechanisms involved in C sequestration and release from soils along geomorphic pump. Figure is from Doetterl et al. (2016).

2.2.1 The impact of earthquake on carbon cycle

Strong earthquakes, as disturbances and extreme events, can significantly impact the terrestrial carbon cycle, even leading to dynamic disequilibrium (This definition is discussed in Section 2.1.2). Generally, the direct impact arises from earthquake-induced geological disasters, which damage regional vegetation and produce large quantities of woody debris. This alters the size of both vegetation and deadwood carbon pools, while it does not disrupt the equilibrium status of carbon cycle for each carbon pool. The process is also often accompanied by substantial material transport, resulting in the burial of soil organic carbon and damaged biomass. Where organic carbon content in fresh

EQTLs deposit has been measured, reported values include 0.17±0.04% for the top 0-10 cm in a tropical forest (Guariguata 1990), 0.15±0.05% for rockslides in western South Alps (Hilton et al. 2008a), and 0.24±0.07% for fresh channel deposits in Wenchuan earthquake affected region (Harvey et al. 2022; Liu et al. 2022). Although the organic carbon content in surface deposits decreases following an earthquake, the overall carbon pool size remains largely unchanged immediately after earthquake. However, due to the random nature of seismic events, especially in tectonically active regions, multiple earthquakes with varying magnitudes, spatial scales, and frequencies can lead to continuous and diverse dynamic disequilibrium. The cumulative effects of these disturbances may have significant long-term impacts on the carbon cycle.

The indirect effects of strong earthquakes primarily influence carbon flux and residence time by altering recovery process, particularly through changes in topography and geological settings. EQTLs result in significant material erosion from high elevations and deposition on hillslopes or in channels. From a morphological perspective, the scar areas of landslides tend to become steeper, slowing the accumulation of organic carbon and exposing geological layers (Velázquez and Gómez-Sal 2008), which may accelerate the oxidation of petrogenic organic carbon—a process that gradually releases carbon into the atmosphere. Alternatively, this exposure can enhance silicate weathering (Chamberlin 1899), which slowly absorbs atmospheric CO_2. Although landslide deposits tend to have gentler slopes, potentially reducing surface organic carbon loss (Walker et al. 1996), the physical and chemical properties of the landslide materials change significantly after the earthquake (Rasigraf and Wagner 2022). This leads to intensified physical erosion, but due to the burial and dilution of soil organic carbon by rocks, the transport rate of ecosystem organic carbon does not necessarily increase. The accumulation of soil organic carbon is influenced not only by rock types but also by grain size distribution, as well as the activity and abundance of soil microorganisms (Bellingham et al. 2001; Walker et al. 1996), all of which collectively determine the system's carbon flux balance. The differences between a single landslide scar and deposit are substantial, and this variability is further amplified by the thousands of coseismic landslides triggered by a major earthquake (Liu et al. 2003; Rosenbloom et al. 2006; Yoo et al. 2005, 2006). Additionally, research has shown that the energy released by earthquakes can raise soil temperatures (Guo et al. 2023; Zhang et al. 2015), which in turn stimulates microbial activity, altering respiration and decomposition rates and affecting carbon residence time. These earthquake-induced perturbations suggest a shift in the equilibrium state of the ecosystem, with a high likelihood that a new balance will be reached during recovery.

Carbon fluxes that affect terrestrial carbon cycling are not limited to exchanges between the terrestrial ecosystem and the atmosphere but also involve carbon transfer between the terrestrial ecosystem and the lithosphere (Hilton and West 2020; Smith et al. 2001). These fluxes are closely linked to post-earthquake sediment cascading, which influence the carbon cycle by altering carbon residence time (Billings et al. 2019; Booth et al. 2023; Rosenbloom et al. 2006). Section 2.2.2 argues that landslide debris, which consists of fractured bedrock, soil, colluvial material, and vegetation, can be stored in mountain ranges for centuries or even millennia. This extended residence time means that buried organic carbon may remain in these ranges for prolonged periods, potentially exerting a long-term influence on the ecosystem's carbon cycle. However, current knowledge on the impact of sediment erosion on the terrestrial carbon cycle remains limited. To better understand the potential regional and global climate impacts, it is crucial to further investigate these processes and mechanisms, particularly in relation to mega-earthquake events.

2.2.2 Carbon mobilization after EQTLs

Numerous studies have quantified the mobilization of organic carbon by landslides, underscoring their significant role in eroding terrestrial organic carbon and transferring it to river systems, thus influencing the global carbon cycle. Research has particularly emphasized the impact of extreme events, such as earthquakes or storms, on montane forests (Clark et al. 2016; Frith et al. 2018; Hilton et al. 2008b; Lu et al. 2010). For instance, in Sierra de Las Minas, rainfall from Hurricane Mitch triggered translational landslides across seven watersheds, resulting in the transfer of approximately 0.43 Mt of carbon, accounting for 3% of the pre-event carbon stored in vegetation and soils (Restrepo and Alvarez 2006). Similarly, Hurricane Katrina caused the loss of around 105 Mt of living carbon in the Gulf Coast forests (Chambers et al. 2007a). Following the 2008 Wenchuan earthquake, forest cover decreased by 0.5%, with approximately 3300 km² of forests disturbed (Chen et al. 2009). This event is estimated to have damaged 13.6 Mt of carbon, equivalent to 68% of China's mean annual carbon sink (Chen et al. 2009; Zhao and Zhou 2006). In Taiwan, landslides induced by Tropical Cyclone Morakot mobilized an estimated 377 ± 87 t C km^{-2} of above-ground biomass across a mountain catchment of 3320 km², with comparable impacts observed throughout mountain island (West et al. 2011).

To quantify the role of high-magnitude, low-frequency events in the erosion of terrestrial organic carbon on centennial time scales, few studies have addressed sustained organic carbon erosion by landslides over multiple decades. One such study examined 13 river

catchments in the western Southern Alps of New Zealand over four decades, estimating that landslides mobilized 7.6 ± 2.9 t C km^{-2} yr^{-1} of terrestrial organic carbon on average (Hilton et al. 2011b). In the Peruvian Andes, a study in the Kosñipata region found that landslides mobilized an average of 26 ± 4 t C km² yr^{-1} based on a 25-year landslide inventory (Clark et al. 2016). The carbon mobilization caused by multiple events over time can be roughly estimated by considering their recurrence intervals. For instance, a storm event with a ~10-year return period triggered landslides in Redwood Creek (714 km²), mobilizing 28 t C km^{-2}, or 2.8 t C km^{-2} yr^{-1} when prorated for the return interval (Madej 2010). Similarly, if Hurricane Mitch is considered a landslide-triggering event with a recurrence interval of 20 or 80 years, the estimated carbon flux rate would be 8–33 t C km^{-2} yr^{-1} (Ramos Scharrón et al. 2012). For the Wenchuan earthquake (M_w 7.9), with an estimated 1000-year recurrence interval and affecting 40,000 km², the event contributed to terrestrial organic carbon mobilization of ~34 t C km^{-2} yr^{-1} (Chen et al. 2009).

Most studies have quantified the mass and flux of terrestrial organic carbon mobilized by landslides using satellite imagery to map landslide occurrences, combined with field-based estimates of carbon stocks in forest biomass (Ramos Scharrón et al. 2012; Ren et al. 2009; Restrepo and Alvarez 2006; West et al. 2011). The intensity of this carbon flux largely depends on the terrestrial organic carbon stock levels in the study area. For example, total organic carbon stocks in tropical and mid-latitude mountain regions differ greatly. Forest carbon stocks on the Tibetan Plateau range from 600 to 2100 Mg ha^{-1} (Wu et al. 2024), while tropical rainforests in lowland Southeast Asia hold between 250 and 349 Mg ha^{-1} (Descloux et al. 2011). At the regional level, the spatial variability of landslide-induced carbon mobilization is influenced by multiple factors that lead to hillslope failure (Densmore and Hovius 2000; Hilton et al. 2011b; Lin et al. 2008). Different landslide triggers, such as rainfall or earthquakes, produce varying outcomes. Rainfall-triggered landslides are typically shallow, smaller in scale, and more concentrated (Basher et al. 2018), while earthquake-triggered landslides tend to involve large rockfalls and debris flows, resulting in greater destruction (Fan et al. 2019b). Extreme events, such as Typhoon Morakot in Taiwan, which caused up to 2965 mm of rainfall in four days, can result in widespread landslides across a majority of mountainous area (West et al. 2011). Earthquake-induced landslides are often more destructive and involve significant redistribution of nutrients, which complicates vegetation recovery due to limited soil nutrients and moisture availability (Ren et al. 2009). Ecosystem processes and carbon stocks also vary due to sharp environmental gradients. In the western Southern Alps, carbon mobilization is strongly influenced by precipitation

patterns and rock exhumation (Hilton et al. 2011b; Molnar et al. 2007). Landslide distribution can, to some extent, indicate the variability of carbon mobilization, although uncertainties persist due to differing approaches of landslide inventory and variations in estimates of soil and vegetation carbon stocks.

To investigate the fate of terrestrial organic carbon mobilized by landslides, it is crucial to determine the degree of connectivity between landslides and stream networks, as this governs the amount of material available for fluvial export (Harvey 2001; Korup and Landforms 2005; Schwab et al. 2008). In extreme cases, such as mountain islands of Taiwan, nearly all carbon released by landslides exits the system and is deposited offshore, indicating high connectivity (West et al. 2011). In contrast, in Sierra de Las Minas, about 30% of the carbon mobilized by landslides is retained on hillslopes or delivered to first-order streams, where there is a higher potential for long-term sequestration (Ramos Scharrón et al. 2012). The remaining 70% reaches higher-order streams, where carbon retention remains uncertain (Ramos Scharrón et al. 2012). The stability of these channel deposits is influenced by their proximity to the active channel and by factors such as stream power, hydraulic roughness, and resistance to erosion (Restrepo et al. 2009). In the western Southern Alps, an estimated $71 \pm 3\%$ of landslide-mobilized TOC remains on hillslopes, corresponding to 5.4 ± 3.0 t C km^{-2}yr^{-1} being retained (Hilton et al. 2011b). Similarly, following the Wenchuan earthquake, studies by Li et al. (2016) revealed that 57% of the total coseismic landslide volume remained on hillslopes, with limited initial influence of connectivity on fine sediment fluxes. A sediment budget analysis for the first decade after the 2008 Wenchuan earthquake by Francis et al. (2022) showed that 88% of the coseismic sediment remained on hillslopes. These findings suggest that a significant portion of clastic sediments likely remains along hillslopes, potentially burying disturbed living biomass and soil organic carbon. In such cases, landslides may contribute to carbon sequestration over shorter timescales if vegetation recovers more rapidly than carbon is exported from the system.

Notwithstanding these findings, the mobilized carbon that remains on hillslopes and in channel deposits may play a critical role in the overall organic carbon budget of mountain ranges. Three primary pathways for this carbon have been proposed. The first suggests that most of the biomass from dead or damaged trees is eventually respired and released into the atmosphere (Billings et al. 2019; Schimel 1995). After significant disturbance events, such as landslides, the carbon stored in coarse woody debris (CWD) is typically released over time through decomposition (Chambers et al. 2007a). A second pathway posits that some of the remaining carbon may become long-term stable, transferring back into soil organic carbon. Coarse woody debris contributes significantly to carbon and

nutrient storage on hillslopes (Richardson et al. 2009). If this carbon is trapped in unchanneled deposits on hillslopes, it could be protected from oxidation due to reduced aeration and become physically stabilized by vegetation regrowth (Velázquez and Gómez-Sal 2008; Walker and Shiels 2008). The third possibility is that mobilized carbon could be temporarily stored within mountain ranges for hundreds and thousands of years (Pearce and Watson 1986; Yanites et al. 2011; Yanites et al. 2010). Eventually, it may be transported out of the system through erosion processes as the landscape turnover. Further research is necessary to fully understand the fate of the remain carbon and its implications for carbon cycling in mountainous regions.

2.2.3 Carbon transportation after EQTLs

Carbon mobilization by landslides does not necessarily equal riverine transfer after landslides. While landslides mobilize carbon into fluvial landscapes, this does not guarantee its transport by rivers. In fluvial systems, particulate organic carbon (POC) is typically measured from the fine fraction (<sand size) of the suspended load (Hatten et al. 2010; Hilton et al. 2008a). However, landslides mobilize carbon across a broad range of grain sizes, including coarse debris, which is often not accounted for in sediment flux measurements (Fan et al. 2018; Harvey et al. 2022). During continuous rainfall, debris flows transport large amounts of material, including driftwood, into gullies (Cui et al. 2012). These debris flows are difficult to capture in sediment flux records. Driftwood from damaged vegetation often forms temporary dams of deposit and wood in main channels and tributaries, which break in a chain reaction, amplifying debris flow intensity and further eroding woody debris buried along with clastic sediments (Cui et al. 2012). Following the Wenchuan earthquake, sediment budgets demonstrate that debris flows are the dominant process of delivering clastic sediment into channels and fluvial systems (Francis et al. 2022; Harvey et al. 2022). The amount of carbon mobilization by landslides is likely greater than that by POC transfer. In the western Southern Alps, landslide sediments deliver an estimated modern organic carbon concentration between 0.01 wt% and 0.1 wt% within catchments, assuming a mixture of clastic sediment, soil, and vegetation. By contrast, riverine export of POC from modern organic carbon sources has been estimated at approximately 40 t C $km^{-2}yr^{-1}$, with a carbon concentration of ~0.3 wt% of total clastic sediment mass (Hilton et al. 2008a). The lower carbon content in landslide deposits shows that landslides, especially when deeper than the soil layer, is expected to contain a lower content of terrestrial organic carbon compared to fluvial systems.

In active mountain belts, especially after mega earthquake, increasing clastic sediments supply high suspended sediment concentrations in rivers (Jin et al. 2016; Wang et al. 2015). Bare slopes with low surface roughness after landslides significantly reduce the capacity for water infiltration. This has the effect of increasing runoff and flow concentration. These processes promote fluvial carbon export. As shown in Figure 2.6, previous studies show that export yields of terrestrial POC are positively related to the yield of suspended sediment (Hilton et al. 2011a; Komada et al. 2004; Wang et al. 2016), revealing that POC export is mostly controlled by physical erosion. Galy et al. (2015) find that terrestrial POC export is primarily controlled by the capacity of rivers to transport POC, and is largely insensitive to the magnitude of terrestrial primary production. However, whether the overall concentration of terrestrial organic carbon in rivers increases or decreases by landsliding remains uncertain. Terrestrial POC is supposed to be diluted by mineral phases at high sediment yield (Galy et al. 2015). While Wang et al. (2016) indicate that the relative contributions of POC from biospheric and petrogenic sources in the fine suspended load remain similar to pre-earthquake levels. This suggests that the fine-grained component of landslide material contributing to suspended sediments in the immediate aftermath (around 4 years) of the earthquake closely resembles pre-earthquake soils. One possible explanation is that small and shallow landslides deliver sediment with higher organic carbon concentrations, as the carbon from soil and vegetation is not significantly diluted by clastic material (Hilton et al. 2008b). This quantitative study after 2008 Wenchuan earthquake capture the transient changes in carbon fluxes over decadal timescale, but it does not necessarily indicate long-term trends.
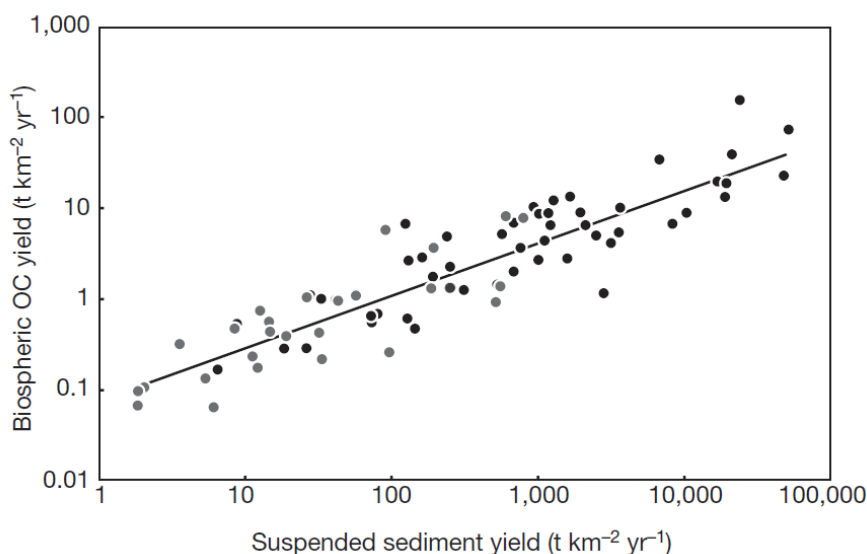
Figure 2.6 Relationship between Terrestrial POC Yield and Suspended Sediment Yield

As for the further fate of terrestrial carbon, more recently, studies suggest it is likely to be buried in offshore or marine sediment, contributing to the long-term carbon sink. Landslides caused a large increase in suspended sediment discharge, which is strongly linked to sediment accumulation and burial efficiency of organic carbon. It is indicated about 70-85% of the organic carbon buried in Bengal Fan is from terrestrial organic carbon, which acting as a long-term sink for atmospheric carbon (Galy et al. 2007). Himalayan erosion contributes to a significant carbon burial in oceanic sediment, with minimal oxidation during transport and burial due to low oxygen availability in depositional environment (Galy et al. 2007; Galy et al. 2015). The role of terrestrial carbon burial acts as dominant carbon fluxes in the overall carbon budget. Frith et al. (2018) examine the sedimentary fill of Lake Paringa, New Zealand, and the carbon isotope analysis reveal a significant increase in terrestrial carbon accumulation following four major earthquakes. This also highlights the supply-limited nature of terrestrial carbon in mountain rivers. These pulses of carbon accumulation account for $23 \pm 5\%$ of the total time recorded, yet contribute $43 \pm 5\%$ of the terrestrial carbon deposited in the sediment core. This demonstrates the substantial contribution of large earthquakes to carbon export from mountain forests over millennia.

2.3 Carbon recovery after earthquake

Carbon recovery in terrestrial ecosystems following an earthquake is primarily driven by the interplay between vegetation regrowth and soil development. Earthquakes can severely disrupt existing vegetation, reducing carbon sequestration via photosynthesis, but they may also stimulate biodiversity and facilitate carbon re-accumulation on exposed landslide surfaces (Dymond 2010; Schomakers et al. 2017). Simultaneously, earthquakes accelerate soil erosion, increasing soil carbon loss while promoting carbon burial, effectively removing carbon from active carbon cycle (Doetterl et al. 2016). The recovery process is highly complex and influenced by multiple factors (Rasigraf and Wagner 2022). However, the most critical determinant is the effect of earthquake triggered geological disasters, which induce distinct physical and chemical changes in hillslope deposits. This differentiates earthquake impacts from other disturbances such as land-use change, fire and etc. Figure 2.7 illustrates a simplified model of primary succession on disturbed soil and vegetation (Rasigraf and Wagner 2022).
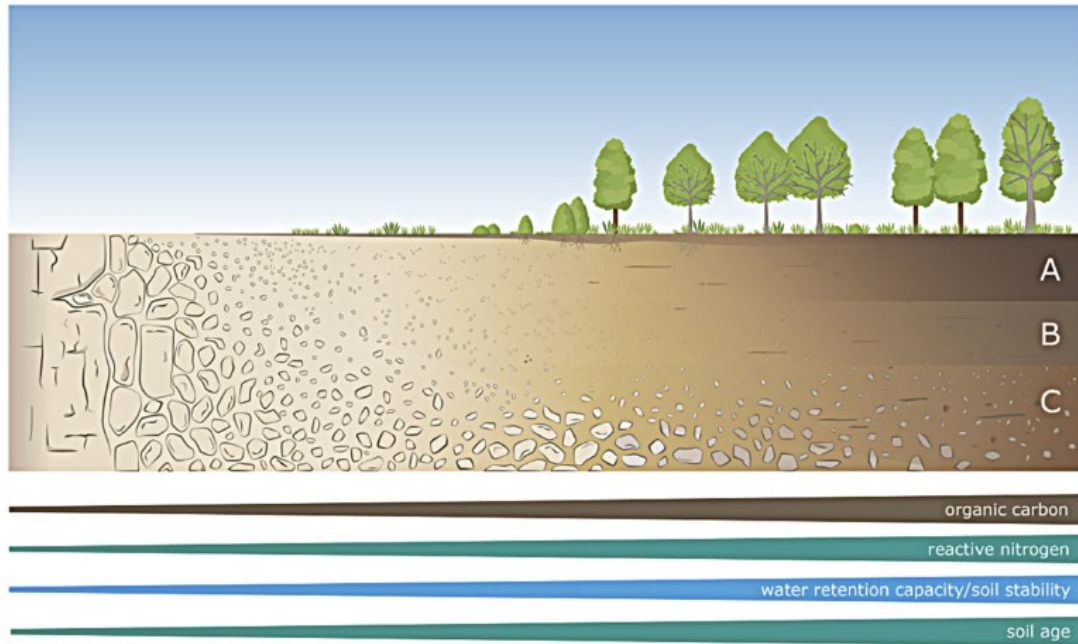
Figure 2.7 Simplified Scheme of Soil Development and Vegetation Regrowth in a Landslide Chronosequence
Soil organic carbon accumulates as grain size distribution decreases and soil aggregate stability increases over time. Concurrently, vegetation biomass increases through colonization and successional processes. Figure is from Rasigraf and Wagner (2022)

2.3.1 Soil carbon recovery

Soil organic carbon (SOC) is a key indicator of soil health and productivity, as it reflects the capacity of soil to store carbon, regulate water, and support biological activity. When a landslide occurs, large amounts of SOC are mobilized along with soil and debris, and the exposed surface becomes prone to further erosion, exacerbating the loss of carbon (Smith et al. 2001). However, over time, the revegetation of landslide-affected areas and the reformation of soil structure can lead to the gradual re-accumulation of soil organic carbon. In the Carpathian Mountains, soil organic carbon stocks, along with nitrogen and phosphorus, increased rapidly during the first 100 years after mass wasting events and reached a steady state thereafter (Vindušková et al. 2019). This rapid initial accumulation phase is crucial for understanding the timeline of ecosystem recovery and the role of early successional species in facilitating soil development.

The rate at which SOC recovers after a landslide depends on multiple factors, including climate, the nature of the landslide, vegetation type and soil characteristics. Understanding these factors is essential for predicting the timeline of soil recovery and for developing restoration strategies that promote carbon sequestration:

Climatic Conditions: Temperature and precipitation are among the most critical factors influencing SOC accumulation rates. Higher temperatures generally enhance microbial activity, which accelerates the decomposition of organic matter and the cycling of nutrients. Conversely, higher precipitation levels facilitate the leaching of nutrients, influencing soil fertility and microbial dynamics. In temperate climates, such as those of New Zealand, SOC recovery rates have been shown to be faster due to optimal conditions for microbial and plant activity (Larsen et al. 2014).

Vegetation Type: The type of vegetation that colonizes the landslide surface plays a significant role in determining the trajectory of SOC accumulation. Early successional species, such as grasses and nitrogen-fixing plants, often dominate the initial stages of revegetation and help establish a foundation for later successional species. In Taiwan, the pioneer grass *Miscanthus floridulus* was found to facilitate initial SOC recovery after landslides, with annual carbon accretion rates of around 200 ± 50 t C km^{-2}yr^{-1} in the early stages (Schomakers et al. 2017). Over time, bamboo species (*Phyllostachys*) invaded the site, further enhancing SOC accumulation. In tropical landslides, species that form symbiotic relationships with nitrogen-fixing bacteria, such as *Rhizobia* and *Cyanobacteria*, play a crucial role in overcoming nitrogen deficiency, which is a key limiting factor for plant growth on newly exposed soils (Bergman et al. 1992; Walker et al. 1996).

Soil Texture and Composition: The physical properties of soil, including its texture, bulk density, and aggregate stability, influence the rate of carbon accumulation. Soils rich in clay particles tend to retain more organic carbon due to their ability to form stable aggregates, which protect organic matter from microbial decomposition (Schomakers et al. 2017). In contrast, sandy soils with low aggregate stability are more prone to erosion and carbon loss. Research from the Carpathian Mountains demonstrated that SOC accumulation was fastest in the accumulation zones of landslides, where fine silt and clay fractions were more abundant (Błońska et al. 2017).

Topography and Slope Stability: The topographic position within the landslide zone also affects SOC recovery rates. Scar zones, located at the highest elevation of the landslide, tend to have the lowest SOC content and slowest recovery rates due to their instability and poor nutrient availability (Adams and Sidle 1987). In contrast, accumulation zones at the base of the landslide tend to accumulate more organic matter and nutrients, supporting faster soil recovery and vegetation establishment (Walker and del Moral 2003; Walker and Shiels 2008).

Despite the progress in understanding SOC recovery after landslides, several challenges remain. One major limitation is the heterogeneity of landslide-affected landscapes, which makes it difficult to generalize findings across different ecosystems. The material transported during a landslide is often a mix of bedrock, soil, and vegetation, creating highly variable conditions for soil formation and carbon accumulation (Hungr et al. 2014). Additionally, the instability of landslide surfaces, particularly in the early stages after the event, can lead to further erosion and loss of SOC before stabilization occurs (Trustrum and De Rose 1988). Another challenge is the lack of long-term studies on SOC recovery. While chronosequence studies provide valuable insights into soil and ecosystem development over time, they often rely on space-for-time substitution, which has been criticized for oversimplifying the complex interactions between soil, climate, and biota (Johnson and Miyanishi 2008). Long-term monitoring of permanent plots offers a more accurate assessment of SOC recovery but requires substantial time and resources (Coradini et al. 2022).

Moreover, the role of microbial communities in SOC recovery remains largely underexplored. Microorganisms, including bacteria and fungi, play a critical role in soil formation and carbon cycling, yet their functional dynamics in landslide-affected soils are not well understood (Lehmann et al. 2017). Studies from other chronosequences, such as glacier forefields, have shown that microbial communities undergo significant shifts during soil succession, with early colonizers such as cyanobacteria and lichens contributing to carbon and nitrogen accumulation (Fernández-Martínez et al. 2017). Similar processes are likely to occur in landslide soils, but more research is needed to clarify the specific contributions of microbial communities to SOC recovery.

Given the increasing frequency and intensity of landslides due to climate change, understanding the factors that influence SOC recovery is more important than ever. Current research efforts are focused on improving the predictability of SOC recovery rates in different climatic and geological settings, as well as exploring the potential for landslide-affected areas to serve as long-term carbon sinks. One promising avenue of research involves the use of remote sensing technologies, such as LiDAR and satellite imagery, to monitor landslide dynamics and soil recovery over large spatial scales (Guzzetti et al. 2012). These tools offer the potential to track changes in vegetation cover, topography, and soil properties in near real-time, providing valuable data for assessing SOC recovery and informing restoration strategies. Another important area of research is the integration of microbial ecology into studies of SOC recovery. By elucidating the functional roles of microbial communities in soil formation and carbon cycling, researchers can develop more effective strategies for enhancing carbon sequestration in

post-landslide landscapes. Understanding the interactions between plants, microbes, and soil aggregates will be crucial for predicting the long-term stability of SOC in these systems (Lehmann et al. 2017). While significant progress has been made in understanding the factors that influence SOC recovery after landslides, much remains to be learned about the complex interactions between soil, climate, and biota. By addressing these knowledge gaps, future research can contribute to the development of effective restoration strategies that promote carbon sequestration and ecosystem resilience in landslide-affected regions.

2.3.2 Vegetation carbon recovery

Vegetation recovery following EQTLs, is a complex ecological phenomenon that involves plant colonization, successional dynamics, and subsequent impact on vegetation biomass and carbon sequestration. Vegetation colonization, the initial phase of revegetation, plays a pivotal role in shaping the subsequent ecological succession (Walker et al. 2009). Depending on species interactions, colonization can either delay or accelerate succession. In some cases, dominant species can spread over disturbed areas and inhibit succession for decades (Vindušková et al. 2019; Walker and del Moral 2003), while in other cases, mutual facilitation between species, particularly those involved in nitrogen-fixing symbioses, can enhance colonization and accelerate (Bellingham et al. 2001). As vegetation re-establishes, carbon is sequestered in vegetation biomass through photosynthesis, contributing to the recovery of ecosystem carbon storage. Effective vegetation recovery restores ecosystem structure and function. Following colonization, the type of plant succession—whether primary or secondary—strongly influences vegetation carbon accumulation. Primary succession occurs when vegetation growth begins from scratch on bare substrates, such as newly exposed landslide areas, whereas secondary succession involves recovery on disturbed soils or substrates containing biological legacies, such as residual plants and disturbed soil organic carbon. The presence of 'biological legacies' (Guariguata 1990; Walker et al. 2009; Walker et al. 1996) in secondary succession have a significant influence on vegetation dynamics and biodiversity, potentially accelerating the recovery process (Prach and Walker 2019).

Vegetation recovery exhibits several key characteristics that shape ecosystem restoration process. Firstly, natural disturbance is an integral driver of forest dynamics, and contribute to the diversity and adaptive capacity of ecosystems (Gutschick and BassiriRad 2003). EQTLs open up new areas of surface where carbon can be fixed, promoting high rates of biomass accumulation in young forest sections (Restrepo et al. 2009; Wardle et al. 2004; Zaehle et al. 2006). In the temperate montane forest of the

southern Alps, the measured net ecosystem productivity (NEP) after landslides is around 3 times the estimated from mature forest (Hilton et al. 2011b). Second, landslides create high abiotic heterogeneity. The geomorphological differences between upper scar zones and lower deposition zones result in varied levels of fertility and stability, leading to different recovery trajectories. In more stable and fertile areas, biomass and species richness increase rapidly, resembling adjacent forest composition, while in unstable and infertile zones, succession progresses slowly and is primarily controlled by abiotic factors (Walker et al. 1996). Lastly, residual vegetation left by landslides provides shade and nutrients to colonizing plants and serving as perches for seed-dispersing animals (del Moral and Wood 1993). In tropical Andean forests, residual vegetation accelerates regeneration and can substantially contribute to early forest recovery on landslide. The positive impact of residual vegetation on canopy height is observed, and its effect can persist for at least 25 years (Freund et al. 2021). Residual vegetation thus plays a vital role in determining the successional pathways and recovery rates of ecosystems after landslides (Shiels and Walker 2003).

Most literature on vegetation succession reveal that a complex interplay of factors affect the vegetation recovery, with soil properties, landslide age and elevation being three of the most significant determinants. Soil properties such as nutrient availability and aggregate stability are crucial for early successional stages. Plant species composition is often shaped by limiting factors like nitrogen and water availability, which vary with topography (Velázquez and Gómez-Sal 2007). Pioneer species can overcome initial nutrient deficiencies by forming symbiotic relationships with nitrogen-fixing bacteria, helping to stabilize soils and promote further vegetation growth (Bergman et al. 1992). However, soil erosion can slow this process by hindering both physical stabilization and successional progression (José et al. 1996). Biomass accumulation and canopy closure rates vary significantly with landslide age, with younger landslides often showing rapid initial growth. Observations from LiDAR data and aerial photography suggest that full canopy closure can take anywhere from 2 to 25 years, depending on the presence of residual vegetation and local environmental conditions (Blodgett and Isacks 2007). Elevation also plays an important role, affecting factors such as temperature, precipitation, and soil moisture, which in turn influence vegetation growth. Higher elevations can provide favourable conditions for vegetation recovery, especially in areas where soil moisture and topography support plant growth (Lu et al. 2012). However, in some regions, such as the tropical Andes, biomass accumulation rates decline with elevation (Freund et al. 2021), indicating the complex relationship between elevation and vegetation growth interacting with other factors.

The rate and time of vegetation carbon recovery following landslides are critical components in understanding terrestrial carbon cycle. Vegetation biomass accumulation varies significantly across different regions and ecosystems globally. For example, studies in the Kokatahi Valley, New Zealand, show high net ecosystem productivity (NEP) with a biomass accumulation rate of 188 ± 21 t km^{-2}yr^{-1}, corresponding to a carbon sequestration rate of 94 ± 11 t C km^{-2}yr^{-1} (Hilton et al. 2011b). This rate is substantially higher compared to global averages, such as the estimated 30 t C km^{-2}yr^{-1} for temperate forests (Dixon et al. 1994) and 37 ± 21 t C km^{-2} yr^{-1} in lowland Amazonian forests (Phillips et al. 1998). However, these are lower than bamboo-dominated landslides in Taiwan, which shows the highest recovery rate of 200 t km^{-2}yr^{-1} after 41 years (Schomakers et al. 2017). In terms of recovery time, vegetation carbon recovery can vary from decades to centuries corresponding to the significant variability in recovery rates. These rates highlight the potential for significant carbon sequestration in post-landslide environments, though the recovery process is highly variable across different geographic locations and climates. Except the environmental factors, these discrepancies arise from different methods applied to estimate vegetation carbon recovery.

The most accurate method for studying vegetation recovery involves calculating vegetation density, species diversity, basal area, vegetation coverage and root density from field data. However, it requires significant manpower, financial resources and time. Monitoring carbon accumulation at a single landslide site can produce reliable results, but its limited scope makes it unsuitable for large-scale or long-term vegetation recovery studies (Qiu et al. 2015; Restrepo et al. 2009; Zeng et al. 2016). In this context, landslide chronosequences have been widely used to examine vegetation succession in initial ecosystems (Clark et al. 2016; Rasigraf and Wagner 2022; Schomakers et al. 2017). This method combines remote sensing to analyse multiple landslide scars over time, identifying their age and developmental stages. The age of a landslide scar is determined by the time elapsed between the landslide event and sample collection, assuming the landslide has not been reactivated. Remote sensing techniques provide a more efficient and scalable approach for monitoring vegetation recovery. By utilizing indices like the Normalized Difference Vegetation Index (NDVI) and Fractional Vegetation Coverage (FVC) (Du et al. 2021; Li et al. 2022; Sun et al. 2021), researchers can track vegetation changes across large areas. However, satellite data has limitations in directly measuring biomass or forest structure, and thresholds for damage extraction can be subjective. Moreover, the availability of high-quality temporal data remains a challenge for long-term assessments. Recently, Freund et al. (2021) combined LiDAR-derived canopy height map coupled with landslide chronosequences to study post-landslide successional

processes in the Peruvian Andes, linking these to biomass recovery at a landscape scale. Canopy height recovery is clearly visible from LiDAR data (Dislich and Huth 2012), but this latter phase of biomass accumulation through compositional change after the canopy has closed is undetectable from LiDAR alone (Freund et al. 2021). Combining spaceborne and field-based methods holds significant potential for reducing uncertainties in the terrestrial carbon budget and improving carbon cycle modelling.

Chapter 3

Study Area

3.1 Longmenshan mountain range

The Longmenshan region encompasses a broad area that includes the Longmen mountain in central Sichuan, the Minshan mountains to the west, the Chengdu Plain to the east, and the Longquan mountains (Deng et al. 1995). This area corresponds to a Mesozoic collisional plate margin, formed during the closure of the Paleo-Tethys Ocean and the collision of the Qiangtang block with the North China-Kunlun-Qaidam and South China blocks (Gorum et al. 2011). As illustrated in Figure 3.1, the Longmenshan thrust belt serves as a central bridge among three major tectonic units at the eastern margin of the Tibetan Plateau, marking a topographic step between the westward Songpan-Ganzi fold belt and the eastern Sichuan Basin (Jiang et al. 2015; Parker et al. 2011; Wang et al. 2001). Elevations rise sharply from approximately 600 m in the Sichuan Basin to over 6500 m within a horizontal distance of less than 50 km (Jiang et al. 2015; Kirby et al. 2002; Kirby et al. 2003; LEI et al. 2009; Sun et al. 2021).

This region is characterized by active orogeny and foreland basin systems, with significant fault zones including the Longmenshan, Xianshuihe, and East Kunlun faults. The Longmenshan Fault, located on the eastern edge of the Bayan Har Block, extends from Luding and Tianquan in the south, traversing through Guanxian, Maowen, Beichuan, and into the northern Guangyuan and Mianxian regions. This faulttrends NE-SW, spanning approximately 500 km in length and 30–40 km in width (Chen et al. 2007). It comprises three primary fault segments: the Guanxian-Jiangyou fracture (hill-front fracture), the Yingxiu-Beichuan fracture (mid-fracture), and the Wenchuan-Mao County fracture (hill-back fracture) (Huang and Engineering 2009; Jia et al. 2006; Wang et al. 2001). Before the 2008 Mw 7.9 Wenchuan earthquake, GPS observations indicated that the slip rate across the Longmenshan Fault Zone did not exceed 2 mm/yr, with individual fault activity rates not surpassing 1 mm/yr (Lei and Zhao 2009; LEI et al. 2009; Meng et al. 2008; Teng et al. 2010; Xu et al. 2008; Zhang et al. 2004). Geomorphic offsets and age determinations suggested that the late Quaternary slip rate for the Longmenshan Fault was only 2–3 mm/yr (Gorum et al. 2011; Zhang 2008). Consequently, historical seismic activity in the Longmenshan thrust belt and its adjacent areas was relatively weak compared to other segments of the north-south seismic structural belt. Notable pre-2008 events included a Mw 7.5 earthquake in 1933 near the Minshan uplift area and a sequence of three earthquakes (Mw 6.7-7.2) in 1976 around Songpan. Additionally, a Mw 6.5 earthquake occurred in 1957 the hill-back fracture, while a Mw 6.2 earthquake was recorded in 1958 along the mid-fracture near Beichuan. The hill-front fracture

experienced three significant events of Mw 6–6.2 in 1970, 1828, and 1327 (Deng et al. 1995; Xu et al. 2008).

However, this seismic pattern dramatically shifted after 2008, when the Longmenshan Fault Zone experienced the Mw 7.9 Wenchuan earthquake. It was the first recorded event exceeding Mw 7.0 along the eastern boundary of the Bayan Har Block. This was followed by a series of major earthquakes, including the 2013 Lushan earthquake, the 2014 Kangding earthquake, the 2017 Jiuzhaigou earthquake, and the 2022 Luding earthquake. Over 15 years, seven significant earthquakes occurred within the eastern Bayan Har Block, primarily along the boundary faults of the Maerkang sub-block. These events indicate that strain accumulation in the region had reached, or was near, the breaking point of the underlying rocks. These seismic activities triggered numerous earthquake-induced landslides and other geological disasters, further exacerbating the region's geological instability (Banghui et al. 2018).
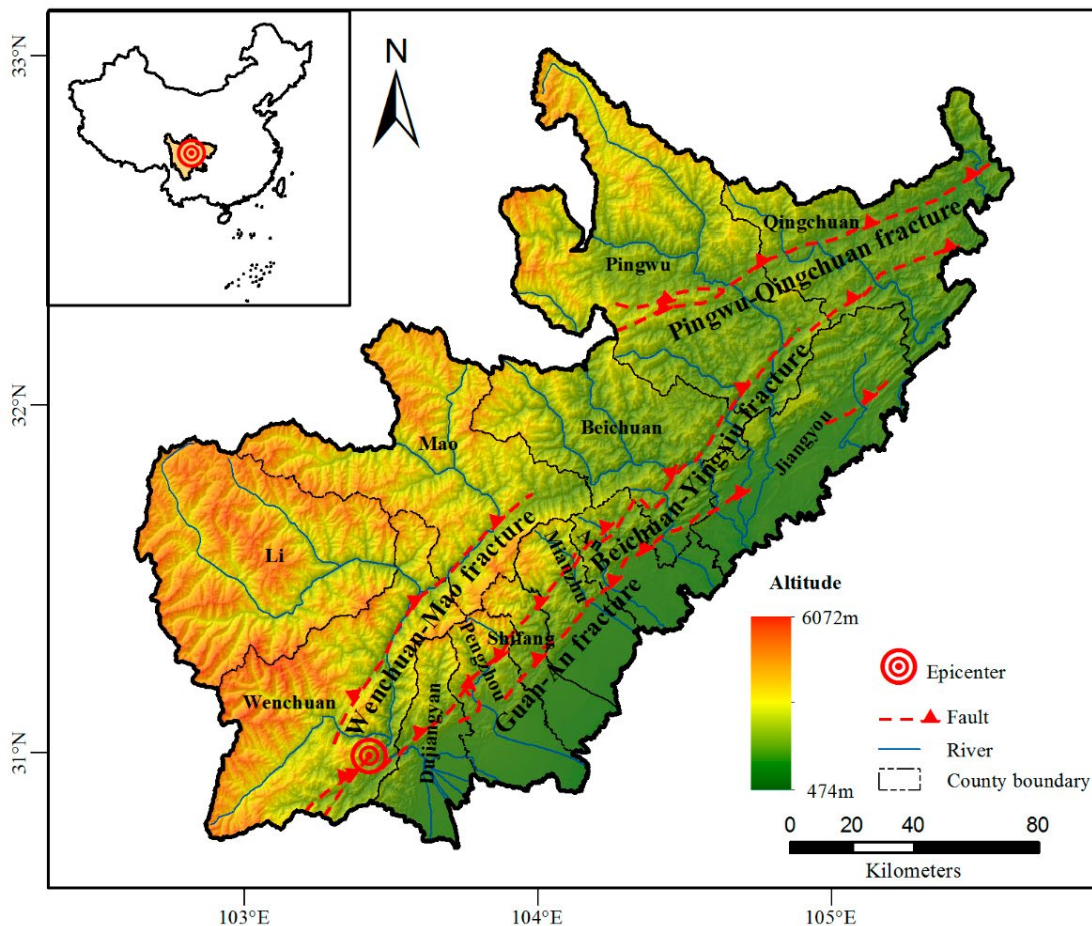
Figure 3.1 Longmenshan Thrust Belt
The Longmenshan Thrust Belt is located in northern Sichuan Province in the transitional zone between the Qinghai-Tibet Plateau and the Sichuan Basin (Figure is from Jiang et al. (2015)).

Three major tectono-stratigraphic units are identified in the Longmenshan region: Mesoproterozoic basement, pre-Indosinian marine sediments from the Sinian

(Neoproterozoic) to the middle Upper Triassic, and syn- to post-Indosinian terrestrial sediments (Upper Triassic Xujiahe Formation to Quaternary) (Chen and Wilson 1996). The Mesoproterozoic basement consists of granite, granodiorite, acidic to intermediate volcanics, and various schists, which were deformed and metamorphosed during the Jinning and Chengjiang movements (Tong 1992; Wang et al. 1989). These basement rocks are exposed in massifs along the southwest margin of the Sichuan Basin (Kirby et al. 2002). Overlying this basement are Sinian (Neoproterozoic) volcanics and dolomites, along with turbidites, shales, and minor limestone and basalt deposits at the southeastern margin of the Songpan-Ganzi fold belt(Chen and Wilson 1996; Kirby et al. 2002). The syn- to post-Indosinian terrestrial sediments comprise wedge-shaped deposits of fluvial mudstone, sandstone, and conglomerate, which accumulated in flexural basins ahead of the thrust zone (Burchfiel et al. 1995; Chen et al. 1994).

The climate of the Longmenshan region is shaped by the humid subtropical monsoon, influenced by both the East Asian and Indian monsoons. The region experiences an average annual precipitation of 1200-1250 mm, with 70-80% concentrated between May and September, contributing to warm and humid summers (Fan et al. 2018; Liu‑Zeng et al. 2011; Wang et al. 2015; Wang et al. 2022). The average annual temperature ranges from 13-15°C, decreasing as elevation increases, exhibiting a west-high, east-low distribution pattern (Fan et al. 2018; Wang et al. 2022; Yunus et al. 2020). Precipitation varies across the region, with the southern high-altitude areas receiving more rainfall than the northern parts during summer (Wang et al. 2022). This substantial summer rainfall also contributes to high suspended sediment concentrations, with 97% of suspended sediments transported during the monsoon season, significantly influencing post-seismic sediment dynamics and frequently triggering debris flows in July and August (Fan et al. 2018; Ge et al. 2015; Tang et al. 2012; Yang et al. 2021). Additionally, the warm, moist climate fosters rich biodiversity, facilitating the rapid revegetation of landslide deposits, with some areas expected to recover within 18 years following the 2008 Wenchuan earthquake (Di et al. 2010; Yunus et al. 2020).

The Longmenshan region exhibits diverse vegetation types due to its varied climate and topography, with distinct vertical zonation in the mountainous areas (Sun et al. 2021; Wang et al. 2022). Subtropical evergreen broadleaf forests occurs below 1800 m, while mixed broadleaf and coniferous forests are formed between 1800 m and 2200 m. At higher altitudes, cold-resistant coniferous forests, predominantly consisting of Abies, Picea, Pinus, and Tsuga. This region supports over 800 species of woody plants from 103 families, featuring significant tree species including Cunninghamia lanceolata, Cryptomeria fortunei, Cinnamomum, and Machilus, along with valuable resources like

Ginkgo biloba, Phellodendron amurense, and wild kiwifruit (Group 1980; Wu et al. 2023). Rare plants such as Davidia involucrata and Tsuga contribute to the region's biodiversity, which includes 10 species of first-class protected plants and 29 species of second-class protected plants, as well as numerous protected animal species (Wang et al. 2012). The eastern mountainous areas are rich in firs, spruces, and pines, while the western regions are largely characterized by semi-arid shrublands, with some areas receiving as little as 600 mm of annual precipitation and primarily supporting sparse alpine perennial plants. Above 5000 m, rocky desert conditions prevail (Wu et al. 2023).

3.2 2008 Wenchuan earthquake

On May 12, 2008, the Wenchuan earthquake struck along the Longmenshan fault, with its epicentre near Yingxiu (31.01°N, 103.42°E), registering a magnitude of Ms 8.0 and a focal depth of 14-19 km (Yueping 2008; Zhang 2008). This seismic event generated a fault approximately 300 km long, with a ~200-km-long surface rupture on the Longmenshan fault zone, exhibiting maximum vertical and horizontal displacements of approximately 5 m (Du et al. 2009; Ji et al. 2008; Wang et al. 2008a; Xu et al. 2008). The earthquake induced simultaneous surface ruptures along the Yingxiu-Beichuan and Guanxian-Jiangyou faults, characterized by a northeast orientation, northwest dip, and right-lateral strike-slip components, forming three co-seismic surface rupture zones (Xu et al. 2008). It represents the most complex surface rupture structure recorded to date (Xu et al. 2008).

The Wenchuan earthquake is the most devastating seismic disaster in China in the past century, causing massive landslides and geological hazards (Huang and Engineering 2009; Lei and Zhao 2009; LEI et al. 2009). Reports from the China Earthquake Administration indicate that the earthquake caused 69,227 fatalities, 17,923 individuals went missing, and 373,843 were injured, with direct economic losses estimated at 845.1 billion RMB. Ten counties, including Wenchuan, Beichuan, Mianzhu, and Qingchuan, were classified as severely impacted (Lei and Zhao 2009; LEI et al. 2009; Zhang et al. 2012a). Huang et al. (2009) highlighted that one-third of the casualties were due to landslides triggered by the earthquake. The geological hazards also led to significant vegetation destruction over an area of 1,250 km², with shrubland accounting for the largest portion at 339 km². Vegetation coverage decreased by 4.76% in nine severely affected cities and counties, and by 12.37% along the Subao River in Beichuan County (Cui et al. 2012; Jiang et al. 2015; Lin et al. 2017). The Sichuan forestry department

estimated forest ecosystem losses at approximately \$3.33 billion, with potential economic losses of approximately 8.395 billion RMB.

The 2008 Wenchuan earthquake prompted significant research into the mapping of landslides induced by seismic activity, with a focus on developing robust methodologies for creating landslide inventories. Table 3.1 presents a collection of landslide inventories for the Wenchuan earthquake. The earliest significant inventory of landslides triggered by the Wenchuan earthquake was conducted by Qi et al. (2010), which utilized remote sensing techniques to identify 13,085 landslides, covering an area of 418.85 km² within a total mapped extent of 31,686.12 km². Subsequent research by Gorum et al. (2011) employed high-resolution satellite imagery and aerial photography, documenting 60,104 landslides. The total landslides area of 184 km², which was considered underestimated due to the application of equations given by Malamud et al. (2004). In 2011, Dai et al. expanded on this research, identifying 56,847 landslides covering a total area of 811 km², thereby highlighting the extensive geographical impact of the seismic event. Parker et al. (2011) introduced a semi-automated detection algorithm that mapped 73,367 landslides with an estimated volume of approximately 2.6 km³, showcasing advancements in automated data collection methodologies. Li et al. (2013) utilized multi-resolution remote sensing techniques to document 43,842 landslides. While Li et al. (2014) employed unsupervised classification techniques, identifying 57,150 landslides. Their findings emphasize the importance of integrating various methodologies to achieve a comprehensive understanding of landslide dynamics following the earthquake. Notably, Xu et al. (2014) compiled three nearly complete inventories, resulting in the identification of 197,481 landslides with a total area of approximately 1,160 km². The discrepancies in these datasets can primarily be attributed to differences in the geographical extent of the study areas. Additionally, variations in the methodologies employed play a significant role. For instance, automated interpretation of remote sensing imagery often fails to accurately differentiate overlapping landslides or those that are too small in size. Nonetheless, these datasets reinforce the severity of the earthquake's impact and provides valuable insights into the spatial distribution of landslides.

This thesis utilized the EQTLs inventory from Li et al. (2014) to calculate sediment and carbon budgets. This dataset covers over 90% of the surface rupture area and regions with the highest landslide density. Only landslide polygon area greater than 5,800 m² is considered for subsequent calculations, aligning with the 30 m × 30 m resolution of the predictive model used to estimate terrestrial carbon recovery. Additionally, I employed the multi-temporal inventory of pre- and coseismic landslides by Fan et al. (2019a) to estimate the landslide proportion following 2008 Wenchuan earthquake. This dataset

spans 42 catchments over 471 km^2, from Yingxiu (the epicentre) to the town of Wenchuan. I calculated the landslide area over catchment area (landslide area proportion) as shown in Table S1. It reveals an average landslides area proportion of 30 ± 17% (±1 standard deviation) with values ranging from 5% to 84% for these severely affected catchments.

Table 3.1 EQTLs inventories of Wenchuan earthquake

Number of mapped landslides	Total landslide area (km2)	Total landslide volume (km3)	Total field area (km2)	Method	Reference
13085	418.85	N/A	31686.12	visual interpretation	(Qi et al. 2010)
60104	184	1.68	34608.3	visual interpretation	(Gorum et al. 2011)
56847	811	N/A	41750	visual interpretation	(Dai et al. 2011)
73367	565.8	2.6±1.2	13800	semi-automated detection algorithm	(Parker et al. 2011)
43842	632	N/A	93000	visual interpretation	(Li et al. 2013)
57150	396	2.83+0.86/-0.65	38270	unsupervised classification and manual screening	(Li et al. 2014)
197481	1160	N/A	110000	visual interpretation	(Xu et al. 2014)
57402	396.23	N/A	37508	automatic and visually cross-checked method	(Parker et al. 2017)
8917	124.10	1.47	471	visual interpretation	(Fan et al. 2019a)

3.3 Study area

3.3.1 Catchment-scale study area

The study area for Chapter 4 is located in the Luoquanwan catchment, near the town of Yingxiu at the epicentre of the Wenchuan earthquake (Figure 3.2). It covers 28.6 km^2 with a channel length of 11.5 km. There is a river that flows within the catchment, which is a tributary of the Minjiang River. The headwater elevation of the catchment is 3233 m a.s.l. and the outlet is located at 1040 m a.s.l. Our multi-temporal inventory of coseismic landslides and post-seismic remobilizations (Fan et al. 2019a) shows that the areal coverage of coseismic landslides in the Luoquanwan catchment is near 35.06%. It is characterized by a low activity of post-seismic landslides, while remobilizations in the form of debris flows are distinctive within the first 3 years after the earthquake. Several catastrophic debris flow events in the Luoquanwan catchment are recorded by the local government in 2011, 2018, and 2019, accompanied by heavy rainstorms. These debris flows are typically supplied by hillslope and channel deposits (mainly from coseismic landslide material), which are presented in our previous multi-temporal inventory of landslides (Fan et al. 2019a). The geomorphic settings, historic events and availability of background data make this an ideal location for our research purpose.
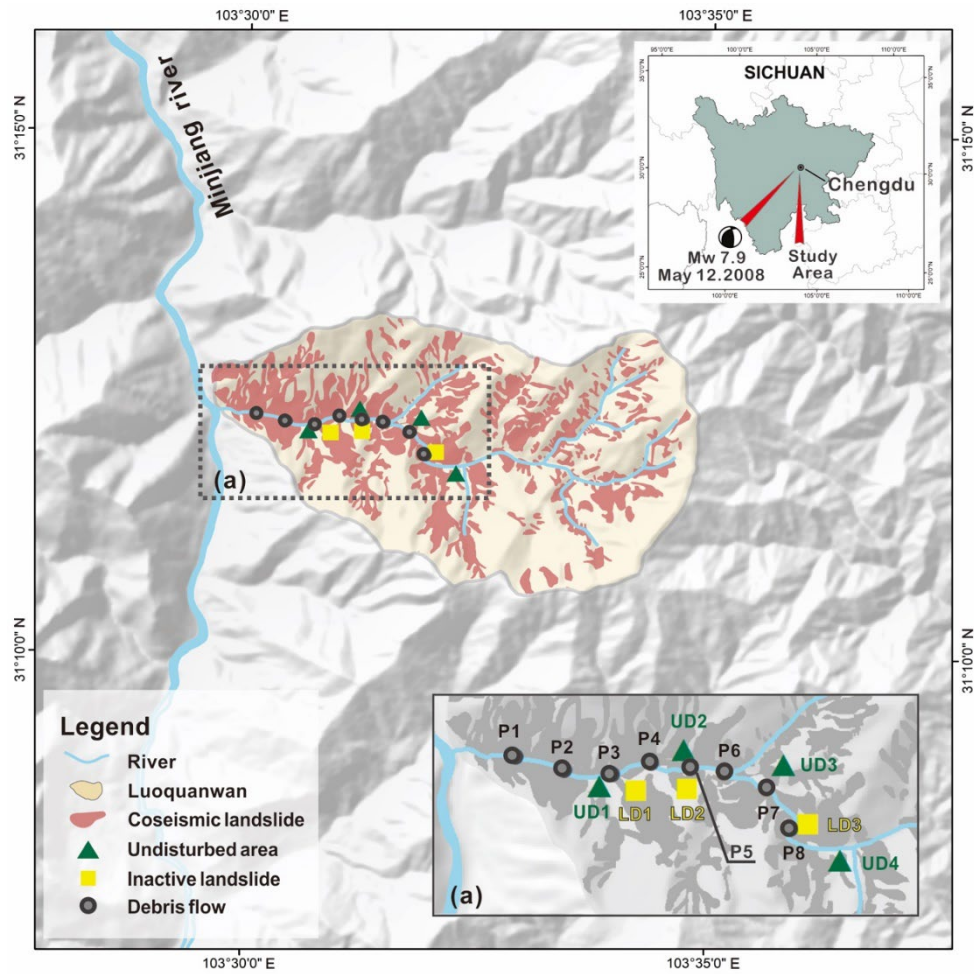
Figure 3.2 Location Map and Sampling Sites in the Luoquanwan Catchment

The map shows sampling sites across undisturbed areas (not impacted by the earthquake), coseismic landslide deposits, and post-seismic debris flow deposits in the Luoquanwan catchment.: (a) Enlarged figure for sampling sites: UD represents undisturbed area, LD represents coseismic landslide area and P1-P8 represents the post-debris flow deposit pits.

3.3.2 Regional-scale study area

The study area for Chapter 5 covers 33, 000 km^2 and the most severely affected counties of the 2008 M$_w$ 7.9 Wenchuan Earthquake, including Wenchuan, Li, Mao, Dujiangyan, Pengzhou, Shifang, Mianzhu, Anzhou, Beichuan, Pingwu, Jiangyou and Qinchuan. EQTLs occur within four large river systems, including Minjiang, Tuojiang, Fujiang and Bailongjiang (Figure 3.3). This area is mountainous with a total relief of 2750 m. The sampling locations in Figure 3.2 are also included in Figure 3.3.
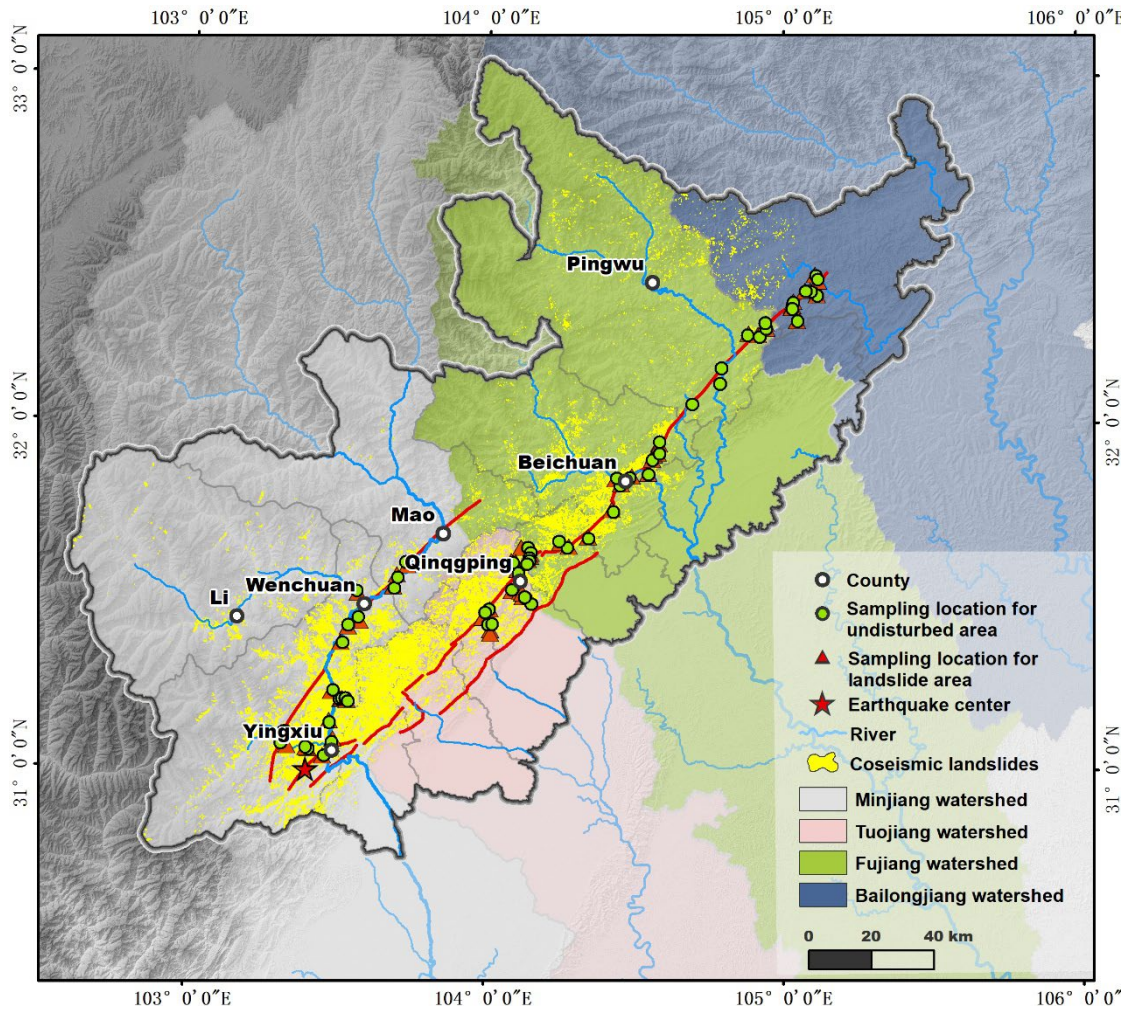
Figure 3.3 Map of the 2008 Mw 7.9 Wenchuan Earthquake Affected Region
This map shows epicentre, surface rupture traces (Red lines) obtained from Alex at al., coseismic landslides (Yellow polygons) obtained by the Li et al. (2014)'s dataset), study area (Grey contour) composed of 12 most destroyed counties), sampling locations (undisturbed area are in green dots and landslides area are in red triangle). Some of the red triangles representing the landslide locations are covered by green dots representing the undisturbed locations due to their close distance on the map. The area with transparent background color shows the watershed of Minjiang (in grey), Tuojiang (in pink), Fujiang (in green) and sub-branch of Balongjiang (in blue).

Chapter 4

Ecosystem Carbon Stock Loss After a

Mega Earthquake

4.1 Background

Large earthquakes can cause extensive mass wasting, affecting both the built-on environment and ecosystem (Fan et al. 2019b).

For example, the 2008 Wenchuan earthquake (Mw 7.9) triggered about 200,000 coseismic landslides resulting in total economic losses of 800 billion RMB and destroyed about 1160 km^2 of land vegetation over an area of more than 110,000 km^2 (Dai et al. 2011; Xu et al. 2014; Xu et al. 2009). The total volume of landslides triggered by the Wenchuan earthquake is estimated to be 5-15 km^3, which deposit on hillslopes and ravines, prone to be remobilized by post-seismic landslides and debris flows during rainstorms (Cui et al., 2012; Gorum et al., 2011; Xu et al., 2014). Between 2008 and 2012, there were 2,333 post-earthquake debris flows (Huang and Fan 2013). In the subsequent years, catastrophic debris flow events have been reported successively within 42 catchments and the impact lasts for over a decade (Fan et al., 2017; Tang et al., 2009, 2011; Xu et al., 2012).

Landslides can critically disturb natural ecosystems by eroding large volumes of soil and vegetation (Clark et al., 2016; Croissant et al., 2019; Cui et al., 2012; Gallo & Lavé, 2014; Ren et al., 2009; Restrepo et al., 2009; Restrepo & Alvarez, 2006). Furthermore, the amount of carbon (C) in soil is more than three times the value of vegetation C and twice the amount of atmospheric C (Dixon et al., 1994; Scharlemann et al., 2014). It is generally accepted that vegetation C and soil C could affect atmospheric CO_2 significantly even with a slight change (Cramer et al. 2001; Fan et al. 1998). Thus, whether the C stock change after a mega earthquake is a contributor to increasing local atmospheric CO_2 merits in-depth research. The Wenchuan earthquake caused a large amount of C loss, which offers a potentially great benchmark to understand how the earthquake-induced geohazards chain contributes to the ecosystem C storage change for the study of regional C cycling.

Over the past three decades, the impact of chemical weathering and erosion on geological C cycle and transfer of C between the atmosphere and rocks over a long timescales has been widely researched (Bouchez et al., 2010; Doetterl et al., 2016; Frith et al., 2018; Galy et al., 2007; Hilton, 2017; Hilton et al., 2008; Hilton & West, 2020; Wang et al., 2016). Yet, the fate of ecosystem C delivery that operates over a short timescale as induced by a mega-earthquake is not well understood. Hilton et al. (2011) assessed the sustained erosion of ecosystem C by landslides and reported that around 7.6 ± 2.9 $t\,km^{-2}y^{-1}$ ecosystem C was mobilized by landslides within 13 studied catchments in

western southern Alps, New Zealand, around 70% of which remained on hillslopes. Considering the majority of coseismic deposits are retained on slope, post-seismic debris flows represents the primary mechanism moving these deposits to channels and the fluvial system.

The area affected by the Wenchuan earthquake is significantly susceptible to debris flows, which plays a major role concerning deposit remobilization (Tang et al., 2011). The amount of ecosystem C stock after geohazards, and ecosystem C mobilized by coseismic landslides and transferred by debris flows after a mega earthquake, still remain uncertain. In the short term, eroded material could be buried in continental sedimentary deposits contributing to C sink (Galy et al., 2015; Ramos Scharrón et al., 2012), while C exposed by landsliding may represent a source of CO_2 due to its oxidation (Bouchez et al., 2010; Emberson et al., 2018; Hilton, 2017). Estimates of terrestrial C stock along with earthquake-triggered geohazards chains are essential for better C management and climate change mitigation.

The 2008 Wenchuan earthquake provides a unique opportunity to investigate the link between earthquakes, ecosystems, and regional C dynamics (Fan et al., 2018, 2019; Jiang et al., 2015; Jin et al., 2016; Liu et al., 2010; Lu et al., 2010; J. Wang et al., 2015). Previous research using a MODIS-based forest mortality model observed that the dead trees in the affected area directly induce a total biomass C loss of ~10.9 Teratonnes C (Tt C) (Zeng et al., 2016). Chen et al. (2009) estimated that ~14 Megatonnes C (Mt C) has been mobilized by the Wenchuan earthquake based on a mean C stock of 41.36 $Mg\ ha^{-1}$ in Chinese forests and a mean damaged forest area of 330 000 ha. For a large study area, remote sensing techniques become a popular methodology through overlapping the SOC stock map, vegetation C map, and interpreted landslide area map. However, the main causes for the uncertainties and inaccuracies among these studies stem from a) incomplete datasets; b) considering soil C or vegetation C separately; c) overlook of C transfer accompanied with sediment cascading; d) lack of field measurement data. The prevalent role of debris flows in sediment cascade in the epicentral area of the Wenchuan earthquake (Francis et al. 2022), suggests that it is important to study the fate of C transfer along the earthquake-induced geohazards chain rather than study landslides impacts individually.

To fill these knowledge gaps, we selected one of the most active catchments with abundant coseismic landslides and post-seismic debris flows in the Wenchuan earthquake region. For the first time, both vegetation and soil organic C (SOC) stock were quantified to examine ecosystem C stock change in a short timescale (from 2008 to 2019). Meanwhile, the debris flow events that act as the major pathway to transfer a large

amount of sediment, are innovatively considered to study SOC loss within the selected catchment. Thus, we estimate the contribution of landslides and debris flow to ecosystem C stock and transfer for catchment-scale C cycle. This study provides one of the first quantifications of the effect of the geohazards chain induced by the Wenchuan earthquake on the local C cycle and has important implications for the role of mega-earthquake on regional C storage and the study of terrestrial ecosystem C cycling.

4.2 Methodology

4.2.1 Plot design

Three landslides, including deep-seated rockslides and shallow landslides, were firstly selected for sampling based on landslide inventory of Luoquanwan catchment. Four undisturbed sampling locations are evenly distributed along the channel with a reachable elevation and every 2 km distance. Eight sampling locations on debris flow deposit occurred in 2019 were selected every 500 m distance along the gully. In-site samples were taken in November and December of 2019 as presented in Figure 3.2.
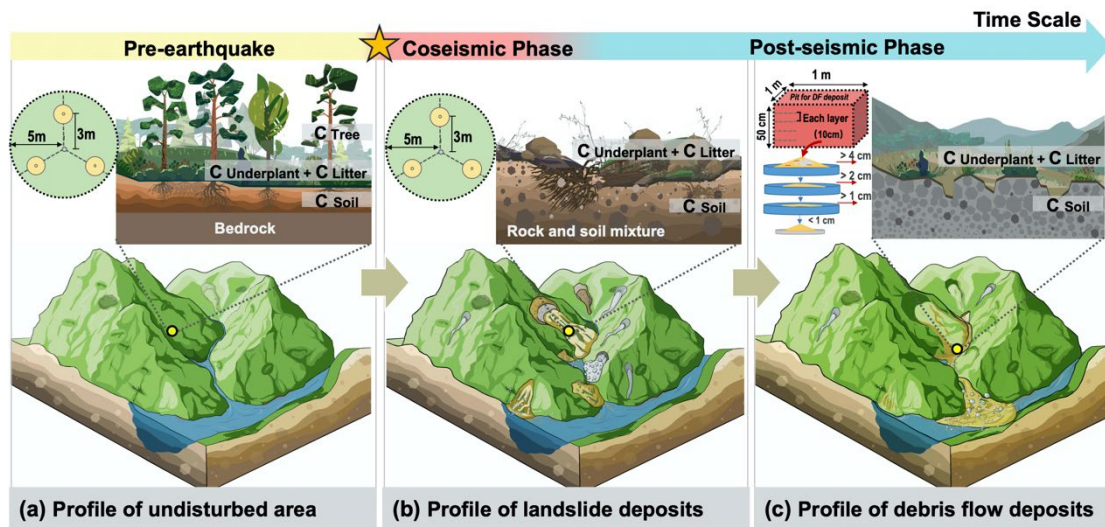
Figure 4.1 Terestrial Ecosystem Carbon Mobilization After Earthquake-Induced Geohazard Chains and Corresponding Sampling Diagram
This diagram outlines the fate of terrestrial ecosystem carbon (C) in undisturbed areas, landslide deposits, and debris flow deposits following earthquake-induced geohazard chains: (a) The vertical profile of undisturbed area where the ecosystem C is predominantly composed of C_{tree}, $C_{underplant}$, C_{litter} and C_{soil}; (b) The vertical profile of landslide deposits where the ecosystem C is composed of $C_{underplant}$, C_{litter} and C_{soil}; (c) The vertical profile of debris flow deposit where the deposit is mainly composed of rocks. The green circle of (a) and (b) illustrates the plot design for undisturbed and landslide area sampling and the yellow cubic of (c) illustrates the debris flow sampling and screening process at site.

As illustrated in Figure 4.1(a), the plot design was proposed based on earthquake-induced geohazard chains. According to previous studies of sampling and estimating ecosystem C stock (Fan et al., 2016; Guan et al., 2015), the pair-plot was used to obtain representative samples for undisturbed areas, landslide and debris flow deposits. In each pair-plot, one plot was established on undisturbed sites as a control plot, which was 500 to 1000 m near the landslide area to make a better reference. The undisturbed area shared the similar climate and topographic conditions with pre-earthquake and coseismic phase, which can avoid the heterogeneity as induced by distance, participation, temperature and topographic characteristics. The other plot was set on landslides or debris flow deposits as affected site by the mega-earthquake (Figure 3.2). The landslide was triggered by 2008

earthquake, which has not been reactivated or disturbed by obvious slope erosion since 2008 based on satellite images and landslide inventory (Fan et al. 2019a). The debris flow deposits were sampled on the same recent event in 2019 to avoid the impact of revegetation. It is assumed that the undisturbed area, landslide deposit and debris flow deposit could present the pre-earthquake ecosystem C status and post-seismic ecosystem C status in 2019 for further calculation.

4.2.2 Vegetation sampling

In each location, a green circle plot with a 5 m radius after slope correction is established (Figure 4.1). Within each green plot, all trees and coarse wood debris with a diameter at breast height (DBH) > 5 cm are recorded, including the DBH, tree hight or dead wood length. Trees with a DBH < 5 cm are considered as understory. To estimate C stock of understory and litter, three 1-m radius yellow circular subplots are set at three directions (0°, 120°, 240° directions and 3 m from the plot centre) within the 5-m radius plots (Figure 4.1). All understory and litter samples within each subplot are weighed and sampled in the field.

4.2.3 Soil sampling

Within the three 1-m radius yellow circular subplots, soil samples are collected down to 50 cm in three layers: 0-10 cm, 10-30 cm, and 30-50 cm, respectively. Soil samples from the same layer are mixed for each given sub-plot location, to get a representative soil sample for each sampling location and each soil layer. Meanwhile, soil cores are taken using ring cores with the diameter of 70 cm for each layer to analyse soil physical properties for undisturbed area.

Soil sampling on post-earthquake debris flow deposit is challenging due to a large number of rocks. In order to obtain both grain size distribution and related C content, our method to sample debris flow deposits is illustrated in Figure 4.1(c) (Harvey et al. 2022). A pit of 1 m×1 m×0.5 m is dug with every 500 m distance along the channel. Each pit is divided into 5 layers (10 cm per layer) along with depth. To overcome the difficulty of obtaining the bulk density and soil sample for OC analysis of debris flow deposit, we weigh and sieve at the site for each layer per pit. The deposit sieved through 0.015 cm is applied for OC content analysis.

4.2.4 Laboratory analysis

Allometric models were applied to estimate aboveground biomass and underground biomass (roots) based on the DBH and height of measured trees and coarse wood debris

(Fan et al. 2016; Guan et al. 2015). All collected understory vegetation and litter samples within three 1-m radius circular subplot were dried at 70°C to a constant weight. Carbon content of 0.5 was used to convert biomass to C stock (Fang et al., 1998; Wang et al., 2011).

In the lab, the soil physical properties, including bulk density (BD), rock content (RC), water content, maximum water holding capacity, capillary moisture, and permeability were analysed following the protocol of Zhang et al. (1999). Identifiable plant residues, root materials and stones were removed. Air-dried soil was sieved through 0. 15 mm. SOC content was analysed using the $K_2Cr_2O_7$-H_2SO_4 wet oxidation method(Zhang et al. 2012b; Zhang et al. 1999). Briefly, 0.1–0.5 g air dried soil samples passing through a 0.15 mm sieve were digested in 5 mL of 0.8 mol·L^{-1} $K_2Cr_2O_7$ and 5 mL concentrated H_2SO_4 (1.84 g·mL^{-1}) for 5 min at 170–180 ℃. Secondly, the digested solution samples were titrated with standardized 0.2 mol·L^{-1} $FeSO_4$ solution mixed with 15 ml concentrated H_2SO_4 per liter to prevent oxidization of $FeSO_4$. After the analysis, the soil organic C stock ($Mg\ ha^{-1}$) for each layer was calculated using the following formula (Xie et al., 2007).

$$\text{SOC}_{\text{stock}} = \text{SOC} \times \text{BD} \times (1 - \text{RC}) \times \frac{\text{D}}{10} \qquad (1)$$

Where the unit for total SOC stock is $Mg\ ha^{-1}$; SOC is the soil OC concentration ($g\cdot kg^{-1}$); BD is bulk density ($g\cdot cm^{-3}$); RC is rock content with the samples > 0.2 cm; D is the depth of the soil layer (cm).

4.2.5 Debris flow SOC stock calculation

As shown in the diagram of Figure 4.1(c), a sample of each layer is sieved through 4 cm, 2 cm, and 1 cm sieves on site. The remaining fraction <1 cm is sampled on-site and sieved in laboratory through 0.5, 0.2, 0.1, 0.05, 0.025 and 0.015 cm. Here, we obtained the bulk density can be obtained through the total weight of pit divided 0.5 m^{-3}, but also the grain size distribution for debris flow deposit is performed. At the same time, the fraction < 0.015 cm is applied to determining SOC concentration. The debris flow OC stock is calculated using the same formula of SOC stock calculation.

4.2.6 Statistical analysis

Descriptive statistics analysis, such as mean, standard deviation and coefficient of variation, were conducted to describe the original data as supplementary (Table 4.1). One-way analysis of variance was conducted to analyse the effects of sampling site (different deposits) on vegetation, soil and ecosystem carbon stock. Two-way analysis

was conducted to analyse the effects of site and soil depth on soil C content and stock. The significance level was p = 0.001.

Table 4.1 Descriptive Statistical Analysis of Soil OC Content, Soil OC Stock and Vegetation C Stock

OC storage		Layers	Mean	Maximum	Minimum	Variance	SD	CV%
Undisturbed area	Soil OC content (%)	0-10cm	6.63	8.08	5.26	1.53	1.24	18.66
		10-30cm	4.03	5.09	3.00	1.27	1.13	27.91
		30-50cm	2.97	4.52	1.85	1.30	1.14	38.32
	Soil OC stock	0-10cm	27.01	33.56	21.72	25.51	5.05	18.70
		10-30cm	39.54	41.05	37.66	2.81	1.68	4.24
		30-50cm	29.83	38.29	23.69	45.13	6.72	22.52
	Vegetation C stock	N/A	0.89	1.40	0.46	0.23	0.48	53.66
Landslide deposit	Soil OC content (5)	0-10cm	0.28	0.32	0.20	0.00	0.06	22.78
		10-30cm	0.27	0.34	0.18	0.01	0.09	31.68
		30-50cm	3.11	5.39	1.51	4.11	2.03	65.16
	Soil OC stock	0-10cm	1.85	2.06	1.57	0.06	0.25	13.47
		10-30cm	1.81	2.25	1.36	0.20	0.44	24.50
		30-50cm	0.25	0.35	0.18	0.00	0.06	22.68
	Vegetation C stock	N/A	0.25	0.38	0.17	0.01	0.07	26.94
Debris flow deposit	Soil OC content (%)	0-10cm	0.28	0.55	0.18	0.02	0.12	42.23
		10-20cm	0.31	0.83	0.18	0.05	0.20	66.27
		20-30cm	0.30	0.85	0.17	0.05	0.21	69.79
		30-40cm	0.25	0.41	0.01	0.02	0.15	59.66
		40-50cm	0.27	0.66	0.05	0.03	0.17	63.58
	Soil OC stock	0-10cm	0.33	1.07	0.03	0.10	0.30	89.52
		10-20cm	0.29	0.98	0.07	0.08	0.27	93.64
		20-30cm	0.37	1.27	0.18	0.14	0.34	92.14
		30-40cm	6.63	8.08	5.26	1.53	1.24	18.66
		40-50cm	4.03	5.09	3.00	1.27	1.13	27.91

Notes: *SD* is standard deviation. *CV* is coefficient of variance.

4.3 Results

4.3.1 Vegetation carbon stock

The measurement results showed that the average amount of vegetation C stock was 34.48 $Mg\ ha^{-1}$ for undisturbed areas and 6.85 $Mg\ ha^{-1}$ for landslide deposits in our study area (Figure 4.2). There was little vegetation on the debris flow deposit. Prior to the earthquake, vegetation C stock of trees with DBH > 5 cm was the major component, contributing to 87.5% of total vegetation C stock. After the earthquake, the vegetation C on landslide deposit changed. Understory plants became one of the important components, and C stock in trees declined to average 59.7% of overall vegetation C. The vegetation C stock, including tree, litter and understory, differed significantly among different deposition types (p < 0.001, Table 4.2). Overall, coseismic landslides lead to an intensive surface material movement, directly causing 80.1% decrease in vegetation C stock from 34.48 $Mg\ ha^{-1}$ to 6.85 $Mg\ ha^{-1}$, even after over 10-year recovery.

Table 4.2 Statistical Analysis Results of OC Stock
p values of two-way analysis of interactions of sampling site and soil depth on soil OC content and stock, and one-way analysis of sampling site on vegetation biomass and ecosystem C stock.

Variables	Soil OC		Vegetation C stock			Ecosystem C stock
	SOC Content	SOC Stock	Tree	Litter	Understory	
Sites	<0.001	<0.001	<0.001	0.00138	<0.001	<0.001
Soil Depth	<0.001	<0.001	NA	NA	NA	NA
Site × Depth	<0.001	<0.001	NA	NA	NA	NA

Note: NA means not available. Sampling sites refer to the samples collecting on different deposits, including undisturbed area, landslide deposit and debris flow deposit.
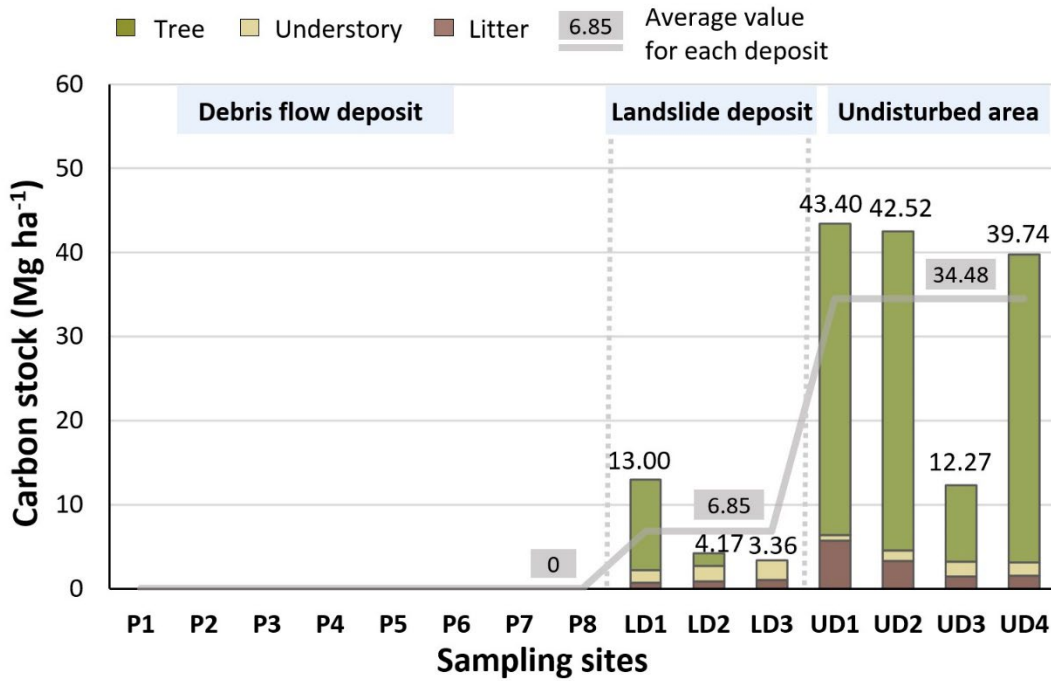
Figure 4.2 Vegetation Carbon Stock on Debris Flow Deposit, Landslide Deposit, and Undisturbed Area

4.3.2 SOC content and stock

SOC content measured in the undisturbed area was significantly higher than that of landslide deposits and debris flow deposits for all soil layers (Figure 4.3 and Table 4.2). As shown in Figure 4.4, measured SOC stock in landslide deposits was more than 3 times higher that of debris flow deposits. SOC stock up to 50 cm was 96.38 $Mg\ ha^{-1}$ in undisturbed areas, which was significantly higher than that of landslide deposit (6.77 $Mg\ ha^{-1}$) and debris flow deposit (2.94 $Mg\ ha^{-1}$).

The distribution of SOC concentration varied significantly with soil depth (p < 0.001, Table 4.2), with a decreasing trend along the soil depth in undisturbed area and landslide deposit, but not for debris flow deposit. Specifically, in undisturbed profiles, SOC content was highest in the top 10 cm layer, in which the SOC stock accounted for 28.07% of total SOC stock. The SOC content between 10-30 cm was double the SOC content found between 30-50 cm. For landslide deposits, the SOC stock of top layer was slightly higher than that of sublayers (except for one sample site), and there was no significant difference between 10-30 cm and 30-50 cm. Biomass and soil OC re-accumulated on the top layer of landslide deposits. When landslide occurred, the topsoil experienced minimal change before burial, for example decomposition and oxidation of SOC, the deep layer had the similar C composition and concentration. Moreover, the biomass and soil OC re-

accumulated on the fresh surface of landslide deposit, which could be explained by the green satellite images.

Debris flow deposits showed an trend that SOC concentration slightly increased along with depth, except for Pit 2 and Pit 6, even though the SOC concentration among sublayers was not greatly different. According to the sieving results of P7 and P8 in Figure 4.3(b) and (c), deeper soil depth had smaller grain size. Correlating the vertical profiles of SOC content and particle size distribution, smaller grain size had higher SOC content. Moreover, The SOC concentration did not change regularly with the distance to catchment outlet. The debris flow pits all had similar SOC contents, except Pit 8 (remarkable higher than other pits). Pit 8 was located at the concave bank where the channel turned, and a large amount of lighter fractions deposited here. the overall size of P8 was smaller than P7. P8 exhibited a higher fraction of fine grains, especially clay content.
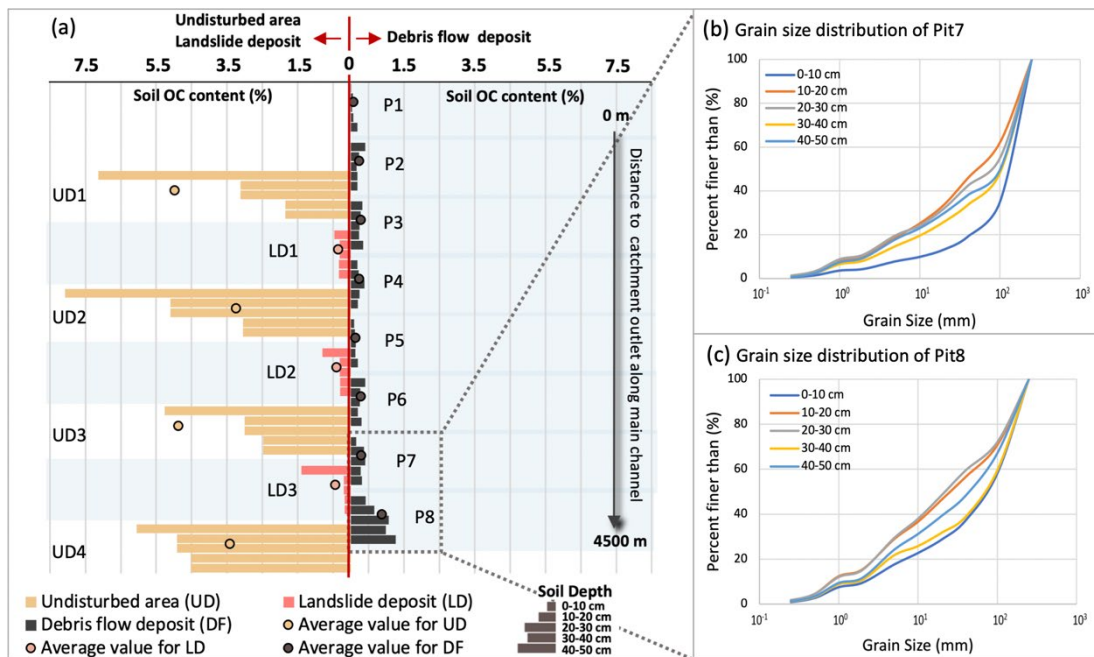
Figure 4.3 Soil Organic Carbon Variation and Vertical Profiles in Catchment Deposits
Spatial variation and vertical profiles of soil organic carbon (SOC) content on undisturbed area, landslide deposit, and debris flow deposit along with catchment channel: (a) SOC content (b) The vertical grain size distribution of P7 and (b) The vertical grain size distribution of P8
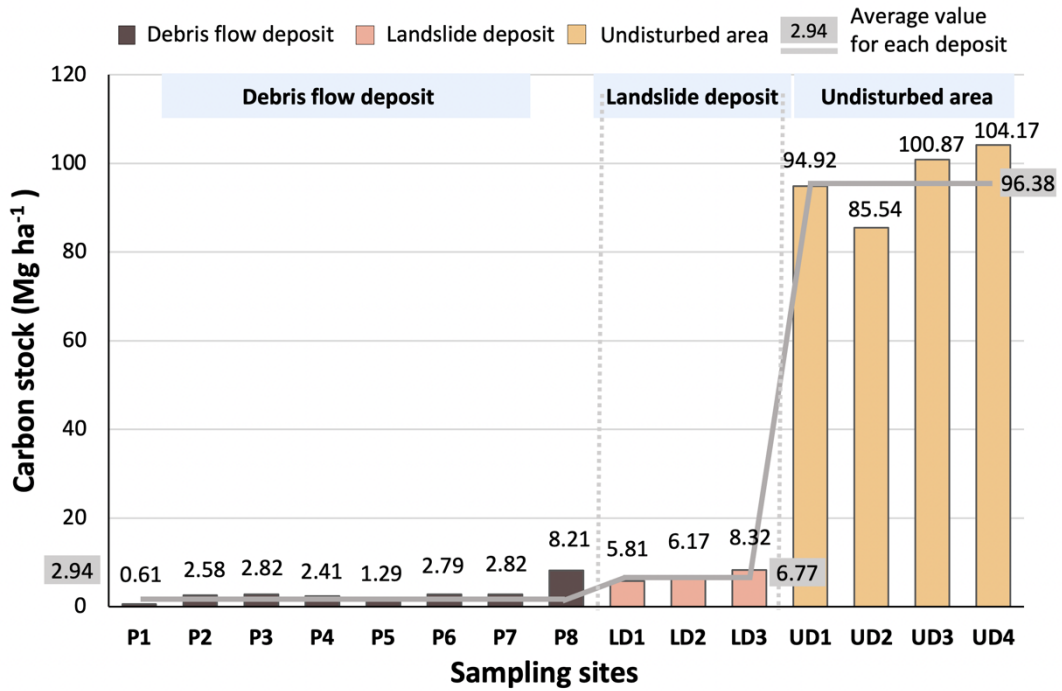
Figure 4.4 Soil Organic Carbon Stock on Debris Flow Deposit, Landslide Deposit, and Undisturbed Area

4.3.3 Total terrestrial carbon stock

Ecosystem C stock was the lowest for the debris flow deposit, intermediate for the landslide deposit, and highest for the undisturbed sites. The total ecosystem C stock in undisturbed area was 130.85 $Mg\ ha^{-1}$, which was significantly higher (p < 0.001) that of landslide (13.62 $Mg\ ha^{-1}$) and debris flow deposits (2.94 $Mg\ ha^{-1}$) (Figure 4.5 and Table 4.2) . SOC was the major component of total ecosystem C stock, accounting for 73.95% of total ecosystem C stock for undisturbed area, while the percentage for landslide deposit reduced to 48.50%.
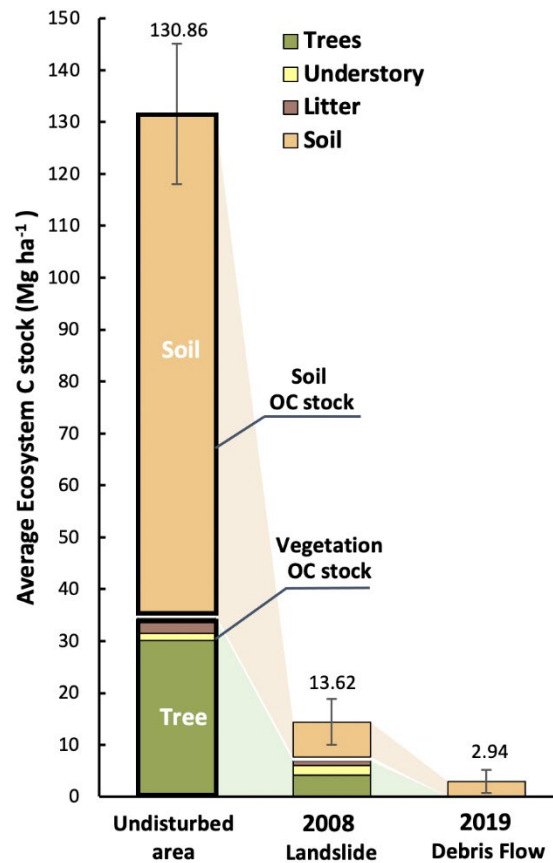
Figure 4.5 Average Terrstrial Ecosystem Carbon Stock and Distribution in the Studied Catchment
The error bars indicate the standard error of total ecosystem C stock.

4.4 Discussion

4.4.1 Terrestrial carbon change caused by landslides and debris flows

While making a comparison between pre-earthquake level and current status, coseismic landslides caused a significant change of ecosystem C stock (117.24 $Mg\ ha^{-1}$), which accounts for 90% of overall ecosystem C stock. The significant C change from geohazards, like landslides and debris flows, were not well considered in previous literatures, especially in the study of terrestrial ecosystem simulation models. Such sharp decrease is mainly due to the land cover change, in the form of landslides denuding the surface vegetation and disturbing soil and rock. As the aboveground vegetation is damaged, the soil erosion is aggravated due to a lack of understory and soil bareness (Guan et al., 2015). Meanwhile, the disturbance to soil enhances the decomposition of

SOC through breaking the physical protection of soil C (Guo and Gifford, 2002; Wang et al., 2011).

Vegetation damage and recovery after the earthquake were evaluated by Normalized Difference Vegetation Index (NDVI) analysis using MODIS or Landsat remote sensing data (i.e. (Yang et al. 2018; Yunus et al. 2020)). According to Yunus et al. (2020), more than 80% of area has been revegetated. However, NDVI can not reflect the recovery of soil OC stock, or understory plants C stock. We found that the recovered vegetation species are mainly grass and shrub, which have much lower capacity to fix atmospheric C, compared to the pre-earthquake vegetation (dominated by evergreen broadleaf forest, deciduous broadleaf forest, evergreen coniferous forest, economic forest). Therefore, revegetation on coseismic landslides from 2008 till now has slight effect on ecosystem C stock. The vegetation C is only composed of the 26% of the ecosystem C stock, and the researches that only rely on remote sensing techniques have greatly underestimated the degree of damage to the ecosystem caused by geohazards. On the contrary, the soil is the major reservoir of ecosystem C in southwest mountainous area with high frequency of tectonic activity. Compared to vegetation C change, SOC change is more sensitive to the geohazards. Improving SOC storage will become the key to improving the carbon sink capacity of ecosystems in earthquake hit regions.

The sieving and SOC results show that fine grain particles have higher OC content compared to coarse particles. Generally, clay and silt sized particles of C enriched are preferentially transported during soil erosion. Our sieving results of debris flow deposits also show that deeper deposition had smaller grain size, which also well illustrated the rheology of debris flow that coarse particles suspended during flow (Pierson 1981). As a result, debris flow events have high transport capacity that not only fine particles but also large size materials are exported out of catchment. Francis et al. (2022) indicates that 5.6 to 15.2 % of coseismic deposit has been transported mainly by post-seismic debris flows to the trunk river, Minjiang river, during the 10 years after the earthquake. Wang et al. (2016) showed that the POC (particulate organic C) concentration in fluvial systems has a positive relationship with suspended sediment concentration. It is indicated that debris flow event is the major process to transport the ecosystem C (Francis et al. 2022) . In this study, debris flows present the lowest of SOC content and lead to a decrease of 10.77 $Mg\ ha^{-1}$ for ecosystem C stock (Figure 4.5). The large amount of sediment transfer decreases C density. The fine particles that are enriched with C are transported more easily. Moreover, the debris flow deposit has limited capacity to hold nutrients.

4.4.2 Estimation of carbon transfer after Wenchuan earthquake

After the earthquake, the ecosystem C stock in landslide scar and deposit was accumulating over time. We sampled three landslide locations in the catchment in order to quantify the transfer of ecosystem C. Eight plots from debris flow deposits were sampled to estimate the further transfer of ecosystem C by sediment transport. Regardless the variation in ecosystem C stock of different landslide types, the overall ecosystem C mobilization of studied catchment can be calculated through multiplying the total area of coseismic landslides and an average ecosystem C stock change induced by coseismic landslides from our measurements. It is estimated that there was around 0.118 Mt or 41.10 $Mg \cdot ha^{-1}$ of ecosystem C transfer induced by coseismic landslides over the whole catchment of 28.60 km^2. Hilton et al. (2011b) estimated that earthquake (M_w>7) mobilization of ecosystem C stock may equal to 5-9 $t\ km^{-2}y^{-1}$ in the western Southern Alps with a return period of ~200 year. However, the Wenchuan earthquake-triggered landslides will directly cause around 68.5 $t\ km^{-2}y^{-1}$ C of ecosystem C mobilized in the Luoquanwan catchment, considering the ~60 years earthquake return period based on the recorded earthquakes (M_w>7) in Longmenshan fault zone (Deng 2013), let alone the post-seismic landslides and post-seismic debris flows induced by rainfall. The result indicates that earthquake-induced landslides within the single catchment of Luoquanwan play a significant role in transferring ecosystem C.

The mega earthquake not only changes the ecosystem C storage, but also changes the C flux due to the land use change. Photosynthesis is significantly reduced after earthquake, while the decomposition is enhanced. The C balance has been broken. On the one hand, majority of sediments produced by the earthquake are still remained on hillslope associated with ecosystem C and petrogenic C, which are buried temporally as C sequestration from ecosystem to sediment. On the other hand, the ecosystem C deposited in channel can be transferred outside of catchment through fluvial system or debris flow events following Figure 4.6, which will be further sedimented as C sink. During the transportation, the ecosystem C can be released into atmosphere through decomposition or oxidation. For a long-term scale, the earthquake enhanced the weathering and erosion, which is regarded as an important mechanism to adjust the CO_2 in atmosphere (Hilton and West 2020). Thus, the question on whether the earthquake drives the ecosystem into a net C sink or a net source is a complicated question, and still requires further research to answer.
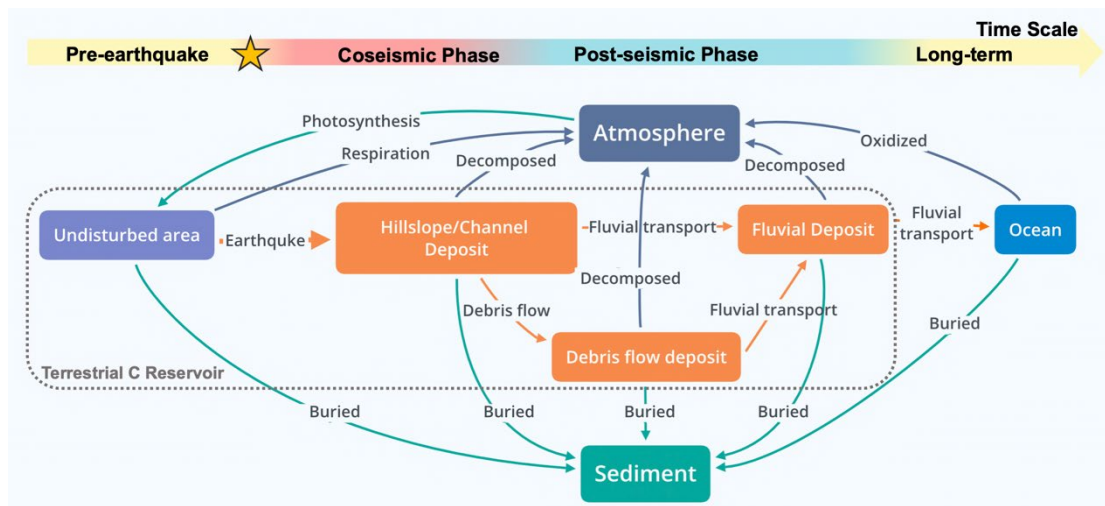
Figure 4.6 The Transfer Route of Terrestrial Ecosystem Carbon after A Mega Earthquake

4.4.3 Environmental implications and uncertainties

Although mega-earthquakes have been reported to significantly affect vegetation, most of the studies used remote sensing technology (Clark et al. 2016; Cui et al. 2012; Zeng et al. 2016), making the quantitively assessment of ecosystem carbon (vegetation and soil) loss difficult. Previous researches were predominantly based on NDVI datasets and historical soil map, which only reflected the vegetation coverage rather than the vertical profile of ecosystem and ignored spatial soil heterogeneity. By collecting field observations, this study quantitively estimated ecosystem carbon storage change after the Wenchuan earthquake, which had important environmental implications to improve our understanding of ecosystem C cycling in terms of global climate change. First, we found a significant loss of both vegetation and soil C after the Wenchuan mega-earthquake, which indicated that the carbon loss should not be neglected after a mega-earthquake in order to accurately estimate reginal carbon cycling. However, to the best of our knowledge, no such study and ecosystem simulation model for C dynamics assessed the effects of earthquake on C storage in their models. Second, although after more than ten year recovery, ecosystem C was still much lower than area without disturbance (Figure 4.5 and Table 4.2), which indicated a slower revegetation and accumulation of vegetation C and soil C. These findings that we should evaluate ecosystem recovery in different aspects, although Yang et al. (2018) and Yunus et al. (2020) assessed the ecosystem recovery using NDVI. Consequently, in order to improve ecosystem C stock or ecosystem recovery, proper ecological restoration measures should be taken. Although our study was a preliminary study of storage and distribution of ecosystem C on landslide and debris flow deposits after the Wenchuan mega-earthquake, our study filled the

knowledge gap of assessing the response of terrestrial ecosystem change after a mega-earthquake to regional C cycling.

Uncertainties still exist in few aspects. Firstly, as we focus on the ecosystem C in this study, the erosion of fossil organic carbon (OC) and inorganic C from sedimentary bedrock by a landslide is not considered here, which plays an important role in the C cycle for a geologic timescale. From the aspect of the disaster chain, we still overlook the effect of post-seismic landslides. Even though the activity of post-seismic landslides declines quickly after the dramatically increasing (Fan et al. 2018; Zhang et al. 2014), it is still promoting sediment transfer and C transfer, especially in the tectonically active region. Secondly, as landslides carry an abundant amount of deposits to hillslopes and channels, the ecosystem C stock is diluted into a relatively larger and deeper area. However, it is not possible to sample all the area and the entire depth of the debris flow deposits, which may cause some uncertainties. Especially, the part of ecosystem C remained in coarse woody debris will be composed into atmosphere or buried permanently. Lastly, the disturbed area may not precisely represent the pre-earthquake status due to the unknown soil erosion in studied area. The number of sampling sites is still limited to apply to a larger affected area and the rough estimation of ecosystem C storage covering the earthquake hit region needs to be further substantiated based on more representative sampling sites. Further study on OC re-accumulation in the Wenchuan earthquake affected area is needed to better understand the ecosystem C fluxes (Parfitt et al., 2013), which is already under our study plan in near future.

4.5 Conclusions

In this chapter, the impact of coseismic landslides and debris flow on ecosystem carbon stock is evaluated based on field sampling data. The results indicate that coseismic landslides have greatly reduced vegetation C stock from 34.48 $Mg\ ha^{-1}$ to 6.85 $Mg\ ha^{-1}$ and surface soil C stock from 96.38 to 6.77 $Mg\ ha^{-1}$, thereby leading to 89.6% reduction for total ecosystem C stock. Similarly, debris flow deposits lead to a reduction of 97.8% of ecosystem C stock. Overall, the estimated carbon loss across the catchment area amounted to approximately 0.118 Mt C, highlighting the substantial carbon redistribution in the earthquake-affected region.

The significant shift in total ecosystem carbon stock underscores the role of the mega-earthquake as a major driver of regional carbon redistribution and transfer. Earthquake-triggered landslides led to the widespread destruction of vegetation biomass and SOC, resulting in a sharp change in ecosystem carbon stock. A significant portion of this carbon was not immediately transported by river systems or released into the atmosphere through oxidation but was temporarily sequestered on hillslopes. However, with the frequent occurrence of post-seismic debris flows and ongoing river transport, sediment and ecosystem carbon continued to be redistributed, affecting ecosystem carbon fluxes. Debris flows are the primary mechanism for mobilizing landslide deposits, transporting large volumes of sediment mixed with woody debris over long distances. This process further amplifies the movement and deposition of organic carbon, thereby reshaping the carbon balance within the region.

Chapter 5

Wenchuan Earthquake Acts as a Capacitor

for Ecosystem Organic Carbon

5.1 Background

Large earthquakes play a dual role in the terrestrial carbon system: they are a source of carbon to the atmosphere through destroying vegetation that then decays(Chen et al. 2009; Stone 2009), and a sink through the incorporation of particulate carbon into the sedimentary system (Carey et al. 2005; Frith et al. 2018; Wang et al. 2016). Earthquake-triggered landslides (EQTL) are the dominant surface processes that perturb the carbon balance of an orogen during an earthquake. Carbon eroded by landslides can take a number of pathways through mountain catchments, resulting in a portion of the carbon being stored on hillslopes, while the rest is exported to the fluvial network and transported to downstream, and ultimately offshore sinks (Hilton et al. 2008a; Hilton et al. 2011b; Ramos Scharrón et al. 2012). Measurements of export of terrestrial carbon from orogens varies from relatively small amounts for the Gorkha earthquake (Märki et al. 2021) to up to 35-40 Mt C per year in Taiwan (Kao et al. 2014b) . Sedimentary evidence from the Lake Paringa, New Zealand suggests that 14±5 Mt C could be eroded in an earthquake event (Frith et al. 2018). The different rates of carbon export from these historical earthquakes could reflect primary differences in the amount of carbon mobilized during an earthquake event, or could reflect the role of EQTLs storing sediment and carbon within orogens, thus acting as a capacitor that slows the release of eroded sediment and carbon from orogens after an earthquake.

Historical EQTL events have generated up to 3 km^3 of landslide debris in an individual event (Fan et al. 2019b). Landslides mix soil carbon and live biomass into their deposits, creating a carbon store whose magnitude depends on the amount of landslide material and the rate it is eroded from landslide debris(Hunter et al. 2024). EQTLs form on hillslopes above the fluvial system, where the sediment and the carbon it incorporates can be stored for hundreds to thousands of years (Francis et al. 2022). The erosion rate of the sediment and carbon is linked to how connected landslides are to the fluvial system. Where this has been measured for the Chi-Chi, Wenchuan and Gorkha earthquakes between 5% and 60% of landslides are connected to the fluvial network, often within low order drainage basins where fluvial erosion is inefficient (Li et al. 2016). The highest post-earthquake sediment export rates measured historically were following the 1970 Madang Earthquake, where up to 50% of the sediment generated by the earthquake was exported in the first year (Pain and Bowlersw 1973). However, there are many examples of much lower fluvial export rates, such as in the Matiri River, New Zealand, where at least 50% to 75% of the sediment generated during the 1929 Murchison Earthquake

remained in the catchment 50 years later (Pearce and Watson 1986). Evacuation of 1999 Chi-Chi Earthquake sediment in the Peikang River, Taiwan is projected to take hundreds of years(Yanites et al. 2011; Yanites et al. 2010). The rate of erosion of this landslide debris, which comprises a mixture of fractured bedrock, soil and colluvial material, and vegetation is an important control on the rate of carbon export after the earthquake. While the majority of existing research focused on sediment fluxes and revegetation (Freund et al. 2021; Rasigraf and Wagner 2022), the critical role of landslide deposits as Organic Carbon (OC) capacitor has been neglected. The rate of erosion of landslide debris plays a crucial role in determining the dynamic capacity for carbon restoration along landslide deposits.

The 2008 M_w7.9 Wenchuan Earthquake is one of the largest historical EQTL events (Fan et al. 2019b). The sedimentary system has been studied intensively following this event, making Wenchuan one of the best understood examples of post-earthquake sedimentary response (Fan et al. 2019b). The earthquake occurred during a period of rapid expansion of satellite technologies, which have allowed researchers to constrain the frequency and intensity of landsliding, the movement of sediment from EQTLs into the fluvial system, and the changes in vegetation coverage after the event (Chou et al. 2009; Yunus et al. 2020). Additionally, well-established river gauging in the affected region has revealed a doubling of POC (Particulate Organic Carbon) transport within the fluvial network in the 4 years after the earthquake (Wang et al. 2016). The scale of the Wenchuan Earthquake EQTL event provides a unique opportunity to understand the carbon dynamics of an end-member earthquake and to constrain the role of large landslides in the storage of terrestrial carbon over hundreds to thousands of years. Here, I produce the first terrestrial carbon budget for the decade after the 2008 Wenchuan earthquake, by integrating field investigation, laboratory analysis, remote sensing techniques, and machine-learning based modelling. The mapping of ecosystem carbon stocks pre- and post-earthquake allows us to define the hillslope carbon mass-balance for this earthquake.

5.2 Methodology

5.2.1 Sampling data

I selected 123 sampling sites for field investigation, in which 59 sampling sites were on inactive co-seismic landslides (disturbed sites) and 64 in undisturbed areas. The disturbed sites are randomly distributed along the ruptured major faults of Longmen Shan as presented in Figure 3.3. We sampled paired plots containing both disturbed and adjacent undisturbed sites, which were identified as having no obvious erosion and slope failure since 2008 within aerial and satellite images.

The plot design for sampling followed the previous studies in Luoquanwan catchment (Harvey et al. 2022; Liu et al. 2022). The measured ecosystem OC is composed of soil, tree, understory plant and litter OC. Within a 5 m radius plot after slope correction, all trees with a diameter at breast height (DBH) >5 cm were recorded for species, DBH and height. Heights of trees were measured in each plot using a Vertex III height meter (Haglöf, Långsele, Sweden). Plants with a DBH < 5 cm are considered as understory. To estimate biomass of understory and litter, three 1-m radius circular subplots were set at three directions (0°, 120°, 240°,3m from the plot centre) within the 5-m radius plots. Understory and litter within each subplot were dried and weighed. Within the three subplots, soil samples were collected in cloth bags down to 50 cm in three layers: 0-10 cm, 10-30 cm, and 30-50 cm, respectively. Soil samples from the same layer were mixed for each given sub-plot location. Soil samples were collected using ring cores with a diameter of 70 cm for each layer to analyse soil physical properties for undisturbed area. Due to the large content of rocks on landslide deposits, a circular bucket with fixed volume was used to obtain the wet density for different layers. A detailed list of collected samples is shown in Table 5.1.

Table 5.1 List for Sampling Sites and Types for Different Purposes on Landslide Deposit and Undisturbed Area

Site	Amount	Soil profile measured	Soil core/bag collected	Soil sample for GSD	Soil sample for water content	Vegetation profile measured	Understory sample collected	Litter sample collected
Landslide deposit	59	177	531	90	531	59	177	177
Undisturbed area	64	192	192	114	576	64	192	192
Total	123	369	723	360	1107	123	369	369

All soil samples were dried in the oven with the temperature of 85°C until the weight remained stable. For the undisturbed sites, bulk density (BD), water content (WC), and gravel fraction (GF) with particles larger than 2 mm were analysed following the standard protocol given of Zhang et al. (1999). For the disturbed sites, we measured the wet density at site and dried, sieved, and weighed the samples in the laboratory to establish BD, WC, and GF. Samples were sieved with the screen size of 0.15 mm, 0.25 mm, 0.5 mm, 1 mm, 2 mm and 5 mm. Identifiable plant residues and root materials were removed during the sieving process. The soil OC content was analysed using the potassium dichromate and sulfuric acid ($K_2Cr_2O_7$-H_2SO_4) wet oxidation method (Fan et al. 2016). The total nitrogen (TN) content in soil was determined by the automatic Kjedahl apparatus method following the Chinese Agriculture Industry Standard (NY/T 1121.24-2012). Both SOC and TN analyses were repeated three times for each soil sample.

5.2.2 Vegetation biomass calculation

Regarding all sampling data, tree biomass was calculated using a dataset of Chinese allometric equations compiled by Luo et al. (2020). We estimated aboveground and belowground biomass by selecting the appropriate allometric relationship based on the tree species, diameter and height range, precipitation, temperature, and geography. For species not found in the database, we applied the general allometry by plant functional group, such as deciduous broad-leaved forest or evergreen broad-leaved forest. We included all major biomass components, including stem, branch, leaf and belowground biomass. The calculation of tree biomass was carried out in Python 3.9. The tree species and related allometric models are given in Table S2. All sampled understory vegetation and litter samples within three 1-m radius circular subplot were dried at 70℃ to a constant weight. Carbon content of 0.5 g•g^{-1} was used to convert biomass to C stock (Fan et al. 2016).

5.2.3 Statistical analysis

For field data, I applied Shapiro-Wilk's test to examine the representativeness and normality of total ecosystem OC stock, soil OC stock and vegetation OC stock for undisturbed area and landslide deposit, respectively. Here, I chose the alpha level as 0.05. One-way analysis of variance (ANOVA), also known as F test, is used to examine whether the effect of earthquake-induced landslides on ecosystem OC stock are distinguishable or not, this can be reflected on the comparison between undisturbed area and landslide deposit regarding all the input covariates and OC stock. The difference

level was set at $p < 0.05$. Descriptive statistical analysis for organic carbon stock of soil, tree, understory and litter are shown in Table 5.2.

Table 5.2 Descriptive Statistical Analysis

Descriptive statistical analysis of soil organic carbon content, soil TN content and soil OC stock along soil depth, and tree carbon stock, understory carbon stock and litter carbon stock and total ecosystem organic carbon stock on undisturbed area and landslide area.

OC storage		Layers	Amount	Mean	Median	Max.	Min.	Range	SD	Trimmed	Mad	Skew	Kurtosis	SE
Undisturbed area	Soil OC content (%)	0-10cm	64	3.62	3.08	9.65	0.21	9.44	2.04	3.46	1.91	0.74	-0.15	0.25
		10-30cm	64	2.39	1.98	5.95	0.36	5.59	1.51	2.25	1.45	0.76	-0.46	0.19
		30-50cm	64	1.83	1.47	4.84	0.27	4.57	1.20	1.70	0.98	0.89	-0.07	0.15
	Soil TN content (‰)	0-10cm	61	3.45	2.90	10.04	1.12	8.92	1.77	3.42	-	1.28	1.96	0.23
		10-30cm	61	2.38	2.06	5.61	0.53	5.08	1.31	2.39	-	0.99	0.16	0.17
		30-50cm	61	1.96	1.80	4.94	0.49	4.45	1.07	1.96	-	1.03	0.46	0.14
	Soil OC stock	0-10cm	64	21.45	21.10	52.40	1.59	50.81	9.62	20.81	10.03	0.69	0.62	1.20
		10-30cm	64	30.11	29.67	67.59	6.17	61.41	14.54	29.32	15.40	0.46	-0.37	1.82
		30-50cm	64	23.06	21.52	55.25	5.85	49.40	11.57	22.39	10.89	0.57	-0.22	1.45
		Total	64	74.63	69.21	152.10	20.88	131.22	32.22	72.90	31.12	0.53	-0.11	4.03
	Tree C stock		64	47.76	32.72	178.45	0.00	178.45	40.62	43.08	31.18	1.17	1.13	5.08
	Understory C stock		64	1.34	0.70	15.01	0.00	15.01	2.37	0.84	0.62	4.31	20.47	0.30
	Litter C stock		64	1.77	1.51	5.75	0.00	5.75	1.15	1.66	0.97	1.23	2.10	0.14
Undisturbed area Total Ecosystem OC Stock			64	125.50	120.39	285.42	38.10	247.33	43.77	122.08	39.94	1.02	2.12	5.47
Landslide area	Soil OC content (%)	0-10cm	59	2.23	1.62	7.69	0.44	7.25	1.64	2.04	1.30	1.18	1.08	0.21
		10-30cm	59	1.50	1.05	5.34	0.00	5.33	1.32	1.33	0.97	1.19	0.60	0.17
		30-50cm	59	1.30	0.84	5.10	0.04	5.05	1.18	1.14	0.80	1.35	1.46	0.15
	Soil TN content (%)	0-10cm	59	2.30	1.96	6.21	0.53	5.68	1.36	2.17	1.49	0.93	0.46	0.18

		N											
	10-30cm	59	1.68	1.46	5.00	0.32	4.68	1.13	1.55	1.06	1.14	0.84	0.15
	30-50cm	59	1.52	1.24	5.33	0.35	4.98	1.05	1.38	0.91	1.46	2.47	0.14
	0-10cm	59	4.82	4.11	23.44	0.55	22.90	4.00	4.29	3.24	2.16	7.24	0.52
Soil OC stock	10-30cm	59	6.39	4.09	30.06	0.01	30.04	6.56	5.37	3.76	1.70	2.77	0.85
	30-50cm	59	5.95	2.94	26.99	0.12	26.87	6.48	4.91	2.90	1.64	2.23	0.84
	Total	59	17.16	10.78	71.50	1.36	70.15	16.23	14.71	8.54	1.55	1.88	2.11
Tree C stock		59	12.26	6.92	64.43	0.00	64.43	15.24	9.43	10.26	1.69	2.54	1.98
Understory C stock		59	1.24	1.05	5.72	0.11	5.60	1.01	1.12	1.06	1.69	5.19	0.13
Litter C stock		59	1.62	1.49	5.91	0.10	5.81	1.08	1.52	1.02	1.36	3.07	0.14
Landslide area Total Ecosystem OC Stock		59	32.28	28.94	81.94	3.58	78.36	19.84	30.82	20.11	0.69	-0.38	2.58

Note: SD is the standard deviation. SE is the standard error of the me

5.2.4 Collected data

Beyond the field sampling data, we have collected published data on terrestrial organic carbon through Science Direct, Google Scholar and Dryad Digital Repository. The dataset focuses on studies that report field sampling data in undisturbed forest and shrub ecosystems, excluding those based on models or satellite data, as well as planted forests. At a minimum, studies needed to include geographical coordinates within our designated study area, and at least one of the following: soil organic carbon, aboveground and belowground biomass or terrestrial carbon. We compiled a robust dataset consisting of 194 entries derived from 25 publications. The spatial distribution of collected data is showed in Figure 5.1. Furthermore, we evaluated data quality of each published dataset by assigning scores based on eight categories: Data Type, Data Information, Climate Information, Geographic Information, Soil Information, Soil Organic Carbon, Vegetation Organic Carbon and Total Terrestrial Organic Carbon. Each category received a quality score ranging from 0-2, with the maximum cumulative score being 16. The score matrix is detailed in Table S3 in Appendix. This dataset aims to serve as a foundational and comprehensive references for further researches conducted along Longmen Shan fault or Tibetan plateau. For the training of predictive models, we utilized datasets scoring above 5, in combination with the observed data, as our input dataset. We normalized soil C stock to a depth of 50 cm. For studies containing soil depth profiles > 50cm, extrapolating was performed by averaging percentage of C content and dry bulk density from known depths and then applying to 50 cm. This collected data helps overcome the limitations inherent in our sampling data: by guaranteeing the quality data, it furnishes the model with an augmented dataset and simultaneously broadens the spatial extent of the input data.
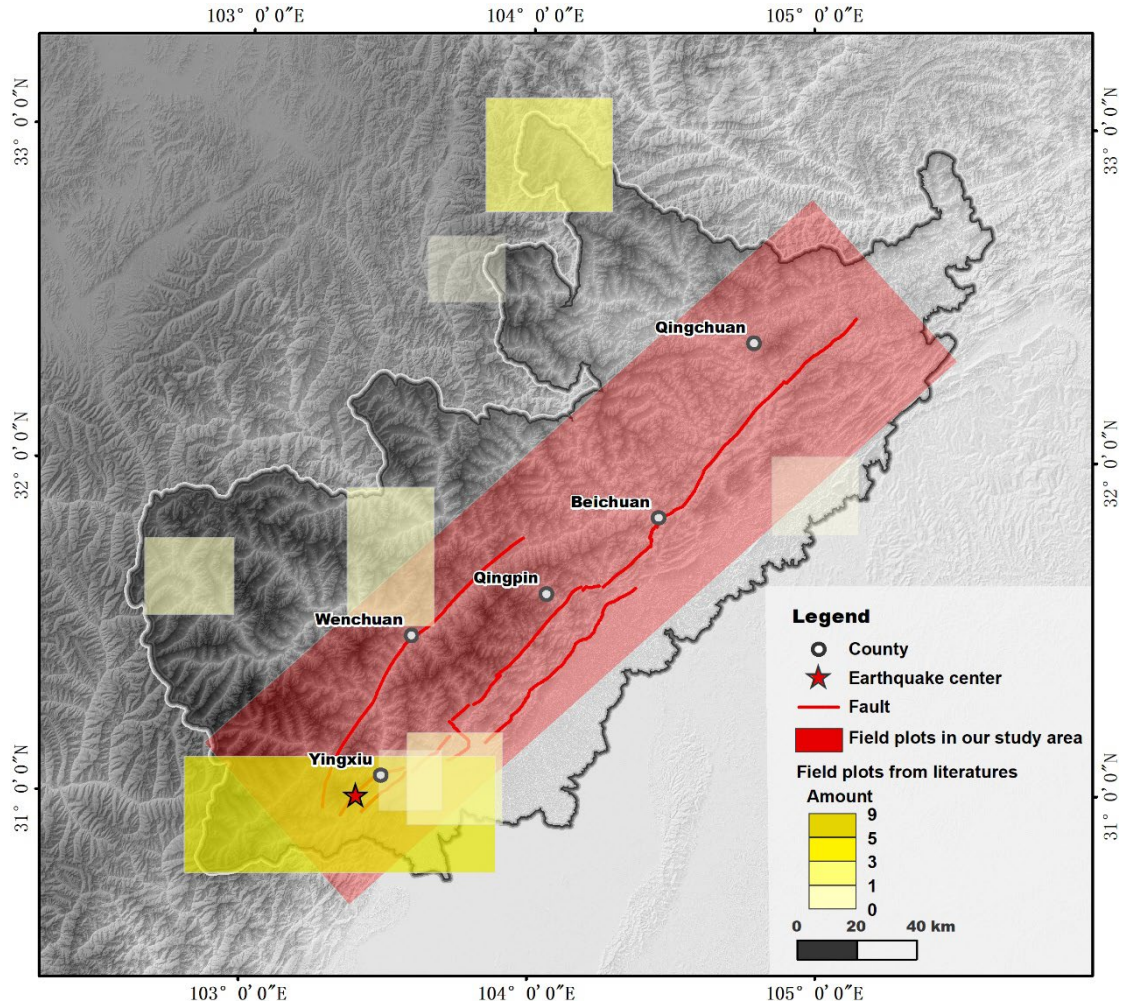
Figure 5.1 The Spatial Distribution of Collected Data and the Field Data
Yellow transparent squares represent the field sampling region from collected dataset. The varying shades of yellow represent the quantity of research literatures associated with each respective area. Red transparent squares denote the distribution of field data observed in this study.

5.2.5 Covariates datasets

Twenty covariates derived from remote sensing data, geographic data and landslide inventory were applied (Dai et al. 2022; Kunkel et al. 2022; Silatsa et al. 2020), including landslide area (ARE), slope (SLO), aspect (ASP), elevation (ELE), lithology (LIT), mean annual precipitation (MAP), mean annual temperature (MAT), land surface temperature (LST), total nitrogen content (TNC), clay content (CLA), bulk density (BD), Landsat derived enhance vegetation index (LAE), normalized difference vegetation index (LAN), red band (LAR) and modified soil adjusted vegetation index (LAM), MODIS derived enhance vegetation index (MOE), normalized difference vegetation (MON), red band (MOR) and modified soil adjusted vegetation index (MOM) and gross primary production (GPP) as specified in Table 5.3. The raster maps of these variables were resampled to 10 m resolution for spatial calculation, consistent with the DEM resolution.

To ensure that our model was only applied to forest ecosystems, we used the 30 m Landsat-derived annual China land cover dataset (Yang and Huang 2021) to define land use types in the research area. These were divided into categories: forest, shrub, grassland, wetland, farmland, urban and other. We then masked all areas that were not identified as forest or shrub.

Table 5.3 List of Covariates Extracted for Prediction Model
List of covariates extracted from Digital Elevation Model (DEM), satellite data and world soil dataset applied in prediction model

Category	Covariates	Code	Resolution		Temporal Span	Resource
			Spatial	Temporal		
Topography	Slope	SLO	30m	Invariant	2019	Digital Elevation Model (DEM) of 2019 from Geospatial Data Cloud; ArcGIS 10.8
	Aspect	ASP	30m	Invariant	2019	Digital Elevation Model (DEM) of 2019 from Geospatial Data Cloud; ArcGIS 10.8
	Elevation	ELE	30m	Invariant	2019	Digital Elevation Model (DEM) of 2019 from Geospatial Data Cloud; ArcGIS 10.8
	Lithology	LIT	1:200000	Invariant	N/A	Compiled from ten 1:200,000 standard geological maps by Tang et al. (2018)
Climate	Mean Annual Precipitation	MAP	1000m	Yearly	2007-2020	Peng et al. (2019) , National Earth System Science Data Center, National Science & Technology Infrastructure of China (Last accessed December 2020)
	Mean Annual Temperature	MAT	1000m	Yearly	2007-2020	Climatic Research Unit (CRU) time series dataset and WorldClim.
	Land Surface Temperature	LST	500m	Monthly	2007-2020	MOD11A2.061 Terra Land Surface Temperature and Emissivity 8-Day Global 1km
Soil	TN content	TNC	250m	Invariant	2020	Global Gridded Surfaces of Selected Soil Characteristics (IGBP-DIS) from World Soil Information's Purpose and Strategy (ISRIC) (Hengl et al. 2017)
	Clay content	CLA	250m	Invariant	2020	Hengl et al. (2017) (last accessed December 2020)
	Bulk density	BD	250m	Invariant	2020	Hengl et al. (2017) (last accessed December 2020)
Vegetation	Landsat, EVI (Enhanced Vegetation Index)	LAE	30m	Yearly	2020	2007-2013: USGS Landsat 7 Collection 1 Tier 1 8-Day EVI Composite; 2014-2020: USGS

				Landsat 8 Collection 1 Tier 1 8-Day EVI Composit
Landsat, NDVI (Normalized Difference Vegetation Index)	LAN 30m	Yearly	2020	2007-2013: USGS Landsat 7 Collection 1 Tier 1 8-Day NDVI Composite; 2014-2020: USGS Landsat 8 Collection 1 Tier 1 8-Day NDVI Composite
Landsat, RED (Red surface reflectance, 0.63-0.69 μm(7) 0.636-0.673 μm(8))	LAR 30m	Yearly	2020	2007-2013: USGS Landsat 7 Level 2, Collection 2, Tier 1; 2014-2020: USGS Landsat 8 Level 2, Collection 2, Tier 1
Landsat, MSAVI (Modified Soil Adjusted Vegetation Index)	LAM 30m	Yearly	2020	2007-2013: USGS Landsat 7 Level 2, Collection 2, Tier; 2014-2020: USGS Landsat 8 Level 2, Collection 2, Tier 1
MODIS, EVI (Enhanced Vegetation Index)	MOE 500m	Yearly	2020	MOD13Q1.061 Terra Vegetation Indices 16-Day Global 250m
MODIS, NDVI (Normalized Difference Vegetation Index)	MON 500m	Yearly	2020	MOD13Q1.061 Terra Vegetation Indices 16-Day Global 250m
MODIS, RED (Red surface reflectance, 0.63-0.69 μm(7) 0.636-0.673 μm(8))	MOR 500m	Yearly	2020	MOD09Q1.061 Terra Surface Reflectance 8-Day Global 250m
MODIS, MSAVI (Modified Soil Adjusted Vegetation Index)	MOM500m	Yearly	2020	MOD09Q1.061 Terra Surface Reflectance 8-Day Global 250m
MODIS, NPP (Net primary productivity)	NPP 500m	Yearly	2020	MOD17A3HGF.061 Terra Net Primary Production Gap-Filled Yearly Global 500m
MODIS, GPP (Gross primary production)	GPP 500m	Yearly	2020	MOD17A2H.006 Terra Gross Primary Productivity 8-Day Global 500m

5.2.6 Modelling of carbon stock

Twenty modelling approaches were used for preliminary screening to identify the predictive models suitable for estimating total ecosystem OC stock in the study area. These included random forest, gradient boosting decision trees (GBDT), extreme gradient boost (XGBoost), decision tree, support vector regression (SVM), k-nearest neighbors regression (KNN), linear weight regression (LWR), etc. The prediction models were built using representative topographic and soil characteristics, climatic, and

vegetation indices across the whole earthquake-affected area. I trained the prediction model using the total terrestrial carbon stock data from our field sites and our 16 remotely sensed covariates. I developed models for disturbed and undisturbed sites trained using 70% of the field sampling data, leaving the remaining 30% for testing. I applied the attribution interrogate method to remove the less important covariates. I used the GBDT method as it had the best performance after training and testing (Table 5.4).

Table 5.4 Comparisons among the predictive performances of typical models.
Different scenarios for total terrestrial organic carbon stock prediction are applied. UD presents undisturbed area and LD presents landslide area; The performance of prediction models area evaluated by R2, Mean Squared Error (MSE) and Variance (VAR)

Prediction	Scenarios	Index	Support vector regression	XGBoost	Random forest	Gradient boosting decision tree
Total terrestrial organic carbon stock prediction	UD+LD	R2	0.447	0.736	0.758	0.768
		MSE	1514.04	723.71	662.10	634.88
		VAR	831.15	2204.05	3053.33	1919.83
	UD	R2	0.419	0.502	0.424	0.569
		MSE	1737.17	1488.89	1724.92	1289.45
		VAR	1443.68	893.10	987.81	1187.15
	LD	R2	-0.617	-0.441	-0.617	0.224
		MSE	860.43	767.10	860.79	413.24
		VAR	842.64	535.86	0.00	156.87

5.2.7 Landslide area and volume estimation

To estimate the volume of landslides, studies (Guzzetti et al. 2009; Larsen et al. 2010) often apply a power law volume-area equation as follows.

$$V = \alpha A^{\gamma} \qquad (1)$$

where α and γ are empirical parameters derived from various landslides inventories. However, this nonlinear form can easily lead to volume overestimation because of amalgamation and overestimation of landslides area (Li et al. 2016; Li et al. 2014; Parker et al. 2011). Different correction methods were proposed to estimate scar areas. For example, Li et al. (2016) applied a scale factor to determine the proportion of landslide

scars. Marc et al. (2019), Marc and Hovius (2015) and Marc et al. (2018b) developed a geometric correction method. In this thesis, the total landslide volume V is estimated as

$$V = \sum V_j = \sum \alpha A_{s,j}^{\gamma} \tag{2}$$

where V_j and $A_{s,j}$ are the volume and scar area of the j-th landslide, respectively. To calculate the scar areas, the correction methods above are both applied.

Regarding the uncertainty calculation, Li et al. (2014) regard Monte Carlo distribution as a standard normal distribution which contradicts their assumption that both α and γ are normally distributed. The sum of log-normally distributed variables does not tend to follow a normal distribution (Naus 1969). Francis et al. (2022) improve the method by deciding uncertainties as the standard deviation of Monte Carlo simulation. In this thesis, I assume that all the parameters mentioned accurately depict the relation between volume and area, indicating their adherence to normal distribution. Moreover, let $\log_{10} \alpha \sim \mathcal{N}\left(\log_{10} \mu_\alpha, \sigma_{\log_{10} \alpha}^2\right)$ and $\gamma \sim \mathcal{N}(\mu_\gamma, \sigma_\gamma^2)$ where $\mathcal{N}$ represents the normal distribution while μ's and σ's are some constants. Then following the rule of linear transformation on normal distribution, for each individual landslide, $\ln V_j$ is normally distributed with mean $\mu_\gamma \ln A_{s,j} + \ln \mu_\alpha$ and variance $\left(\sigma_\gamma \ln A_{s,j}\right)^2 + \left(\ln 10 \cdot \sigma_{\log_{10} \alpha}\right)^2$.

Thus

$$EV_j = \sqrt{c_j} M_j \text{ and } \text{Var}(V_j) = c_j(c_j - 1)M_j^2 \tag{3}$$

where $M_j = \mu_\alpha \cdot A_{s,j}^{\mu_\gamma}$ and $c_j = \exp\left\{\left(\ln A_{s,j} \cdot \sigma_\gamma\right)^2 + \left(\ln 10 \cdot \sigma_{\log_{10} \alpha}\right)^2\right\}$. Moreover, the expected value EV and variance $\text{Var}(V)$ of the total volume can be calculated as follows.

$$EV = \sum EV_j = \sum \sqrt{c_j} M_j \tag{4}$$

and

$$\text{Var}(V) = \sum \text{Var}(V_j) = \sum c_j(c_j - 1)M_j^2 \tag{5}$$

The total volume is $EV \pm \sqrt{\text{Var}(V)}$.

Following Marc's method (Marc et al. 2019; Marc et al. 2018a), for a landslide polygon with given perimeter P and area A, its scar area is estimated as

$$A_s = 1.5W^2 = \frac{6A}{\pi K} \tag{6}$$

where K is the equivalent ellipse aspect ratio defined as

$$K = \frac{1}{2}\left(\frac{4}{9}\left(\frac{P}{\sqrt{\pi A}} + 1\right)^2 - 2 + \sqrt{\left(\frac{4}{9}\left(\frac{P}{\sqrt{\pi A}} + 1\right)^2 - 2\right)^2 - 4}\right) \tag{7}$$

In contrast, Li et al. (2016) determined a scale factor f_{scar} considering uncertainty from mapping approach. For each landslide, area is multiplied by the estimated f_{scar} equivalent to $70 \pm 6\%$ for Wenchuan landslides. Assume that f_{scar} is log-normally distributed, say $\ln f_{scar} \sim N(\ln f, \sigma_{\ln f}^2)$, it can be obtained that

$$EV_j = \sqrt{dc_j' M_j'} \text{ and } \mathrm{Var}(V_j) = dc_j' M_j'^2 \left(c_j' e^{\sigma_\gamma^2 \sigma_{\ln f}^2} - 1\right) \tag{8}$$

where $d = \exp\{2\mu_\gamma \ln f + \ln^2 f \, \sigma_\gamma^2 + \mu_\gamma^2 \sigma_{\ln f}^2\}$, c_j' and M_j' are defined as c_j and M_j except for changing the scar area to total area.

Overall, the landslide volume with the updated uncertainty as induced by 2008 Wenchuan earthquake is estimated according to the parameters obtained from Guzzetti et al. (2009), Larsen et al. (2010) and Parker et al. (2011) in

Table **S4**. The average value is applied to estimate the total sediment mass in our study area that flows through the Minjiang, Tuojiang, Fujiang and Bailongjiang catchments in Table 5.5.

Table 5.5 Detailed Information of the Study Area

The detailed information of our study area (described as four basins) that flows through the Minjiang, Tuojiang, Fujiang and Bailongjiang catchments and the corresponding landslide number, area and estimated mass based on the landslide inventory by Li et al. (2014).

Major rivers	Drainage area (km²)	Study area (km²)	Forest area (km²)	Landslides amount	Landslide area (km²)	Landslide deposit (km²)	Landslide volume (km³)	Landslide sediment (Mt)
Minjiang	30968.73	12680.28	8414.05	13597	253.18	75.95±0.2	1.448±0.482	2896±1067
Tuojiang	11642.69	3731.20	1574.55	5162	127.72	38.32±0.22	0.958±0.414	1915±885
Fujiang	31860.53	12912.94	9604.72	4118	82.05	24.62±0.44	0.894±1.569	1788±3184
Bailongjiang	12366.89	3681.08	3303.79	175	2.16	0.65±0.01	0.009±0.004	19±8
Total	86838.84	33005.50	22897.11	23052	465.20	139.56±0.54	3.334±2.037	6667±4239

Table 5.6 Terresreial Ecosystem Organic Carbon Mass in the Study Area
The total terrestrial ecosystem organic carbon mass calculated through gridded data, as distributed in our study area before earthquake, and mobilized and recovered after earthquake.

Major rivers	Before earthquake			After earthquake		
	Total ecosystem OC storage (Mt)	Hillslope ecosystem OC stock (Mg/ha)	Total mobilized ecosystem OC (Mt)	Hillslope recovered ecosystem OC stock (Mg/ha)	Hillslope recovered ecosystem OC (Mt)	Total reaccumulated ecosystem OC via NPP (Mt)
Minjiang	139.1±15	155.3±23.4	3.66±0.004	58.5±12.7	1.31±0.006	1.99
Tuojiang	54.7±10.2	172.0±27.3	2.02±0.007	56.9±11.0	0.64±0.007	0.80
Fujiang	176.5±33.6	129.2±28.5	1.09±0.01	52.7±13.3	0.41±0.009	0.72
Bailongjiang	46.1±7.2	141.5±21.9	0.03±0.0002	68.7±12.0	0.01±0.0005	0.02
Total	416.4±38.9	149.5±12.7	6.8±0.01	59.2±6.1	2.36±0.01	3.52

5.2.8 Carbon budget estimation

The total ecosystem OC is denuded from undisturbed area by co-seismic landslides and then deposited along hillslopes. This amount of OC is described as mobilized carbon, and mixed with hillslope deposits. Subsequently, the mobilized carbon can be either buried along hillslope for temporarily or long-term sink, or distributed along channel and exported through fluvial system or other mass wasting processes.

Source

$$S_s = \sum \rho V = \sum \rho \alpha A_s^\gamma \tag{9}$$

$$OC_m = \sum OC_p \times A_p \tag{10}$$

where $\sum$ sums over all co-seismic landslides; S_s represents total sediment generated by earthquake; V indicates the volume of the landslide; A_p and A_s denote the area for one pixel and the scar area for one landslide, respectively; α and γ are the empirical parameters discussed in previous section; ρ is the sediment density; OC_m and OC_p mark the mobilized OC and the predicted OC tock of one pixel pre-earthquake, respectively.

Hillslope

$$S_h = S_s \times r_h \tag{11}$$

$$OC_h = OC_{ud} + OC_{ld} \tag{12}$$

$$\Delta OC_h = \Delta OC_{ud}(\approx 0) + \Delta OC_{ld} = \Delta OC_{ld} \tag{13}$$

$$\Delta OC_h = OC_{rt} + OC_{rc} - OC_s \tag{14}$$

where S_h represents the sediment stored on the hillslope; r_h represents the proportion of sediment stored on the hillslope that is quantified by Francis et al. (2022); OC_h, OC_{ud}, and OC_{ld} denote the OC on the hillslope, OC in the undisturbed region and OC in the landslide region, respectively; Δ represents the difference of corresponding OC induced by mega earthquake; OC_{rt} along hillslope that represents the part of mobilized carbon being remained along hillslope after ~10-year erosion, is different from OC_{rc} along hillslope that represents the carbon being reaccumulated along landslide surface through soil development and plant regrowth. The OC_{rc} is predicted according to the field investigation on landslide surface, where we only sampled the 50-cm depth. The OC_{rt} is the amount of source OC OC_s mixed with the landslide deposit volume of 3.33 ± 2.04 km³. The small amount of ecosystem carbon between these two overlapped in the surface 50 cm is ignored. Thus, the OC_h here reflects the OC_{rt}. It is calculated by the sediment budget according to the assumption that ecosystem OC is completely mixed with

sediments, which cannot be true in reality. Instead of field sampling, OC_{rc} can be compared to NPP using remote sensing datasets.

$$OC_{rt} = OC_m \times r_h \tag{15}$$

$$OC_{rc} = \sum OC_p \times A_p \tag{16}$$

$$OC_{rc} = \sum N_p \times A_p - OC_{sr} - OC_{se} \tag{17}$$

where N_p is the net primary productivity of one pixel; OC_{sr} and OC_{se} denote the OC respired and eroded in the surface soil along landslide deposit. This approach provides quantification of the processes of soil respiration and erosion occurring along the landslide deposits. The calculated carbon budget along hillslope is presented in Table 5.6.

Channel and Fluvial

$$S_c = S_m - S_h - S_d \tag{18}$$

$$OC_c = OC_m - OC_{rt} - OC_d \tag{19}$$

where S_c, S_m and S_d denote the sediment of channel and fluvial, mobilized sediment, and the sediment mass being directly exported outside through debris flows, respectively; OC_c and OC_d denote the OC of channel and fluvial, and OC of debris flow, respectively; The organic carbon content has been sampled in the study conducted by Liu et al. (2022), yielding very low values that are not comparable to those found in typical ecosystems. However, the substantial sediment load can contribute to a relatively significant carbon mass. In this study, the carbon being transported by debris flow is estimated according to the following equations.

$$S_d = S_h \times r_d \tag{20}$$

$$OC_d = OC_{rt} \times r_d \tag{21}$$

where r_d is the proportion of sediment transported by debris flow given by Francis et al. (2022).

5.3 Results

5.3.1 Spatial distribution of terrestrial organic carbon

Our study involved extensive field data collection from 123 sites, including landslide deposits and undisturbed areas, complemented by 194 entries from previous literatures within studied area (Table S5). A subset of these entries, scored for high quality, was incorporated into model predictions. This comprehensive dataset forms the foundation for our model. Using gradient boosting decision trees (GBDT), known for their superior performance among popular machines learning models, we modelled the spatial distribution of carbon stocks prior the earthquake (Figure 5.2). We used over 20 raster layers, both invariant or variant, to extrapolate the limited field data into a regional scale. These layers encompass parameters such as landslide area, aspect, elevation, slope, precipitation, temperature, lithology, gross primary production, total nitrogen, clay content and bulk density. The importance for training samples through GBDT is presented in Figure 5.3.
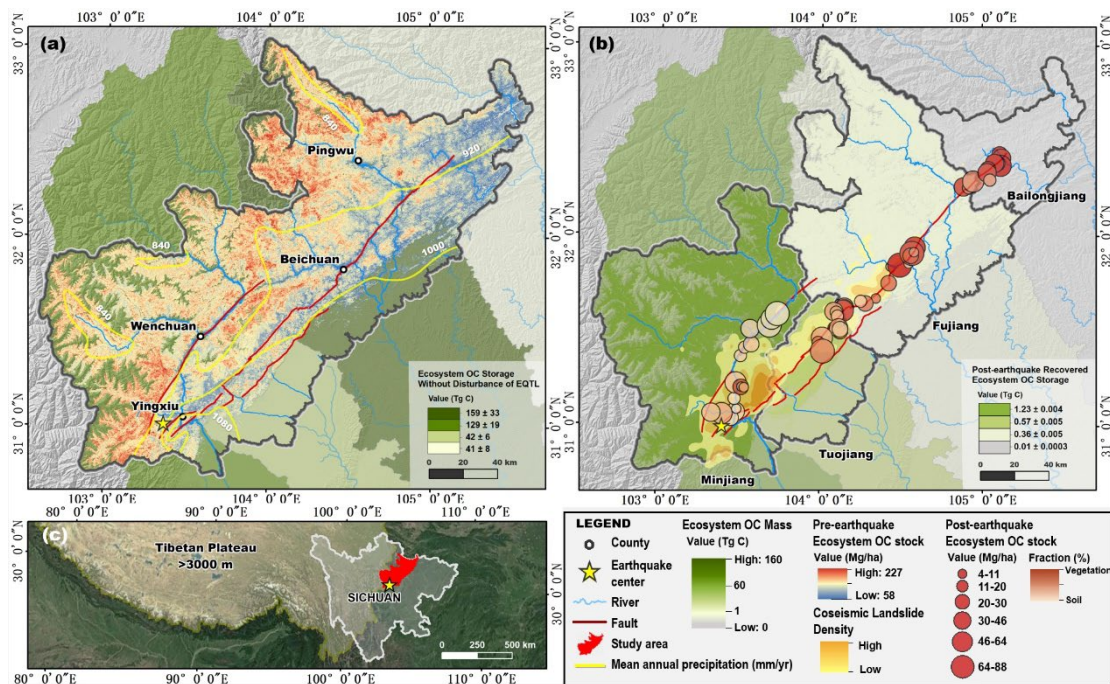
Figure 5.2 Spatial Distribution of Terrestrial Ecosystem Organic Carbon
(a) terrestrial ecosystem organic carbon (OC) stock distribution pre-earthquake; (b) recovered OC stock post-earthquake, the grey boundaries show the basins areas for four major river systems: Minjiang, Tuojiang, Fujiang and Bailongjiang; (c) location of our study area and Sichuan province of China, on the southeastern margin of Tibetan Plateau, with the boundary of the Tibetan Plateau delineated as elevations >3000 meters. The green background in (a) and (b) with transparency reflects total ecosystem OC mass in each basin, where different colour represents different magnitudes of carbon mass. Specifically, subfigure (a) and Subfigure (b) reflect the total OC mass (unit: Mt C) as removed by earthquake-induced coseismic landslides and recovered after earthquake until 2020, respectively. Both maps are applied to the land use type of forest and shrub. The bubble size reflects the total ecosystem OC stock (unit: Mg C ha^{-1})

after one decade recovery on landslide sampling deposits. In comparison, the colour of bubble reflects the fraction of vegetation and soil in total terrestrial carbon stock.

(a) Undisturbed area   **(b) Landslide area**
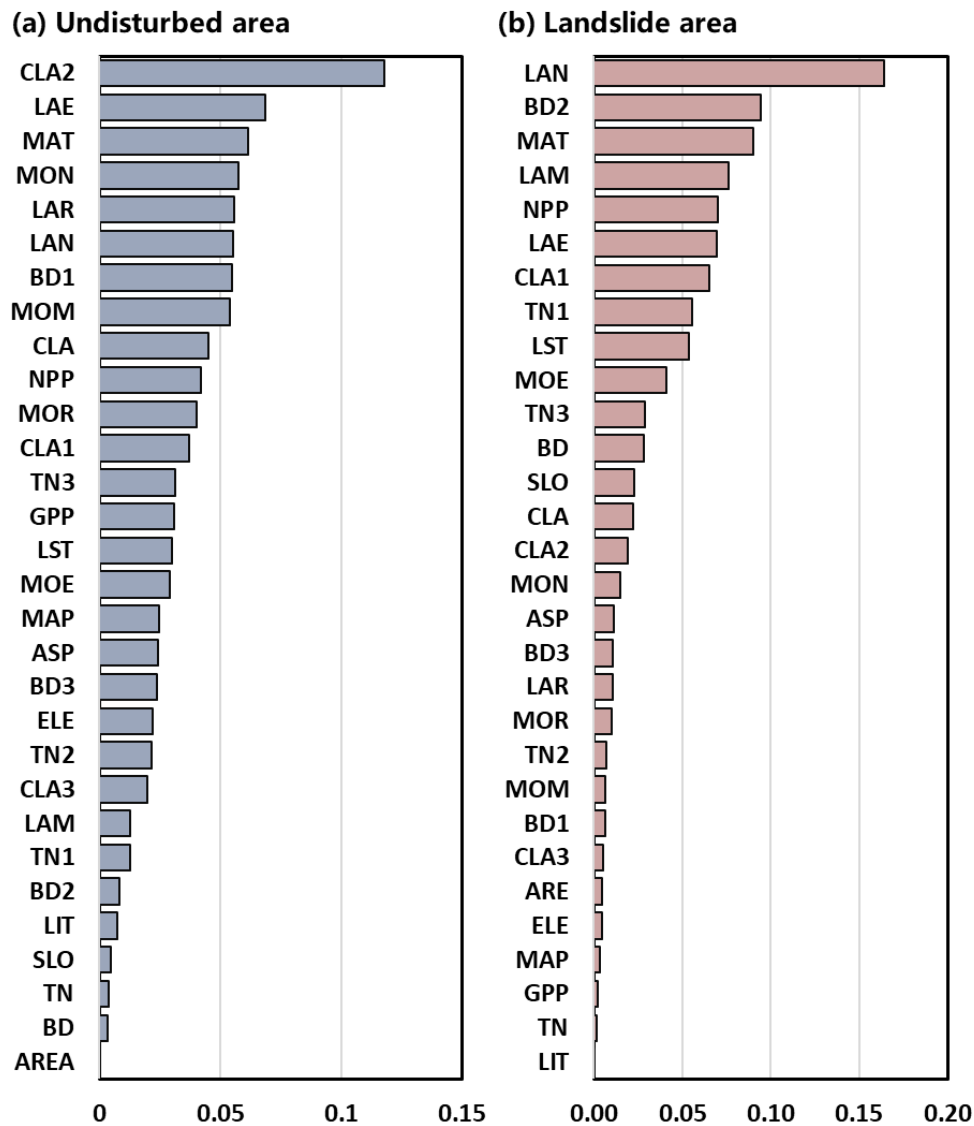
Figure 5.3 The importance for training samples on undisturbed area (UD) and landslide area (LD) through GBDT.
Covariates are detailed in Section 5.2.5.

Prior to the earthquake the average ecosystem OC stock across the whole landscape was 136 ± 25 megagram carbon per hectare (Mg C ha^{-1}), exhibiting significant variability with values ranging from a low of 50 to a high of 260 Mg C ha^{-1} (all uncertainties are measured as ±1 standard deviation, unless otherwise noted; all units for carbon mass is Mt C and Gt C, carbon stock is presented as Mg C ha^{-1} and carbon flux is expressed as t C km^2 yr^{-1} to facilitate comparisons with other studies). The spatial distribution of pre-earthquake terrestrial carbon stock correlates with topography and climate. The intensity of total ecosystem OC stock demonstrates an increasing trend with elevation, ranging

from 500m to 2000m (Figure 5.4 and Figure 5.5). Beyond this elevation range, variations in ecosystem OC are minimal. As shown in Figure 5.2(a), the highest concentration of terrestrial carbon is found on the steepest mountains close to range-front where average precipitation rates are highest, suggesting an orographic control on the distribution of pre-earthquake carbon stock. Other parts of the mountain range, particularly those further north, have equally high total OC stocks, but the proportions differ. Samples collected along the range front have by far the highest soil OC content (Figure 5.2b).
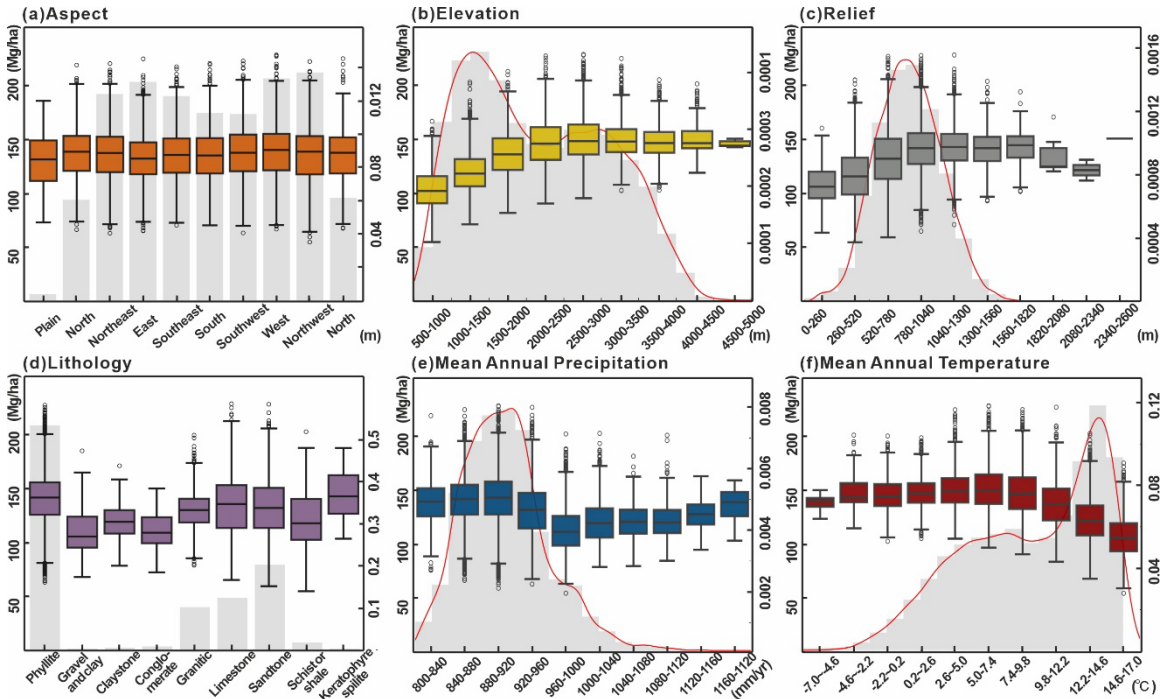
Figure 5.4 Terrestrial Ecosystem Organic Caron Stock Across Topographic and Environmental Gradients

The distribution of total ecosystem organic carbon stock across various gradients without earthquake disturbance includes: (a) aspect, (b) elevation ranges, (c) relief, (d) lithologies, (e) mean annual precipitation (MAP) and (f) mean annual temperature (MAT), respectively. The grey shading denotes the frequency of corresponding covariates
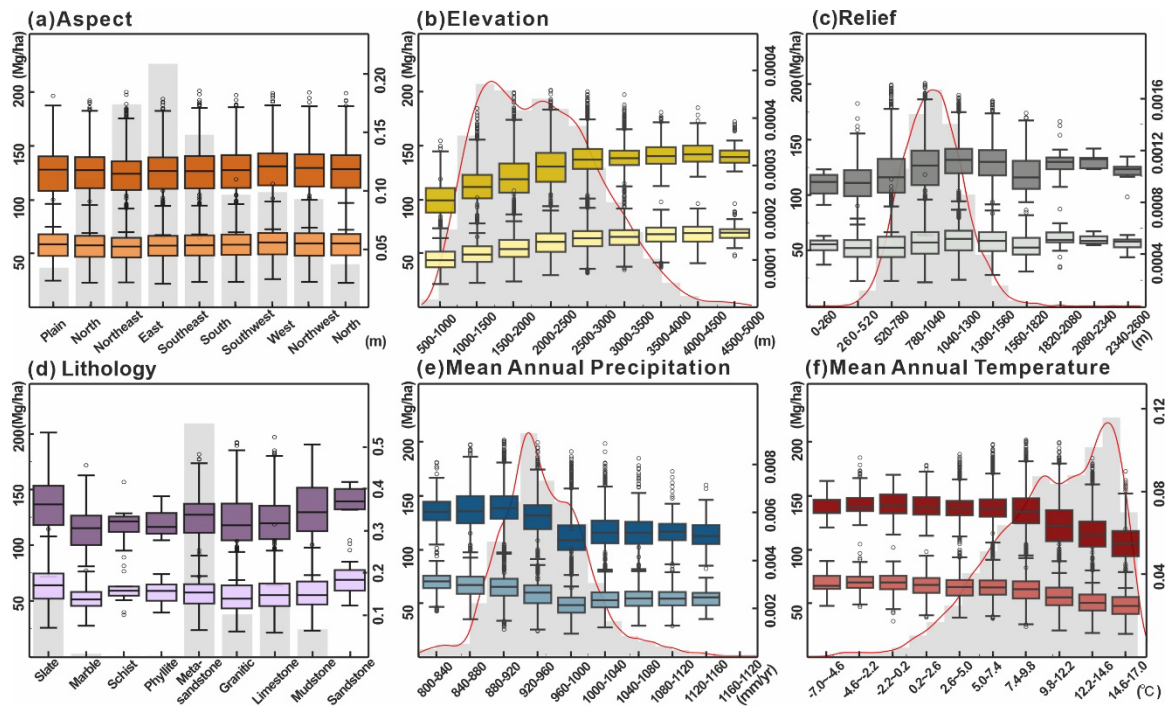
Figure 5.5 Recovered Ecosystem Organic Carbon Stock After the 2008 Wenchuan Earthquake
The distribution of recovered ecosystem organic carbon (OC) stock across various topographic and environmental gradients in landslide deposits (light colours), compared to the undisturbed state (deep colours), includes: (a) aspect, (b) elevation ranges, (c) relief, (d) lithologies, (e) mean annual precipitation (MAP) and (f) mean annual temperature (MAT), respectively. The relative deep grey shading denotes the frequency of corresponding covariates

Wenchuan Earthquake landslides eroded 5.5 ± 0.01 Mt C, amounting to 2 - 6 wt. % of global annual ecosystem carbon erosion (Lal 2003). EQTLs in Wenchuan have a strong spatial distribution related to the topography, lithology, and position relative to the fault rupture (Gorum et al. 2011; Li et al. 2014). The majority (2.5 ± 0.6 km³) of EQTLs occurred within the Minjiang and Tuojiang basins allowing us to compare the mobilized carbon across a spatial gradient of damage. Correspondingly, the terrestrial carbon mass that was eroded by Minjiang and Tuojiang landslides equals 4.5 ± 0.006 Mt C, which accounts for 83% of the total carbon mass denuded by EQTL. The strong spatial control on carbon erosion means that the large carbon store in the Fujiang catchment remained largely intact, consistent with the spatial distribution of pre-and post-earthquake net primary production (NPP), which saw little change over this area (Figure 5.6).
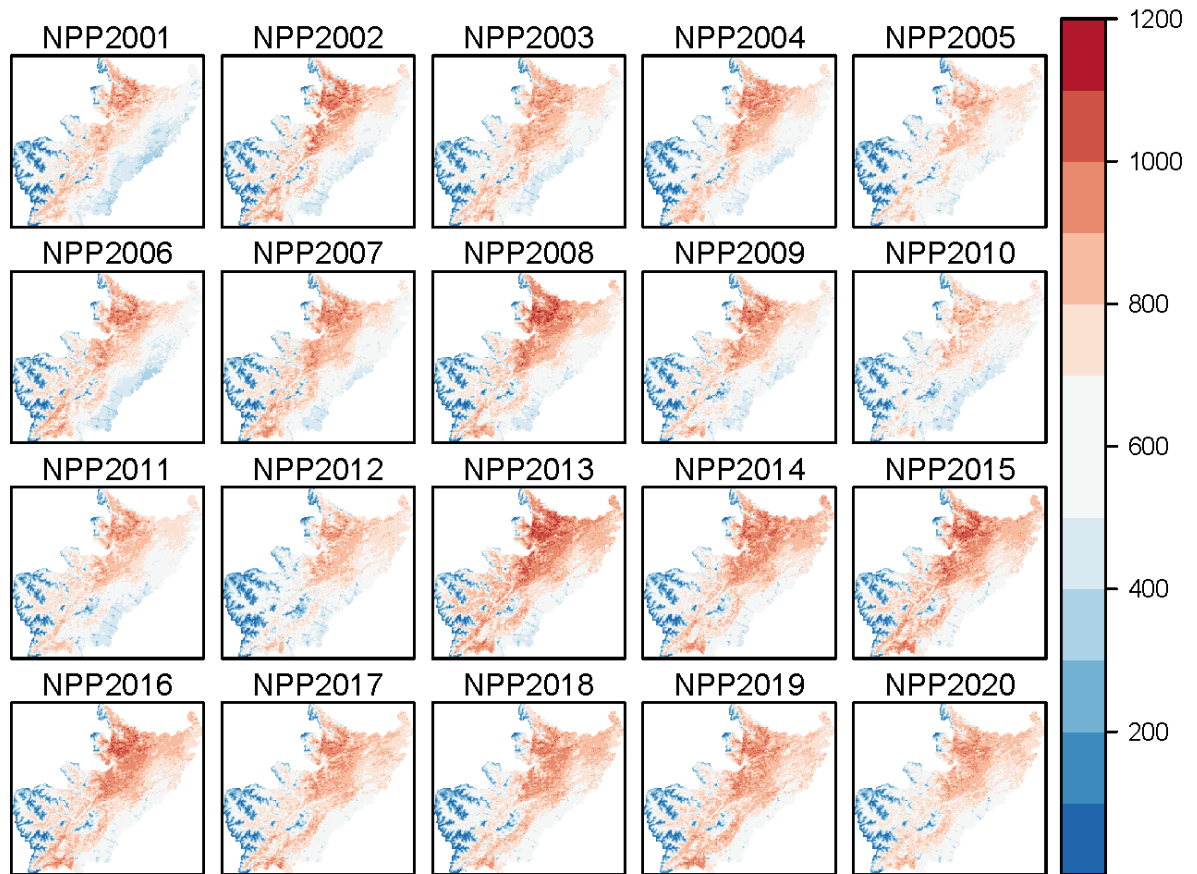
Figure 5.6 The Annual NPP Distribution from 2001 to 2020
This figure covers the period before and after Wenchuan earthquake in our study area. Obtained from MODIS NPP product (MOD17A3).

5.3.2 Recovery of terrestrial organic carbon

Over decade after the Wenchuan earthquake, landslide sites have a total OC of 33 ± 21 Mg C ha^{-1}. The recovery rate of total terrestrial OC was 475 ± 110 t C km^{-2} yr^{-1} on landslide surfaces and 5.5 ± 0.02 t C km^{-2} yr^{-1} when applied to the overall affected area. The major components of the total ecosystem OC storage are soil OC ($55 \pm 29\%$) and tree biomass ($32 \pm 29\%$). The soil vertical profile shows no obvious increase or decrease in carbon stock with depth, suggesting the profiles are well mixed with depth (Figure 5.7). Soil OC content is positively correlated with total soil nitrogen content for all sites (TN) (Figure 5.8). New vegetation that has regrown on landslide scars accounts for 15 ± 16 Mg C ha^{-1}, which is a quarter of the pre-earthquake OC stock. Recovery is characterised by a major change in the species composition of the forest from pre-earthquake forests dominated by *Pinus tabuliformis*, *Cupressus funerbrism* and *Cryptomeria fortune* to recovered forests of *Alnus cremastogyne*, *Populus alba* and *Ziziphus jujuba* (Figure 5.9). Some of these new species are distinguished by their rapid

growth rates, resilient capacity for colonizing disturbed sites, while others have both ecological and economic value and may be linked to the conservation policies and projects in southwest China (Jing et al. 2012).
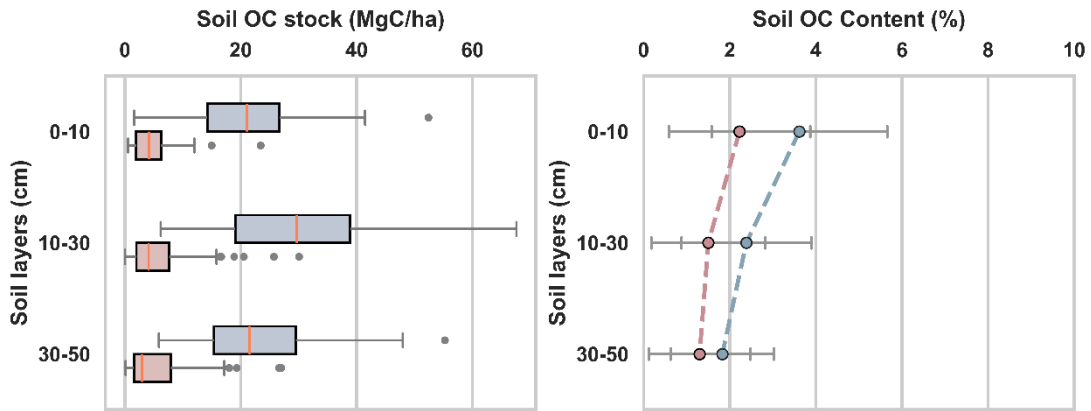
Figure 5.7 Soil Organic Carbon Trends Along Soil Depth
Soil organic carbon stock trend along soil depth (0-10 cm, 10-30 cm and 30-50 cm) (Left), and soil organic carbon content trend along soil depth (Right) based on field sampling data. Overall, the blue colour reflects the samples on undisturbed deposits (UD) and red colour reflects the samples on landslide deposits (LD).
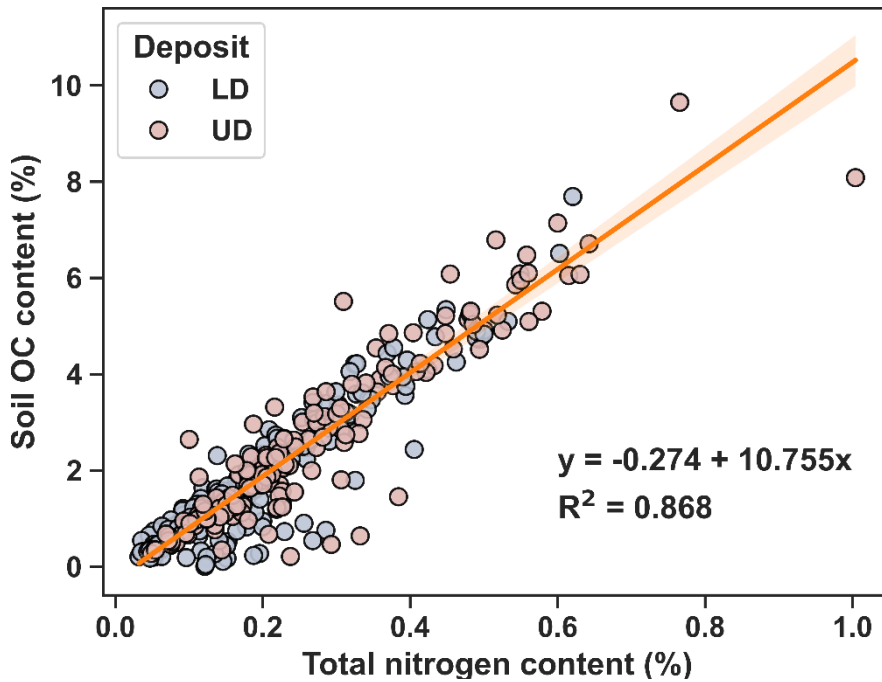
Figure 5.8 Correlation Between Soil Organic Carbon Content and Total Nitrogen Content Pre- and Post-Earthquake for
This analysis shows the relationship between soil organic carbon (SOC) content and total nitrogen (TN) content before and after the earthquake based on field sampling data. The line represents the best linear fit, along with 95% confidence intervals, indicating the strength and significance of the correlation.
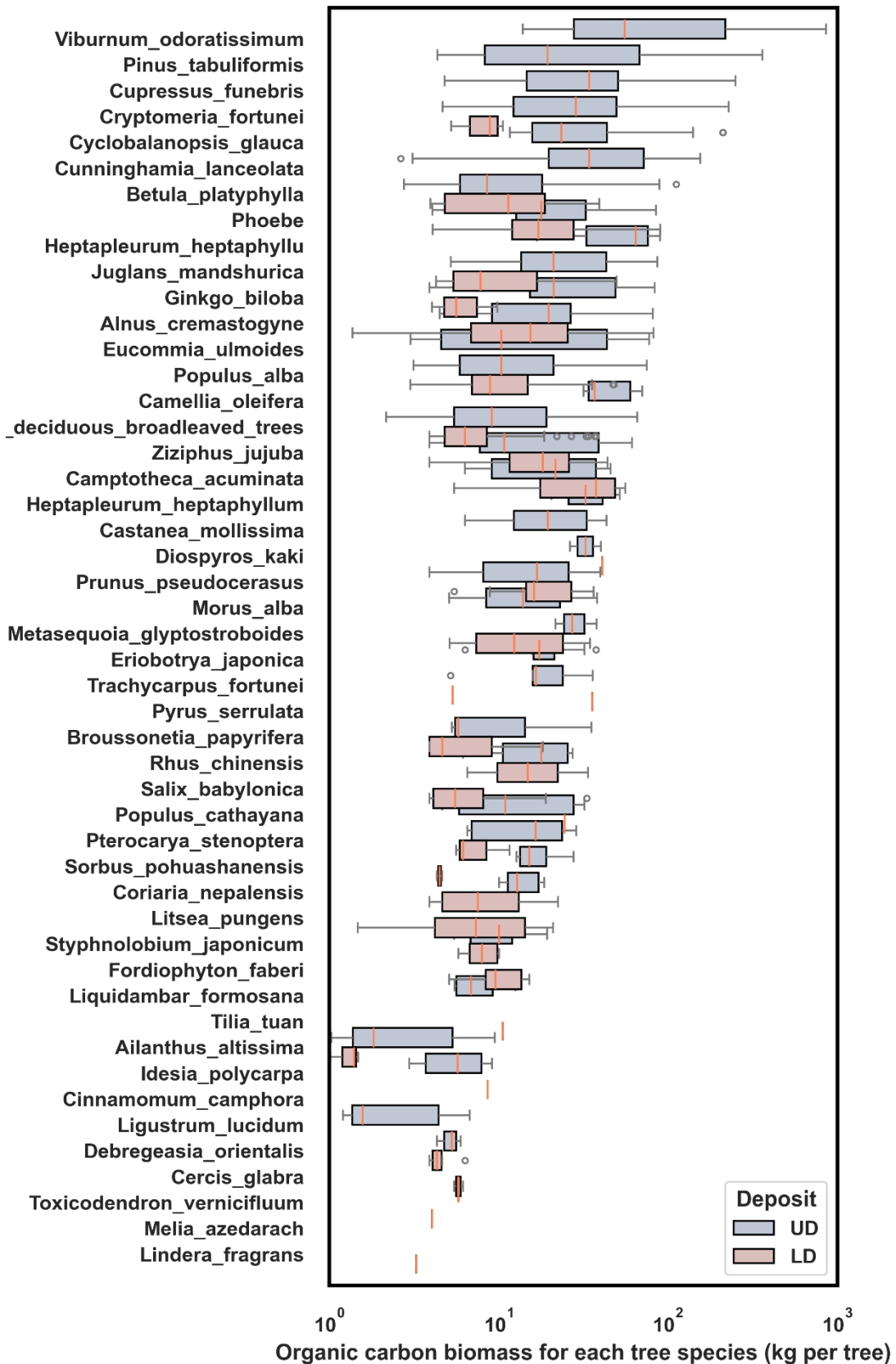
Figure 5.9 Organic Carbon Mass for Each Tree Species before and after the Earthquake
This is based on field sampling data. The blue colour represents the samples on undisturbed deposits (UD)
and red colour represents the samples on landslide deposits (LD)

Vegetation coverage of landslide surfaces had recovered to 80-90% of pre-earthquake levels within a decade of the earthquake, as inferred from metrics including normalized difference vegetation index (NDVI), enhanced vegetation index (EVI), leaf area index (LAI) (Sun et al. 2021; Wang et al. 2024; Yunus et al. 2020). This observation is consistent with time series of net primary productivity (NPP) change in our study area (Figure 5.10(b)). The NPP of both the whole landscape and landslide areas decreased immediately after the earthquake. The average NPP of the landslide deposits suddenly dropped from 760±110 t C km^{-2} yr^{-1} in 2007 to a low point of 580±120 t C km^{-2} yr^{-1} in 2010. NPP recovered rapidly between 2010 and 2015, when it returned to pre-earthquake levels. Despite the rapid increase in NPP during this initial stage of recovery, total carbon storage within the landscape remained deficient due to the slower return of soil carbon and vegetation biomass. Landslide surfaces sequestered 3.5±0.01 Tg C via NPP, amounting to around half of the total OC mobilized by landslides. The measured OC for landslides surface is 2.2±0.01 Tg C, which is much smaller than the pre-earthquake level. The difference between NPP-sequestered OC and field-measured OC indicates that carbon fluxes of fluvial transport, decomposition and respiration release contribute to the regulation of carbon storage.
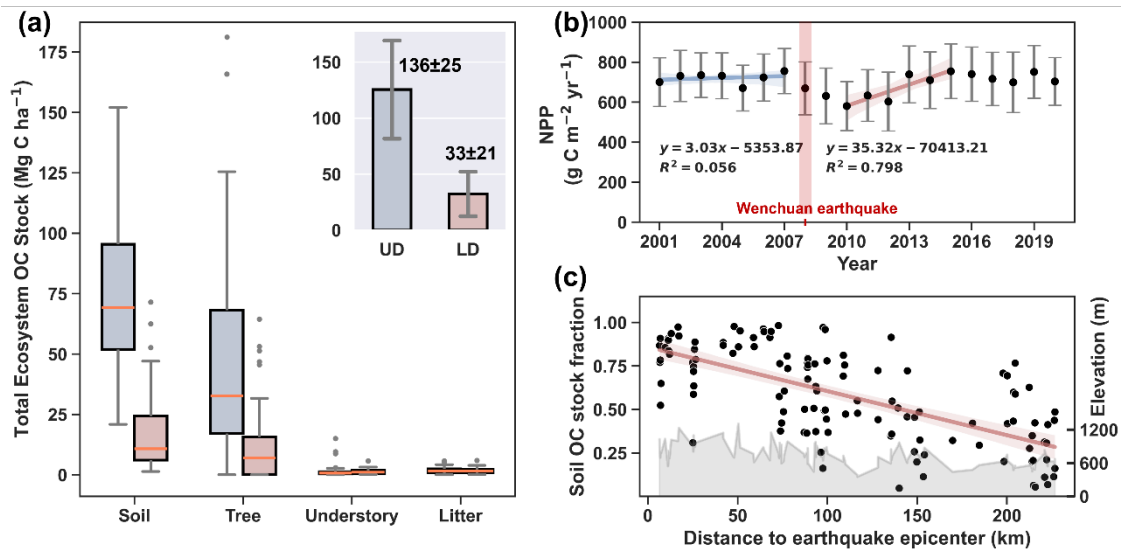
Figure 5.10 Terrestrial Ecosystem Organic Carbon Stock Obtained from Sampling Datasets
(a) shows the components of soil organic carbon (OC), tree OC, understory plant OC and litter OC. The inset shows the average value of total ecosystem OC stock undisturbed area and landslides deposits (b) shows the yearly NPP trend of EQTLs deposits; (c) shows the soil OC stock fraction (compared to the total ecosystem OC stock) along the distance to epicentre obtained from sampling datasets. In Subfigure (a), the blue colour reflects the samples on undisturbed deposits (UD) that represents the pre-earthquake level, and red colour reflects the samples on landslide deposits (LD) that represents the post-earthquake level. The box limits reflect the range of the central 50% of the data, with central line marking the median value. The grey dots reflect the outliers. The error bar reflects the standard deviation.

5.3.3 Hillslope carbon budget after an earthquake

Based on our estimates of burial and recovery of terrestrial carbon after the Wenchuan Earthquake, we calculated the hillslope carbon budget for the decade after the earthquake. We focus on hillslopes as we have good constraints on the rates of sediment storage and export into the fluvial system from Francis et al., 2021 (Figure 5.11). The total volume of carbon stored in EQTLs assume that pre-earthquake soil and vegetation carbon is eroded and well mixed into landslide deposits. 12% of the carbon stored in EQTLs deposits has been eroded, primarily by debris flows (Francis et al. 2022). As an upper bound for erosion, we can also assume that all of the EQTLs deposits that are connected to the fluvial network have eroded all of that material, resulting in erosion of 43% of carbon deposited (Li et al. 2016). Considering this range, hillslopes result in between 3.1 and 4.8 Mt C of terrestrial carbon burial. Based on field observations and the detailed sediment budget of Francis et al. (2022), storage is likely to be closer to this upper bound of 4.8 Mt C. Based on our field measurements, 2.2 ± 0.01 Mt C recovered along hillslopes. Compared to the accumulated carbon via NPP, the difference indicates that a sizeable portion of carbon flux reflects decomposition and respiration release. Overall, the Wenchuan Earthquake has stored 5.3~7.0 Mt C on hillslopes as erodible sediment. Hence this earthquake behaves in a similar manner to a capacitor, temporarily storing carbon and releasing it slowly through time.
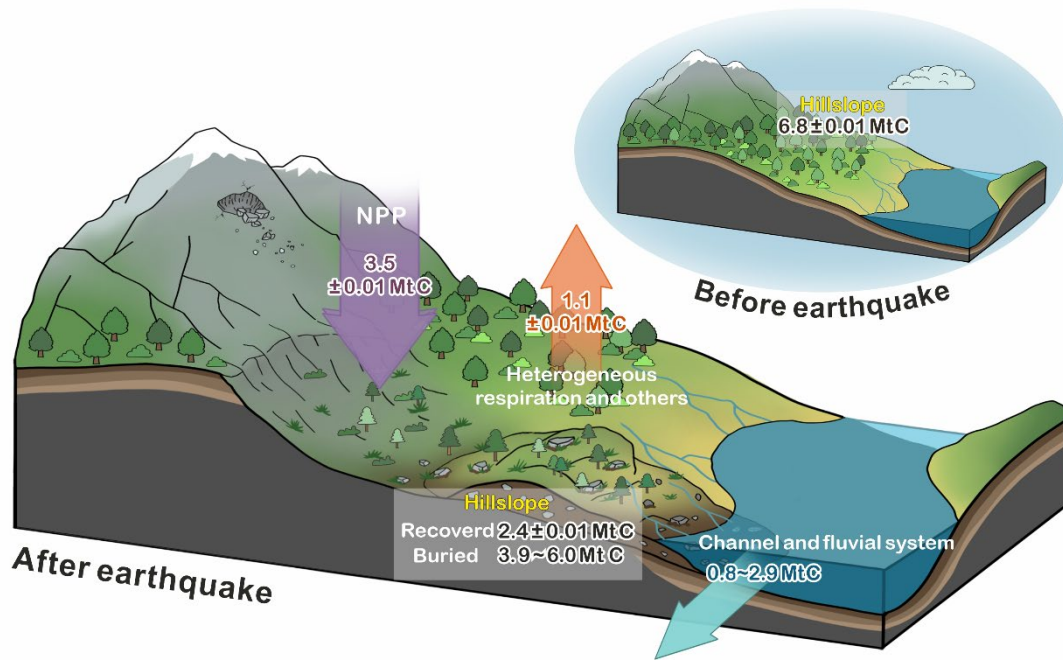
Figure 5.11 Overview of Hillslope Ecosystem Organic Carbon Budget before and after 2008 Wenchuan Earthquake
It illustrates how ecosystem OC flows and how much ecosystem OC being recovered and buried along hillslope deposits before and after the 2008 Wenchuan earthquake, including the carbon exchange between deposit and atmosphere, carbon transportation from source to fluvial systems absorbed (major fluxes are shown on the diagram). The hillslope budget is quantified according to the prediction map in this study, in which the flux is specifically focused on the landslide area pre-earthquake and 12 years post-earthquake. The channel and fluvial system budget are estimated in tandem with previous sediment budget, in which the flux is focused on the whole study area. The portion of carbon being released to atmosphere is estimated by the difference between recovered carbon and the reaccumulated carbon via NPP, which could be caused by other processes, like heterotrophic respiration etc.

5.4 Discussions

5.4.1 Correlation between landslide activity and terrestrial carbon stock

Terrestrial OC stocks prior to earthquake is spatially correlated with landslide activity following earthquake, with both being highly concentrated along the range front of the Longmen Shan. The spatial correlation of high terrestrial OC and landsliding could be coincidental: moderate elevation exhibits high terrestrial OC, and low temperatures at high elevations can facilitate OC preservation in soils by inhibiting respiration, meanwhile steep slopes at these elevations drive more landsliding. But the observed relationship is also consistent with feedback between soil carbon accumulation and landslide susceptibility. Vegetation and soil developed in landslide-prone terrain are frequently disturbed and buried. Prior work suggests that this kind of disturbance may

facilitate soil OC assimilation and preservation, in part because biomass and soil carbon that is reworked by landslides can increase soil fertility, favouring the physical and microbial stabilization of OC (Rammig et al. 2006; Velázquez and Gómez-Sal 2007; Walker and Shiels 2008). In field experiments, buried plants and soil by landslides increased organic matter accumulation in soils formed on deposits more rapidly than natural plant litter (Shiels et al. 2005). In other studies, young landslide scars have been shown to store more OC in soils than in plant biomass, indicating the important role of landslides in storing soil OC (Walker and Shiels 2008).

In this study, the recovered terrestrial OC mainly comes from soil OC accumulation and preservation that may reflect the strong stochastic landslide disturbance in this part of the Longmenshan (Rasigraf and Wagner 2022). Within catchments with the highest proportion of EQTLs (Minjiang and Tuojiang) the soil OC stock accounts for 87% and 59% of total ecosystem OC post-earthquake, while the tree OC stock accounts for 85% and 67% in EQTLs deposits in Bailongjiang and Fujiang. The spatial differences suggest either that there has been inheritance of soil OC in range-front locations or that differences in the post-earthquake accumulation of soil carbon are due to lithology, precipitation, and/or grain size of landslide deposits. Where EQTLs deposit soil OC content has been measured in other studies it is close to zero: reported values include $0.17 \pm 0.04\%$ for the top 0-10 cm in a tropical forest (Guariguata 1990), $0.15 \pm 0.05\%$ for rockslides in western Southern Alps (Hilton et al. 2008a), and $0.24 \pm 0.07\%$ for fresh channel deposits in Wenchuan earthquake affected region (Harvey et al. 2022; Liu et al. 2022). There is usually not enough inherited OC for deposit surface and disturbed terrestrial OC might be diluted or deeply buried with generated sediments. The typical carbon sink of forests ranged between 66 and 122 t C km^{-2} yr^{-1} in Southwest China (Guo et al. 2013; Pan et al. 2011). The soil carbon accumulation rate after disturbances is expected to be higher compared to undisturbed mature soil. In Taiwan, the rate of soil OC accumulation on landslide scar area was approximately 200 t C km^{-2} yr^{-1} following the initial of revegetation. For Wenchuan sites, if we assume that there was no inherited soil carbon, then soil carbon accumulation rates would range between 12 and 596 t C km^{-2} yr^{-1}. The upper bound is much higher than similar sites, suggesting either very rapid accumulation of soil carbon or inheritance. Considering that the initial OC content of fresh deposits is less than ~10% of current OC content, it is unlikely that direct and immediate transfer of soil OC can account for large differences we see in the OC re-accumulation along hillslopes. Instead, it suggests a legacy effect wherein carbon rich soil and debris contribute to recovered soil carbon.

Rates of ecosystem carbon burial and recovery after the Wenchuan Earthquake is within the range reported for other landslide events (Table 5.7). At the short timescales over which our measurements were made, the role of petrogenic carbon is small, hence our focus on terrestrial carbon. While no other study has attempted a full terrestrial carbon budget for an earthquake, the total ecosystem OC sequestered by the Wenchuan Earthquake is amongst the highest recorded. Landslide events associated with other major earthquakes such as the Alpine Fault or typhoons associated with the Chi-Chi Earthquake(Dadson et al. 2004) generated between 3 and 14 Mt C. Rates of carbon accumulation after the Wenchuan Earthquake are higher than other studies, likely reflecting the climate of the region. Additionally, export rates of fluvial particulate OC after disturbance are lower in Wenchuan, likely due to the nature of deposition of coseismic landslide debris above the fluvial network. The tectonically active ranges of the Narayani basin in central Himalaya in response to the 2015 Gorkha earthquake revealed that the co-seismic landslides did not significantly perturb sediment and carbon fluxes (Märki et al. 2021). A possible explanation for this based on our observations after the Wenchuan Earthquake is that most of the sediment and ecosystem OC generated by coseismic landslides are buried within mountain ranges in the short-term (Francis et al. 2022; Francis et al. 2020). However, the fluvial POC export of 6.2 ± 1.1 t C km^{-2} yr^{-1} indicated a relative higher magnitude of background carbon flux in Himalaya compared to Longmen Shan. Overall, our terrestrial carbon budget highlights the importance of landslides as a carbon store within orogens, with carbon export rate dependent on the processes governing landslide triggering, deposition and erosion.

Table 5.7 Summary of Reported Values Associated with Landslides
Summary of the reported values associated with landslides-generalized ecosystem organic carbon (OC), fluvial POC and ecosystem OC recovery rate.

Study Site	Study area (km²) [a]	Disturbance (return period)	Terrestrial OC mobilized by landslides (Mt C) [b]	Terrestrial OC yield averaged by return period (t C km⁻² yr⁻¹) [c]	Fluvial POC export (t C km⁻² yr⁻¹) [d]	Terrestrial OC recovery rate (t C km⁻² yr⁻¹) [e]	Cita-tion
Kotatahi valley, Western Southern Alps	2434	Landslides (~40 years)	0.7±0.3	7.6±2.9	39	94±11	(Hilton et al. 2008a; Hilton et al. 2011b)
Windbag basin, Western Southern Alps	60	EQTL (250-350 years)	8.0±4.0 to14.0±5.0	5±2 to 9±4	NA	NA	(Frith et al. 2018; Hilton 2017; Hilton et al. 2008a)

Sierra de Las Minas mountain range	657	Hurrican Mitch in October 1998 (20-80 years)	0.4×10^6	8-33	NA	4.42-22.12	(Ramos Scharrón et al. 2012)
Zagunao river, Longmen Shan, Tibetan plateau	4629	EQTL	0.2±0.0	1.23	1.23±0.57	NA	(Wang et al. 2015; Wang et al. 2016)
Longmen Shan, Tibetan plateau	33005	EQTL (~80 years)	5.5±0.01	2.1±0.004	1.45±0.1	5.5 ±0.02 (475 ±110)	This study
LiWu river, Taiwan's Central Mountain Range	3320	Typhoon Morakot in August 2009 (~50 years)	3.9±0.6	23.7±3.9	16-202	~200 (282-445)	(Hilton et al. 2008b; West et al. 2011)
Alsea River, Oregon Coast Range	865	Landslides	NA	NA	3.8	NA	(Hatten et al. 2010)
Redwood Creek, California Coast Range	718	Storm triggered landslides (10 years)	0.02	2.8	NA	NA	(Madej 2010)
Kosnipata Valley, Andean Plateau	143	Landslides (25 years)	0.1±0.0	26±4	NA	NA	(Clark et al. 2017; Clark et al. 2016)

[a] Study area is considered as drainage area for catchment studies, except our study area is Wenchuan earthquake affected area covering 80% of the co-seismic landslide area.

[b] Terrestrial OC mass mobilized by landslides is extracted by landslide area and total ecosystem OC stock pre-earthquake or without the disturbance of landslides (per unit area).

[c] Terrestrial OC yield is the total generalized OC averaged by corresponding return period of disturbance. Unit of t C km^{-2} yr^{-1} equals to g C m^{-2} yr^{-1}.

[d] Fluvial POC export is extracted by POC content and suspended sediments discharge, which may include petrogenic POC and ecosystem POC. The POC export in LiWu river is estimated by the suspended sediments collected at Lushui gauging station, LiWu river from 1970. It does not give the POC export as induced by Typhoon Morakot in 2009. Our study estimates increased ecosystem POC as induced by Wenchuan earthquake.

[e] Terrestrial OC recovery rate is the total ecosystem OC reaccumulated after disturbance over a specific period, which can be directly sampled by forest plots or indirectly characterized by NEP or other indices. Bracket gives the total recovered terrestrial carbon amount being applied to denuded landslide area post-earthquake, instead of whole study area.

5.4.2 Capacitor effects on terrestrial carbon storage

The terrestrial OC budget for the Wenchuan Earthquake – the first of its kind – demonstrates how the total terrestrial carbon stock may recover after a large landslide event (Figure 5.12). Prior to the earthquake, the Longmenshan region contained a mature

forest ecosystem that was approaching an equilibrium state characterized by total OC stock of 5.5±0.01 Tg C. Immediately after the earthquake, living biomass and pre-existing soil carbon was buried in landslides. Some sediment and OC from landslide deposits was evacuated to the fluvial system (Marc et al. 2015). But despite removal of some material, approximately 88% of OC associated with landslides remained on the hillslopes a decade after the earthquake (Francis et al. 2022). This storage of OC in landslide deposits, which has not been widely-considered in prior work on post-earthquake carbon dynamics, may play an important role in the evolution of total OC stocks on the landscape. As vegetation regrows on these deposits, the total OC stock increases in the years following landsliding. However, over time, the OC stored in landslide deposits will be lost, either via in situ decomposition or erosion of the material in these deposits.

While the rates of these processes are not well known, they are expected to take many decades to hundreds of years, with the large volume of material from landslides from the Wenchuan Earthquake likely evacuated on a similar timescale as the return period of large earthquakes in the region (Francis et al. 2020). Over these timescales, hillslopes act as an organic carbon capacitor, storing carbon in landslide deposits and slowly releasing it by respiration and erosion. Consequently, terrestrial OC increases immediately after the event and diminishes as it is exhausted from hillslopes (Figure 5.12). The net effect of terrestrial OC stock depends on the balance between carbon inputs, such as vegetation regrowth, and carbon outputs, including respiration, decomposition, and erosion. The role of mega earthquakes causes an immediate redistribution of hillslope carbon pools, leading to dynamic changes in carbon fluxes. Following Wenchuan earthquake, the carbon inputs surpass the carbon outputs, resulting in a carbon sink. While this trend could potentially transition into carbon source under different climatic, tectonic and topographic settings. From a long-term perspective, if the response time of ecosystem carbon stocks to mega earthquakes exceeds the earthquake return period, mountains may act as a net carbon sink.
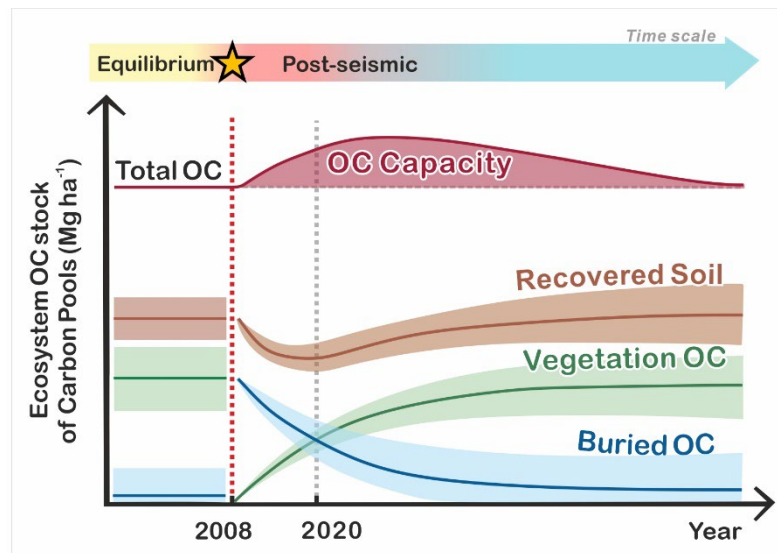
Figure 5.12 Hypothetical Framework Showing Evolution of Ecosystem Carbon Stock for Major Carbon Pools and Processes along Hillslope that Might be Altered by the Wenchuan Earthquake
The soil carbon flux and vegetation carbon flux represent the amount of carbon (per year) that finalized reaccumulated in soil and vegetation (trees, understory and litters) due to the soil development and forest production after earthquake, which can be assessed by NPP and respiration. The processes of decomposition, oxidation, weathering and etc. occurring for a longer time scale between hillslopes and atmosphere is classified as others. The total carbon mass represents the total ecosystem OC storage as altered by mega earthquake, while the long-term trend is not considered in this study.

5.5 Conclusions

The carbon budget post-Wenchuan Earthquake provides valuable insights into the carbon dynamics of orogenic systems. Our study estimates that Wenchuan Earthquake landslides eroded 5.5 ± 0.01 Mt C and deposited along hillslope and channel. A decade after, the hillslope carbon storage ranges from 5.3 to 7.0 Mt C, representing an average increase of approximately 10% compared to pre-earthquake levels. Among this stored carbon, nearly 60% is buried within landslide sediments, while the remainder is recovered from shallow soil and new vegetation. This significant storage capacity underscores the role of hillslopes acting as organic carbon capacitors following an earthquake. Mountain ranges temporarily store carbon through burial and recovery, and gradually releasing carbon through erosion, decomposition, and respiration. In the Longmenshan region, the high rates of ecosystem carbon burial and recovery post-earthquake creates a carbon sink that may last decades and hundreds of years.

Pre-earthquake modelling demonstrated that the spatial distribution of ecosystem organic carbon was significantly influenced by topography and climate, with higher concentrations along mountain ranges. The high concentration of EQTLs and pre-earthquake carbon stock along the range-front of the Longmenshan facilitated the efficient burial of soil carbon and vegetation biomass. The inheritance of soil OC in range-front locations likely contributes to the high accumulation rate of soil OC, suggesting a legacy effect where carbon-rich soil and debris contribute to recovered soil carbon. Through this mechanism, it is probably that frequent EQTLs might enhance the soi organic carbon sequestration. However, the overall recovery process also involves significant carbon fluxes through decomposition, respiration and erosion. This highlights the importance of understanding the processes governing EQTLs triggered carbon fluxes for predicting the long-term carbon cycle in tectonically active regions.

Chapter 6

Earthquakes Enhance Ecosystem Organic

Carbon Storage Capacity

6.1 Background

Seismic events have long been considered as an important component of the terrestrial ecosystem carbon cycle via landslides shaping mountain topography and denuding large areas of forest (Garwood et al. 1979a), supposedly leading to enhanced carbon mobilization and declined terrestrial primary productivity. The denuded hillslopes with a mixture of soil and vegetation biomass debris undergo a series of physicochemical processes that reaccumulates organic carbon (Rasigraf and Wagner 2022). Chapter 5 demonstrated that hillslope acts as carbon capacitor for local ecosystem carbon cycle after a mega earthquake, accumulating a total mass of 5.3~7.0 Mt C with the accumulation rate of 5.5 ± 0.02 t C km^{-2} yr^{-1}. Multiple case studies have provided solid evidence indicating that extensive landslides triggered by extreme events, should be a net carbon sink over specific study period (Frith et al. 2018; Galy et al. ; Galy et al. 2015; Hilton and West 2020). This raises the following research questions: in the context of frequent earthquake events, how is carbon sequestered by landslides? And how do earthquake-triggered landslides (EQTLs) affect the local ecosystem carbon balance, and the timescale for this impact? Exploring the temporal dynamics of ecosystem carbon storage, particularly in response to frequent earthquakes, is essential to comprehending the implications of tectonic activities on the global or regional carbon cycle, and further climate change.

Over 250 biochemical models aim to predict the ecosystem carbon balance (Luo et al. 2015; Luo et al. 2017; Luo and Weng 2011). The majority of these models simulate biochemical reactions, such as photosynthesis, respiration and decomposition. They typically follow the mathematical formulations of ordinary differential equations (ODEs) (Luo et al. 2017; Luo and Weng 2011; Sierra and Müller 2015). However, many models fail to consider external forces other than climatic change factors, such as topographic control and geomorphic processes that can distribute carbon across diverse landscape reservoirs. These forces disrupt the equilibrium of local carbon balance by altering internal C processes and pool sizes. For example, EQTLs affect carbon balance in various ways: they erode living material, depositing this carbon as particulate matter with sedimentary deposits; they promote carbon accumulation along landslide surface through plants regrowth and soil development; they change the volume of sediment which directly affects the concentration of carbon in sediment, which in turn affects the rate of soil carbon and dead debris export outside. It is a grand challenge to couple geomorphic processes with terrestrial C cycle models.

Recent efforts to address this gap include incorporating erosion processes into carbon cycling, with some studies detailing effects of soil aggregates, moisture, and soil depth on carbon fluxes (Billings et al. 2019; Booth et al. 2023; Doetterl et al. 2016; Doetterl et al. 2012). However, increasing model complexity necessitates extensive field data for calibration. Although certain cases studies quantify and integrate the rate of soil C erosion, deposition and accumulation to determine temporal change in carbon storage, the lack of a fundamental ecological model for new vegetation regrowth restricts the broad applicability of specific hillslope attribute to regional or global scale (Rosenbloom et al. 2006; Yoo et al. 2005, 2006). A promising development is the application of a coupled landslide-carbon model to quantify the impacts of rainfall-induced landslides on ecosystem carbon stocks in temperate rainforests, connecting geomorphic and biogeochemical processes (Booth et al. 2023). This study offers valuable insights and it constructs the model by making certain assumptions. Like all models, these assumptions shape the outcomes, but they highlight areas for further refinement. More attention should be given to erosion processes. Earthquake-induced mass movements immediately alter the size and distribution of vegetation and soil carbon pools. They disrupt the existing carbon balance, and more importantly, change carbon erosion processes. Numerous studies have demonstrated that landslide-generated sediments can remain on hillslopes for hundreds or even thousands of years (Francis et al. 2022; Li et al. 2016; Pain and Bowlersw 1973; Pearce and Watson 1986), indicating that the burial of carbon by landslides can have long-lasting effects. To accurately quantify regional carbon dynamics, it is essential to consider sediment mass balance into the carbon balance model.

This chapter aims to model the role of EQTLs in the ecosystem carbon cycle for mountain ranges. I develop a zero-dimensional carbon balance model that incorporates both the stochastic generation of landslide debris by earthquakes and subsequent changes in biochemical cycling of terrestrial ecosystem carbon. Using this model, I firstly investigate the temporal trends of each carbon pool in catchments affected by varied landslide area and scales. Then, I incorporate multiple earthquake events into the carbon balance model to evaluate their impact on long-term carbon storage capacity. This chapter builds upon the hillslope carbon budget discussed in Chapter 5, utilizing empirical data to establish essential parameters for the carbon balance model.

6.2 Methodology

6.2.1 Model theory

6.2.1.1 Carbon cycle

Throughout the carbon cycle, carbon is stored in different forms within various carbon pools, and it flows between these pools through carbon fluxes driven by both biochemical and geomorphic processes. As shown in Figure 6.1, plants absorb CO_2 from the atmosphere via photosynthesis, converting it into organic carbon. This process, denoted by P_{AB}, is the primary pathway for carbon to enter the biosphere from the atmosphere. The plant carbon pool is referred to as the P pool.

As plants undergo growth, aging, death, and decay, their branches, leaves, and roots become litter, thereby transferring carbon from the P pool to the litter carbon pool (L pool). This carbon flux is denoted as T_{PL}. Due to the close connection between the P pool and L pool, they are often considered as a single carbon pool-the aboveground carbon pool, denoted as the B pool.

Over time, the litter biomass undergoes a series of complex biochemical processes, including mechanical decomposition, microbial decomposition, and the activity of soil fauna. Through these processes, carbon transitions into the soil. This flux is denoted T_{BS}, and the soil carbon pool is referred to as the S pool. Meanwhile, continuous external disturbances such as rainfall-induced landslides can disrupt vegetation and bury it in the soil, forming woody debris. The carbon flux of burial process is denoted as E_{BD}. Carbon in woody debris differs from that in the S pool, and is thus referred to as the D pool. However, similar to the carbon in the L pool, carbon in the D pool is also subject to biochemical processes that ultimately transfer it to the S pool, with this flux denoted as T_{DS}.

As carbon circulates through various carbon pools, it exits the terrestrial ecosystem in multiple ways. Plants release CO_2 into the atmosphere through autotrophic respiration, a process denoted as R_{PA}. The Microorganisms, including bacteria and fungi, along with soil fauna, decompose organic carbon from the L pool and D pool into CO_2 and carbon compounds. These decomposition fluxes are denoted as D_{LA} and D_{DA}, respectively. These organisms also metabolize the organic carbon compounds by heterotrophic respiration, releasing carbon dioxide from S pool, which are denoted as R_{SA}.

In addition, geomorphic processes play a crucial role in returning carbon to the external environment. These processes include broader erosional mechanisms such as mass

movements by significant disturbances and soil erosion by water or storms. Through geomorphic processes, carbon from the S pool and D pool is transported into channels and fluvial systems. These fluxes are denoted as E_{SC} and E_{DC}, respectively.
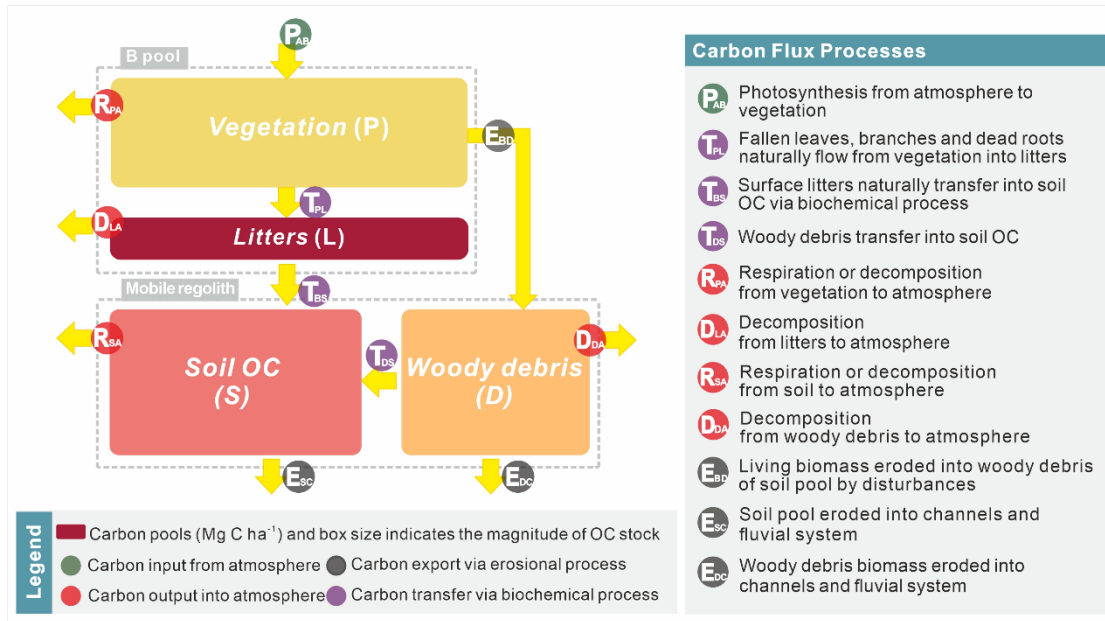
Figure 6.1 Terrestrial Ecosystem Carbon Pool and Flux Diagram
It shows key pools, fluxes and processes relevant to the hillslope deposits within mountain ranges. P indicates the living biomass of trees, understory plants and roots per unit area; L indicates litter biomass. D indicates the total biomass of woody debris per unit area by disturbances; S indicates the total soil OC stock.

In summary, the temporal changes in each carbon pool can be expressed by the following equations.

Change of OC in vegetatation biomass (P)

$\qquad$ = OC input by photosyhthesis − OC transferred into litters

$\qquad$ − OC respired by vegetation

$\qquad$ − OC eroded into woody biomass via disturbances.$\qquad$ (22)

Change of OC in litters (L)

$\qquad$ = OC transfer from vegetation − OC transferred into soil

$\qquad$ − OC decomposed in litters $\qquad$ (23)

Change of OC in woody debris (D)

$\qquad$ = OC eroded from vegetation − OC transferred into soil

$\qquad$ − OC decomposed in woody debris

$\qquad$ − OC eroded into channel and fluvial system. $\qquad$ (24)

Change of OC in soil (S)

= OC transferred from litters + OC transferred from woody debris

− OC respired in soil

− OC eroded into channel and fluvial system (25)

Accordingly, the Equations (22)-(25) can be depicted as follows:

$$\frac{dP}{dt} = P_{AB} - T_{PL} - R_{PA} - E_{BD};$$ (26)

$$\frac{dL}{dt} = T_{PL} - T_{BS} - D_{LA};$$ (27)

$$\frac{dD}{dt} = E_{BD} - T_{DS} - D_{DA} - E_{DC};$$ (28)

$$\frac{dS}{dt} = T_{BS} + T_{DS} - R_{SA} - E_{SC}.$$ (29)

To further simplify the equations, the P pool and L pool are regarded as a single B pool.

$$\frac{dB}{dt} = P_{AB} - T_{BS} - R_{BA} - D_{BA} - E_{BD};$$ (30)

$$\frac{dD}{dt} = E_{BD} - T_{DS} - D_{DA} - E_{DC};$$ (31)

$$\frac{dS}{dt} = T_{BS} + T_{DS} - R_{SA} - E_{SC}.$$ (32)

Equations (30)-(32) are the basis of the carbon cycle model. It is a dynamic balance between carbon inputs and outputs, where soil carbon inputs primarily come from vegetation (T_{BS}) and woody debris (T_{DS}), and carbon outputs are mainly respiration and decomposition (R_{SA}) and erosion (E_{SC}).In Section 6.2.2, these equations are converted into ODEs to track the temporal changes in carbon. Moreover, the model is based on a zero-dimensional framework, which averages spatial complexities to focus on temporal variations. This approach treats the entire study area as a whole, without distinguishing between landslide and non-landslide areas or source and deposition zones. All carbon pool units are standardized to Mg C ha^{-1} (where Mg C ha^{-1} can be multiplied by 100 to convert it to t C km^{-2}), while carbon fluxes are expressed in units of Mg C ha^{-1}yr^{-1}.

6.2.1.2 Sediment mass balance

The carbon from the soil pool and woody debris pool is transported outside through soil erosion. To quantify these two carbon fluxes, it is essential to discuss the sediment transport processes. The thickness of the sediment experiences continuous erosion at a stable rate, denoted as e_r (m·yr^{-1}). The erosion rate is considered as a constant in the

study area. Meanwhile, sediment production in the study area primarily originates from two sources.

The first is the continuous soil production by physiochemical processes at the bedrock-mobile regolith interface, characterized by a production rate, a_r (m·yr^{-1}). This production rate follows an exponential relationship with the depth of mobile regolith, expressed as $a_r = \alpha e^{\beta \cdot h}$, where h (m) is the depth of mobile regolith, α (m·yr^{-1}) and β (m^{-1}) are empirical parameters. The sediment mass balance implies that over time, sediment production and erosion will reach dynamic equilibrium, maintaining a consistent sediment thickness, denoted as h_∞. Consequently, over long timescales, the production rate should equal the erosion rate, namely, $\alpha e^{\beta h_\infty} = e_r$, which leads to the relationship $\alpha = e_r e^{-\beta h_\infty}$.

Another process is the instantaneous generation of sediment caused by earthquake-triggered landslides (EQTLs). As shown in Figure 6.2(c), EQTLs cut into bedrock, producing transportable debris. All sediments from the landslide scar area are then transferred to the deposit area. In addition to continuous soil production, the generation of new mobile regolith from bedrock is the primary factor contributing to the increased thickness of mobile regolith across the entire catchment.
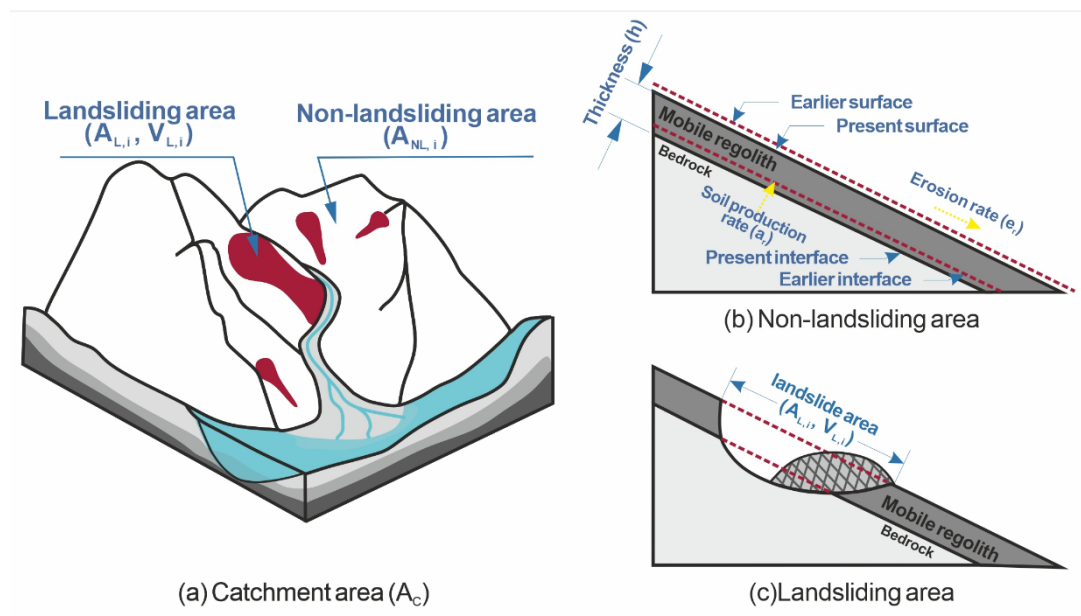
Figure 6.2 Schematic Presentation of the Landslide Affected Area

(a) Schematic Presentation of Study Area. (b) Schematic Cross Section of Non-Landsliding Slope and (c) Landsliding Slope. The study area is designated for ecosystem carbon cycle modelling. The slope sediment is generated with a rate, a_r ($m \cdot yr^{-1}$), at interface between bedrock and mobile regolith and eroded with the constant rate, e_r ($m \cdot yr^{-1}$), at surface of mobile regolith.

It is important to note that the instantaneous generation of sediment triggered by EQTLs also leads to carbon redistribution among different carbon pools. Due to the impact of EQTLs, vegetation in landslide areas is almost completely destroyed and, along with litter, is mixed into the mobile regolith, becoming woody debris. This corresponds to the processes of E_{BD} described in subsection 6.2.1.1. The woody debris then entirely moves into the landslide deposit area. At the same time, carbon from the soil pool in the scar area is also transferred to the deposit area.

From a catchment-wide perspective, the B pool transfers carbon to the D pool, while the Spool remains unchanged. This carbon flux is directly related to the scale of the landslides in the region. This change will further be quantified in Section 6.2.3.3.

6.2.1.3 Earthquake-triggered landslides stochasticity

Following a single earthquake event, the carbon balance, whether at the catchment or regional scale, can eventually return to its initial equilibrium over the long term. The model assumes that the system was in dynamic equilibrium before the earthquake. If the turnover rates within the system remain constant over time, the ecosystem will eventually reach the same equilibrium state, regardless of variations in initial carbon stock values. However, the turnover rate associated with carbon export is closely linked to sediment cascading and varies with changes in the sediment volume within the catchment. Assuming a sediment mass balance, any sediment debris produced by landslides will be transported out of the catchment until the sediment volume returns to its pre-earthquake level. Consequently, the corresponding turnover rate continuously changes after the earthquake until the sediment volume stabilizes, restoring the initial turnover rate. In the long run, a single landslide event does not change local carbon stocks. To address this, multiple earthquake events are modelled by integrating a stochastic earthquake model with the carbon cycle model, to evaluate the cumulative effects of multiple earthquakes on regional carbon stock. This model begins by randomly sampling earthquake magnitudes within a fixed time period, based on the empirical distribution of earthquake magnitude and frequency. Once an earthquake is initiated, its magnitude determines the total landslide size, following a logarithmic scaling relation between landslide volume and earthquake magnitude. The model uncertainties are estimated by a Monte Carlo simulation based on the distribution of earthquakes and EQTLs. This comprehensive approach integrates both historical data and probabilistic methods to simulate and understand the dynamics of earthquake-induced landslides. Specific details of this stochastic earthquake model are provided in subsection 6.2.3.2.

6.2.2 Model implementation

Section 6.2.1 provides a foundational understanding of the carbon balance in relation to sediment mass balance following EQTLs. This section introduces key assumptions and parameters necessary for constructing a carbon cycle model. The total area of the study area is denoted as A_C . Utilizing the earthquake stochastic model outlined in subsection 6.2.1.3, a dataset of earthquakes over a fixed time period is established. For each earthquake, the total landslide area A and volume V are recorded. Before each earthquake, the thickness of the mobile regolith is assumed to be h_{before}, and the values of the three carbon pools—B pool, D pool, and S pool—are represented as B_{before}, D_{before}, and S_{before}, respectively.

According to subsection 6.2.1.2, following an earthquake, the newly added sediment is the portion of the total landslide volume that is not part of the original mobile regolith. Thus, the average thickness of new mobile regolith across the entire area, denoted as h_0 , can be expressed as follows:

$$h_0 = h_{\text{before}} + \frac{V - h_{\text{before}} \cdot A}{A_C}.\tag{33}$$

Recalling the impact of EQTLs on carbon storage, the carbon in the B pool in the landslide area is entirely transferred to the D pool, and the S pool remains unchanged. Therefore, the values of the B pool, D pool, and S pool after the earthquake, denoted as B_0, D_0 and S_0, can be expressed as follows:

$$B_0 = \left(1 - \frac{A}{A_C}\right) \cdot B_{\text{before}};\tag{34}$$

$$D_0 = D_{\text{before}} + \frac{A}{A_C} \cdot B_{\text{before}};\tag{35}$$

$$S_0 = S_{\text{before}}.\tag{36}$$

Equations (34)-(36) demonstrate that the landslide area proportion (A/A_C) is the primary indicator describing the impact of EQTLs on the carbon distribution. An increase in this proportion directly correlates with a larger carbon transfer from the B pool to the D pool. Between seismic events, sediment and carbon redistribution follow the processes outlined in Equations (30)-(32), where soil erosion plays a key role. Equation (33) further suggests that greater EQTLs sediment thickness corresponds to a thicker average mobile regolith post-seismically. Recall the estimation of landslide volumes using the area-volume power-law relationship in Chapter 3. G. Li et al. (2014) proved that given a fixed total landslide area (A), a larger average landslide area leads to more total landslide

volume. This introduces the concept of landslide area scale, representing the magnitude of average landslide size. A larger landslide area scale indicates a larger average landslide size. Section 6.2.3.3 will further quantify how landslide area proportion and landslide area scale, significantly affects post-seismic carbon dynamics. However, more assumptions for each process must be provided.

6.2.2.1 Mobile regolith thickness

Based on subsection 6.2.1.2, in the absence of instantaneous generation, the variation in thickness variation of mobile regolith is governed by the continuous sediment production rate $a_r(t)$ and the constant sediment erosion rate e_r. The relationship is expressed as:

$$\frac{dh(t)}{dt} = a_r(t) - e_r. \tag{37}$$

The expression for $a_r(t)$ is provided as $a_r(t) = \alpha e^{\beta \cdot h(t)} = e_r e^{-\beta(h_\infty - h(t))}$ where h_∞ represents the thickness of mobile regolith at equilibrium. Therefore, at time t post-earthquake, the thickness of mobile regolith is given by:

$$h(t) = -\frac{1}{\beta}\ln\left(\left(e^{-\beta h_0} - e^{-\beta h_\infty}\right)e^{\beta e_r t} + e^{-\beta h_\infty}\right). \tag{38}$$

6.2.2.2 Carbon cycle in Vegetation and Litters (B)

Equation (30) in subsection 6.2.1.1 illustrates how the B pool changes over time. Consider the photosynthesis is P_{AB}, a linear relationship between P_{AB} and the B pool is assumed, expressed as: $P_{AB} = k_0 - k_1 B$. Here, the k_0 (Mg C ha^{-1}yr^{-1}) represents the initial rate of total biomass production, indicating the capacity for primary vegetation succession. The term k_1(yr^{-1}) is the rate constant reflecting the decline in vegetation productivity as the B pool increases, and also implies the upper limit of vegetation capacity in the region.

For other carbon fluxes deriving from the B pool, T_{BS}, R_{BA}, D_{BA} and E_{BD}, it is always assumed that they constitute fixed proportions (Booth et al. 2023). Specifically, the net turnover rate for plant respiration and litter decomposition is represented by modelled k_2 (yr^{-1}). The rate constant that characterizes the biochemical process transferring carbon into the soil via fallen leaves, branches, and dead roots is denoted as k_3 (yr^{-1}). The proportion of total aboveground biomass carbon that becomes due to distribution other than EQTLs is denoted as k_4 (yr^{-1}).

The change in the B pool can be expressed as:

$$\frac{dB}{dt} = P_{AB} - R_{BA} - D_{BA} - T_{BS} - E_{BD} = k_0 - k_1 B - k_2 B - k_3 B - k_4 B. \tag{39}$$

By incorporating the initial value of the B pool after the disturbance, the value of the B pool at time t can be determined:

$$B(t) = C_B e^{-k_B t} + B_\infty \tag{40}$$

where $k_B = k_1 + k_2 + k_3 + k_4$, $B_\infty = \frac{k_0}{k_B}$, and $C_B = B_0 - \frac{k_0}{k_B}$.

6.2.2.3 Carbon cycle in Woody Debris (D)

Equation (31) in subsection 6.2.1.1 illustrates how the D pool changes over time. The flux E_{DC}, representing the carbon lost to the channel and fluvial system due to soil erosion, is determined by the variation in sediment thickness. Considering the thorough mixing of soil due to EQTLs, it is assumed that carbon in the D pool is uniformly distributed within the mobile regolith, leading to the expressions:

$$E_{DC}(t) = \frac{e_r}{h(t)} D(t). \tag{41}$$

For other fluxes deriving from D pool, T_{DS} and D_{DA}, fixed proportions are also assumed. The net turnover rate of decomposition of woody debris is denoted by k_7 (yr⁻¹). The exchange between the S and D pools occurs as woody debris enriches soil organic matter through soil development and microbial decomposition, characterized by the turnover rate k_6 (yr⁻¹).

The change in the D pool can be expressed as:

$$\frac{dD}{dt} = E_{BD} - T_{DS} - D_{DA} - E_{DC} = k_4 B - k_6 D - k_7 D - \frac{e_r}{h} D. \tag{42}$$

Unlike ordinary differential equation (ODE) (39), ODE (42) does not have an analytical solution due to the complex structure of $h(t)$. Therefore, the Generalized Bilinear Transformation is employed to discretize ODE (38) for model operability. A discretization factor $0 \le \alpha \le 1$, and a time interval Δt are selected. This leads to the following recursive expression of the D pool:

$$D(t + \Delta t) = \left(\left(1 - \Delta t \cdot (1 - \alpha) \left(k_6 + k_7 + \frac{e_r}{h(t)} \right) \right) D(t) \right.$$

$$\left. + \frac{k_4 C_B}{k_B} \left(e^{-k_B t} - e^{-k_B(t + \Delta t)} \right) + \Delta t \cdot k_4 B_\infty \right)$$

$$\left/ \left(1 + \Delta t \cdot \alpha \left(k_6 + k_7 + \frac{e_r}{h(t + \Delta t)} \right) \right) \right. \tag{43}$$

Equation (43) provides the numerical solutions illustrating temporal trends of D pool.

6.2.2.4 Carbon cycle in Soil (S)

Equation (32) in subsection 6.2.1.1 illustrates how the S pool changes over time. Similar to the D pool, the flux of carbon from the soil pool to the channel and fluvial system is expressed as:

$$E_{SC}(t) = \frac{e_r}{h(t)} S(t). \tag{44}$$

The net turnover rate of respiration in the S pool, denoted as k_5 (yr^{-1}), represents the metabolic processes by which living organisms decompose organic carbon, producing CO_2. It is assumed that this rate remains constant. The change in the S pool can be expressed as:

$$\frac{dS}{dt} = T_{BS} + T_{DS} - R_{SA} - E_{SC} = k_3 B + k_6 D - k_5 S - \frac{e_r}{h} S \tag{45}$$

Similarly, the Generalized Bilinear Transformation is employed to discretize ODE (41), with a discretization factor $0 \leq \alpha \leq 1$, and a time interval Δt. This leads to the followingrecursive expression of the S pool:

$$S(t + \Delta t) = \left(\left(1 - \Delta t \cdot (1 - \alpha) \left(k_5 + \frac{e_r}{h(t)} \right) \right) S(t) + \frac{k_3 C_B}{k_B} \left(e^{-k_B t} - e^{-k_B(t+\Delta t)} \right) \right.$$

$$\left. + \Delta t \cdot k_3 B_\infty + \Delta t \cdot k_6 \big((1 - \alpha)D(t) + \alpha D(t + \Delta t) \big) \right)$$

$$\bigg/ \left(1 + \Delta t \cdot \alpha \left(k_5 + \frac{e_r}{h(t + \Delta t)} \right) \right) \tag{46}$$

Equation (46) provides the numerical solutions showing temporal trends of the S pool.

6.2.2.5 Steady states

If the interval between earthquakes is sufficiently long, Equations (37), (39), (42), and (45) indicate that the thickness of mobile regolith and the values of the three carbon pools will converge to steady values. This convergence is invariant to the initial post-earthquake values. The specific values of the three carbon pools are as follows:

$$B_\infty = \frac{k_0}{k_1 + k_2 + k_3 + k_4}; \tag{47}$$

$$D_\infty = \frac{k_4 B_\infty}{k_6 + k_8 + \frac{e_r}{h_\infty}}; \tag{48}$$

$$S_\infty = \frac{k_3 B_\infty + k_6 D_\infty}{k_5 + \dfrac{e_r}{h_\infty}}. \tag{49}$$

6.2.3 Model parameterization

In the case study of 2008 Wenchuan earthquake, extensive field data were collected on terrestrial organic carbon stock in both non-landslide (NL) area and landslide (LD) area post-earthquake, along with various satellite datasets encompassing the entire study area. A machine learning model was employed to map the distribution of ecosystem carbon stock in Longmenshan region, facilitating the determination of the initial states of all carbon pools. A simplified carbon balance model was developed for 2008 Wenchuan earthquake, which provides essential parameters for modelling. This section will also include parameterization and uncertainty details. The Python code for this model is available at GitHub (https://github.com/liujie1408/carbon-dynamics-model.git).

6.2.3.1 Parameters in carbon cycle

In the carbon cycle model, the total carbon pool is divided into three components: the aboveground carbon pool (B pool), the woody debris carbon pool (D pool), and the soil carbon pool (S pool). The B pool consists of vegetation and litter biomass, and the D pool includes woody debris resulting from disturbances.

To address the complexity and diversity of carbon pools and fluxes, the analysis focuses on the overall carbon exchange among the three pools (B pool, D pool and S pool) and their interactions with the external environment, thereby simplifying the parameterization of all k's mentioned in Section 6.2.2. The simplified carbon cycle model is illustrated in Figure 6.3. Specifically, F_{AB} represents the annual carbon input from the atmosphere to the B pool. F_{DA} and F_{SA} denote the annual carbon loss from the D pool and S pool to the environment, respectively. F_{BD} denotes the annual carbon transfer from the B pool to the D pool. F_{BS} and F_{DS} denote the annual average carbon flux from the B pool and D pool to the S pool, respectively.
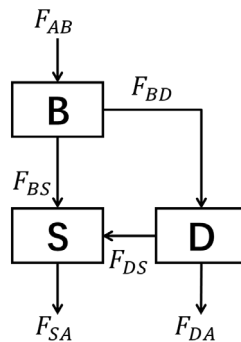
Figure 6.3 Simplified Terrestrial Ecosystem Carbon Cycle Framework

Recall subsection 6.2.1.1 and Section 6.2.2. All carbon fluxes are as follows:

$$F_{AB} = P_{AB} - R_{BA} - D_{BA} = k_0 - (k_1 + k_2)B; \tag{50}$$

$$F_{BS} = T_{BS} = k_3 B; \tag{51}$$

$$F_{BD} = E_{BD} = k_4 B; \tag{52}$$

$$F_{DS} = T_{DS} = k_6 D; \tag{53}$$

$$F_{DA} = D_{DA} + E_{DC} = \left(k_7 + \frac{e_r}{h}\right)D; \tag{54}$$

$$F_{SA} = D_{SA} + E_{SC} = \left(k_5 + \frac{e_r}{h}\right)S. \tag{55}$$

To estimate all the parameters, the mobile regolith thickness h is treated as a constant, allowing a constant k_8 to denote e_r/h. The ODE (35), (38) and (41) as reformulated as follows:

$$\frac{dB}{dt} = k_0 - (k_1 + k_2 + k_3 + k_4)B; \tag{56}$$

$$\frac{dD}{dt} = k_4 B - (k_6 + k_7 + k_8)D; \tag{57}$$

$$\frac{dS}{dt} = k_3 B + k_6 D - (k_5 + k_8)S. \tag{58}$$

where the general solutions are as follows:

$$B(t) = C_B e^{-k_B t} + \frac{k_0}{k_B}; \tag{59}$$

$$D(t) = \frac{k_4}{k_D - k_B} C_B e^{-k_B t} + C_D e^{-k_D t} + \frac{k_0 k_4}{k_B k_D}; \tag{60}$$

$$S(t) = \frac{k_4 k_6 + k_3(k_D - k_B)}{(k_D - k_B)(k_S - k_B)} C_B e^{-k_B t} + \frac{k_6}{k_S - k_D} C_D e^{-k_D t} + C_S e^{-k_S t}$$
$$+ \frac{k_0 k_4 k_6 + k_0 k_3 k_D}{k_S k_B k_D}; \tag{61}$$

where $k_B = k_1 + k_2 + k_3$, $k_D = k_6 + k_7 + k_8$ and $k_S = k_5 + k_8$, with C_B, C_D and C_S being constants.

To determine the values of k's and C's in this model, it is essential to establish the initial and boundary conditions for the ODEs (33)-(35). These conditions include the equilibrium values of the three pools, their initial values immediately after the earthquake,

and their stock values at specific time points during post-earthquake recovery. Field data collected in study area provide valuable information for this purpose, including the carbon storage in the B pool and the surface S pool (top 50 cm) in non-landsliding area, as well as carbon storage in landsliding area 12 years after the earthquake. Since the carbon stocks of the B and the S pool in NL area are at equilibrium, their values are directly assumed to represent the equilibrium levels, denoted as B_∞ and S_∞. For the equilibrium value of the D pool, D_∞, previous studies (Booth et al. 2023; Junren et al. 2009) indicate that it accounts for approximately 10% of the B pool, hence $D_\infty = 0.1B_\infty$.

Recall that the EQTLs thoroughly mixed all carbon from the landslide scar area and deposited it in the landslide deposit area. During this process, the B pool in the entire LD region is reset to zero, while the D and S pools from the scar area are fully transferred to the deposit area. Consequently, the initial pool values for the deposit area are expressed as:

$$B_0 = 0, \qquad D_0 = \frac{(B_\infty + D_\infty)}{p}, \qquad S_0 = \frac{S_\infty}{p} \tag{62}$$

where p represents the proportion of the deposit area within the entire LD region, which is set to 0.3 based on previous studies (Li et al. 2016). Field data sampling was conducted 12 years after the earthquake. During this year, B_{12} denotes the 12-year recovery of carbon stock of B pool, and S_{surface} denotes the 12- year recovery of soil organic carbon in the top 50cm surface. According to the sediment budget from Francis et al. (2022), 12% of the earthquake-generated sediments were removed within ten years post-earthquake, so the carbon stock of S pool, S_{12} is calculated as:

$$S_{12} = S_{\text{surface}} - \frac{0.5}{h_{LD}}S_0 + (1 - 0.12)S_0 \tag{63}$$

where h_{LD} is the regolith thickness in the deposit area after the earthquake, determined by $h_{LD} = \frac{V_{LD}}{p \cdot A_{LD}}$. The landslide volume V_{LD} is obtained using the landslide volume estimation methods described in subsection 6.2.1.3. The rate constant $k_4(yr^{-1})$ is calculated based on extensive remote sensing and landslide interpretation data from the Wenchuan earthquake study (Wang et al. 2024). From 2000-2007, the steady state of study area shows an average landslide area of $1.97 \times 10^7 m^2$ over the whole study area of $18213\ km^2$, leading to $k_4 = 0.00108\ yr^{-1}$. Due to the same mechanism, it is also assumed that the respiration of soil carbon and the decomposition of woody debris are equal, leading to $k_5 = k_7$. By the known parameters $B_0, D_0, S_0, \ B_\infty, D_\infty, S_\infty, \ B_{12},$

S_{12} and k_2, the carbon cycle model can be completed. The calculation of the corresponding parameters follows the procedure outlined in Figure 6.4.

$$C_1 = B_0 - B_\infty$$

$$k_B = \frac{\ln\left(\frac{(B_{12} - B_\infty)}{C_B}\right)}{-12}$$

$$k_0 = k_B B_\infty$$

$$k_D = \frac{k_0 k_4}{k_B D_\infty}$$

$$C_D = D_0 - D_\infty - \frac{C_B}{k_D - k_B} k_4$$

$$k_7 + k_8 = k_D - k_6, \qquad k_S = k_7 + k_8, \qquad k_3 = \frac{S_\infty k_B k_D k_S - k_0 k_4 k_6}{k_0 k_D}, \qquad k_1 + k_2 = k_B - k_3 - k_4$$

$$C_S = S_0 - S_\infty - \frac{k_4 k_6 + k_3(k_D - k_B)}{(k_D - k_B)(k_S - k_B)} C_B - \frac{k_6}{k_S - k_D} C_D$$

$$\frac{k_4 k_6 + k_3(k_D - k_B)}{(k_D - k_B)(k_S - k_B)} C_B e^{-12 k_B} + \frac{k_6}{k_S - k_D} C_D e^{-12 k_D} + C_S e^{-12 k_S} + S_\infty - S_{12} = 0$$
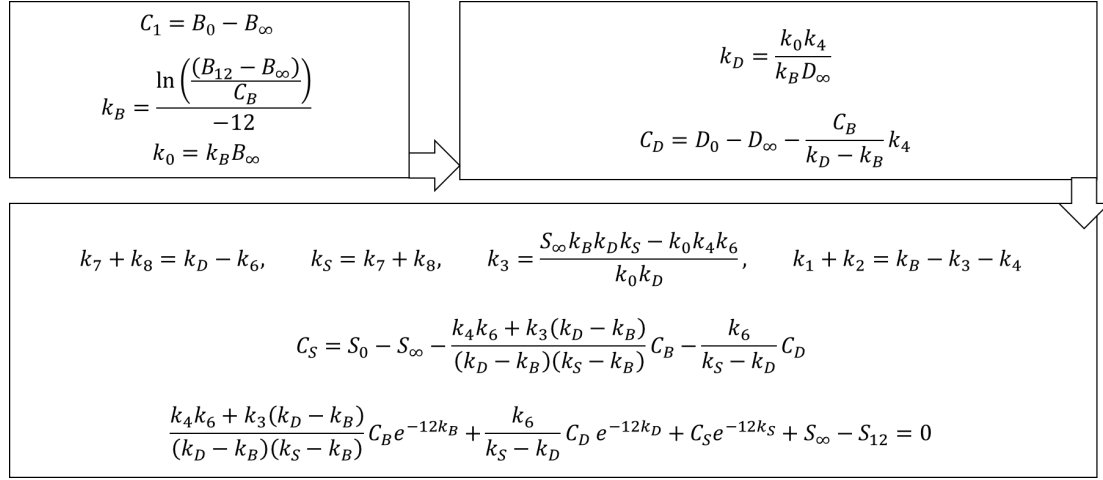
Figure 6.4 Parameter Calculation Flowchart for 2008 Wenchuan Earthquake

6.2.3.2 Parameters in earthquake stochastic model

Before determining the parameters related to sediment mass balance, this subsection focuses on the earthquake stochastic model.

Earthquake frequency and magnitudes

Gutenberg and Richter (1956) showed that the frequency of earthquakes with moment magnitude equal to or greater than a given value can be expressed by the function:

$$\log_{10} N = a - b \cdot M \tag{64}$$

where N is the number of earthquakes that occurs above a certain magnitude M in a year, where a and b are empirical coefficients. Keefer (1994) calibrated this model using the data from Espinosa et al. (1985) and Kanamori (1977), revealing a magnitude-frequency relationship in Peru and adjacent regions. To apply the model to Longmenshan region, Li et al. (2017b) calibrated Equation (64) with historical and instrumental catalogs from 1970 to 2015, which gives $a = 3.93$ and $b = 0.91$.

By Equation (64), the frequency density of earthquakes with a certain magnitude m in a year, denoted by the $f(m)$ ($yr \cdot Mw^{-1}$), satisfies:

$$N = \int_M^\infty f(m) dm$$

$$\Rightarrow \int_M^\infty f(m) dm = 10^{a - bM}$$

$$\Rightarrow f(m) = (10^{a-bm})' = 10^{a-bM} \cdot \ln 10^b \tag{65}$$

The probability density function of earthquakes that occurs with a certain magnitude m, denoted by $p(m)$, can be expressed by $f(m)$ as follows:

$$p(m) = \frac{f(m)}{\int_{5.5}^{8} f(m)dm} \tag{66}$$

where only events of $M \geq 5.5$ are considered based on the following reasons: a) landslides are rarely triggered by smaller earthquakes ($M \leq 4$) (Keefer 1984); b) the carbon cycle model is built upon large earthquakes; c) the lowest boundary of earthquake magnitude for landslides area estimation is 5.5 (Keefer and Wilson 1989).

Notice that Equation (64) is derived through linear regression on the dataset $\{(M_j, N_j)\}_{0 \leq j \leq n}$, where $M_0 < M_1 < \cdots < M_n$ are the magnitudes existing in the complete earthquake inventory and N_j is the number of earthquakes with magnitude no less than M_j. Suppose the earthquake inventory covers a time period of duration t. The optimal values of a and b are obtained by minimizing the difference between the observed values $\{(M_j, N_j)\}_{0 \leq j \leq n}$ and the theoretical values $\{(M_j, t \times 10^{a-bM_j})\}_{0 \leq j \leq n}$. To estimate time interval T, between the current earthquake and the previous one, the sampled earthquakes (including the newly added one) are sorted in ascending order by magnitude $M_0 < M_1 < \cdots < M_n$. The time interval T is then calculated as follows:

$$T = \frac{1}{n+1} \sum_{j=0}^{n} \frac{N_j}{10^{a-bM_j}} - T' \tag{67}$$

where T' is the time duration from the first sampled earthquake to the previous one. As the number of samples increases, the sampled earthquakes inventory converges to the relation in Equation (64). For this model, the 101st sample is used as the first earthquake to avoid the initial data oscillation over one multiple earthquakes cycle.

Total volume of EQTLs

Keefer et al. (Keefer 1994; Keefer and Wilson 1989) proposed a linear-regression equation relating total landslide volume to earthquake moment magnitude. Malamud et al. (2004) refined this empirical correlation based on detailed field investigations and aerial photographs from 16 historical earthquakes. Marc et al. (2016) further enhanced the model by incorporating seismogenic characteristics, such as seismic moment and asperity depth, landscape steepness, and material sensitivity, to predict the total volume of EQTLs. Combining both empirical regression model and seismologically-based

model, Li et al. (2017a) derived an earthquake magnitude-landslide volume scaling relation specific to the Longmenshan region:

$$\log_{10} V = 23.77 \log_{10} M - 11.97 \ (\pm 0.07) \tag{68}$$

where $V(km^3)$ is the total volume of landslide sediments. The error bounds (± 0.07) represent the standard deviation of the fit, providing a measure of the model's precision.

Landslide number and area

For a given earthquake magnitude, the landslides are randomly sampled following the landslide area frequency distribution given by Malamud et al. (2004). This three-parameter inverse-gamma distribution is expressed as follows:

$$p(A_L; \rho, \alpha, s) = \frac{1}{\alpha \Gamma(\rho)} \left(\frac{\alpha}{A_L - s} \right)^{\rho+1} \exp\left(-\frac{\alpha}{A_L - s} \right) \tag{69}$$

where $\Gamma(\rho)$ is the gamma function of ρ. The inverse-gamma distribution exhibits a power-law decay with exponent $-(\rho + 1)$ for medium and large areas, alongside an exponential rollover for small areas. Valagussa et al. (2019) argued that the intensity of ground motion significantly influences landslides size distribution, noting that stronger ground shaking can trigger larger landslides. However, data from Tanyaş et al. (2019) concerning 45 EQTLs inventories (Fan et al. 2019b) did not reveal a compelling relationship. Consequently, the relationship between earthquake magnitude and power-law exponents in landslide size distribution remains ambiguous. To derive the probability distribution for the Longmenshan fault, the landslide inventory from Li et al. (2014) of 2008 Wenchuan earthquake was applied (Li et al. 2016). The maximum likely hood fit to Equation (69) yielded $\rho = 1.81, \alpha = 7.62 \times 10^3$, and $s = -1.31 \times 10^3$, with a coefficient of determination $r^2 = 0.87$. The power-law tail exhibits an exponent of $\rho + 1 = 2.81$. The concept of the landslide area scale factor (θ) is introduced to study the impact of landslide scale on carbon cycle. The landslide area frequency distribution is adjusted by the θ, which is applied to both α and s, ensuring that the mean landslide area becomes θ times the mean value defined in Equation (59).

This sampling process will ultimately conclude, constrained by the finite total volume of landslides triggered by a single earthquake. The empirical scaling relationship between landslide area and volume is applied until it meets the threshold of total landslide volume. The empirical scaling relationship is as follows:

$$V_j = \overline{\alpha A_{scar,J}^{\gamma}} \tag{70}$$

where α and γ are empirical parameters, and $A_{scar,j}$ is the scar area of the jth landslide. Here, the landslide scar area is assumed to account for 70% of the total landslide area. Overbar represents the mean of the parameters from references applicable to Longmenshan fault from Guzzetti et al. (2009), Larsen et al. (2010) and Parker et al. (2011). Details are shown in Supporting materials.

6.2.3.3 Parameters in sediment mass balance

Based on Equations (65)-(67) in subsection 6.2.3.2, the expectation of earthquake magnitude is derived as follows:

$$\bar{M} = \int_{M_{min}}^{M_{max}} m \cdot p(m)dm = \frac{M_{max} \cdot 10^{a-bM_{max}} - M_{min} \cdot 10^{a-bM_{min}}}{10^{a-bM_{max}} - 10^{a-bM_{min}}} + \frac{1}{b \ln 10} \quad (71)$$

The expectation of time interval between two adjacent earthquakes is given by:

$$\bar{t} = \int_{M_{min}}^{M_{max}} 10^{-a+bm}p(m)dm = \frac{b \ln 10\,(M_{max} - M_{min})}{10^{a-bM_{min}} - 10^{a-bM_{max}}} \quad (72)$$

Francis et al. (2020) demonstrated that the sediment change induced by an earthquake of average magnitude $\bar{M}$ must be eroded within an average time interval $\bar{t}$. The condition $V_{(\bar{t})} - V_{\infty} = (1 - 99.99\%)V_{\infty}$ is imposed to solve for β in sediment production rate. Conducting 100 simulations leads to a robust estimate of the parameter $\beta = -47.238 \pm 6.888$. This approach ensures that the model accurately reflects the dynamic balance of sediment volume in response to both continuous processes and discrete seismic events.

6.2.3.4 Summary

Table 1.1 shows all parameters utilized in carbon cycle and sediment mass balance model. Due to the limited availability and constraints of empirical data, the calculation are simplified, and specific assumptions are made in subsection 6.2.3.1, which fails to obtain k_5 and k_7. Given that they are situated within the same external environment of mobile regolith, it is assumed that k_5 equals k_7. The case study after 2008 Wenchuan earthquake suggests a value of k_5 0.00591±0.00149 (yr⁻¹). In practice, $k_5 + k_7$ is often calculated as heterotrophic respiration effluxes, while k_2 refers to the autotrophic respiration effluxes. Based on field measurements in deciduous broadleaved and coniferous forests of Southwest China, Wang et al.(Wang et al. 2008b) propose an average constant rate of k_2 of 0.01598 (yr⁻¹).

Table 1.1 Parameters Applied in Carbon Cycle Model

Flux	Parameters	Unit	Value	Standard deviation	Description
P_{AB}	k_0	Mg C ha^{-1}yr^{-1}	2.73021	1.23480	Case study of 2008 Wenchuan earthquake (Obtained from empirical data in Chapter 5)
P_{AB}, R_{BA}, D_{BA}	$k_1 + k_2$	yr^{-1}	0.04032	0.01130	Case study of 2008 Wenchuan earthquake (Obtained from empirical data in Chapter 5)
T_{BL}	k_3	yr^{-1}	0.00959	0.00466	Case study of 2008 Wenchuan earthquake (Obtained from empirical data in Chapter 5)
E_{BD}	k_4	yr^{-1}	0.00108	0.00000	Case study of 2008 Wenchuan earthquake (Obtained from empirical data in Chapter 5)
E_{BD}	k_4	yr^{-1}	0.00108	0.00019	Case study of 2008 Wenchuan earthquake (Wang et al. 2024)
D_{SA}	k_5	yr^{-1}	0.00591	0.00149	Case study of 2008 Wenchuan earthquake (Obtained from empirical data in Chapter 5)
T_{DS}	k_6	yr^{-1}	0.00427	0.00149	Case study in 2008 Wenchuan earthquake (Obtained from empirical data in Chapter 5)
E_{DC}, E_{SC}	β	m^{-1}	-47.238	6.888	Sediment mass balance in 2008 Wenchuan earthquake
E_{DC}, E_{SC}	h_∞	m	1	NA	Sediment mass balance in 2008 Wenchuan earthquake
NA	A_C	km^2	10	NA	Catchment scale modelling
NA	A_T	km^2	4600	NA	Regional scale modelling

In terms of geomorphic process, the k_4 of denuding aboveground biomass into mobile regolith is obtained via the study of Wang et al. (2024). This study applies the continuous change detection and classification (CCDC) approach of time-series Landsat images to investigate the temporal trend of landslide area after Wenchuan earthquake. According to the landslide activity pre-earthquake, the steady state of study area shows an average landslide area of $1.97 \times 10^7 \text{m}^2$ over the entire study area of 18213 km^2, leading to the $k_4 = 0.00108 \ yr^{-1}$. Li et al. (2017a) derive an exhumation rate of $0.62(+0.14 -$

$0.08)mm \cdot yr^{-1}$ through apatite fission track analysis. This exhumation rate is applied to represent e_r.

6.3 Results

6.3.1 Geomorphic and biochemical impact on carbon cycle

The modelling of a single earthquake event is based on the 2008 $M_W 7.9$ Wenchuan earthquake, which caused approximately 13% of the total area ($4600\ km^2$) to be affected by EQTLS. In severely impacted regions, the total landslide area within individual catchments ranges from approximately 10% to 50%. For catchments of 10 km², the number of landslides is estimated to range between 100 and 600, depending on the proportion of the area affected (Figure 6.5(a)). The correlation between landslide numbers and the proportion of landslide area shows an almost linear relationship. Environmental factors such as topography, geomorphology, and lithology play a significant role in the distribution of individual landslide areas. In the Longmenshan region, with a fixed landslide area proportion of 13% and a landslide area scale of 1, approximately 200 landslides are expected. As the landslide area scale increases, indicating larger individual landslide sizes, the number of landslides decreases, showing a nonlinear relationship (Figure 6.5(b)).
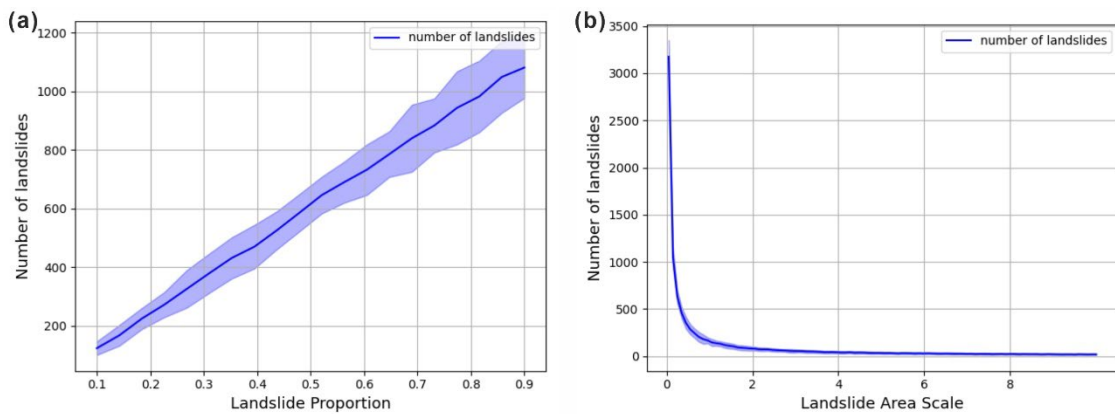
Figure 6.5 Number of Landslides Change with Landslide Area and Size
(a) Landslide Area Proportion (Landslide Proportion); (b) Landslide Area Distribution Scale Factor (Landslide Area Scale). The uncertainty stems from Monte Carlo random sampling method.

The modelling of multiple earthquakes is based on the stochastic model in subsection 6.2.3.1, derived from historical data on earthquakes and landslides in the Longmenshan region. As shown in Figure 6.6, earthquake magnitudes less than Mw 6.5 result in relatively small numbers of landslides and limited total landslide area. However, once

the magnitude exceeds Mw 6.5, there is an exponential increase in both the number of landslides and total landslide area. For example, at Mw 7.9, landslide numbers exceed 70,000, and the total landslide area reaches 600 km². This sharp increase in landslide activity directly affects the magnitude of ecosystem disturbances, influencing both the carbon pool balance and the duration of carbon recovery. Larger earthquakes, particularly mega-earthquakes (Mw > 7.5), result in more extensive and prolonged disruptions to carbon storage, with significant implications for long-term carbon dynamics.

.
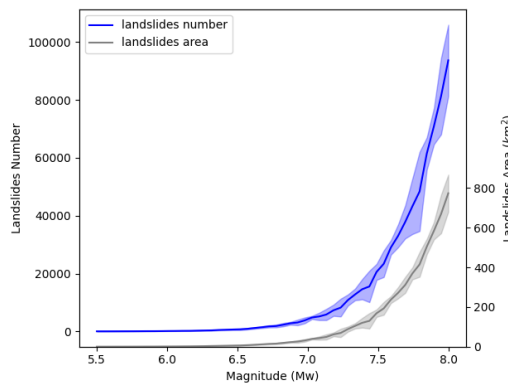
Figure 6.6 Number of Landslides and Landslide Area Change with Earthquake Magnitude

The modelling exhibits varying sensitivity to different parameters. Figure 6.7(a) illustrates the effects of photosynthesis, autotrophic respiration, and heterotrophic respiration (decomposition) on the carbon stock of various pools. As the photosynthesis turnover rate (k_0) increases, carbon stocks in all pools exhibit a linear increase (Figure 6.7(a)), with the least change observed in woody debris. Autotrophic respiration influences both vegetation and soil carbon stocks. Lower autotrophic respiration turnover rates ($k_1 + k_2$) result in higher steady-state carbon stocks (Figure 6.7(b)), with the most significant impact occurring when $k_1 + k_2$ ranges between 0 and 0.02 yr⁻¹. In the Longmenshan region, $k_1 + k_2$ is estimated at 0.04 ± 0.01 yr⁻¹. In contrast, heterotrophic respiration primarily affects soil carbon stocks, with minimal influence on woody debris and vegetation biomass (Figure 6.7(c)). The most pronounced effect on soil carbon occurs when the heterotrophic respiration turnover rate $k_5 + k_7$ is between 0 and 0.01 yr⁻¹. In the Longmenshan region, $k_5 + k_7$ is measured at 0.0118 yr⁻¹. Overall, biochemical processes significantly influence carbon stock levels, particularly under stable external conditions in the Longmenshan region. The biochemical processes cause carbon stock variations within the range of 0 to 600 Mg C ha⁻¹. In comparison, physical erosion has a lesser impact, primarily affecting soil carbon stocks, which decrease almost linearly as erosion rates increase (Figure 6.7(d)).
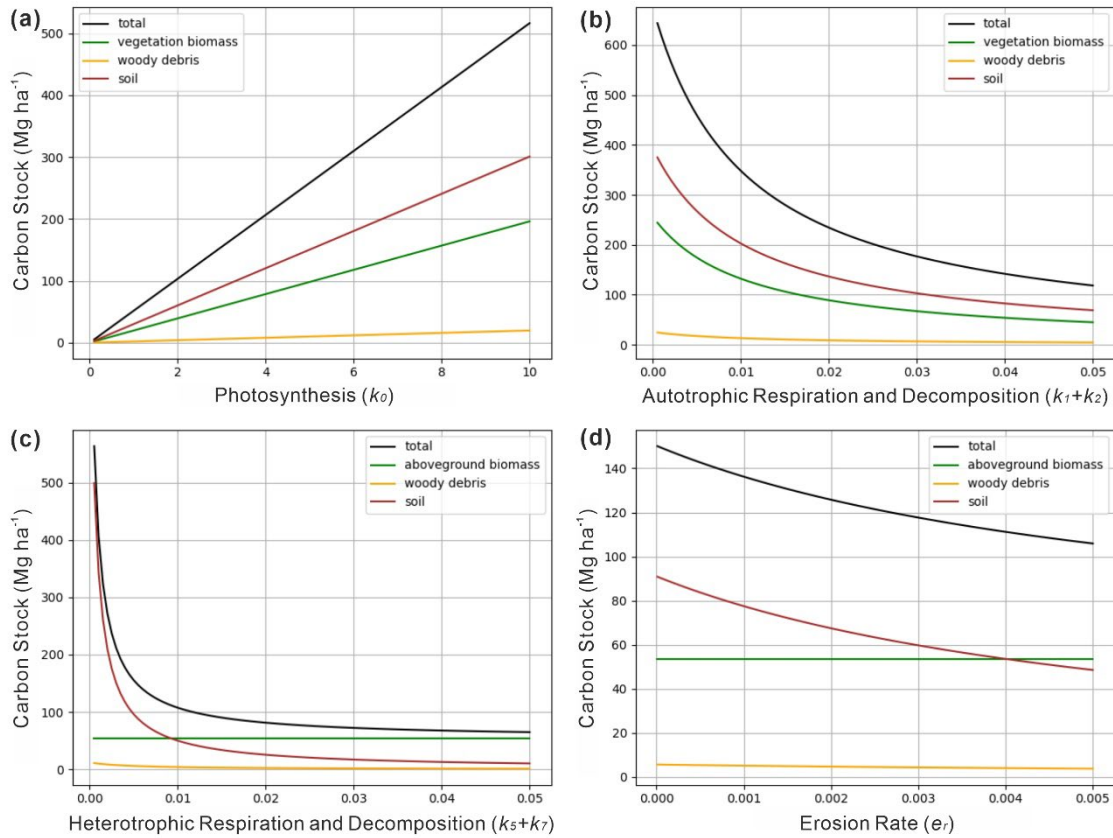
Figure 6.7 Impact of Biochemical and Erosional Processes on Ecosytem Organic Carbon Stock at Equilibrium State
(a) Photosynthesis (k_0); (b) Autotrophic Respiration and Decomposition ($k_1 + k_2$); (c)Heterotrophic Respiration and Decomposition ($k_5 + k_7$); (d) Erosion Rate (e_r). The black colour represents total terrestrial organic carbon pool (Total). The green colour represents the vegetation and litter carbon pool (B pool). The orange colour represents the woody debris carbon pool (D pool). The red colour represents the soil carbon pool (S pool).

6.3.2 Carbon cycle for single earthquake event

Following the single earthquake event, total terrestrial organic carbon stock varies over time (Figure 6.8(a)), with the temporal trend being influenced by individual carbon pools, including the B pool, S pool, and D pool. The landslide buries the living biomass into landslide deposits and transfers it to the woody debris carbon pool. Soil carbon remains unchanged. Shortly thereafter, both the soil and woody debris carbon pools begin to decrease, whereas living biomass carbon shows a rapid upward trend due to vegetation regrowth. This results in a net increase in the total terrestrial organic carbon pool in the earthquake-affected area, with peak values reaching ~3% of equilibrium state (Figure 6.8(a)). Over time, the carbon stored by vegetation and soil becomes stable, and the organic carbon from landslide-generated debris is physically eroded away, leading to a decrease in total carbon storage towards a state of equilibrium. When examining the change rates of these carbon pools following the earthquake (Figure 6.8(b)), the vegetation biomass and woody debris carbon exhibit nonlinear increasing or decreasing

trends, effectively balancing each other. The soil carbon pool, in particular, undergoes two distinct transitions around 10 years and 200 years: shifting from a negative to a positive rate of change, and then reverting to a negative rate until reaching zero. The variation in the soil carbon pool highlights the impact of EQTL.
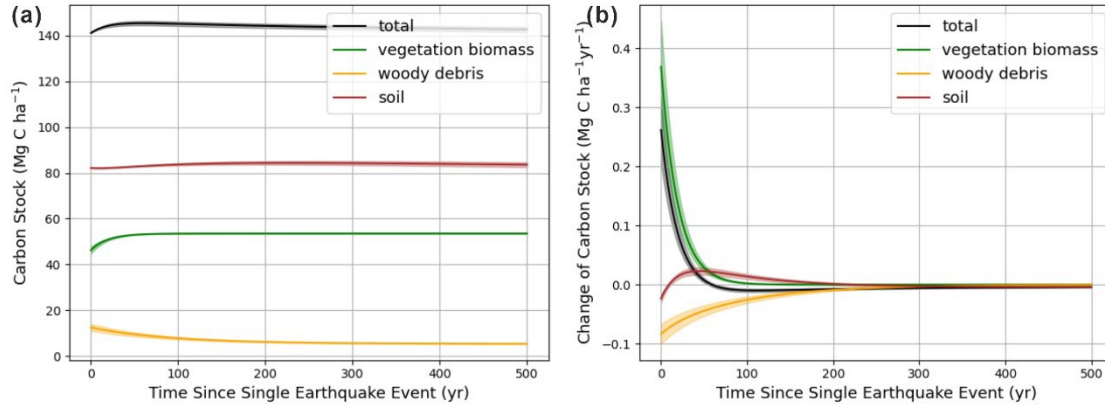
Figure 6.8 Terrestrial Ecosystem Organic Carbon Stock Change After Single Earthquake Event
(a) Carbon Pools Over Time ($Mg\ ha^{-1}$); (b) Rate of Change in Carbon Pools Over Time ($Mg\ ha^{-1}\ yr^{-1}$). The results are with a fixed landslide area proportion of 13% and a fixed landslide area scale of 1 at catchment scale. The black colour represents total terrestrial organic carbon pool (Total). The green colour represents the vegetation and litter carbon pool (B pool). The orange colour represents the woody debris carbon pool (D pool). The red colour represents the soil carbon pool (S pool).

Figure 6.9 illustrates the modelled temporal changes in soil organic carbon stock. Initially, there is a reduction in soil organic carbon stock, followed by a nonlinear increase after approximately 10 years, reaching a maximum around 200 years. After this peak, soil organic carbon begins to decrease monotonically. The curve demonstrates a three-phase temporal pattern. The increasing uncertainty suggests that this pattern is consistent across all model simulations. During Phase I, the immediate response of EQTLs reduces both soil carbon inputs and outputs, with the decrease in inputs surpassing the reduction in outputs, leading to an overall decrease in total soil carbon. Soil organic carbon acts as a carbon source. The lowest point in the curve is defined as the first inflection point, representing the peak carbon release. In Phase II, vegetation recovery significantly increases living biomass, with the accumulation rate of soil surface carbon far exceeding the gradual loss in soil carbon due to erosion, respiration and decomposition. The increased volume of mobile regolith by EQTLs enhances the capacity for soil to store ecosystem carbon before it is eventually released or exported. The peak in this phase is defined as the second inflection point, reflecting the peak carbon storage of the "Capacitor Effects". In Phase III, the soil carbon stock begins to decrease. This decline is driven by the stabilization and limitation of vegetation growth, the continued increase in soil carbon erosion, and ongoing decrease in soil carbon input from woody debris.
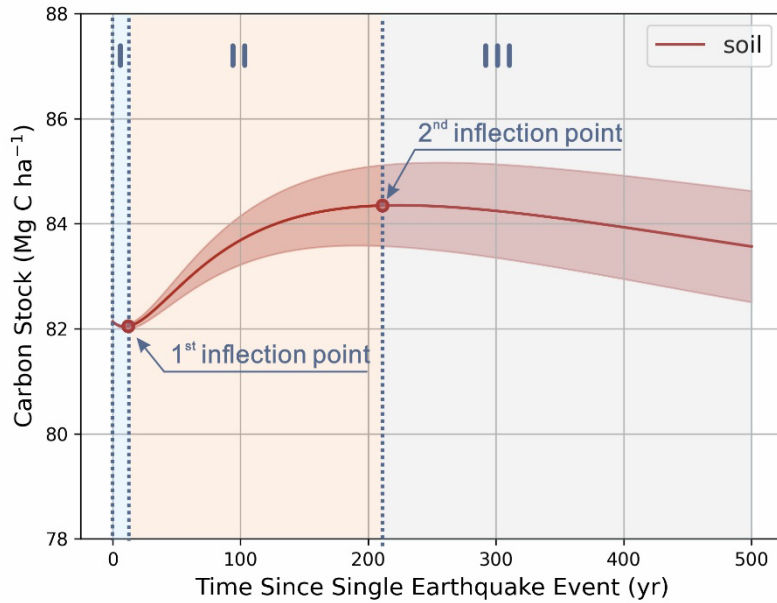
Figure 6.9 Soil Carbon Pool Dynamics Over time
The results are based on environmental settings and parameters of 2008 Wenchuan Earthquake. The uncertainty stems from Monte Carlo random sampling method.

Figure 6.10 shows the temporal evolution in various carbon fluxes over a 500-year period following this single earthquake event. These carbon fluxes are based on the carbon pool and flux diagram presented in Figure 6.1. The most significant carbon flux is carbon uptake by vegetation through photosynthesis (P_{AB}). Initially, this flux is high, reaching approximately 1.7 Mg C ha^{-1} yr^{-1}, but decreases sharply within the first 50 years and stabilizes at around 1.4 Mg C ha^{-1} yr^{-1} for the remaining period. As vegetation biomass increases, carbon release through autotrophic respiration (R_{BA}) also rises. This flux increases over the first 100 years, eventually stabilizing at approximately 0.9 Mg C ha^{-1} yr^{-1}. The solid and dash-dotted lines in orange (Figure 6.10) represent the carbon fluxes between pools through biochemical processes, specifically carbon transfer into soil through litter decomposition (T_{BS}) and carbon transfer into soil through woody debris decomposition (T_{DS}). T_{BS} show a gradual increase before reaching a steady state, while T_{DS} shows a gradual decrease over time. This contrasting trend is attributed to the post-earthquake reduction in living biomass and is sudden increasing in woody debris due to the initial decreasing and increasing in vegetation biomass and woody debris. As vegetation biomass recovers, litter decomposition contributes more to soil carbon, while the initial abundance of woody debris leads to a temporary increase in decomposition, which declines as the debris is depleted. In contrast to biochemical processes, carbon fluxes related to physical erosion-represented by grey lines-remain relatively stable at much slower levels through this 500-year period.
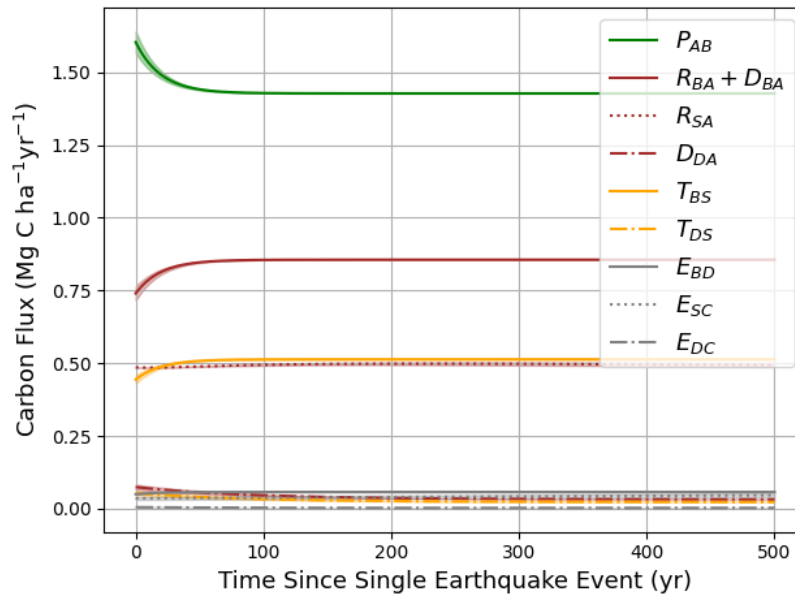
Figure 6.10 Carbon Fluxes Change Over Time for Each Component of the Carbon Model
The results are obtained with a fixed landslide area proportion of 13% and a fixed landslide area scale of 1 at catchment scale. The legend identifies each carbon flux as: P_{AB}:Photosynthesis of vegetation; $R_{BA} + D_{BA}$: Respiration and decomposition of vegetation; R_{SA}: Respiration of soil; D_{DA}: Decomposition of woody debris; T_{BS}: Transfer from vegetation biomass to soil; T_{DS}: Transfer from woody debris to soil; E_{BD}: Erosion from vegetation biomass to woody debris by disturbance; E_{SC}: Erosion from soil to channel and fluvial systems; E_{DC}: Erosion from woody debris to channel and fluvial systems. The green colour represents the carbon intake process. The red colour represents carbon released into atmosphere. The orange colour represents the biochemical process within carbon pools. The grey colour represents the erosional processes by sediment transport.

It is worth noting that soil carbon-related fluxes, including T_{BS}, R_{SA}, T_{DS} and E_{SC}, exhibit different trends. Among these, carbon transfer from vegetation to soil (T_{BS}) and carbon release from soil (R_{SA}) contribute the most in terms of flux intensity and stabilize the fastest. In contrast, carbon transfer from woody debris to soil (T_{DS}) takes longer to reach equilibrium and occurs with relatively lower intensity. Although soil carbon erosion (E_{SC}) contributes less in terms of magnitude compared to the other fluxes, it persists over a much longer period. As shown in Figure 6.11, the carbon erosion through denuding living biomass into woody debris (E_{BD}) gives the highest intensity, while it stabilizes after approximately 100 years, due to the stabilization of vegetation biomass. Despite the woody debris sharing the same sediment erosion rate with soil carbon pool, the carbon eroded from woody debris (E_{DC}) remains the lowest and most stable of the three erosion-related fluxes, contributing minimally to overall carbon dynamics. The E_{SC} gradually increases over time and persists throughout the 1000-year period. This sustained flux continuously removes carbon from the soil, with a slightly increasing trend. Its persistence plays a critical role in long-term stabilization of the carbon cycle.
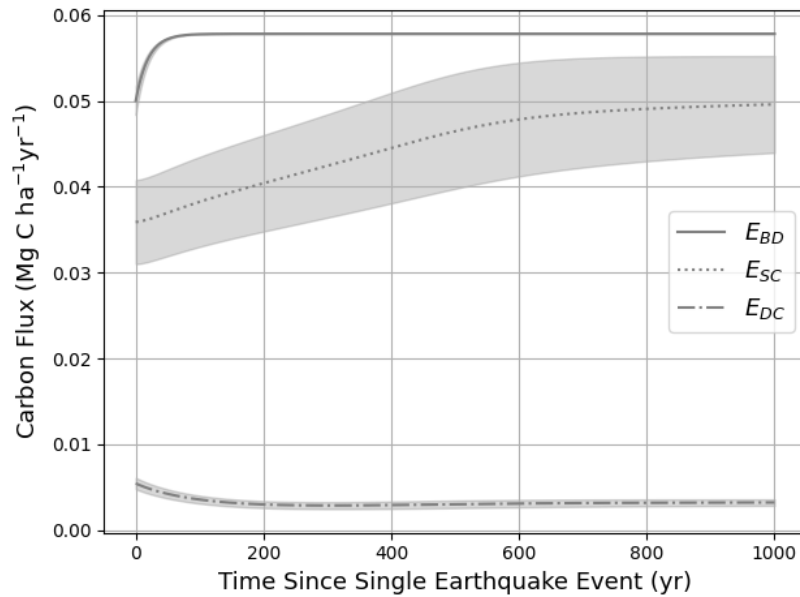
Figure 6.11 Biochemical and Erosional Process-Based Carbon Fluxes
E_{BD}: *Erosion from vegetation biomass to woody debris by disturbance;* E_{SC}: *Erosion from soil to channel and fluvial systems;* E_{DC}: *Erosion from woody debris to channel and fluvial systems. The uncertainty stems from Monte Carlo random sampling method.*

6.3.3 Carbon cycle for multiple earthquakes

Based on historical earthquake records and data from the Longmenshan fault zone, our stochastic earthquake model simulates multiple earthquakes over an 8000-year period. Figure 6.12 presents earthquake magnitudes over time and the corresponding landslide volumes generated. The distinctive peaks and troughs in landslide volume are not solely determined by the magnitude of mega earthquakes but also the frequency of earthquake events. As illustrated in Figure 6.6, the relationship between single earthquake magnitude and landslide area is clear, but when large earthquakes occur in clusters, sediment generation becomes more significant. For instance, the 4916th, 6062th and 7533th years experienced M_W 7.9 earthquakes, yet the peaks and duration of landslide volumes differ. This suggests that even earthquakes of the same magnitude can have varying impacts on sediment generation and, potentially, on carbon storage capacity.
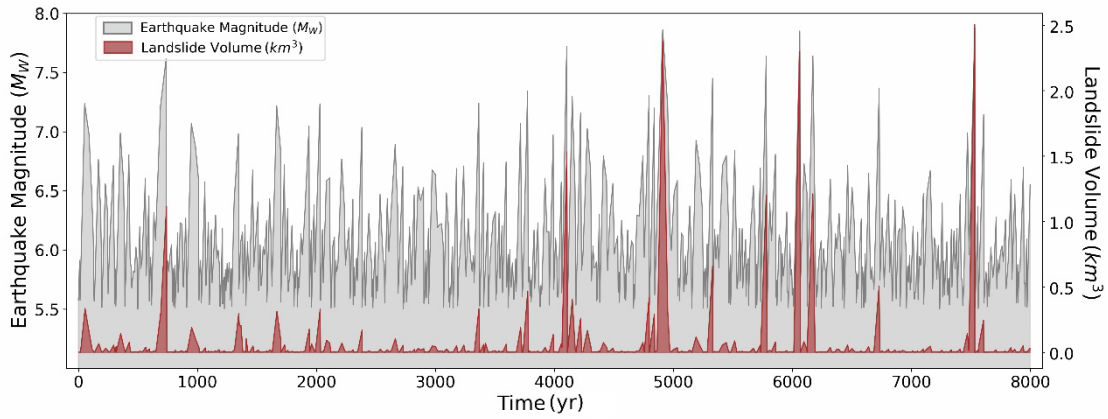
Figure 6.12 Simulated One Earthquake Cycle: Earthquake Magnitude Over Time
The cycle spans 8000 years, with magnitudes ranging from Mw5.5 to Mw8.0. The results are obtained using the stochastic earthquake model, as detailed in Methods section.

Figure 6.13 illustrates the changes in various ecosystem carbon pools in response to successive earthquakes, corresponding to the earthquake magnitudes and frequencies depicted in Figure 6.12. The results demonstrate that the accumulation of mega earthquakes leads to a substantial increase in ecosystem carbon stock. While random, smaller earthquakes occur intermittently, their effects on carbon storage are minimal, allowing the terrestrial ecosystem to return to near-equilibrium states. However, when two or three large earthquakes occur in rapid succession, total ecosystem carbon stocks increase dramatically, especially over a timescale of 2,000 to 3,000 years. The peaks in landslide volume, triggered by these earthquakes, align with peaks in total ecosystem carbon stock shown in Figure 6.13(a), underscoring the "capacitor effect". This effect occurs as earthquake-triggered landslides (EQTLs) generate significant sediment volumes, which enhance carbon storage. In the absence of such sediment generation, carbon stocks return to their equilibrium state.

The response of each carbon pool to successive earthquakes also reveals distinct recovery periods, with a consistent lag time of approximately 10 years across all carbon pools following each earthquake. However, the recovery periods of the vegetation carbon pool (Figure 6.13(c)) and woody debris carbon pool (Figure 6.13(d)) are much shorter than that of the soil carbon pool (Figure 6.13(b)). Frequent earthquakes have a considerable impact on the vegetation and woody debris, reducing the vegetation carbon by up to 26% and increasing woody debris by as much as 93% at their respective peaks. The woody debris pool appears to be sensitive to seismic disturbances. Both the carbon pools of vegetation and woody debris recovery quickly, indicating the ecosystem's resilience to withstand disturbances. In contrast, the soil carbon pool may not have sufficient time to fully recover to pre-earthquake levels between successive earthquakes. The behavior of

the soil carbon pool largely determines the pattern of total ecosystem carbon stock. Thus, the accumulation effects in the soil carbon stock in the active fault region can influence total carbon dynamics over thousands of years.
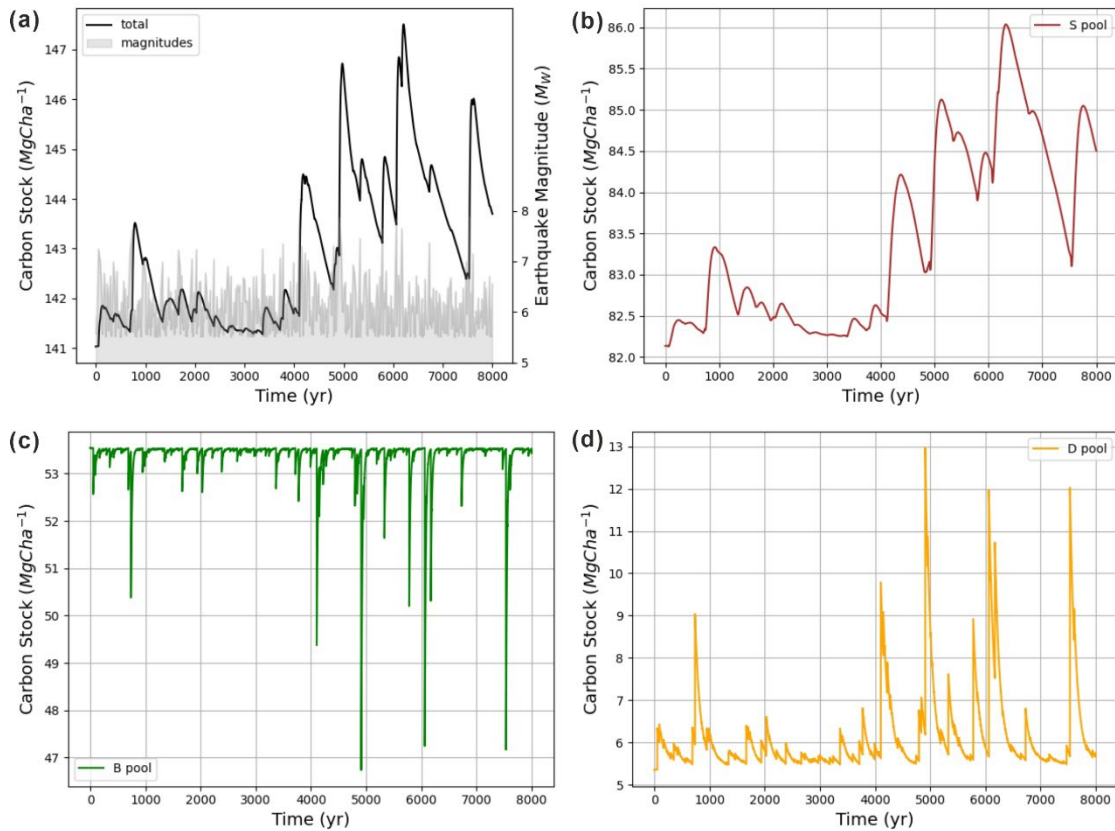
Figure 6.13 Terrestrial Ecosystem Organic Carbon Stock Change with the Modelled Earthquakes
(a)Total Terrestrial Organic Carbon Pool; (b)Soil Carbon Pool; (c) Vegetation and Litter Carbon Pool; (d)Woody Debris Carbon Pool. Subfigure (a) includes a grey background shadow, indicating the earthquake magnitudes over time. The uncertainty stems from Monte Carlo random sampling method, which relies on a stochastic earthquake model.

6.3.4 EQTLs impact on terrestrial organic carbon stock

An increase in total landslide area amplifies soil carbon storage, leading to deeper troughs and larger peaks in carbon stock (Figure 6.14(a)). In Phase I, the expansion of landslide area significantly destroys ecosystem primary production, creating a substantial drop in carbon input from vegetation. At the same time, the mixing of carbon-poor bedrock sediments with ecosystem carbon -rich surface soils results in a reduction in the soil carbon export through the fixed erosion rate (Figure 6.14(b)). Field measurements indicate that the post-earthquake transport ratios of terrestrial particulate organic carbon (POC) to petrogenic POC in river systems remain nearly the same as pre-earthquake levels. Contrary to expectations, there is no observed decrease in the ecosystem carbon distribution in river transport, despite the lower concentration of ecosystem carbon in deposit debris. This can be attributed to the sharp increase in physical erosion following

the earthquake (Galy et al. 2007; Galy et al. 2015), which accelerates the mobilization of carbon-rich soil that has not be directly impacted by landslides (Doetterl et al. 2016; Larsen et al. 2014), and changes in external factors such as rainfall, which enhance river system's capacity to transport finer and carbon rich sediments, while most sediments are primarily transported by debris flow. These observations do not conflict with the model results. On a decadal timescale, the increase in landslide proportion primarily disrupts the biochemical processes of terrestrial organic carbon, with a relatively smaller impact on erosion processes of soil carbon. This leads to a decline in soil organic carbon stock during this phase. However, the duration of this decreasing trend will not be extended by an increase in landslide area, as landslide size does not influence the recovery rate of vegetation.

Phase II represents the primary stage of soil organic carbon accumulation. The increase in landslide area enhances the carbon storage capacity of mountain ranges. The key mechanism here is that more landslides introduce more bedrock materials, increasing the thickness of the mobile regolith and lowering the concentration of soil organic carbon in surface sediments. Simultaneously, large volumes of organic carbon from the original ecosystem are buried, while sediment erosion rates limit the removal of this stored carbon (Märki et al. 2021; Wang et al. 2016), thereby extending its residence time in the mountain system. Additionally, surface vegetation accumulates organic carbon at a faster rate compared to later stages section (Restrepo et al. 2009; Wardle et al. 2004; Zaehle et al. 2006), further boosting soil carbon storage capacity as landslide area increases. Another process contributing to soil carbon storage, though of lower intensity, is the transfer of carbon from woody debris to soil. This occurs because landslides can generate woody debris that exceeds its original volume by over tenfold, resulting in heightened carbon transfer when the woody debris carbon is at a high concentration. In Phase III, the carbon storage capacity of surface vegetation stabilizes. At this stage, the reduction in soil organic carbon is primarily governed by sediment erosion processes. Post-earthquake, carbon erosion rates exhibit a gradual increase (Figure 6.11). However, larger landslide areas lead to lower initial carbon erosion rates, thus extending the overall residence time of soil carbon in the mountain ranges.
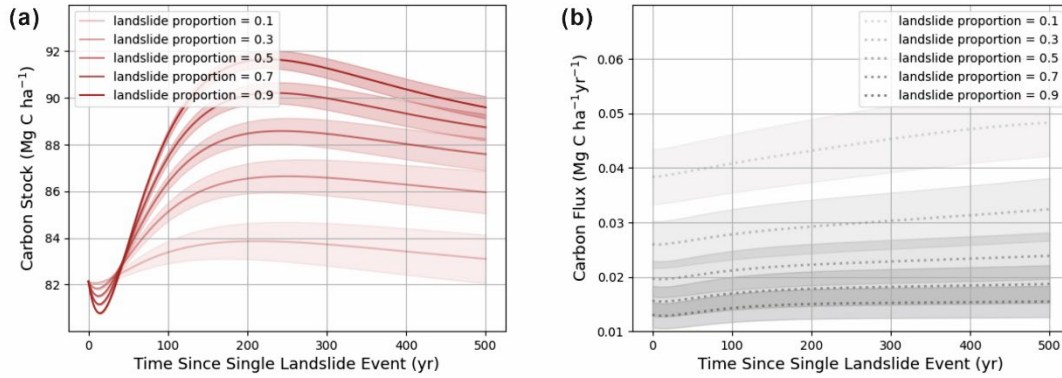
Figure 6.14 Impact of EQTLs on Soil Organic Carbon Pool
(a) Carbon Stock Change Over Time with Varying Landslide Proportions; (b) Carbon Erosion Change Over Time with Varying Landslide Proportions. The uncertainty stems from Monte Carlo random sampling method.

An increase in individual landslide area leads to a higher total carbon stock, indicating that larger landslide stores more carbon (Figure 6.14(a)). As the landslide area scale increases, it results in fewer and larger landslides, but keeps the landslide proportion for catchment area unchanged. Consequently, the mobilization of living biomass carbon remains relatively constant, and the landslide area scale has little impact on the carbon stocks in both vegetation and woody debris pools (Figure 6.15(c) and (d)). The primary contribution in increasing total carbon storage is the soil organic carbon pool. Larger landslides lead to an increase in total sediment volume, which increases the thickness of mobile regolith and thus enhances its carbon storage capacity. When the landslide area scale ranges between 0 and 1, smaller landslides stimulate a higher accumulation rate of soil carbon. Previous studies have shown that fragmented landslide scars enhance ecosystem diversity and adaptive capacity, potentially boosting soil carbon accumulation (Gutschick and BassiriRad 2003). However, when the landslide area scale exceeds 1, the positive effect of larger landslides on soil carbon storage diminishes. Ecologically, larger landslide slows down post-seismic ecosystem recovery. It is revealed significant differences in post-earthquake organic carbon recovery between the landslide scar and deposit areas, as well as between the landslide edges and centre, particularly in the case of large landslides. Unlike shallow landslides, large landslides are often accompanied by massive material displacement, and the accumulation of loose debris can trigger secondary hazards such as debris flows, which accelerate localized erosion.
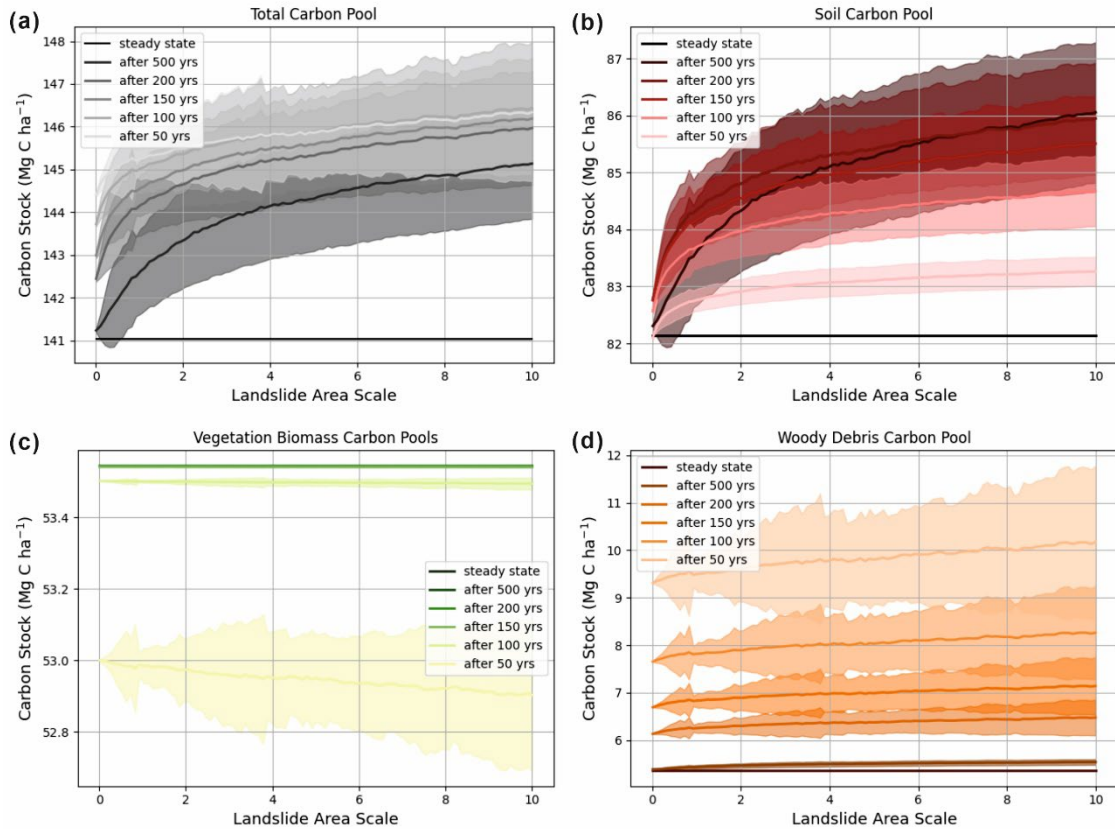
Figure 6.15 Terrestrial Ecosystem Organic Carbon Stock Change with Landslide Area Scale
(a)Total Ecosystem Organic Carbon Pool; (b)Soil Carbon Pool; (c) Vegetation and Litter Carbon Pool; (d)Woody Debris Carbon Pool. Each subfigure uses gradient colours to depict temporal changes at various years following an earthquake. The results are obtained with a fixed landslide area proportion of 10% at catchment scale. The uncertainty stems from Monte Carlo random sampling method.

6.4 Discussion

6.4.1 EQTLs impact on carbon storage capacity

In this study, the carbon storage capacity can be characterized by the fluctuations in soil organic carbon stock following earthquakes, with the difference between peak and trough values serving as key indicators. The total area triggered by earthquake is a critical factor influencing the carbon storage capacity of mountain ranges. Depending on the proportion of landslide area within catchment, carbon storage capacity can fluctuate by as much as 15% (Figure 6.16(a)). For example, following the 2008 Wenchuan earthquake, the landslide proportion ranged from 10% to 50%, causing the soil organic carbon stock fluctuating between 2 to 7 $Mg\ ha^{-1}$, resulting in a 9% variation in soil carbon storage. This temporary storage of active carbon in the soil carbon pool plays a potentially significant role in reducing regional atmospheric CO_2 concentrations. While the increase in individual landslides area also contributes to enhance carbon storage capacity, its impact on soil organic carbon stock remains within the model's margin of errors,

suggesting that the total landslides area exerts a more substantial influence. However, if an ecosystem's physical structure is completely destroyed, severe degradation can lead to an alteration of ecosystem functions. This disrupts nutrient cycling processes and hinders recovery to its original state (Foley et al. 2005). The carbon cycle model employed in this thesis may no longer be applicable under conditions of severe ecological collapse.
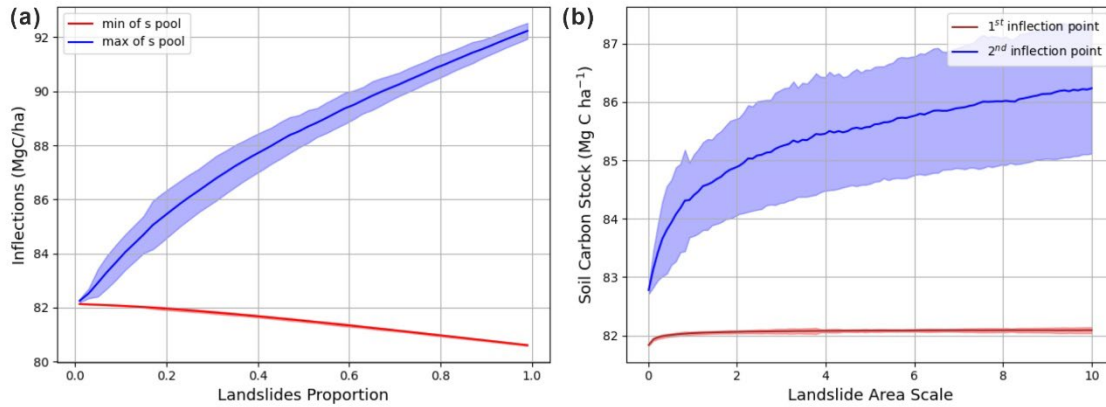
Figure 6.16 EQTLs Impact on the Size of Capacitor Effects
(a) Landslide Proportion; (b) Landslide Area Scale. This figure is correlated with Figure 6.5 presenting soil organic carbon change over time. Blue colour indicates the trough (first inflection point) and red colour indicates the peak (second inflection point). The uncertainty stems from Monte Carlo random sampling method.

The time scale of carbon storage can be characterized by the time required to reach the peak value of soil organic carbon stock following the earthquake, which represents the duration of net carbon sink. Although recovery time—the period needed for a carbon pool to return to equilibrium—also reflects the time scale of carbon storage, the uncertainties increase significantly during the period between peak to equilibrium state. In this duration, soil organic carbon slowly decreases due to physical erosion processes, with carbon erosion fluxes remaining at relatively low intensity. It may take hundreds to thousands of years for the ecosystem to fully stabilize. Compared to the century-scale period required to reach the carbon stock peak, the millennial timescale for stabilization introduces greater potential for error in determining the final equilibrium state.

This thesis investigates the impact of landslides area proportion and landslide area scale on the time required for soil organic carbon to reach its peak value. The impact of total landslide area on the time scale is not as monotonically increasing as the impact of individual landslide area (Figure 6.17(a)). When the landslide proportion is approximately 30% or less, a greater number of landslides extends the duration of the net carbon sink. However, when the landslide proportion exceeds a specific threshold, additional landslides shorten the net carbon sink duration. This change reflects a shift in the mechanisms affecting carbon storage as landslide volume increases. When the

landslide-affected area is relatively small, the erosional process is dominant. As landslide area increases, the carbon erosion export decreases, which slows the overall rate of carbon output and prolongs the net carbon sink duration. In contrast, when the landslide-affected area is large, biochemical processes become dominant. The increased burial of vegetation enhances the decomposition and respiration of woody debris, leading to an accelerated rate of overall carbon output. Meanwhile, the decreasing trend of soil erosion slows down. This reduces the net carbon sink duration. The dominant process is not necessarily determined by intensity but rather by the relative rates and trends for carbon fluxes. Our findings indicate that the balance between these two mechanisms occur at a landslide proportion of approximately 30% ~ 40%.

In contrast, the increasing of landslide area scale leads to the increased time to reach the peak (Figure 6.17(b)). It reveals an overall trend that the larger the landslides the longer the carbon storage. When individual landslides are small, shallow landslides are more common. They disturb the surface mobile regolith without mixing with bedrock sediments. It results in an almost unchanged carbon erosion rate and a consistent net carbon sink duration. However, as the area of individual landslide become bigger, more sediments mix with soil organic carbon, reducing the rate at which erosion process transports soil OC. It ultimately extends the time needed to reach carbon balance.
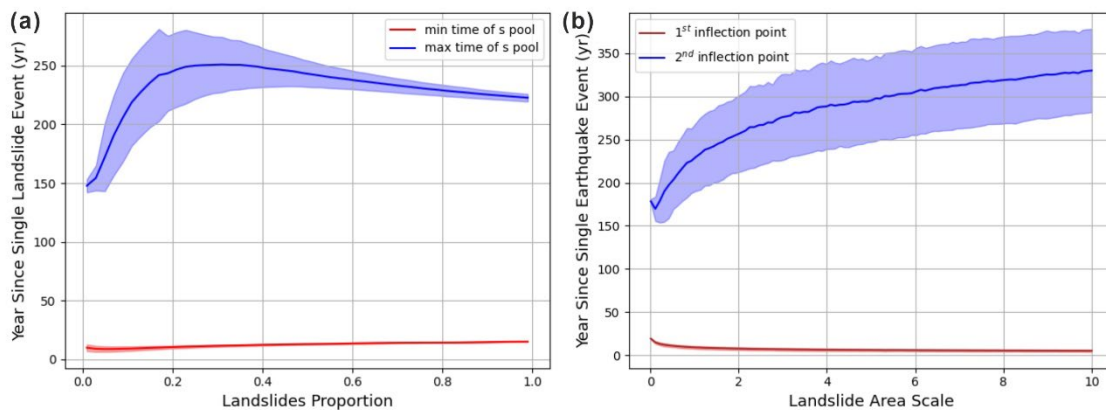
Figure 6.17 Impact on the Time Scale of Carbon Storage
(a) Landslide Proportion; (b) Landslide Area Scale. This figure is correlated with Figure 6.5 presenting soil organic carbon change over time. Blue colour indicates the first inflection point and red colour indicates the second inflection point.

The impact of EQTLs on ecosystem carbon storage unfolds over multiple timescales. The time required to reach equilibrium is primarily determined by long-term mass movements. Reaching pre-earthquake levels of carbon storage does not necessarily indicate that the ecosystem has reached equilibrium. True carbon balance is achieved when both the carbon pools and carbon fluxes within the system have stabilized.

Observations indicate that the vegetation carbon pool is the first to stabilize. When the soil carbon pool reaches its peak storage around 200 years, this indicates that vegetation biomass has stabilized and the transfer of carbon from vegetation to soil has reached its maximum. Subsequently, the woody debris carbon pool and soil carbon pool recover to 99% of their pre-earthquake equilibrium levels within approximately 700 years. However, due to the burial effects of sediment cascading, an additional 1000 years is needed for total ecosystem carbon to achieve the final 1% balance. This delay underscores the complexity of sediment transport and its impact on carbon cycling (Hilton et al. 2008a). In practice, this 1% difference may be offset or overlooked due to other factors. The zero-dimensional model used in this study does not account for spatial heterogeneity, so local factors such as intense rainfall events or sudden temperature fluctuations could abruptly change carbon fluxes.

Determining the time required to reach an equilibrium state involves inherent uncertainty, mainly due to differences in calculation methods. Most studies define a system as being in equilibrium when it has recovered 99.99% of its pre-earthquake state. However, a 0.01% deviation in a carbon pool with high reserves compared to one with low reserves can result in vastly different equilibrium times, given the same carbon flux intensity. The total ecosystem carbon stock in the Longmenshan region ranges from 58 to 227 $Mg\ ha^{-1}$, whereas in the temperate rainforest of southeast Alaska, it can vary between 542 and 821 $Mg\ ha^{-1}$ (Buma and Thompson 2019). Soil organic carbon for alpine meadow also reach 600~ 900 $Mg\ ha^{-1}$ (Wu et al. 2024), while the woody debris carbon in our study area is around 10 $Mg\ ha^{-1}$. Given these differences, we set a threshold based on the actual level of local ecosystem carbon stock and define equilibrium as when the carbon stock deviates from the steady state by only $0.001 Mg\ ha^{-1}$. When comparing two calculation methods, we identified a discrepancy of about 300 years. Although there may be some error in estimating the time required to return to pre-earthquake levels, our model can still quantitatively assess the carbon balance dynamics and the influence of time scales under consistent settings.

6.4.2 Earthquakes impact on long-term carbon storage

The impact of a mega earthquake on the storage capacity of ecosystem carbon is particularly significant. As shown in Figure 6.18, soil organic carbon stock increases with the earthquake magnitude. At lower magnitudes, specifically below Mw 6.5, earthquake magnitude has minimal influence on soil carbon storage. Only when earthquake magnitude is large enough to trigger substantial landslides do they notably affect carbon storage (Figure 6.6). When the magnitude exceeds 6.5, the number of landslides

significantly rises, which greatly enhances the "capacitor effect". A mega earthquake can increase the carbon storage capacity of the entire region by approximately 4%, equivalent to about $3\ Mg\ C\ ha^{-1}$. For our study area, this corresponds to an increase in carbon storage of $1.38\ Mt\ C$. As the earthquake magnitudes increase, extensive landslides cause greater disruption to vegetation, soil and woody debris carbon pools. This widespread disturbance prolongs the recovery process, as more time is required for each carbon pool to return to equilibrium, referred to as the "balance time". However, the response times vary significantly among the different carbon pools. Vegetation carbon is the first to recover, followed by woody debris carbon, while soil carbon, the slowest, can take centuries to millennia to stabilize. The recovery of the ecosystem's total carbon storage is therefore a phased and prolonged process. Notably, the balance time shows a steep increase around Mw 7, indicating that soil organic carbon recovery time becomes increasingly sensitive to earthquake magnitude in this range, with greater variability observed. This also highlights the potential error margins associated with the methods used to determine balance time.

In the case of 2008 Wenchuan earthquake, with a magnitude of M_W 7.9, surface vegetation is expected to recover to equilibrium (pre-earthquake levels) within about 174±1 years. This modelling balance time is faster than typical primary succession processes in most mountainous forest systems, likely due to the specific vegetation types in the Longmenshan region and the relatively low overall vegetation carbon storage. The woody debris generated by this seismic event is expected to be entirely transported out of the study area and reach equilibrium in approximately 1054±480 years. Soil OC will stabilize in approximately 1763±488 years, leading to the restoration of the overall system's carbon balance. The interval between earthquakes with a magnitude of M_W 7.9 or greater in the Longmenshan region, is approximately 1815 years (Gutenberg and Richter 1956; Li et al. 2017b). This interval exceeds the recovery time required for the local ecosystem's carbon storage to return to equilibrium after such a significant event. However, during this period, other earthquakes less than M_W 7.9 frequently occur, indicating that the impact is not limited to a single earthquake event.
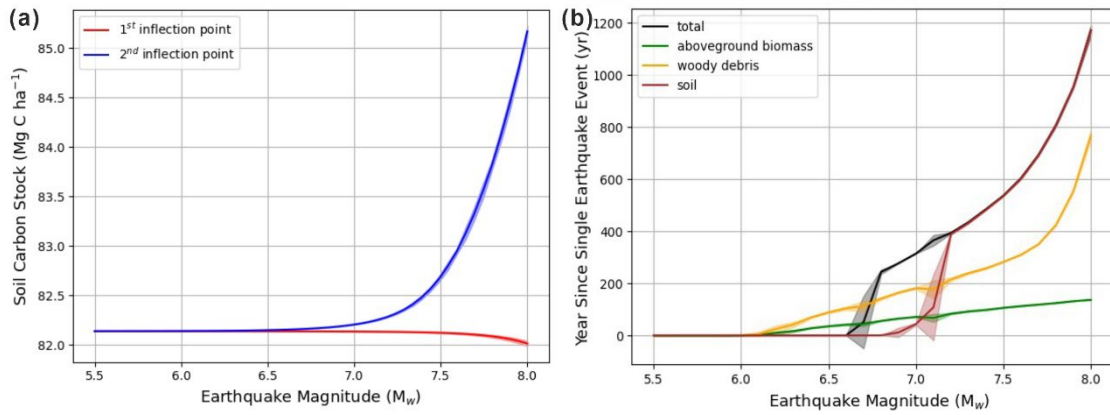
Figure 6.18 Impact of Single Earthquake Event on Capacitor Effects and Balance Time
(a) Correlation between Earthquake Magnitude and Peak Value of Soil Carbon Pool; (b) Balance Time for Ecosystem Carbon Return to Pre-Earthquake Level.

Even through the Monte Carlo simulations average out the fluctuations for successive earthquakes, the carbon balance model, coupled with the stochastic earthquake model, emphasizes the cumulative effects—particularly when the time interval between earthquakes is shorter than the recovery time required to restore balance after each earthquake. Typically, for single earthquake event, the turnover rate associated with carbon export is closely linked to sediment cascading and varies with changes in sediment volume within the catchment. Our sediment mass balance assumption posits that any sediment debris produced by landslides will be continuously transported out of the catchment, maintaining a constant mobile regolith. Consequently, the turnover rate continuously adjusts after an earthquake until the sediment volume stabilizes, restoring the initial turnover rate. In this long run, a single earthquake event does not significantly alter local carbon stocks. However, the modelling results reveal an upward trend in ecosystem carbon storage due to the cumulative effects of multiple earthquakes events (Figure 6.19). Mechanistically, this increase in soil carbon storage may be due to EQTLs-generated sediments mixing with living biomass, which remain stored in the mountain ranges without being exported. However, this would result in an ever-thickening layer of mobile regolith, conflicting with our initial assumptions. Another possibility is that the retention time of soil organic carbon in mountain ranges exceeds the intervals between earthquakes, as modelled by the stochastic earthquake framework. The more frequent the seismic events, the higher the soil organic carbon storage, but the use of Monte Carlo simulations helps address the randomness introduced by the stochastic model. Therefore, the slow increase in soil organic carbon stock is likely a product of both the unique environmental conditions of the Wenchuan region and the underlying assumptions of the carbon cycle framework in the model. It is proposed that in the Longmenshan region, continuous seismic activity leads to a gradual accumulation of soil organic carbon.

In Longmenshan active region, EQTLs contribute to a carbon sink effect at an annual rate of 0.02~0.08 $t\ km^2\ yr^{-1}$. This carbon is primarily stored in the form of buried and decomposed organic matter within soil sediments. This observation aligns with our field sampling finding in Chapter 5, where landslide-prone areas, such as steep slopes and ridges, have relatively high soil organic carbon stocks. Frequent EQTLs in mountain ranges promote the accumulation of soil organic carbon, based on the assumption that sediment erosion rates remain constant before and after seismic events. However, this model, while generally applicable, may require adjustments depending on the biochemical and erosional parameters specific to each region. Factor such as temperature, precipitation, geography, and topography play a crucial role in influencing carbon dynamics by affecting photosynthesis, respiration, and erosion processes. These factors interact to establish the carbon stock's equilibrium state. Therefore, while a net carbon sink may be observed in Longmenshan region, it is possible that other seismically active regions may exhibit different patterns. Overall, more empirical data and validation are needed to determine whether similar cumulative carbon sink effects exist across other fault zones.
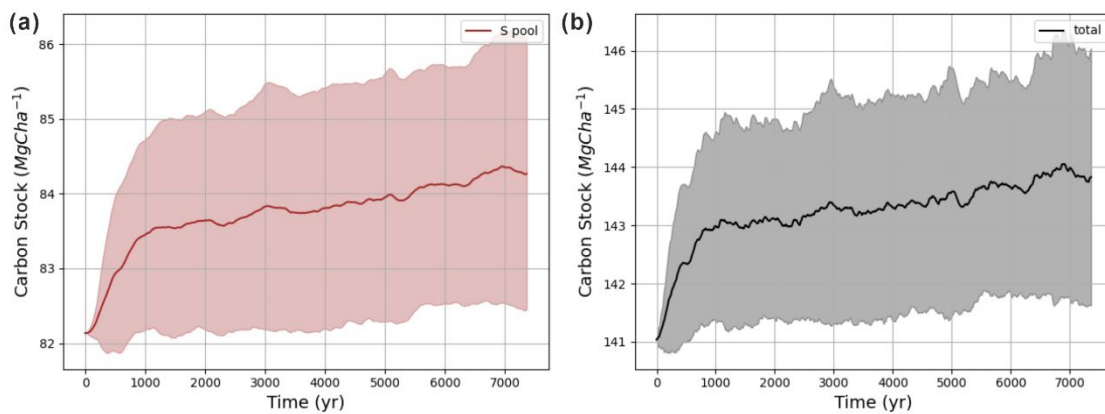
Figure 6.19 Cumulative Trend of Terrestrial Ecosystem Organic Carbon Stock Under Modelled Earthquake Cycles
(a) Soil Carbon Pool; (b) Total Ecosystem Organic Carbon Pool. These results are obtained on 100 earthquake cycles using stochastic earthquake model. The uncertainty is quantified by the standard deviation of the calculated values for each year.

Earthquakes contribute to the long-term storage capacity of ecosystem carbon storage, although their intensity is not significant compared to other major long-term fluxes. Over long timescales, Hilton and West (2020) provide an emerging review of the intensity of carbon flux within the geological carbon cycle. The primary processes of organic carbon fluxes include biospheric organic erosion and rock organic carbon oxidation. While ecosystem carbon fluxes related to net primary production occur on a short-term scale, organic carbon burial (including rock and terrestrial organic carbon) is a long-term process. Given that active fault zones occupy about 10% of the global land area, it is

roughly estimated that the rate of ecosystem carbon burial due to EQTLs is approximately 0.1% of the total organic carbon burial flux (unit: $Mt\ C\ year^{-1}$). Although this contribution is small on a global scale, repeated seismic events indeed influence the terrestrial organic carbon balance by facilitating long-term carbon storage in mountain ranges.

6.5 Conclusions

Following an earthquake, vegetation and woody debris are disrupted and buried within landslide deposits, forming a primary reservoir for carbon storage. The limited sediment transport contributes to the retention of terrestrial organic carbon by reducing its export through erosion. Additionally, the regrowth of vegetation on exposed surfaces following landslides enhances surface carbon accumulation. As a result, EQTLs function as a net carbon sink, with the soil carbon pool storing the majority of ecosystem carbon compared to other reservoirs.

EQTLs have a significant impact on ecosystem carbon storage capacity, with the effects varying based on landslide proportion and scale. When the landslide proportion is below 30%, carbon storage increases linearly with the proportion of landslides. However, beyond this threshold, the landscape's ability to store carbon diminishes due to resource constraints, indicating a saturation effect. While larger landslides increase soil organic carbon (SOC) storage by deepening mobile regolith layers, they also slow ecosystem recovery, causing the growth in carbon storage to decelerate. Overall, landslide proportion exerts a greater influence on carbon storage than landslide scale. In severely impacted catchments, EQTLs can enhance carbon storage capacity by up to 15%, with the soil carbon pool playing the primary role in carbon sequestration.

EQTLs also influence the duration of soil carbon sinks, but the effect of landslide proportion on net carbon sink duration is not monotonically increasing. At lower proportions, soil carbon storage is limited by physical erosion, and the accumulation of buried organic carbon prolongs the carbon sink period. As the landslide proportion increases, biochemical processes become the limiting factor, reducing vegetation's photosynthetic capacity and the transfer of carbon to the soil, which slows or even reverses the net carbon sink duration. The threshold for this shift in mechanisms appears at a landslide proportion of approximately 30%.

In the Longmenshan region, the 2008 Wenchuan M_w 7.9 earthquake significantly enhanced storage by triggering large-scale landslides, increasing soil carbon storage by approximately 3%-10%. Vegetation biomass carbon is expected to take around 200 years to return to pre-earthquake equilibrium, while woody debris carbon will take approximately 1000 years. Soil organic carbon will require even longer, around 1700 years, to stabilize, primarily due to the long-term effects of sediment cascading triggered by EQTLs. However, before the soil carbon pool fully stabilizes, subsequent seismic events may disrupt the carbon balance, initiating new cycles of carbon redistribution. The

cumulative effect of multiple earthquakes leads to a long-term increase in soil organic carbon storage, creating a sustained carbon sink effect. While earthquakes contribute modestly to global carbon burial fluxes, their impact on regional carbon cycles, especially in mountainous areas, is significant. This has profound implications for global carbon budgeting and carbon cycle modelling.

Chapter 7

Discussions and Conclusions

The thesis presents a comprehensive study on the impact of earthquake-triggered landslides on ecosystem carbon storage and cycling in mountainous regions, with a particular focus on the Wenchuan earthquake of 2008. Five key conclusions from the study are as follows:

Earthquakes redistribute carbon on hillslopes: Earthquake-triggered landslides and debris flows lead to reductions in surface ecosystem carbon stocks. In the case of the Wenchuan earthquake, vegetation and surface soil carbon stocks were reduced by 89.6% and 97.8%, respectively, across the catchment area. This highlights the role of mega-earthquakes as significant drivers of regional carbon redistribution.

Earthquakes increase hillslope carbon storage: A decade after the 2008 Wenchuan Earthquake, total hillslope carbon storage increased by approximately 10%, with 5.3 to 7.0 Mt C stored, highlighting the role of hillslopes as temporary carbon reservoirs. About 60% of this stored carbon is buried in landslide sediments, while the rest is recovered from shallow soil and new vegetation.

Mountain ranges may act as an ecosystem carbon capacitor controlling the release of carbon into downstream sinks: EQTLs temporarily store ecosystem organic carbon in mountainous regions, releasing it gradually over time. This "capacitor effect" is primarily driven by high rates of carbon burial and surface recovery. The soil organic carbon pool plays a central role in this process, acting as a key component that connects biochemical and physical erosion processes.

The proportion of landslides and their size distribution within a catchment is a significant control on carbon storage: The capacity of the landscape to store carbon is significantly influenced by landslide proportion. Below a threshold of 30%, carbon storage increases linearly with the proportion of landslides. However, beyond this threshold, resource limitations lead to a saturation effect, reducing the landscape's ability to store additional carbon. Larger landslides, while increasing soil organic carbon (SOC) storage, also slow ecosystem recovery, decelerating overall carbon sequestration.

Earthquakes have long-term impacts on carbon sequestration: The recovery times for different carbon pools vary significantly. While vegetation biomass takes around 200 years to return to pre-earthquake levels, woody debris requires approximately 1000 years, and soil organic carbon may take as long as approximately 1800 years to reach equilibrium. The long-term impact of sediment cascading prolongs the stabilization of soil carbon storage. The cumulative effects of multiple seismic events contribute to soil carbon sequestration at an annual rate of about 0.1% of the total organic carbon burial flux.

This thesis has also answered the initial three research questions:

1. How and where do earthquake-triggered landslides and post-seismic debris flows store and redistribute ecosystem carbon?

Earthquake-triggered landslides and post-seismic debris flows primarily store ecosystem carbon on hillslopes, where a significant portion of organic carbon (vegetation and soil carbon) is buried within landslide deposits. The redistribution of carbon occurs as debris flows transport these carbon-rich sediments across the landscape and into the fluvial system. While some carbon is exported downstream, the majority remains stored in landslide deposits, acting as temporary carbon sinks. The sediment and organic matter stored on hillslopes can remain sequestered for extended periods, slowing carbon release through erosion and decomposition processes. The findings indicate that sediment export rates influence how much of the buried carbon is eventually transported out of the region.

2. What is the spatial distribution of carbon storage and recovery after a mega earthquake?

Prior to the Wenchuan Earthquake, the spatial distribution of carbon stocks was heavily influenced by topography and climate, with higher concentrations found at elevations between 500 and 2000 meters, especially along the steep range fronts of the Longmen Shan. After the earthquake, carbon storage in landslide-affected areas showed spatial variability. The majority of eroded carbon occurred within the Minjiang and Tuojiang basins, accounting for 83% of the total carbon mass denuded by earthquake-triggered landslides (EQTL). Spatial differences in recovery rates were influenced by factors such as lithology, precipitation, and the characteristics of landslide deposits, with higher recovery in areas with carbon-rich soils and favorable environmental conditions.

3. How do earthquakes affect carbon storage capacity?

Earthquakes enhance ecosystem carbon storage capacity by creating large reservoirs of carbon-rich sediment through landslides, which can act as long-term carbon sinks. The burial of organic carbon in landslide deposits reduces its immediate release into the atmosphere and preserves it within the landscape for extended periods. However, the capacity for carbon storage is influenced by the proportion and scale of landslides. When landslide proportions exceed 30%, the landscape's ability to store additional carbon diminishes due to resource constraints and slower ecosystem recovery. In contrast, regions with lower sediment export rates, such as the Longmenshan region, show greater potential for long-term carbon retention. The cumulative effect of multiple earthquakes results in a sustained carbon sink, as successive landslides continue to bury organic carbon and delay its release through slow erosion and decomposition processes.

Several limitations and areas for further exploration remain in this thesis, which are essential for refining and expanding upon the current findings. The future research directions suggested here aim to address these limitations, with a focus on improving model accuracy, understanding spatial and temporal variability, and integrating additional environmental factors:

1. Temporal Field Data for Model Validation

One of the key limitations identified in this research is the lack of time-series field data, which is crucial for validating parameters in both the machine learning predictions and the carbon cycle models. Current models rely on point-in-time field measurements and simulations, which, while useful, do not capture the full dynamic nature of post-seismic carbon cycling. Collecting long-term field data at multiple time points after seismic events would provide valuable insights into how carbon stocks evolve over time. Such data would enhance model parameterization and allow for more accurate predictions of carbon fluxes and storage in the aftermath of earthquakes. Incorporating these time-series datasets into machine learning algorithms would improve the robustness of predictive models, allowing them to better account for temporal changes in ecosystem recovery, vegetation regrowth, and carbon export through sediment transport.

2. Improving Spatial Models through Field and Remote Sensing Data

In the development of the carbon cycle model, this study utilized a zero-dimensional approach, which does not account for spatial heterogeneity. However, existing research has shown that the spatial variability of landslides, particularly in terms of their size, shape, and connection to the fluvial network, plays a critical role in carbon redistribution. Landslide-prone areas exhibit pronounced spatial differences in carbon storage and export rates, which can have significant effects on the overall carbon budget. As more field data becomes available and remote sensing technologies continue to advance, future research should aim to construct spatially explicit models that can capture these heterogeneities. By integrating high-resolution remote sensing data with field measurements, researchers can develop more sophisticated models that quantify the spatial distribution of carbon storage and the variability across different landslides. This will provide a more nuanced understanding of how landscape-scale processes affect carbon cycling in tectonically active regions.

3. Incorporating Biochemical Processes in Carbon Cycling Models

While this study primarily focused on geomorphic processes, such as mass movements and sediment transport, it became clear that biochemical processes play a significant role

in shaping ecosystem carbon cycles, particularly following landscape-altering events like landslides. Changes in soil chemistry, physical properties, and microbial communities following landslides have a profound impact on soil respiration and carbon fluxes. Future research should include laboratory-based experiments to quantify these biochemical processes, particularly the impact of microbial activity on soil carbon release. Understanding how microbial communities adapt to post-seismic environments and influence soil respiration rates will help refine the carbon cycle models, leading to a more comprehensive representation of the complex interactions between geomorphic and biochemical processes. These laboratory studies can serve as a critical supplement to field observations, offering a controlled environment to test hypotheses about soil chemistry, respiration, and carbon decomposition.

4. Coupling Earthquake Effects with Environmental Factors

This dissertation did not account for the combined effects of environmental factors such as rainfall and temperature, which can amplify or mitigate the impacts of earthquake-triggered landslides on ecosystem carbon cycles. Climate change, particularly rising temperatures and changing precipitation patterns, has the potential to significantly influence the rate of vegetation regrowth, soil respiration, and sediment transport, all of which are crucial components of carbon cycling. As global temperatures continue to rise, understanding how these environmental factors interact with seismic and geomorphic processes is increasingly important. Future studies should aim to develop models that couple seismic activity with climate variables, thereby providing a more holistic view of how earthquake-driven carbon cycles are influenced by broader environmental changes. This integrative approach will not only enhance our understanding of carbon cycling in tectonically active regions but will also provide critical insights for Earth system models, especially in predicting how ecosystems may respond to multiple stressors in the future.

Appendix

ID	Name	Area	Landslide number	Landslide area	Landslide proportion
1	Luoquan	28592537	299	10024397	0.350594877
2	Qishuping/Douhongkou	3597207	44	450231	0.125161271
3	Lengjin	3909604	339	713153.37	0.182410641
4	Sunjia/Yanfengdong/Hetaoshu	2262002	66	428823.07	0.189576786
5	Chunya/Shuangyangzi/Zhichang	5925606	281	706883.23	0.119292985
6	Dacaotou/Dagou	6609177	157	1012819.8	0.153244466
7	Laohuzui/Santaidi	1868221	19	1575463	0.843295841
8	Douyaping/Mayangdian/Maliuwan/Qingling/Guanshan	6715633	288	2752421.5	0.409852876
9	Xiaojigou	8109073	212	3047828.3	0.375854096
10	Pubugou/Xiezi/Wuming	5591788	72	2663532	0.476329217
11	wasi/erhaoqiao/yihaoqiao	4015955	74	2320965.1	0.577936033
12	Yinxingping	7250291	89	2482181	0.342356052
13	yinchang	7794687	116	3593666.45	0.461040507
14	Dayin	23833626	179	5300945.3	0.222414554
15	Xiangjia	2622611	81	1400139.8	0.533872465
16	Gan/1#qian/luobaoshu	7091817	188	2418894.1	0.341082419
17	Baijialin	2393338	34	1073591	0.448574752
18	Hongchun/Shaofang	5937117	240	1861388.7	0.313517268
19	Bayi/gongjia	8546830	373	2347233.2	0.274632021
20	Maliu/Huangyang/Dashui/liquantai/majiawuji	4838591	217	959154.16	0.198230055

21	Jiangjia/Shuijuping	4444840	31	203033.1	0.045678382
22	Niujuan/Zhangjiaping	13314654	323	3874211.7	0.290973517
23	Yeliu	24525708	398	8660704.4	0.3531276
24	Guxi	13909704	209	5169047	0.37161445
25	Zaojiaowan	4035792	86	2346897.7	0.581520975
26	Yiwanshui/zhangjiagou/Mozi	7368016	94	3322770	0.450972148
27	Taoguan	50912950	816	9173383.8	0.180177809
28	Yiwanshui	4123448	104	834073	0.20227562
29	NA	6891973	87	653724.1	0.094852969
30	Yangling	5526998	71	781301.9	0.141360988
31	Chediguan	17597218	206	5118653.5	0.290878564
32	Gaojia	4475795	108	2398986.4	0.535991126
33	Xiaojia/Wangyimiao/Mozi1#	6704411	275	2319708.7	0.345997389
34	NA	6865279	77	1383189	0.201476007
35	NA	10377240	116	810619.4	0.078115125
36	Er	39775190	536	7591432.77	0.190858492
37	NA	21715569	123	5395016	0.248440002
38	NA	4806360	41	529428.4	0.110151632
39	NA	26308375	1042	8514411.1	0.323638807
40	NA	33680615	418	5449137	0.161788524
41	Zhucao	3795019	286	753959.55	0.198670824
42	Jianping	3483222	42	395233.4	0.113467761

Table S2 Allometric Equations of Tree Species
Allometric equations of different trees applied in this study, including the tree species, components and sources, which are originally summarized by Luo et al. (2020).

No	Tree Species	Component	Equation form	Coeff. a	Coeff. b	Coeff. c	Sources
1	Ailanthus_altissima	Total stem	$W=a+b*(D^2*H)$	0.447	0.007	/	Yang, 2013
2	Ailanthus_altissima	Total branch	$W=a+b*(D^2*H)$	0.076	0.002	/	Yang, 2013
3	Ailanthus_altissima	Total leaf	$W=a+b*(D^2*H)$	0.045	0.001	/	Yang, 2013

				a	b		
4	Ailanthus_altissima	Total belowground	$W=a+b*(D^2*H)$	0.118	0.001	/	Yang, 2013
5	Ailanthus_altissima	Total tree	$W=a+b*(D^2*H)$	0.876	0.0124	/	Yang, 2013
6	Alnus_cremastogyne	Total stem	$W=a*(D^2*H)^b$	0.0422	0.8631	/	Shi et al., 1996, 1997
7	Alnus_cremastogyne	Total branch	$W=a*(D^2*H)^b$	0.0242	0.7332	/	Shi et al., 1996, 1997
8	Alnus_cremastogyne	Total leaf	$W=a*(D^2*H)^b$	0.0735	0.4462	/	Shi et al., 1996, 1997
9	Alnus_cremastogyne	Total aboveground	$W=a*(D^2*H)^b$	0.117	0.7577	/	Shi et al., 1996, 1997
10	Alnus_cremastogyne	Total belowground	$W=a*(D^2*H)^b$	0.0157	0.8378	/	Shi et al., 1996, 1997
11	Betula_platyphylla	Total stem	$W=a*D^b$	0.018	2.935	/	Wang et al., 2010
12	Betula_platyphylla	Total branch	$W=a*D^b$	9.50E-04	3.533	/	Wang et al., 2010
13	Betula_platyphylla	Total leaf	$W=a*D^b$	0.0186	1.9057	/	Wang et al., 2010
14	Betula_platyphylla	Total belowground	$W=a*D^b$	0.0159	2.7047	/	Wang et al., 2010
15	Betula_platyphylla	Total tree	$W=a*D^b$	0.033	2.9314	/	Wang et al., 2010
16	Betula_platyphylla	Stem wood	$\ln(W)=a+b*\ln(D^2*H)$	-3.4668	0.9311	/	Xiao, 1988
17	Betula_platyphylla	Stem bark	$\ln(W)=a+b*\ln(D^2*H)$	-5.017	0.9124	/	Xiao, 1988
18	Betula_platyphylla	Total branch	$\ln(W)=a+b*\ln(D^2*H)$	-3.8492	0.8145	/	Xiao, 1988
19	Betula_platyphylla	Total leaf	$\ln(W)=a+b*\ln(D^2*H)$	-4.6873	0.7259	/	Xiao, 1988
20	Betula_platyphylla	Total belowground	$\ln(W)=a+b*\ln(D^2*H)$	-4.8779	1.0378	/	Xiao, 1988
21	Camellia_oleifera	Stem wood	$W=a*D0^b$	0.2614	2.356	/	Zheng et al., 2008
22	Camellia_oleifera	Stem bark	$W=a*D0^b$	0.06	1.9143	/	Zheng et al., 2008
23	Camellia_oleifera	Coarse branch	$W=a*D0^b$	0.4278	2.0513	/	Zheng et al., 2008

24	Camellia_oleifera	Fine branch	W=a*D0^b	0.1304	2.1745	/	Zheng et al., 2008
25	Camellia_oleifera	Total leaf	W=a*D0^b	0.4269	2.1692	/	Zheng et al., 2008
26	Camellia_oleifera	Stump and coarse root (Φ>20mm)	W=a*D0^b	0.197	2.1614	/	Zheng et al., 2008
27	Camellia_oleifera	Medium root (2mm≤Φ≤20mm)	W=a*D0^b	0.0117	2.1144	/	Zheng et al., 2008
28	Camellia_oleifera	Fine root (Φ<2mm)	W=a*D0^b	0.0025	2.0888	/	Zheng et al., 2008
29	Camellia_oleifera	Total tree	W=a*D0^b	1.4927	2.1778	/	Zheng et al., 2008
30	Camellia_oleifera-evergreen broadleaved trees	Total stem	W=a*(D^2*H)^b	0.02543	0.9858	/	Feng et al., 1999
31	Camellia_oleifera-evergreen broadleaved trees	Total branch	W=a*(D^2*H)^b	0.02026	0.8635	/	Feng et al., 1999
32	Camellia_oleifera-evergreen broadleaved trees	Total leaf	W=a*(D^2*H)^b	0.01092	0.7792	/	Feng et al., 1999
33	Camellia_oleifera-evergreen broadleaved trees	Total belowground	W=a*(D^2*H)^b	0.0142	0.8903	/	Feng et al., 1999
34	Cinnamomum_camphora	Stem wood	W=a*D^b	0.0709	2.2789	/	Wang et al., 2012c
35	Cinnamomum_camphora	Stem bark	W=a*D^b	0.023	1.9342	/	Wang et al., 2012c
36	Cinnamomum_camphora	Total branch	W=a*D^b	0.0114	2.8589	/	Wang et al., 2012c
37	Cinnamomum_camphora	Total leaf	W=a*D^b	0.0014	3.2323	/	Wang et al., 2012c
38	Cinnamomum_camphora	Total belowground	W=a*D^b	0.0335	2.4369	/	Wang et al., 2012c
39	Cinnamomum_camphora	Total tree	W=a*D^b	0.1039	2.535	/	Wang et al., 2012c
40	Cryptomeria fortunei	Total stem	W=a*(D^2*H)^b	0.1117	0.7096	/	Huang, 1986
41	Cryptomeria fortunei	Tree crown	W=a*(D^2*H)^b	0.1386	0.6017	/	Huang, 1986
42	Cryptomeria fortunei	Total belowground	W=a+b*(D^2*H)	0.1246	0.003246	/	Huang, 1986

43	Cryptomeria_fortunei	Total stem	W=a*D^b	0.2907	1.738	/	Huang, 1986
44	Cryptomeria_fortunei	Tree crown	W=a*D^b	0.2302	1.51	/	Huang, 1986
45	Cryptomeria_fortunei	Total belowground	W=a*exp(b*D)	0.7552	0.1626	/	Huang, 1986
46	Cunninghamia_lanceolata	Stem wood	W=a*D^b	0.0524	2.0795	/	Xiao et al., 2012
47	Cunninghamia_lanceolata	Stem bark	W=a*D^b	0.0143	1.8722	/	Xiao et al., 2012
48	Cunninghamia_lanceolata	Total branch	W=a*D^b	0.0103	2.2504	/	Xiao et al., 2012
49	Cunninghamia_lanceolata	Total leaf	W=a*D^b	0.0327	2.1229	/	Xiao et al., 2012
50	Cunninghamia_lanceolata	Total belowground	W=a*D^b	0.0361	2.0158	/	Xiao et al., 2012
51	Cunninghamia_lanceolata	Total tree	W=a*D^b	0.1456	2.0817	/	Xiao et al., 2012
52	Cupressus_funebris	Total stem	W=a*(D^2*H)^b	0.039	0.9093	/	An et al., 1991
53	Cupressus_funebris	Total branch	W=a*(D^2*H)^b	0.28588	0.42953	/	An et al., 1992
54	Cupressus_funebris	Total leaf	W=a*(D^2*H)^b	0.10216	0.53916	/	An et al., 1993
55	Cupressus_funebris	Total aboveground	W=a*(D^2*H)^b	0.12703	0.79775	/	An et al., 1994
56	Cupressus_funebris	Total belowground	W=a*(D^2*H)^b	0.1155	0.56696	/	An et al., 1995
57	Cupressus_funebris	Stem wood	W=a*(D^2*H)^b	0.0111	1.0669	/	Yang et al., 1987
58	Cupressus_funebris	Stem bark	W=a*(D^2*H)^b	0.0162	0.747	/	Yang et al., 1987
59	Cupressus_funebris	Total branch	W=a*(D^2*H)^b	0.0093	0.9638	/	Yang et al., 1987
60	Cupressus_funebris	Total leaf	W=a*(D^2*H)^b	0.0098	0.9605	/	Yang et al., 1987
61	Cupressus_funebris	Total belowground	W=a*(D^2*H)^b	0.7017	0.3678	/	Yang et al., 1987
62	Cyclobalanopsis glauca	Total stem	W=a+b*D	-33.719	6.367	/	Yu, 1999

No.	Species	Component	Equation	a	b	c	Source
63	Cyclobalanopsis glauca	Total branch	W=a+b*D	-13.003	2.785	/	Yu, 1999
64	Cyclobalanopsis glauca	Total leaf	W=a+b*D+c*D^2	-10.096	2.218	-0.0648	Yu, 1999
65	Cyclobalanopsis glauca	Total aboveground	W=a+b*D	-48.123	9.745	/	Yu, 1999
66	Cyclobalanopsis glauca	Total belowground	W=a+b*D	-14.314	2.777	/	Yu, 1999
67	Cyclobalanopsis glauca	Stem wood	W=a*D^b	0.651	1.6086	/	Zheng et al., 2008
68	Cyclobalanopsis glauca	Stem bark	W=a*D^b	0.0598	1.3405	/	Zheng et al., 2008
69	Cyclobalanopsis glauca	Coarse branch	W=a*D^b	0.112	1.4827	/	Zheng et al., 2008
70	Cyclobalanopsis glauca	Fine branch	W=a*D^b	0.0619	1.2934	/	Zheng et al., 2008
71	Cyclobalanopsis glauca	Total leaf	W=a*D^b	0.2071	0.9169	/	Zheng et al., 2008
72	Cyclobalanopsis glauca	Stump and coarse root (Φ>20mm)	W=a*D^b	0.2485	0.8636	/	Zheng et al., 2008
73	Cyclobalanopsis glauca	Medium root (2mm≤Φ≤20mm)	W=a*D^b	0.0369	1.0145	/	Zheng et al., 2008
74	Deciduous_broadleaved_trees	Total stem	W=a*(b+D)^2	0.1793	-0.619	/	Dang et al., 1994b
75	Deciduous_broadleaved_trees	Total branch	W=a+b*D	-0.8228	0.421	/	Dang et al., 1994b
76	Deciduous_broadleaved_trees	Total leaf	W=a+b*D^3	-0.0116	0.0071	/	Dang et al., 1994b
77	Deciduous_broadleaved_trees	Stump	W=a+b*D^2	0.0149	0.0303	/	Dang et al., 1994b
78	Deciduous_broadleaved_trees	Roots	W=a*(b+D)^2	0.0277	-0.4184	/	Dang et al., 1994b
79	Deciduous_broadleaved_trees	Total stem	W=a*(D^2*H)^b	0.065	0.84	/	Wang et al., 2007a
80	Deciduous_broadleaved_trees	Total branch	W=a*(D^2*H)^b	1.59	0.38	/	Wang et al., 2007a
81	Deciduous_broadleaved_trees	Total leaf	W=a*(D^2*H)^b	0.218	0.34	/	Wang et al., 2007a

82	Deciduous_broadleaved_trees	Total belowground	W=a*(D^2*H)^b	0.291	0.55	/	Wang et al., 2007a
83	Eucommia_ulmoides	Stem wood	lg(W)=a+b*lg(D^2*H)	-1.3527	0.8979	/	Pan et al., 2000
84	Eucommia_ulmoides	Stem bark	lg(W)=a+b*lg(D^2*H)	-2.219	0.8252	/	Pan et al., 2000
85	Eucommia_ulmoides	Total branch	lg(W)=a+b*lg(D^2*H)	-2.1076	0.9216	/	Pan et al., 2000
86	Eucommia_ulmoides	Total leaf	lg(W)=a+b*lg(D^2*H)	-1.7761	0.605	/	Pan et al., 2000
87	Eucommia_ulmoides	Total belowground	lg(W)=a+b*lg(D^2*H)	-1.8241	0.8306	/	Pan et al., 2000
88	Idesia_polycarpa	Total stem	W=a*D^b	0.1881	1.9371	/	Zhao et al., 2012
89	Idesia_polycarpa	Tree crown	W=a*D^b	0.0751	1.6816	/	Zhao et al., 2012
90	Idesia_polycarpa	Total aboveground	W=a*D^b	0.2678	1.8682	/	Zhao et al., 2012
91	Juglans mandshurica	Total stem	lg(W)=a+b*lg(D)	-0.782	2.194	/	Wang, 2006
92	Juglans_mandshurica	Total branch	lg(W)=a+b*lg(D)	-2.359	2.898	/	Wang, 2006
93	Juglans_mandshurica	Total leaf	lg(W)=a+b*lg(D)	-1.414	1.639	/	Wang, 2006
94	Juglans_mandshurica	Total aboveground	lg(W)=a+b*lg(D)	-0.765	2.287	/	Wang, 2006
95	Juglans_mandshurica	Roots (Φ≥5mm)	lg(W)=a+b*lg(D)	-1.784	2.412	/	Wang, 2006
96	Juglans_mandshurica	Total belowground (Φ≥5mm)	lg(W)=a+b*lg(D)	-1.734	2.397	/	Wang, 2006
97	Ligustrum_lucidum	Total stem	W=a+b*(D^2*H)	0.437	0.004	/	Yang, 2013
98	Ligustrum_lucidum	Total branch	W=a+b*(D^2*H)	0.075	0.004	/	Yang, 2013
99	Ligustrum_lucidum	Total leaf	W=a+b*(D^2*H)	0.163	0.002	/	Yang, 2013
100	Ligustrum_lucidum	Total belowground	W=a+b*(D^2*H)	0.232	0.001	/	Yang, 2013
101	Ligustrum_lucidum	Total tree	W=a+b*(D^2*H)	0.907	0.01	/	Yang, 2013
102	Liquidambar_formosana	Stem wood	W=a*(D^2*H)^b	0.0252	0.9614	/	Ouyang et al., 2010
103	Liquidambar_formosana	Stem bark	W=a*(D^2*H)^b	0.005	0.9553	/	Ouyang et al., 2010

				a	b		
104	Liquidambar_formosana	Total branch	$W=a*(D^2*H)^b$	0.0053	1.0132	/	Ouyang et al., 2010
105	Liquidambar_formosana	Total leaf	$W=a*(D^2*H)^b$	0.0072	0.8658	/	Ouyang et al., 2010
106	Liquidambar_formosana	Total belowground	$W=a*(D^2*H)^b$	0.0015	1.0622	/	Ouyang et al., 2010
107	Litsea_pungens	Total stem	$W=a+b*(D^2*H)$	0.1071	0.0254	/	Feng et al., 1999
108	Litsea_pungens	Total branch	$W=a*(D^2*H)^b$	0.0125	0.9054	/	Feng et al., 1999
109	Litsea_pungens	Total leaf	$W=a*(D^2*H)^b$	5.50E-06	1.666	/	Feng et al., 1999
110	Litsea_pungens	Total belowground	$W=a*(D^2*H)^b$	0.0143	0.8607	/	Feng et al., 1999
111	Metasequoia_glyptostroboides	Total stem	$lg(W)=a+b*lg(D^2*H)$	-1.3693	0.8428	/	Gao et al., 1992
112	Metasequoia_glyptostroboides	Total branch	$ln(W)=a+b*D$	-0.2238	0.1434	/	Gao et al., 1992
113	Metasequoia_glyptostroboides	Total leaf	$ln(W)=a+b*D$	-0.7865	0.1127	/	Gao et al., 1992
114	Metasequoia_glyptostroboides	Total aboveground	$lg(W)=a+b*lg(D^2*H)$	-1.0967	0.8026	/	Gao et al., 1992
115	Metasequoia_glyptostroboides	Total belowground	$lg(W)=a+b*lg(D)$	-1.4455	2.0887	/	Gao et al., 1992
116	Phoebe_bournei	Stem wood	$lg(W)=a+b*lg(D^2*H)$	-1.4299	0.9419	/	Ma et al., 1989
117	Phoebe_bournei	Stem bark	$lg(W)=a+b*lg(D^2*H)$	-2.8452	1.0106	/	Ma et al., 1989
118	Phoebe_bournei	Total branch	$lg(W)=a+b*lg(D^2*H)$	-2.3262	0.9952	/	Ma et al., 1989
119	Phoebe_bournei	Total leaf	$lg(W)=a+b*lg(D^2*H)$	-2.8632	1.0108	/	Ma et al., 1989
120	Phoebe_bournei	Total aboveground	$lg(W)=a+b*lg(D^2*H)$	-1.3695	0.9599	/	Ma et al., 1989
121	Phoebe_bournei	Total belowground	$lg(W)=a+b*lg(D^2*H)$	-4.7629	1.7222	/	Ma et al., 1989
122	Pinus tabuliformis	Stem wood	$ln(W)=a+b*ln(D)$	-2.577	2.238	/	Liu, 2010; Liu et al., 2001

123	Pinus tabuliformis	Stem bark	ln(W)=a+b*ln(D)	-1.973	1.501	/	Liu, 2010; Liu et al., 2001
124	Pinus tabuliformis	Total branch	ln(W)=a+b*ln(D)	-5.522	3.021	/	Liu, 2010; Liu et al., 2001
125	Pinus tabuliformis	Total leaf	ln(W)=a+b*ln(D)	-3.612	1.793	/	Liu, 2010; Liu et al., 2001
126	Pinus tabuliformis	Total belowground	ln(W)=a+b*ln(D)	-4.962	2.722	/	Liu, 2010; Liu et al., 2001
127	Pinus_tabuliformis	Stem wood	W=a*D^b	0.0192	2.5914	/	Li et al., 2007c
128	Pinus_tabuliformis	Stem bark	W=a*D^b	0.0293	1.8589	/	Li et al., 2007c
129	Pinus_tabuliformis	Total branch	W=a*D^b	0.003	3.3507	/	Li et al., 2007c
130	Pinus_tabuliformis	Total leaf	W=a*D^b	0.1486	1.6701	/	Li et al., 2007c
131	Pinus_tabuliformis	Fruit	W=a*D^b	0.0043	2.5844	/	Li et al., 2007c
132	Pinus_tabuliformis	Total aboveground	W=a*D^b	0.0716	2.5533	/	Li et al., 2007c
133	Pinus_tabuliformis	Total belowground	W=a*D^b	0.0649	1.9243	/	Li et al., 2007c
134	Populus_alba	Stem wood	W=a*D^b	0.0428	2.4494	/	Wu, 2009; Wu et al., 2009
135	Populus_alba	Stem bark	W=a*D^b	0.0155	2.303	/	Wu, 2009; Wu et al., 2009
136	Populus_alba	Total branch	W=a*D^b	0.0336	2.186	/	Wu, 2009; Wu et al., 2009
137	Populus_alba	Total leaf	W=a*D^b	0.0362	1.6803	/	Wu, 2009; Wu et al., 2009
138	Populus_alba	Total belowground	W=a*D^b	0.1098	1.6341	/	Wu, 2009; Wu et al., 2009

Table S3 Scoring Details for Assessing the Collected Data from Literatures across Eight Perspectives

Data Quality Score		2	1	0	Note
Data type (2)		A national scale datasets covering the individual point data from literatures (ND)	A regional scale datasets covering the individual point data from literatures (RD)	Individual point data (ID), self-sampling data	Data amount is determined by how many sampling sites can be used in our datasets, not the sampling sites presented in literatures. The data presented as an average value of more than one sampling results is regarded as one sampling site.
Data information (2)	**Sampling date (1)**	NA	Sampling date is given for purpose to study trends in time series.	Sampling date is not given, while it might be obtained in other circumstances	Even the sampling is not given in the literature, while it can be obtained in other datasets or contacting with authors. Otherwise, the sampling date will be year paper submitted.
	Publication (1)	NA	Data is published in a peer reviewed journal/datasets	Date is published in thesis, report or unpublished data and etc.	Data published in Chinese journal or datasets is also regarded as publish in a peer reviewed journal.
Climate information (2)	**Precipitation (1)**	NA	Annual precipitation in study area is given	Annual precipitation in study area is not given.	If the range is given, the average value is applied for the purpose of prediction model.
	Temperature (1)	NA	Annual temperature in study area is given	Annual temperature in study area is not given.	NA
Geographic information (2)	**Coordinates (1)**	NA	Coordinate for sampling sites is given.	None of the coordinate of sampling is given.	The range of coordinates is not considered. The average of maximum and minimum coordinates is only applied for the purpose of spatial distribution and mapping.

	Elevation (1)	NA	Elevation for sampling sites is given.	Elevation for sampling site is not given.	The range of elevation is not considered. The average of maximum and minimum elevation is noly applied for the purpose of prediction model
Soil property (2)	**Soil depth (1)**	NA	Soil profile is given with different soil layers in details.	Soil depth is not mentioned or not soil profile is not given in details.	NA
	Soil bulk density (1)	NA	Soil bulk density is given.	Soil bulk density is not given.	NA
Soil organic carbon (2)	**Soil OC content (1)**	NA	Soil organic carbon content is given.	Soil organic carbon content is not given.	NA
	Soil OC stock (1)	NA	Soil organic carbobn stock is given directly and indirectly.	Soil organic carbobn stock is not given neither directly nor indirectly.	All soil organic matters is converted carbon content by multipling 0.58 if the carbon concentration is not given.
Vegetation organic carbon (2)	**AGB/BGB carbon (1)**	NA	Aboveground or belowground biomass and carbon density is given.	Aboveground or belowground biomass and carbon density is not given.	The aboveground biomass included plant aboveground components, shrub and litter if it is applicable. Belowground biomass normally included root. Biomass is converted to carbon density by multipling 0.5 if the carbon concetration is not given.
	Total vegetation carbon (1)	NA	Vegetation biomass and carbon is given.	Vegetation biomass and carbon is not given.	Total vegetation included both aboveground and belowground parts of plants. Biomass is converted to carbon density by multipling 0.5 if the carbon concetration is not given.

Total Ecosystem organic carbon (2)	Total ecosystem organic carbon stock given or calculable	NA	Total ecosystem organic carbon stock not given or calculable	Total ecosystem OC stock is the sum of total vegetation carbon stock and soil organic carbon stock, or the sum of aboveground carbon stock, belowground carbon stock and soil organic carbon stock.

Table S4 Landslide Area-Volume Scaling Relationships in the Wenchuan Region

Landslide area-volume scaling relationships applicable to Wenchuan Region based on parameters with G from Guzzetti et al. (2009), L1, L2 and L3 from Larsen et al. (2010), P1 and P2 from Parker et al. (2011). Considering the separation of landslide scar area and deposit area, both methodologies by Marc et al. (2018b)and Li et al. (2014) are conducted to calculate the total volume of landslide inventory by Li et al. (2014).

Major rivers	Reference	Log_Alpha	Gamma	Total_Volume (km3)	Total_Volume Marc (km3)	Total_Volume Li (km3)
Minjiang	G	-1.131	1.45±0.009	2.01756±0.00532	0.47244±0.00208	1.20575±0.00318
Minjiang	L1	-0.836±0.015	1.332±0.005	1.14334±0.00158	0.29221±0.00061	0.71212±0.00098
Minjiang	L2	-0.73±0.06	1.35±0.01	1.78624±0.00675	0.45005±0.00263	1.10554±0.00418
Minjiang	L3	-0.59±0.03	1.36±0.01	2.71947±0.00788	0.68003±0.00307	1.67725±0.00486
Minjiang	P1	-0.974±0.366	1.388±0.087	3.27445±0.1896	0.76017±0.07423	2.0008±0.11586
Minjiang	P2	-0.995±0.366	1.392±0.087	3.2554±0.18987	0.75362±0.07434	1.98638±0.11586
Tuojiang	G	-1.131	1.45±0.009	1.36053±0.0155	0.28347±0.00162	0.81309±0.00926
Tuojiang	L1	-0.836±0.015	1.332±0.005	0.70336±0.00355	0.16668±0.00051	0.43808±0.00221
Tuojiang	L2	-0.73±0.06	1.35±0.01	1.11408±0.01506	0.25878±0.00218	0.68953±0.00932
Tuojiang	L3	-0.59±0.03	1.36±0.01	1.70877±0.01878	0.3927±0.00252	1.0539±0.01158
Tuojiang	P1	-0.974±0.366	1.388±0.087	2.25535±0.63751	0.45864±0.05628	1.3781±0.38955

Tuojiang	P2	-0.995±0.366	1.392±0.087	2.24999±0.64318	0.45545±0.05625	1.3729±0.39247
Fujiang	G	-1.131	1.45±0.009	1.29057±0.08884	0.28911±0.02191	0.77128±0.05309
Fujiang	L1	-0.836±0.015	1.332±0.005	0.55324±0.01644	0.13208±0.00457	0.34458±0.01024
Fujiang	L2	-0.73±0.06	1.35±0.01	0.89889±0.06978	0.21238±0.01937	0.55634±0.04319
Fujiang	L3	-0.59±0.03	1.36±0.01	1.39825±0.09152	0.32857±0.02475	0.86238±0.05644
Fujiang	P1	-0.974±0.366	1.388±0.087	2.31094±4.26822	0.507±0.9486	1.41206±2.6081
Fujiang	P2	-0.995±0.366	1.392±0.087	2.32432±4.33116	0.50874±0.95905	1.41825±2.64286
Bailongjiang	G	-1.131	1.45±0.009	0.01294±0.00018	0.00275±4e-05	0.00773±0.00011
Bailongjiang	L1	-0.836±0.015	1.332±0.005	0.00796±7e-05	0.00188±2e-05	0.00496±4e-05
Bailongjiang	L2	-0.73±0.06	1.35±0.01	0.01228±0.00028	0.00285±7e-05	0.0076±0.00018
Bailongjiang	L3	-0.59±0.03	1.36±0.01	0.01856±0.00032	0.00427±8e-05	0.01145±0.0002
Bailongjiang	P1	-0.974±0.366	1.388±0.087	0.02075±0.00615	0.00438±0.00125	0.01268±0.00376
Bailongjiang	P2	-0.995±0.366	1.392±0.087	0.02057±0.00613	0.00433±0.00124	0.01255±0.00374
Study Area	G	-1.131	1.45±0.009	4.71804±0.0949	1.0563±0.02373	2.81964±0.05672
Study Area	L1	-0.836±0.015	1.332±0.005	2.4185±0.01765	0.59475±0.00495	1.50633±0.011
Study Area	L2	-0.73±0.06	1.35±0.01	3.82994±0.07494	0.9276±0.02099	2.37044±0.04638
Study Area	L3	-0.59±0.03	1.36±0.01	5.87483±0.0981	1.41144±0.02681	3.62334±0.06051
Study Area	P1	-0.974±0.366	1.388±0.087	7.93389±4.55845	1.74754±1.03086	4.84788±2.78545

Study Area	P2	-0.995±0.366	1.392±0.087	7.92384±4.62566	1.73983±1.04234	4.83496±2.82257

Table S5 OC Data Collected from the Literatures
This table aims to serve as a foundational and comprehensive references for further researches conducted along Longmen Shan fault or Tibetan plateau, and it is accessible in supporting materials.

ID	Plot_Site	Plot_Time	Plot_Elevation	Plot_Slope	Plot_Aspect	Climate_MAT	Climate_MAP	Soil_pH	Soil_Depth	Soil_BD	Soil_OC	Soil_OCS	Soil_C/N	Soil_N	Forest_Type	Tree_DBH	Vegetation_Carbon	AGBC	BGBC	Total
1	Banruosi, Dujiangyan	2007	703.05	20.00	Partially shaded slope/65	15.2	1225	5.5-6	0-10	1.12	37.49	75.70	1.25		evergreen broadleaf forest					NA
2	Banruosi, Dujiangyan	2007	703.05	20.00	Partially shaded slope/65	15.2	1225	5.5-6	10-20	1.44	9.67	25.00	1.11		evergreen broadleaf forest					NA
3	Banruosi, Dujiangyan	2007	703.05	20.00	Partially shaded slope/65	15.2	1225	5.5-6	20-40	1.52	7.43	20.30	1.08		evergreen broadleaf forest					NA
4	Banruosi, Dujiangyan	2007	703.05	20.00	Partially shaded slope/65	15.2	1225	5.5-6	40-60	1.57	7.41	19.70	1.04		evergreen broadleaf forest					NA
5	Banruosi, Dujiangyan	2007	703.05	20.00	Partially shaded	15.2	1225	5.5-6	60-80	1.64	6.67	19.60	0.94		evergreen broadleaf forest					NA

					slope/65										
6	Banruosi, Dujiangyan	2007	703.05	20.00	Partially shaded slope/65	15.2	1225	5.5-6	0-80	1.50	11.27	160.30	1.11	evergreen broadleaf forest	NA
7	Banruosi, Dujiangyan	2007	812.34	16.00	Sunny slope/180	15.2	1225	5.5-6	0-10	1.07	49.98	45.30	2.96	Secondary evergreen broadleaf forest	NA
8	Banruosi, Dujiangyan	2007	812.34	16.00	Sunny slope/180	15.2	1225	5.5-6	10-20	1.22	24.04	24.90	1.75	Secondary evergreen broadleaf forest	NA
9	Banruosi, Dujiangyan	2007	812.34	16.00	Sunny slope/180	15.2	1225	5.5-6	20-40	1.24	15.79	33.30	1.26	Secondary evergreen broadleaf forest	NA
10	Banruosi, Dujiangyan	2007	812.34	16.00	Sunny slope/180	15.2	1225	5.5-6	40-60	1.39	7.59	17.90	0.74	Secondary evergreen broadleaf forest	NA
11	Banruosi, Dujiangyan	2007	812.34	16.00	Sunny slope/180	15.2	1225	5.5-6	60-80	1.46	6.77	17.50	0.86	Secondary evergreen broadleaf forest	NA
12	Banruosi, Dujiangyan	2007	812.34	16.00	Sunny slope/180	15.2	1225	5.5-6	0-80	1.31	16.79	138.90	1.46	Secondary evergreen broadleaf forest	NA
13	Banruosi, Dujiangyan	2007	759.97	23.00	Partially sunny slope/120	15.2	1225	5.5-6	0-10	1.16	17.39	17.10	1.25	Secondary evergreen broadleaf forest	NA
14	Banruosi, Dujiangyan	2007	759.97	23.00	Partially sunny slope/120	15.2	1225	5.5-6	11-20	1.27	9.52	10.20	0.85	Secondary evergreen broadleaf forest	NA

No	Location	Year			Habitat									Forest type		
15	Banruosi, Dujiangyan	2007	759.97	23.00	Partially sunny slope/120	15.2	1225	5.5-6	21-40	1.39	5.35	12.60	0.59	Secondary evergreen broadleaf forest		NA
16	Banruosi, Dujiangyan	2007	759.97	23.00	Partially sunny slope/120	15.2	1225	5.5-6	41-60	1.45	5.26	12.30	0.68	Secondary evergreen broadleaf forest		NA
17	Banruosi, Dujiangyan	2007	759.97	23.00	Partially sunny slope/120	15.2	1225	5.5-6	61-80	1.52	3.87	9.80	0.52	Secondary evergreen broadleaf forest		NA
18	Banruosi, Dujiangyan	2007	759.97	23.00	Partially sunny slope/120	15.2	1225	5.5-6	0-80	1.39	6.98	62.00	0.76	Secondary evergreen broadleaf forest		NA
19	Kuanba forest region in Longmen mountain, Pingwu County	2006	1400.00	20-25		11	1187	4.8±0.09	0-10	1.00	112.59	28.15	3.93	mixed evergreen broad-leaved natural forest		NA
20	Kuanba forest region in Longmen mountain, Pingwu County	2006	1400.00	20-25		11	1187	4.9±0.1	0-10	0.90	77.72	27.66	2.86	natural regenerated forest	3.2-6.9	NA
21	Kuanba forest region in Longmen mountain, Pingwu County	2006	1400.00	20-25		11	1187	4.8±0.09	10-20	1.21	49.76	21.14	2.34	mixed evergreen broad-leaved natural forest		NA
22	Kuanba forest region in Longmen mountain, Pingwu County	2006	1400.00	20-25		11	1187	5.1±0.1	10-20	1.10	33.45	20.96	1.63	natural regenerated forest	3.2-6.9	NA
23	Kuanba forest region in Longmen mountain, Pingwu County	2006	1400.00	20-25		11	1187	4.8±0.05	20-30	1.23	32.65	19.26	1.68	mixed evergreen broad-leaved natural forest		NA

#	Location	Year											Forest type			
24	Kuanba forest region in Longmen mountain, Pingwu County	20 06	140 0.00	20-25	11	118 7	5.1 ±0.09	20-30	1.21	26.87	20.39	1.33	natural regenerated forest	3.2-6.9		N A
25	Kuanba forest region in Longmen mountain, Pingwu County	20 06	140 0.00	20-25	11	118 7	4.9 ±0.07	30-50	1.20	24.64	17.57	1.36	mixed evergreen broad-leaved natural forest			N A
26	Kuanba forest region in Longmen mountain, Pingwu County	20 06	140 0.00	20-25	11	118 7	5.2 ±0.07	30-50	1.21	19.80	17.59	1.09	natural regenerated forest	3.2-6.9		N A
27	Kuanba forest region in Longmen mountain, Pingwu County	20 06	140 0.00	20-25	11	118 7	4.84± 0.034	0-50	1.17	48.86	22.89	2.13	mixed evergreen broad-leaved natural forest			N A
28	Kuanba forest region in Longmen mountain, Pingwu County	20 06	140 0.00	20-25	11	118 7	5.10± 0.039	0-50	1.13	35.53	22.21	1.60	natural regenerated forest	3.2-6.9		N A
29	Eastern Slope of Gongga Mountain	19 99	365 0.00		2.1	965	5.48	30-50					evergreen broad-leaved+deciduous broad-leaved+coniferous forest	97.40	279.819	N A
30	Eastern Slope of Gongga Mountain	19 99	358 0.00		2.5	172 0	5.50	30-50					evergreen broad-leaved+deciduous broad-leaved+coniferous forest	42.11	282.558	N A
31	Eastern Slope of Gongga Mountain	19 99	315 0.00		3	188 1	5.80	30-50					evergreen broad-leaved+deciduous broad-leaved+coniferous forest	68.35	544.519	N A
32	Eastern Slope of Gongga Mountain	19 99	304 0.00		3.9	198 8	4.70	30-50					evergreen broad-leaved+deciduous broad-	60.53	351.844	N A

leaved+coniferous forest

33	Eastern Slope of Gongga Mountain	1999	2920.00			4.3	1898	5.00	30-50				evergreen broad-leaved+deciduous broad-leaved+coniferous forest	64.24	425.863			NA
34	Eastern Slope of Gongga Mountain	1999	2780.00			5.4	1874	5.80	30-50				evergreen broad-leaved+deciduous broad-leaved+coniferous forest	87.05	568.008			NA
35	Eastern Slope of Gongga Mountain	1999	2570.00			6.2	1620	5.60	30-50				evergreen broad-leaved+deciduous broad-leaved+coniferous forest	76.14	367.225			NA
36	Eastern Slope of Gongga Mountain	1999	2200.00			9.5	1346	5.90	30-50				evergreen broad-leaved+deciduous broad-leaved forest	73.15	220.082			NA
37	Wanglang National Nature Reserve, Pingwu County	2008	2730.00	42.00	SE10	1.7±0.7	801-825	6.5±0.9	0-20	0.45	43.10	42.01	herb community		7.37	5.67	1.7	49.338
38	Wanglang National Nature Reserve, Pingwu County	2008	2680.00	30.00	SE10	1.7±0.7	801-825	6.5±0.9	0-20	0.45	46.35	62.57	willow shrub		34.87	26.54	8.33	97.44
39	Wanglang National Nature Reserve, Pingwu County	2008	2605.00	40.00	SE30	1.7±0.7	801-825	6.5±0.9	0-20	0.45	46.42	76.64	Secondary birch forest	12.40	73.74	62.54	11.2	150.38
40	Wanglang National Nature Reserve, Pingwu County	2008	2704.00	38.00	EN35	1.7±0.7	801-825	6.5±0.9	0-20	0.45	73.35	101.75	Secondary mixed forest	22.50	119.9	10.93	18.97	221.

#	Location																		
																			655
41	Wanglang National Nature Reserve, Pingwu County	2008	2854.00	4.00	EN35	1.7±0.7	801-825	6.5±0.9	0-20	0.45	65.43	85.94		Secondary fir forest	28.30	430.86	367.12	63.74	516.80
42	Wanglang National Nature Reserve, Pingwu County	2008	2730.00	42.00	SE10	1.7±0.7	801-825	6.5±0.9	20-40	0.45	20.48	38.41		herb community		7.37	5.67	1.7	45.78
43	Wanglang National Nature Reserve, Pingwu County	2008	2680.00	30.00	SE10	1.7±0.7	801-825	6.5±0.9	20-40	0.45	22.71	50.78		willow shrub		34.87	26.54	8.33	85.65
44	Wanglang National Nature Reserve, Pingwu County	2008	2605.00	40.00	SE30	1.7±0.7	801-825	6.5±0.9	20-40	0.45	29.01	63.20		Secondary birch forest	12.40	73.74	62.54	11.2	136.94
45	Wanglang National Nature Reserve, Pingwu County	2008	2704.00	38.00	EN35	1.7±0.7	801-825	6.5±0.9	20-40	0.45	42.29	73.47		Secondary mixed forest	22.50	119.9	100.93	18.97	193.37
46	Wanglang National Nature Reserve, Pingwu County	2008	2854.00	4.00	EN35	1.7±0.7	801-825	6.5±0.9	20-40	0.45	31.64	47.07		Secondary fir forest	28.30	430.86	367.12	63.74	477.93
47	Wanglang National Nature Reserve, Pingwu County	2008	2730.00	42.00	SE10	1.7±0.7	801-825	6.5±0.9	40-60	0.45	4.34	13.62		herb community		7.37	5.67	1.7	20.99

No.	Location	Year												Vegetation					
48	Wanglang National Nature Reserve, Pingwu County	2008	2680.00	30.00	SE10	1.7±0.7	801-825	6.5±0.9	40-60	0.45	5.72	19.07		willow shrub		34.87	26.54	8.33	53.94
49	Wanglang National Nature Reserve, Pingwu County	2008	2605.00	40.00	SE30	1.7±0.7	801-825	6.5±0.9	40-60	0.45	7.55	26.05		Secondary birch forest	12.40	73.74	62.54	11.2	99.79
50	Wanglang National Nature Reserve, Pingwu County	2008	2704.00	38.00	EN35	1.7±0.7	801-825	6.5±0.9	40-60	0.45	25.31	46.99		Secondary mixed forest	22.50	119.9	100.93	18.97	166.89
51	Wanglang National Nature Reserve, Pingwu County	2008	2854.00	4.00	EN35	1.7±0.7	801-825	6.5±0.9	40-60	0.45	21.09	33.65		Secondary fir forest	28.30	430.86	367.12	63.74	464.51
52	Wanglang National Nature Reserve, Pingwu County	2008	2730.00	42.00	SE10	1.7±0.7	801-825	6.5±0.9	0-60	0.45	15.63	94.04	6.00	herb community		7.37	5.67	1.7	101.41
53	Wanglang National Nature Reserve, Pingwu County	2008	2680.00	30.00	SE10	1.7±0.7	801-825	6.5±0.9	0-60	0.45	19.22	132.43	6.00	willow shrub		34.87	26.54	8.33	167.30
54	Wanglang National Nature Reserve, Pingwu County	2008	2605.00	40.00	SE30	1.7±0.7	801-825	6.5±0.9	0-60	0.45	22.64	165.89	6.00	Secondary birch forest	12.40	73.74	62.54	11.2	239.63
55	Wanglang National Nature Reserve, Pingwu County	2008	2704.00	38.00	EN35	1.7±0.7	801-825	6.5±0.9	0-60	0.45	44.52	222.20		Secondary mixed forest	22.50	119.9	100.93	18.97	342.2

																			10
56	Wanglang National Nature Reserve, Pingwu County	2008	2854.00	4.00	EN35	1.7±0.7	801-825	6.5±0.9	0-60	0.45	37.71	166.65	6.00	Secondary fir forest	28.30	430.86	367.12	63.74	597.51
57	Wanglang National Nature Reserve, Pingwu County	2008	2840.00	25.00	EN15	1.7±0.7	801-825	6.5±0.9	0-60	0.45	38.88	170.58	6.00	Secondary spruce forest	35.80	535.37	463.18	72.19	705.95
58	Wanglang National Nature Reserve, Pingwu County	2008	3350.00			1.7±0.7	801-825	6.5±0.9	0-60	0.45	30.00	153.36	6.00	Secondary cypress forest	21.50	82.07	67.12	14.95	235.43
59	Wanglang National Nature Reserve, Pingwu County	2008	2840.00	25.00	EN15	1.7±0.7	801-825	6.5±0.9	0-20	0.45	65.44	84.16		Secondary spruce forest	35.80	535.37	463.18	72.19	619.53
60	Wanglang National Nature Reserve, Pingwu County	2008	3350.00			1.7±0.7	801-825	6.5±0.9	0-20	0.45	47.55	65.98		Secondary cypress forest	21.50	82.07	67.12	14.95	148.05
61	Wanglang National Nature Reserve, Pingwu County	2008	2840.00	25.00	EN15	1.7±0.7	801-825	6.5±0.9	20-40	0.45	34.82	51.79		Secondary spruce forest	35.80	535.37	463.18	72.19	587.16
62	Wanglang National Nature Reserve, Pingwu County	2008	3350.00			1.7±0.7	801-825	6.5±0.9	20-40	0.45	24.63	52.07		Secondary cypress forest	21.50	82.07	67.12	14.95	134.

																			14
63	Wanglang National Nature Reserve, Pingwu County	2008	2840.00	25.00	EN15	1.7±0.7	801-825	6.5±0.9	40-60	0.45	21.75	34.62		Secondary spruce forest	35.80	535.37	463.18	72.19	569.99
64	Wanglang National Nature Reserve, Pingwu County	2008	3350.00			1.7±0.7	801-825	6.5±0.9	40-60	0.45	24.63	35.32		Secondary cypress forest	21.50	82.07	67.12	14.95	117.39
65	Miyaluo Forest Region, Li County	2003-2005	2813-3608	35.00		6.1	864		0-80			254.10		Natural secondary birch forest		77.8			331.90
66	Miyaluo Forest Region, Li County	2003-2005	2950-3552	36.67		6.1	864		0-80			248.10		Natural secondary fir and birch mixed forest		110.9			359.00
67	Miyaluo Forest Region, Li County	2003-2005	2890-3598	31.67		6.1	864		0-80			256.40		Natural old growth forest		376.6			633.00
68	Miyaluo Forest Region, Li County	2003-2005	2813-3608	35.00		6.1	864		0-10			62.38		Natural secondary birch forest		77.8			140.18
69	Miyaluo Forest Region, Li County	2003-	2813-3608	35.00		6.2	865		10-20			60.82		Natural secondary birch forest		77.8			138.

70	Miyaluo Forest Region, Li County	20 05						6 2
70	Miyaluo Forest Region, Li County	20 03 - 20 05	281 3- 360 8	35. 00	6.3	866	20- 30	56 .1 9	Natural secondary birch forest	77.8	1 3 3. 9 9
71	Miyaluo Forest Region, Li County	20 03 - 20 05	281 3- 360 8	35. 00	6.4	867	30- 40	32 .0 8	Natural secondary birch forest	77.8	1 0 9. 8 8
72	Miyaluo Forest Region, Li County	20 03 - 20 05	281 3- 360 8	35. 00	6.5	868	40- 60	24 .8 5	Natural secondary birch forest	77.8	1 0 2. 6 5
73	Miyaluo Forest Region, Li County	20 03 - 20 05	281 3- 360 8	35. 00	6.6	869	60- 80	17 .7 8	Natural secondary birch forest	77.8	9 5. 5 8
74	Miyaluo Forest Region, Li County	20 03 - 20 05	295 0- 355 2	36. 67	6.1	864	0- 10	76 .9 9	Natural secondary fir and birch mixed forest	110.9	1 8 7. 8 9
75	Miyaluo Forest Region, Li County	20 03 - 20 05	295 0- 355 2	36. 67	6.2	865	10- 20	51 .5 2	Natural secondary fir and birch mixed forest	110.9	1 6 2. 4 2
76	Miyaluo Forest Region, Li County	20 03 -	295 0- 355 2	36. 67	6.3	866	20- 30	44 .6 7	Natural secondary fir and birch mixed forest	110.9	1 5 5.

		20 05									5 7
77	Miyaluo Forest Region, Li County	20 03 - 20 05	295 0- 355 2	36. 67	6.4	867	30- 40	32 .4 3	Natural secondary fir and birch mixed forest	110.9	1 4 3. 3 3
78	Miyaluo Forest Region, Li County	20 03 - 20 05	295 0- 355 2	36. 67	6.5	868	40- 60	23 .9 1	Natural secondary fir and birch mixed forest	110.9	1 3 4. 8 1
79	Miyaluo Forest Region, Li County	20 03 - 20 05	295 0- 355 2	36. 67	6.6	869	60- 80	18 .5 8	Natural secondary fir and birch mixed forest	110.9	1 2 9. 4 4 8
80	Miyaluo Forest Region, Li County	20 03 - 20 05	289 0- 359 8	31. 67	6.1	864	0- 10	70 .9 4	Natural old growth forest	376.6	4 4 7. 5 4
81	Miyaluo Forest Region, Li County	20 03 - 20 05	289 0- 359 8	31. 67	6.2	865	10- 20	55 .2 8	Natural old growth forest	376.6	4 3 1. 8 8
82	Miyaluo Forest Region, Li County	20 03 - 20 05	289 0- 359 8	31. 67	6.3	866	20- 30	44 .7 1	Natural old growth forest	376.6	4 2 1. 3 1
83	Miyaluo Forest Region, Li County	20 03 -	289 0- 359 8	31. 67	6.4	867	30- 40	20 .4 1	Natural old growth forest	376.6	3 9 7.

No.	Location	Year								Forest type					
		20 05													0 1
84	Miyaluo Forest Region, Li County	2003 - 2005	2890- 3598	31. 67	6.5	868	40- 60		34 .5 0	Natural old growth forest		376.6			4 1 1. 1 0
85	Miyaluo Forest Region, Li County	2003 - 2005	2890- 3598	31. 67	6.6	869	60- 80		30 .5 7	Natural old growth forest		376.6			4 0 7. 1 7
86	Songpan+Jiuzhai+Heishui	20 06	2400- 3500		5.8- 9.1	556. 6- 836. 8	0- 20	26 .9 0	55 .0 4	Alpine coniferous forest	18. 92 ±4. 17	127.0 5	11 3.1 7	13. 88	1 8 2. 0 9
87	Songpan+Jiuzhai+Heishui	20 06	2400- 3500		5.8- 9.1	556. 6- 836. 8	20- 40	14 .7 0	31 .4 1	Alpine coniferous forest	18. 92 ±4. 17	127.0 5	11 3.1 7	13. 88	1 5 8. 4 6
88	Songpan+Jiuzhai+Heishui	20 06	2400- 3500		5.8- 9.1	556. 6- 836. 8	40- 60	11 .2 0	26 .3 2	Alpine coniferous forest	18. 92 ±4. 17	127.0 5	11 3.1 7	13. 88	1 5 3. 3 7
89	Songpan+Jiuzhai+Heishui	20 06	2400- 3500		5.8- 9.1	556. 6- 836. 8	60- 80	9. 40	22 .6 8	Alpine coniferous forest	18. 92 ±4. 17	127.0 5	11 3.1 7	13. 88	1 4 9. 9 7 3
90	Songpan+Jiuzhai+Heishui	20 06	2400- 3500		5.8- 9.1	556. 6- 836. 8	80- 10 0	8. 30	20 .6 6	Alpine coniferous forest	18. 92 ±4. 17	127.0 5	11 3.1 7	13. 88	1 4 7.

No	Location	Year	Elevation		Direction				Depth					Vegetation					
																			71
91	Songpan+Jiuzhai+Heishui	2006	2400-3500			5.8-9.1	556.6-836.8		0-100	14.10	156.11			Alpine coniferous forest	18.92±4.17	127.05	113.17	13.88	283.16
92	Lingyan Mountain, Sichuan	2006	919.9-930.9			15.2	1243	4.5-5.5	0-100	11.21	150.40	8.37		Secondary broadleaf and conifer mixed forests					NA
93	Lingyan Mountain, Sichuan	2006	919.9-930.10			15.2	1243	4.5-5.5	0-20	17.21	47.40	8.88		Secondary broadleaf and conifer mixed forests					NA
94	Lingyan Mountain, Sichuan	2006	919.9-930.11			15.2	1243	4.5-5.5	20-40	10.98	30.60	7.40		Secondary broadleaf and conifer mixed forests					NA
95	Lingyan Mountain, Sichuan	2006	919.9-930.12			15.2	1243	4.5-5.5	40-60	9.97	26.30	7.64		Secondary broadleaf and conifer mixed forests					NA
96	Lingyan Mountain, Sichuan	2006	919.9-930.13			15.2	1243	4.5-5.5	60-80	9.15	23.40	8.58		Secondary broadleaf and conifer mixed forests					NA
97	Lingyan Mountain, Sichuan	2006	919.9-930.14			15.2	1243	4.5-5.5	80-100	8.76	22.70	9.36		Secondary broadleaf and conifer mixed forests					NA
98	West of Lonmen mountain, Yingxiu	2007	2730.00	20.00	N17°W	15.2	1225		0-100	27.39	212.45	10.87	2.52	Deciduous broadleaf forests					NA

167

99	West of Lonmen mountain, Yingxiu	20 07	237 0.00	35. 00	S35°W	15.2	122 5	0-10 0	22 .6 2	16 4. 37	10 .9 8	2. 0 6	Broadleaf and conifer mixed forests			N A
100	West of Lonmen mountain, Yingxiu	20 07	286 5.00	15. 00	N15° W	15.2	122 5	0-10 0	34 .6 0	27 1. 50	11 .6 1	2. 9 8	Coniferous forests			N A
101	West of Lonmen mountain, Yingxiu	20 07	239 7.00	35. 00	S10°W	15.2	122 5	0-10 0	31 .5 8	18 8. 04	12 .5 8	2. 5 1	Coniferous forests			N A
102	West of Lonmen mountain, Yingxiu	20 07	288 8.00	34. 00	S30°W	15.2	122 5	0-10 0	41 .3 0	22 0. 40	12 .8 7	3. 2 1	Coniferous forests			N A
103	West of Lonmen mountain, Yingxiu	20 07	711. 00	23. 00	S30°E	15.2	122 5	0-10 0	8. 40	75 .7 5	10 .7 7	0. 7 8	Deciduous broadleaf forests			N A
104	West of Lonmen mountain, Yingxiu	20 07	759. 00	20. 00	N25°E	15.2	122 5	0-10 0	14 .9 3	13 4. 39	13 .8 2	1. 0 8	Evergreen broadleaf forests			N A
105	West of Lonmen mountain, Yingxiu	20 07	812. 00	16. 00	S0°W	15.2	122 5	0-10 0	21 .4 4	17 2. 55	14 .2 0	1. 5 1	Deciduous broadleaf forests			N A
106	West of Lonmen mountain, Yingxiu	20 07	288 0.00	24. 00	N48°E	15.2	122 5	0-10 0	28 .8 8	27 0. 63	10 .2 4	2. 8 2	Shrub			N A
107	Minshan Mountain	20 03	232 0- 250 0	20- 52		10	864						Secondary Quercus forest	35. 50	488.4 9	N A
108	Jiangyou	20 11	610. 00	12. 00		16	114 3.4	0-10 0	2. 74	42 .7 9			Forest		22.13	6 4. 9 2
109	Jiangyou	20 11	610. 00	12. 00		16	114 3.4	0-20	4. 32	14 .2 9			Forest		22.13	3 6. 4 2

110	Jiangyou	20 11	610. 00	12. 00		16	114 3.4	20- 40	2. 42	8. 12	Forest	22.13	3 0. 2 5
111	Jiangyou	20 11	610. 00	12. 00		16	114 3.4	40- 60	2. 33	7. 89	Forest	22.13	3 0. 0 2
112	Jiangyou	20 11	610. 00	12. 00		16	114 3.4	60- 10 0	1. 87	12 .5 0	Forest	22.13	3 4. 6 3
113		20 04	292 0.00			8.4	861. 8				Shrub		15. 25 09 5	NA
114		20 05	175 0.00	36. 00	NW23	11	500				Shrub		7.5 00 81 6	NA
115		20 05	195 7.00	47. 00	NW24	11	500				Shrub		15. 08 00 26 5	NA
116		20 05	216 5.00	44. 00	NW25	11	500				Shrub		18. 12 39 79 5	NA
117		20 05	178 1.00	31. 00	SE29	11	500				Shrub		5.1 26 78 25	NA
118		20 05	198 5.00	46. 00	SE30	11	500				Shrub		6.1 17	NA

119		20 05	220 0.00	28. 00	SE31	11	500					Shrub		8.8 23 19 5		N A
120	Qingchuan	20 08				13.7	102 1.7					Shrub	5.493 7899	4.6 64 59 96 5	0.8 29 19 02 5	N A
121	Li	20 08				8.95	825					Shrub	4.541 0845 5	3.6 82 92 06	0.8 58 16 39 5	N A
122	Beichuan	20 08				15.6	139 9.1					Shrub	4.950 3208 5	4.3 02 65 38 5	0.6 47 66 7	N A
123	Pingwu	20 08				14.7	866. 5					Shrub	7.854 7963 5	6.5 24 77 05	1.3 30 02 58 5	N A
124	LI	20 07	160 5.00	36. 00	North-facing	10.5	550	8.5 0	0- 20	17 .6 0	1. 3 0	Shrub		1.6 68 75	10. 99 4	N A
125	LI	20 07	162 6.00	32. 00	South-facing	10.5	550	7.6 0	0- 20	17 .6 8	1. 5 7	Shrub		2.7 18 75	13. 42 2	N A
126	LI	20 07	184 0.00	30. 00	South-facing	10.5	550	7.5 0	0- 20	32 .3 6	2. 3 4	Shrub		1.0 12 5	19. 31 16 3	N A

127	LI	20 07	1842.00	35.00	North-facing	10.6	550	8.00	0-20	14.89	1.20	Shrub	1.06875	15.596	NA
128	Mao	20 07	1685.00	30.00	North-facing	10.7	550	8.20	0-20	14.77	1.11	Shrub	1.25625	3.23721	NA
129	Mao	20 07	1688.00	35.00	South-facing	10.8	550	8.30	0-20	19.07	2.32	Shrub	1.3125	13.84186	NA
130	Mao	20 07	1600.00	30.00	South-facing	10.9	550	7.60	0-20	48.51	3.31	Shrub	1.39688	17.714	NA
131	Mao	20 07	1618.00	38.00	North-facing	10.10	550	7.50	0-20	36.53	2.46	Shrub	1.59375	16.52093	NA
132		20 10	3085.00	23.00	SE13°	7.5	400-600		10	15.18		Forest			NA
133		20 10	3085.00	23.00	SE13°	7.5	400-600		0-10	39.04		Forest			NA
134		20 10	3085.00	23.00	SE13°	7.5	400-600		10-20	17.13		Forest			NA
135		20 10	3085.00	23.00	SE13°	7.5	400-600		20-30	12.33		Forest			NA
136		20 10	3085.00	23.00	SE13°	7.5	400-600		30-40	10.28		Forest			NA
137		20 10	3085.00	23.00	SE13°	7.5	400-600		40-60	9.94		Forest			NA
138		20 10	3085.00	23.00	SE13°	7.5	400-600		60-80	8.89		Forest			NA

139	20 10	308 5.00	23. 00	SE13°	7.5	400-600	80-10 0	8. 65	Forest	N A
140	20 10	275 4.00	20. 00	SE7°	7.5	400-600	10 0	20 .7 7	Forest	N A
141	20 10	275 4.00	20. 00	SE7°	7.5	400-600	0-10	52 .7 6	Forest	N A
142	20 10	275 4.00	20. 00	SE7°	7.5	400-600	10-20	33 .2 7	Forest	N A
143	20 10	275 4.00	20. 00	SE7°	7.5	400-600	20-30	15 .9 4	Forest	N A
144	20 10	275 4.00	20. 00	SE7°	7.5	400-600	30-40	9. 90	Forest	N A
145	20 10	275 4.00	20. 00	SE7°	7.5	400-600	40-60	11 .5 5	Forest	N A
146	20 10	275 4.00	20. 00	SE7°	7.5	400-600	60-80	11 .1 0	Forest	N A
147	20 10	275 4.00	20. 00	SE7°	7.5	400-600	80-10 0	10 .8 6	Forest	N A
148	20 10	261 9.00	22. 00	SE12°	7.5	400-600	10 0	17 .8 4	Shrub	N A
149	20 10	261 9.00	22. 00	SE12°	7.5	400-600	0-10	17 .6 5	Shrub	N A
150	20 10	261 9.00	22. 00	SE12°	7.5	400-600	10-20	24 .4 2	Shrub	N A

151		20 10	261 9.00	22. 00	SE12°	7.5	400- 600	20- 30	22 .4 1		Shrub	N A
152		20 10	261 9.00	22. 00	SE12°	7.5	400- 600	30- 40	20 .5 0		Shrub	N A
153		20 10	261 9.00	22. 00	SE12°	7.5	400- 600	40- 60	14 .4 4		Shrub	N A
154		20 10	261 9.00	22. 00	SE12°	7.5	400- 600	60- 80	12 .7 6		Shrub	N A
155		20 10	261 9.00	22. 00	SE12°	7.5	400- 600	80- 10 0	12 .6 8		Shrub	N A
156	Jiangyou	20 09	223 8.00	20. 00	N	11	500	0- 60	17 .5 2	10 4. 15	Secondary forest	N A
157	Jiangyou	20 09	223 8.00	20. 00	N	11	500	0- 20	27 .6 9	49 .2 2	Secondary forest	N A
158	Jiangyou	20 09	223 8.00	20. 00	N	11	500	20- 40	14 .5 2	31 .6 8	Secondary forest	N A
159	Jiangyou	20 09	223 8.00	20. 00	N	11	500	40- 60	10 .3 4	23 .2 5	Secondary forest	N A
160	Jiangyou	20 09	240 7.00	25. 00	NE38°	11	500	0- 60	17 .0 6	10 0. 84	Shrub	N A
161	Jiangyou	20 09	240 7.00	25. 00	NE38°	11	500	0- 20	26 .9 9	48 .9 7	Shrub	N A
162	Jiangyou	20 09	240 7.00	25. 00	NE38°	11	500	20- 40	13 .0 8	27 .6 7	Shrub	N A

163	Jiangyou	20 09	240 7.00	25. 00	NE38°	11	500	40-60	11 .1 1	24 .0 2	Shrub				N A
164	Jiangyou	20 09	220 0.00	20. 00	N	11	500	0-60	15 .5 2	97 .3 5	Shrub				N A
165	Jiangyou	20 09	220 0.00	20. 00	N	11	500	0-20	23 .0 5	46 .1 8	Shrub				N A
166	Jiangyou	20 09	220 0.00	20. 00	N	11	500	20-40	13 .6 8	28 .8 2	Shrub				N A
167	Jiangyou	20 09	220 0.00	20. 00	N	11	500	40-60	9. 82	22 .3 6	Shrub				N A
168	Tibetan Alpine Vegetation Transects (TAVT)	19 99 - 20 00	456 0.00			8.84 2	673. 472				Natural Shrub	9.395	3.7 5	5.6 45	N A
169	Tibetan Alpine Vegetation Transects (TAVT)	19 99 - 20 00	378 0.00			8.06 4	440. 783				Natural Shrub	12.20 5	4.7 65	7.4 4	N A
170	Tibetan Alpine Vegetation Transects (TAVT)	19 99 - 20 00	465 2.00			8.79 2	393. 694				Natural Shrub-Meadow	8.955	4.6 45	4.3 1	N A
171	Tibetan Alpine Vegetation Transects (TAVT)	19 99 - 20 00	407 3.00			8.84 2	673. 472				Primary Forest	81.20 5	70. 89	10. 31 5	N A

172	Tibetan Alpine Vegetation Transects (TAVT)	1999-2000	4450.00	8.842	673.472	Primary Forest	76.845	63.54	13.305	NA
173	Tibetan Alpine Vegetation Transects (TAVT)	1999-2000	3050.00	7.182	830.5	Primary Forest	99.195	81.455	17.74	NA
174	Tibetan Alpine Vegetation Transects (TAVT)	1999-2000	2200.00	7.182	830.5	Primary Forest	221.865	174.315	47.55	NA
175	Tibetan Alpine Vegetation Transects (TAVT)	1999-2000	3100.00	8.842	673.472	Primary Forest	55.79	41.52	14.27	NA
176	Tibetan Alpine Vegetation Transects (TAVT)	1999-2000	1900.00	7.182	830.5	Primary Forest	116.325	82.6	33.725	NA
177	Tibetan Alpine Vegetation Transects (TAVT)	1999-2000	3620.00	-0.397	720.422	Primary Forest	25.945	16.95	8.995	NA
178	Tibetan Alpine Vegetation Transects (TAVT)	1999-2000	3080.00	8.842	673.472	Primary Forest	64.07	37.94	26.13	NA

179	Tibetan Alpine Vegetation Transects (TAVT)	1999-2000	3780.00	8.842	673.472			Primary Forest	508.69	497.99	10.7	NA
180	Tibetan Alpine Vegetation Transects (TAVT)	1999-2000	3700.00	7.182	830.5			Primary Forest	124.605	121.115	3.49	NA
181	Tibetan Alpine Vegetation Transects (TAVT)	1999-2000	3800.00	8.842	673.472			Primary Forest	445.2	420.71	24.49	NA
182	Tibetan Alpine Vegetation Transects (TAVT)	1999-2000	3000.00	7.182	830.5			Primary Forest	196.605	184.7	11.905	NA
183	Tibetan Alpine Vegetation Transects (TAVT)	1999-2000	2850.00	7.182	830.5			Primary Forest	258.62	240.8805	17.815	NA
184	Nyingchi + Qamdo	2011-2012	2900-3100	10.3±1.6	769.4±85.2	92.70	5.74	montane forest	68.55±17.39	259.73		NA
185	Nyingchi + Qamdo	2011-2012	3100-3300	9.25±0.7	499.7±56.8	58.70	4.66	montane forest	35.18±9.09	202.883434		NA

No.	Location	Year																	
186	Nyingchi + Qamdo	2011 - 2012	3300-3500		9.4±1.2	449.5±36.0				83.90		4.37	montane forest	34.32±6.85	177.8905472			NA
187	Nyingchi + Qamdo	2011 - 2012	3500-3700		7.86±1.4	451.1±26.7				54.60		3.46	montane forest	34.59±17.1	170.5396981			NA
188	Nyingchi + Qamdo	2011 - 2012	3700-3900		6.4±1.5	449.2±26.3				81.60		4.96	montane forest	35.89±20.7	167.1093019			NA
189	Nyingchi + Qamdo	2011 - 2012	3900-4100		5.5±2.6	409.9±24.6				71.70		4.58	montane forest	33.59±11.71	135.7456792			NA
190	Nyingchi + Qamdo	2011 - 2012	4100-4400		1.4±0.8	331.9±26.7				43.50		2.67	montane forest	28.14±1.81	86.7400188 7			NA
191	Tibet Nyingchi Alpine Forest Ecosystem National Field Scientific Observation Research Station, Nyingchi	2006	3850.00		-0.73	1134.1	5.10	0-12	0.74	42.42	35.92	1.18	montane forest	45.60	424.519	187.646	24.6135	NA
192	Tibet Nyingchi Alpine Forest Ecosystem National Field Scientific Observation Research Station, Nyingchi	2006	3850.00		-0.73	1134.1	6.18	12-30	0.94	22.66	35.95	0.63	montane forest	45.60	424.519	187.646	24.6135	NA
193	Tibet Nyingchi Alpine Forest Ecosystem National	2006	3850.00		-0.73	1134.1	5.54	30-55	1.34	9.93	34.22	0.29	montane forest	45.60	424.519	187.646	24.6135	NA

	Field Scientific Observation Research Station, Nyingchi																
194	Tibet Nyingchi Alpine Forest Ecosystem National Field Scientific Observation Research Station, Nyingchi	2006	385 0.00		-0.73	113 4.1	5.6 1	0-55	1.08	21 .1 7	35 .5 5	0. 6 0	montane forest	45. 60	312.9 87	26 3.7 6	49. 22 7	N A

References

Adams, P.W., & Sidle, R.C. (1987). Soil conditions in three recent landslides in Southeast Alaska. *Forest Ecology and Management, 18*, 93-102

Banghui, L., Zu'an, C., Wuming, B., & Xu, C.J.A.S.S. (2018). Seismogenic mechanism and the intermediate-and long-term earthquake risks of the 2008 Wenchuan and 2013 Lushan earthquakes*, 40*, 279-290

Basher, L., Betts, H., Lynn, I., Marden, M., McNeill, S., Page, M., & Rosser, B. (2018). A preliminary assessment of the impact of landslide, earthflow, and gully erosion on soil carbon stocks in New Zealand. *Geomorphology, 307*, 93-106

Bellingham, P.J., Walker, L.R., & Wardle, D.A. (2001). Differential facilitation by a nitrogen-fixing shrub during primary succession influences relative performance of canopy tree species*, 89*, 861-875

Bergman, B., Johansson, C., & Söderbäck, E. (1992). Tansley Review No. 42. The Nostoc-Gunnera Symbiosis. *New Phytol, 122*, 379-400

Bianchi, T.S., Cui, X., Blair, N.E., Burdige, D.J., Eglinton, T.I., & Galy, V. (2018). Centers of organic carbon burial and oxidation at the land-ocean interface. *Organic Geochemistry, 115*, 138-155

Billings, S.A., Richter, D.d.B., Ziegler, S.E., Prestegaard, K., & Wade, A.M. (2019). Distinct Contributions of Eroding and Depositional Profiles to Land-Atmosphere CO2 Exchange in Two Contrasting Forests*, 7*

Blodgett, T.A., & Isacks, B.L. (2007). Landslide Erosion Rate in the Eastern Cordillera of Northern Bolivia %J Earth Interactions*, 11*, 1-30

Błońska, E., Lasota, J., Piaszczyk, W., Wiecheć, M., & Klamerus-Iwan, A. (2017). The effect of landslide on soil organic carbon stock and biochemical properties of soil. *Journal of Soils and Sediments, 18*, 2727-2737

Booth, A.M., Buma, B., & Nagorski, S. (2023). Effects of Landslides on Terrestrial Carbon Stocks With a Coupled Geomorphic-Biologic Model: Southeast Alaska, United States, *128*, e2022JG007297

Bouchez, J., Beyssac, O., Galy, V., Gaillardet, J., France-Lanord, C., Bourgoin, L., & Moreira-Turcq, P. (2010a). Oxidation of petrogenic organic carbon in the Amazon floodplain as a source of atmospheric CO2. *Geology, 38*

Bouchez, J., Beyssac, O., Galy, V., Gaillardet, J., France-Lanord, C., Maurice, L., & Moreira-Turcq, P. (2010b). Oxidation of petrogenic organic carbon in the Amazon floodplain as a source of atmospheric CO2. *Geology, 38*, 255-258

Buma, B., & Thompson, T. (2019). Long-term exposure to more frequent disturbances increases baseline carbon in some ecosystems: Mapping and quantifying the disturbance frequency-ecosystem C relationship. *PLOS ONE, 14*, e0212526

Burchfiel, B.C., Zhiliang, C., Yupinc, L., & Royden, L.H.J.I.G.R. (1995). Tectonics of the Longmen Shan and adjacent regions, central China, *37*, 661-735

Burdige, D.J. (2005). Burial of terrestrial organic matter in marine sediments: A re-assessment, *19*

Burdige, D.J. (2007). Preservation of Organic Matter in Marine Sediments: Controls, Mechanisms, and an Imbalance in Sediment Organic Carbon Budgets? *Chemical Reviews, 107*, 467-485

Burke, A., Present, T.M., Paris, G., Rae, E.C.M., Sandilands, B.H., Gaillardet, J., Peucker-Ehrenbrink, B., Fischer, W.W., McClelland, J.W., Spencer, R.G.M., Voss, B.M., & Adkins, J.F. (2018). Sulfur isotopes in rivers: Insights into global weathering budgets, pyrite oxidation, and the modern sulfur cycle. *Earth and Planetary Science Letters, 496*, 168-177

Calmels, D., Gaillardet, J.r.m., Brenot, A.s., & France-Lanord, C. (2007). Sustained sulfide oxidation by physical erosion processes in the Mackenzie River basin: Climatic perspectives. *Geology, 35*, 1003-1006

Carey, A.E., Gardner, C.B., Goldsmith, S.T., Lyons, W.B., & Hicks, D.M. (2005). Organic carbon yields from small, mountainous rivers, New Zealand. *Geophysical Research Letters, 32*

Chamberlin, T.C. (1899). An Attempt to Frame a Working Hypothesis of the Cause of Glacial Periods on an Atmospheric Basis, *7*, 545-584

Chambers, J.Q., Fisher, J.I., Zeng, H., Chapman, E.L., Baker, D.B., & Hurtt, G.C. (2007a). Hurricane Katrina's carbon footprint on U.S. Gulf Coast forests. *Science, 318*, 1107

Chambers, J.Q., Fisher, J.I., Zeng, H., Chapman, E.L., Baker, D.B., & Hurtt, G.C. (2007b). Hurricane Katrina's Carbon Footprint on U.S. Gulf Coast Forests, *318*, 1107-1107

Chen, G., Ji, F., Zhou, R., Xu, J., Zhou, B., Li, X., Ye, Y.J.S., & Geology (2007). Primary research of activity segmentation of Longmenshan fault zone since late-quaternary, *29*, 657-673

Chen, H., Wu, N., Yuan, X., Gao, Y., & Zhu, D. (2009). Aftermath of the Wenchuan earthquake. *Frontiers in Ecology and the Environment, 7*, 72

Chen, S.F., Wilson, C., Luo, Z.L., & Deng, Q.D.J.J.o.S.A.E.S. (1994). The evolution of the western Sichuan foreland basin, southwestern China, *10*, 159-168

Chen, S.F., & Wilson, C.J.J.J.o.S.G. (1996). Emplacement of the Longmen Shan Thrust—Nappe Belt along the eastern margin of the Tibetan Plateau, *18*, 413-430

Chou, W.C., Lin, W.T., & Lin, C.Y. (2009). Vegetation recovery patterns assessment at landslides caused by catastrophic earthquake: a case study in central Taiwan. *Environ Monit Assess, 152*, 245-257

Ciais, P., Chris, S., Govindasamy, B., Bopp, L., Brovkin, V., Canadell, J., Chhabra, A., Defries, R., Galloway, J., & Heimann, M. (2013). Carbon and other biogeochemical cycles. *Climate Change 2013: The Physical Science Basis*, 465-570

Clark, K.E., Hilton, R.G., West, A.J., Robles Caceres, A., Gröcke, D.R., Marthews, T.R., Ferguson, R.I., Asner, G.P., New, M., & Malhi, Y. (2017). Erosion of organic carbon from the Andes and its effects on ecosystem carbon dioxide balance. *Journal of Geophysical Research: Biogeosciences, 122*, 449-469

Clark, K.E., West, A.J., Hilton, R.G., Asner, G.P., Quesada, C.A., Silman, M.R., Saatchi, S.S., Farfan-Rios, W., Martin, R.E., Horwath, A.B., Halladay, K., New, M., & Malhi, Y. (2016). Storm-triggered landslides in the Peruvian Andes and implications for topography, carbon cycles, and biodiversity. *Earth Surface Dynamics, 4*, 47-70

Coradini, K., Krejčová, J., & Frouz, J. (2022). Potential of vegetation and woodland cover recovery during primary and secondary succession, a global quantitative review, *33*, 512-526

Cramer, W., Bondeau, A., Woodward, F.I., Prentice, I.C., Betts, R.A., Brovkin, V., Cox, P.M., Fisher, V., Foley, J.A., & Friend, A.D.J.G.c.b. (2001). Global response of terrestrial ecosystem structure and function to CO2 and climate change: results from six dynamic global vegetation models, *7*, 357-373

Cui, P., Lin, Y.-m., & Chen, C. (2012). Destruction of vegetation due to geo-hazards and its environmental impacts in the Wenchuan earthquake areas. *Ecological Engineering, 44*, 61-69

Dadson, S.J., Hovius, N., Chen, H., Dade, W.B., Lin, J.-C., Hsu, M.-L., Lin, C.-W., Horng, M.-J., Chen, T.-C., Milliman, J., & Stark, C.P. (2004). Earthquake-triggered increase in sediment delivery from an active mountain belt. *Geology, 32*, 733-736

Dai, F.C., Xu, C., Yao, X., Xu, L., Tu, X.B., & Gong, Q.M. (2011). Spatial distribution of landslides triggered by the 2008 Ms 8.0 Wenchuan earthquake, China. *Journal of Asian Earth Sciences, 40*, 883-895

Dai, L., Ge, J., Wang, L., Zhang, Q., Liang, T., Bolan, N., Lischeid, G., & Rinklebe, J. (2022). Influence of soil properties, topography, and land cover on soil organic carbon and total nitrogen concentration: A case study in Qinghai-Tibet plateau based on random forest regression and structural equation modeling. *Sci Total Environ, 821*, 153440

del Moral, R., & Wood, D.M. (1993). Early Primary Succession on the Volcano Mount St. Helens. *Journal of Vegetation Science, 4*, 223-234

Deng, Q., Chen, S., & Zhao, X. (1995). Tectonics, Scismisity and Dynamics of Longmenshan Mountains and Its Adjacent Regions. In, *Chinese Science Abstracts Series B* (p. 59)

Deng, S.J.J.o.X.U. (2013). Earthquakes on the Longmen Mt.—Minshan fault zone, *32*, 18-22

Densmore, A.L., & Hovius, N. (2000). Topographic fingerprints of bedrock landslides. *Geology, 28*, 371-374

Descloux, S., Chanudet, V., Poilvé, H., & Grégoire, A. (2011). Co-assessment of biomass and soil organic carbon stocks in a future reservoir area located in Southeast Asia. *Environmental Monitoring and Assessment, 173*, 723-741

Dessert, C., Dupré, B., Gaillardet, J., François, L.M., & Allègre, C.J. (2003). Basalt weathering laws and the impact of basalt weathering on the global carbon cycle. *Chemical Geology, 202*, 257-273

Dewey, J.F., & Horsfield, B. (1970). Plate Tectonics, Orogeny and Continental Growth. *Nature, 225*, 521-525

Di, B., Zeng, H., Zhang, M., Ustin, S.L., Tang, Y., Wang, Z., Chen, N., & Zhang, B.J.R.S.o.E. (2010). Quantifying the spatial distribution of soil mass wasting processes after the 2008 earthquake in Wenchuan, China: a case study of the Longmenshan area*, 114*, 761-771

Dislich, C., & Huth, A. (2012). Modelling the impact of shallow landslides on forest structure in tropical montane forests. *Ecological Modelling, 239*, 40-53

Dixon, R.K., Solomon, A.M., Brown, S., Houghton, R.A., Trexier, M.C., & Wisniewski, J. (1994). Carbon Pools and Flux of Global Forest Ecosystems. *Science, 263*, 185-190

Doetterl, S., Berhe, A.A., Nadeu, E., Wang, Z., Sommer, M., & Fiener, P. (2016). Erosion, deposition and soil carbon: A review of process-level controls, experimental tools and models to address C cycling in dynamic landscapes. *Earth-Science Reviews, 154*, 102-122

Doetterl, S., Six, J., Van Wesemael, B., & Van Oost, K. (2012). Carbon cycling in eroding landscapes: geomorphic controls on soil organic C pool composition and C stabilization*, 18*, 2218-2232

Du, H.-L., Xu, L.-S., & Chen, Y.-T.J.C.J.G. (2009). Rupture process of the 2008 great Wenchuan earthquake from the analysis of the Alaska-array data*, 52*, 372-378

Du, W., Jin, C., Yu, K., Zhang, K., & Grasso, S. (2021). Evaluation of MODIS-based Vegetation Restoration After the 2008 Wenchuan Earthquake. *E3S Web of Conferences, 308*

Dymond, J.R. (2010). Soil erosion in New Zealand is a net sink of CO2*, 35*, 1763-1772

Edmond, J.M., & Huh, Y. (2003). Non-steady state carbonate recycling and implications for the evolution of atmospheric PCO2. *Earth and Planetary Science Letters, 216*, 125-139

Emberson, R., Hovius, N., Galy, A., & Marc, O. (2016). Oxidation of sulfides and rapid weathering in recent landslides. *Earth Surface Dynamics, 4*, 727-742

Espinosa, A.F., Casaverde, L.A., Michael, J.A., Alva-Hurtado, J., & Vargas-Neumann, J. (1985). Earthquake catalog of Peru. In, *Open-File Report*: U.S. Geological Survey

Fan, S., Gloor, M., Mahlman, J., Pacala, S., Sarmiento, J., Takahashi, T., & Tans, P.J.S. (1998). A large terrestrial carbon sink in North America implied by atmospheric and oceanic carbon dioxide data and models*, 282*, 442-446

Fan, S., Guan, F., Xu, X., Forrester, D., Ma, W., & Tang, X. (2016). Ecosystem Carbon Stock Loss after Land Use Change in Subtropical Forests in China. *Forests, 7*

Fan, X., Domènech, G., Scaringi, G., Huang, R., Xu, Q., Hales, T.C., Dai, L., Yang, Q., & Francis, O. (2018). Spatio-temporal evolution of mass wasting after the 2008 Mw 7.9 Wenchuan earthquake revealed by a detailed multi-temporal inventory. *Landslides, 15*, 2325-2341

Fan, X., Scaringi, G., Domènech, G., Yang, F., Guo, X., Dai, L., He, C., Xu, Q., & Huang, R.J.E.S.S.D. (2019a). Two multi-temporal datasets that track the enhanced landsliding after the 2008 Wenchuan earthquake, *11*, 35-55

Fan, X., Scaringi, G., Korup, O., West, A., Westen, C.J., Tanyas, H., Hovius, N., Hales, T., Jibson, R., Allstadt, K., Zhang, L., Evans, S., Xu, C., Li, G., & Pei, X. (2019b). Earthquake-induced chains of geologic hazards: patterns, mechanisms, and impacts. *Reviews of Geophysics*

Fernández-Martínez, M.A., Pérez-Ortega, S., Pointing, S.B., Allan Green, T.G., Pintado, A., Rozzi, R., Sancho, L.G., & de los Ríos, A. (2017). Microbial succession dynamics along glacier forefield chronosequences in Tierra del Fuego (Chile). *Polar Biology, 40*, 1939-1957

Foley, J.A., DeFries, R., Asner, G.P., Barford, C., Bonan, G., Carpenter, S.R., Chapin, F.S., Coe, M.T., Daily, G.C., Gibbs, H.K., Helkowski, J.H., Holloway, T., Howard, E.A., Kucharik, C.J., Monfreda, C., Patz, J.A., Prentice, I.C., Ramankutty, N., & Snyder, P.K. (2005). Global Consequences of Land Use, *309*, 570-574

France-Lanord, C., & Derry, L.A. (1997). Organic carbon burial forcing of the carbon cycle from Himalayan erosion. *Nature, 390*, 65-67

Francis, O., Fan, X., Hales, T., Hobley, D., Xu, Q., & Huang, R. (2022). The Fate of Sediment After a Large Earthquake. *Journal of Geophysical Research: Earth Surface, 127*

Francis, O.R., Hales, T.C., Hobley, D.E.J., Fan, X., Horton, A.J., Scaringi, G., & Huang, R. (2020). The impact of earthquakes on orogen-scale exhumation. *Earth Surf. Dynam., 8*, 579-593

Freund, C.A., Clark, K.E., Curran, J.F., Asner, G.P., & Silman, M.R. (2021). Landslide age, elevation and residual vegetation determine tropical montane forest canopy recovery and biomass accumulation after landslide disturbances in the Peruvian Andes, *109*, 3555-3571

Frings, P.J. (2019). Palaeoweathering: How Do Weathering Rates Vary with Climate? *Elements, 15*, 259-265

Frith, N.V., Hilton, R.G., Howarth, J.D., Gröcke, D.R., Fitzsimons, S.J., Croissant, T., Wang, J., McClymont, E.L., Dahl, J., & Densmore, A.L. (2018). Carbon export from mountain forests enhanced by earthquake-triggered landslides over millennia. *Nature Geoscience, 11*, 772-776

Gabet, E.J., & Mudd, S.M. (2009). A theoretical model coupling chemical weathering rates with denudation rates. *Geology, 37*, 151-154

Gaillardet, J., Dupré, B., Louvat, P., & Allègre, C.J. (1999). Global silicate weathering and CO_2 consumption rates deduced from the chemistry of large rivers. *Chemical Geology, 159*, 3-30

Galy, V., France-Lanord, C., Beyssac, O., Faure, P., Kudrass, H., & Palhol, F. Efficient organic carbon burial in the Bengal fan sustained by the Himalayan erosional system. *Nature, 450*, 407-410

Galy, V., France-Lanord, C., Beyssac, O., Faure, P., Kudrass, H., & Palhol, F. (2007). Efficient organic carbon burial in the Bengal fan sustained by the Himalayan erosional system. *Nature, 450*, 407-410

Galy, V., Peucker-Ehrenbrink, B., & Eglinton, T. (2015). Global carbon export from the terrestrial biosphere controlled by erosion. *Nature, 521*, 204-207

Garwood, N.C., Janos, D.P., & Brokaw, N. (1979a). Earthquake-caused landslides-a major disturbance to tropical forests. *Science, 205*, 997-999

Garwood, N.C., Janos, D.P., & Brokaw, N. (1979b). Earthquake-Caused Landslides: A Major Disturbance to Tropical Forests*, 205*, 997-999

Ge, Y.-g., Cui, P., Zhang, J.-q., Zeng, C., & Su, F.-h.J.J.o.M.S. (2015). Catastrophic debris flows on July 10 th 2013 along the Min River in areas seriously-hit by the Wenchuan earthquake*, 12*, 186-206

Gomez, B., Trustrum, N.A., Hicks, D.M., Rogers, K.M., Page, M.J., & Tate, K.R. (2003). Production, storage, and output of particulate organic carbon: Waipaoa River basin, New Zealand. *Water Resources Research, 39*

Gorum, T., Fan, X., van Westen, C.J., Huang, R.Q., Xu, Q., Tang, C., & Wang, G. (2011). Distribution pattern of earthquake-induced landslides triggered by the 12 May 2008 Wenchuan earthquake. *Geomorphology, 133*, 152-167

Group, T.S.V.C. (1980). *Sichuan Vegetation*. Sichuan People's Publishing House

Guan, F., Tang, X., Fan, S., Zhao, J., & Peng, C. (2015). Changes in soil carbon and nitrogen stocks followed the conversion from secondary forest to Chinese fir and Moso bamboo plantations. *Catena, 133*, 455-460

Guariguata, M.R. (1990). Landslide Disturbance and Forest Regeneration in the Upper Luquillo Mountains of Puerto Rico. *Journal of Ecology, 78*, 814-832

Guo, A., Xu, Y., Jiang, N., Wu, Y., Gao, Z., Li, S., Xu, T., & Bastos, L. (2023). Analyzing correlations between GNSS retrieved precipitable water vapor and land surface temperature after earthquakes occurrence. *Science of the Total Environment, 872*, 162225

Guo, Z., Hu, H., Li, P., Li, N., & Fang, J. (2013). Spatio-temporal changes in biomass carbon sinks in China's forests from 1977 to 2008. *Science China Life Sciences, 56*, 661-671

Gutenberg, B., & Richter, C.F. (1956). Magnitude and energy of earthquakes. *Annals of Geophysics, 9*

Gutschick, V.P., & BassiriRad, H. (2003). Extreme events as shaping physiology, ecology, and evolution of plants: toward a unified definition and evaluation of their consequences*, 160*, 21-42

Guzzetti, F., Ardizzone, F., Cardinali, M., Rossi, M., & Valigi, D. (2009). Landslide volumes and landslide mobilization rates in Umbria, central Italy. *Earth and Planetary Science Letters, 279*, 222-229

Guzzetti, F., Mondini, A.C., Cardinali, M., Fiorucci, F., Santangelo, M., & Chang, K.-T. (2012). Landslide inventory maps: New tools for an old problem. *Earth-Science Reviews, 112*, 42-66

Harvey, A.M. (2001). Coupling between hillslopes and channels in upland fluvial systems: implications for landscape sensitivity, illustrated from the Howgill Fells, northwest England. *Catena, 42*, 225-250

Harvey, E.L., Hales, T.C., Hobley, D.E.J., Liu, J., & Fan, X. (2022). Measuring the grain-size distributions of mass movement deposits, *47*, 1599-1614

Hatten, J.A., Goñi, M.A., & Wheatcroft, R.A. (2010). Chemical characteristics of particulate organic matter from a small, mountainous river system in the Oregon Coast Range, USA. *Biogeochemistry, 107*, 43-66

Hengl, T., Mendes de Jesus, J., Heuvelink, G.B.M., Ruiperez Gonzalez, M., Kilibarda, M., Blagotić, A., Shangguan, W., Wright, M.N., Geng, X., Bauer-Marschallinger, B., Guevara, M.A., Vargas, R., MacMillan, R.A., Batjes, N.H., Leenaars, J.G.B., Ribeiro, E., Wheeler, I., Mantel, S., & Kempen, B. (2017). SoilGrids250m: Global gridded soil information based on machine learning. *PLOS ONE, 12*, e0169748

Hilley, G.E., Chamberlain, C.P., Moon, S., Porder, S., & Willett, S.D. (2010). Competition between erosion and reaction kinetics in controlling silicate-weathering rates. *Earth and Planetary Science Letters, 293*, 191-199

Hilton, R.G. (2017). Climate regulates the erosional carbon export from the terrestrial biosphere. *Geomorphology, 277*, 118-132

Hilton, R.G., Galy, A., & Hovius, N. (2008a). Riverine particulate organic carbon from an active mountain belt: Importance of landslides. *Global Biogeochemical Cycles, 22*

Hilton, R.G., Galy, A., Hovius, N., Chen, M.-C., Horng, M.-J., & Chen, H. (2008b). Tropical-cyclone-driven erosion of the terrestrial biosphere from mountains. *Nature Geoscience, 1*, 759-762

Hilton, R.G., Galy, A., Hovius, N., Horng, M.-J., & Chen, H. (2011a). Efficient transport of fossil organic carbon to the ocean by steep mountain rivers: An orogenic carbon sequestration mechanism. *Geology, 39*, 71-74

Hilton, R.G., Meunier, P., Hovius, N., Bellingham, P.J., & Galy, A. (2011b). Landslide impact on organic carbon cycling in a temperate montane forest. *Earth Surface Processes and Landforms, 36*, 1670-1679

Hilton, R.G., & West, A.J. (2020). Mountains, erosion and the carbon cycle. *Nature Reviews Earth & Environment, 1*, 284-299

Horan, K., Hilton, R.G., Dellinger, M., Tipper, E., Galy, V., Calmels, D., Selby, D., Gaillardet, J., Ottley, C.J., Parsons, D., & Burton, K. (2019). *Carbon dioxide emissions by rock organic carbon oxidation and the net geochemical carbon budget of the Mackenzie River Basin*. American Journal of Science (AJS)

Horan, K., Hilton, R.G., Selby, D., Ottley, C.J., Gröcke, D.R., Hicks, M., & Burton, K.W. (2017). Mountain glaciation drives rapid oxidation of rock-bound organic carbon, *3*, e1701107

Huang, R., & Fan, X.J.N.g. (2013). The landslide story, *6*, 325-326

Huang, R., Li, Geology, W.J.B.o.E., & Environment, t. (2009). Analysis of the geo-hazards triggered by the 12 May 2008 Wenchuan Earthquake, China, *68*, 363-371

Huang, R.J.C.J.o.R.M., & Engineering (2009). Mechanism and geomechanical modes of landslide hazards triggered by Wenchuan 8.0 earthquake, *28*, 1239-1249

Hungr, O., Leroueil, S., & Picarelli, L. (2014). The Varnes classification of landslide types, an update. *Landslides, 11*, 167-194

Hunter, B.D., Roering, J.J., Silva, L.C.R., & Moreland, K.C. (2024). Geomorphic controls on the abundance and persistence of soil organic carbon pools in erosional landscapes. *Nature Geoscience, 17*, 151-157

Intergovernmental Panel on Climate, C. (2014). *Climate Change 2013 – The Physical Science Basis: Working Group I Contribution to the Fifth Assessment Report of the Intergovernmental Panel on Climate Change*. Cambridge: Cambridge University Press

Jacobson, A.D., & Blum, J.D. (2003). Relationship between mechanical erosion and atmospheric CO_2 consumption in the New Zealand Southern Alps. *Geology, 31*, 865-868

Ji, C., Liu, Z., Hudnut, K., Liu, J., & Shao, G.J.C.E.C., Palm Springs, Calif (2008). Heterogeneous rupture of 2008 Wenchuan earthquake constrained by jointly inverting seismic and InSAR data, paper presented at 2008 SCEC Annual Meeting, S, 6-11

Jia, D., Wei, G., Chen, Z., Li, B., Zeng, Q., & Yang, G.J.A.b. (2006). Longmen Shan fold-thrust belt and its relation to the western Sichuan Basin in central China: New insights from hydrocarbon exploration*, 90*, 1425-1447

Jiang, W.-G., Jia, K., Wu, J.-J., Tang, Z.-H., Wang, W.-J., & Liu, X.-F. (2015). Evaluating the Vegetation Recovery in the Damage Area of Wenchuan Earthquake Using MODIS Data. *Remote Sensing, 7*, 8757-8778

Jin, Z., West, A.J., Zhang, F., An, Z., Hilton, R.G., Yu, J., Wang, J., Li, G., Deng, L., & Wang, X. (2016). Seismically enhanced solute fluxes in the Yangtze River headwaters following the A.D. 2008 Wenchuan earthquake. *Geology, 44*, 47-50

Jing, X.F., Chen, Y.L., Chen, H., & Cai, Z.Y. (2012). Discussion on the Reconstruction of the Wenchuan Earthquake-Damaged Ecosystems. *Applied Mechanics and Materials, 209-211*, 1668-1673

Johnson, E.A., & Miyanishi, K. (2008). Testing the assumptions of chronosequences in succession*, 11*, 419-431

José, C., Clemente, I., & Tomás, F. (1996). Landslides : proceedings of the Eighth International Conference and Field Trip on Landslides, Granada, Spain, 27 - 28 September 1996. In, *International Conference and Field Trip on Landslides ; 8*. Rotterdam [u.a.], Granada: Balkema;

Junren, X., Yuanbin, Z., Tingxing, H., Kaiyun, W., & Hua, Y. (2009). Carbon stock and allocation of five restoration ecosystems in subalpine coniferous forest zone in Western Sichuan Province, Southwest China. *Acta Ecologica Sinica, 29*, 51-55

Kanamori, H. (1977). The energy release in great earthquakes*, 82*, 2981-2987

Kao, S.J., Hilton, R.G., Selvaraj, K., Dai, M., Zehetner, F., Huang, J.C., Hsu, S.C., Sparkes, R., Liu, J.T., Lee, T.Y., Yang, J.Y.T., Galy, A., Xu, X., & Hovius, N. (2014a). Preservation of terrestrial organic carbon in marine sediments offshore Taiwan: mountain building and atmospheric carbon dioxide sequestration. *Earth Surf. Dynam., 2*, 127-139

Kao, S.J., Hilton, R.G., Selvaraj, K., Dai, M., Zehetner, F., Huang, J.C., Hsu, S.C., Sparkes, R., Liu, J.T., Lee, T.Y., Yang, J.Y.T., Galy, A., Xu, X., & Hovius, N. (2014b). Preservation of terrestrial organic carbon in marine sediments offshore Taiwan: mountain building and atmospheric carbon dioxide sequestration. *Earth Surface Dynamics, 2*, 127-139

Keefer, D.K. (1984). Landslides caused by earthquakes. *GSA Bulletin, 95*, 406-421

Keefer, D.K. (1994). The importance of earthquake-induced landslides to long-term slope erosion and slope-failure hazards in seismically active regions. *Geomorphology, 10*, 265-284

Keefer, D.K., & Wilson, R.C. (1989). Predicting earthquake-induced landslides, with emphasis on arid and semi-arid environments. In

Keller, C.K., & Bacon, D.H.J.G.B.C. (1998). Soil respiration and georespiration distinguished by transport analyses of vadose CO_2, $^{13}CO_2$, and $^{14}CO_2$, *12*, 361-372

Kirby, E., Reiners, P.W., Krol, M.A., Whipple, K.X., Hodges, K.V., Farley, K.A., Tang, W., & Chen, Z.J.T. (2002). Late Cenozoic evolution of the eastern margin of the Tibetan Plateau: Inferences from 40Ar/39Ar and (U‑Th)/He thermochronology*, 21*, 1-1-1-20

Kirby, E., Whipple, K.X., Tang, W., & Chen, Z.J.J.o.G.R.S.E. (2003). Distribution of active rock uplift along the eastern margin of the Tibetan Plateau: Inferences from bedrock channel longitudinal profiles*, 108*

Kolbe, S.E., Miller, A.I., Townsend-Small, A., Cameron, G.N., & Culley, T.M. (2016). Impact of Land-Use History and Forest Trees on Soil Organic Carbon and Nitrogen Stocks*, 80*, 1089-1097

Komada, T., Druffel, E.R.M., & Trumbore, S.E. (2004). Oceanic export of relict carbon by small mountainous rivers*, 31*

Korup, O.J.E.S.P., & Landforms (2005). Geomorphic imprint of landslides on alpine river systems, southwest New Zealand*, 30*, 783-800

Kunkel, V.R., Wells, T., & Hancock, G.R. (2022). Modelling soil organic carbon using vegetation indices across large catchments in eastern Australia. *Sci Total Environ, 817*, 152690

Lal, R. (2003). Soil erosion and the global carbon budget. *Environment International, 29*, 437-450

Larsen, I.J., Almond, P.C., Eger, A., Stone, J.O., Montgomery, D.R., & Malcolm, B. (2014). Rapid Soil Production and Weathering in the Southern Alps, New Zealand*, 343*, 637-640

Larsen, I.J., Montgomery, D.R., & Korup, O. (2010). Landslide erosion controlled by hillslope material. *Nature Geoscience, 3*, 247-251

Lehmann, A., Zheng, W., & Rillig, M.C. (2017). Soil biota contributions to soil aggregation. *Nature Ecology & Evolution, 1*, 1828-1835

Lei, J., & Zhao, D.J.G., Geophysics, Geosystems (2009). Structural heterogeneity of the Longmenshan fault zone and the mechanism of the 2008 Wenchuan earthquake (Ms 8.0)*, 10*

LEI, J.S., ZHAO, D.P., SU, J.R., ZHANG, G.W., & Li, F.J.C.J.o.G. (2009). Fine seismic structure under the Longmenshan fault zone and the mechanism of the large Wenchuan earthquake*, 52*, 112-119

Li, G., West, A.J., Densmore, A.L., Hammond, D.E., Jin, Z., Zhang, F., Wang, J., & Hilton, R.G. (2016). Connectivity of earthquake-triggered landslides with the fluvial network: Implications for landslide sediment transport after the 2008 Wenchuan earthquake. *Journal of Geophysical Research: Earth Surface, 121*, 703-724

Li, G., West, A.J., Densmore, A.L., Jin, Z., Parker, R.N., & Hilton, R.G. (2014). Seismic mountain building: Landslides associated with the 2008 Wenchuan earthquake in the context of a generalized model for earthquake volume balance. *Geochemistry, Geophysics, Geosystems, 15*, 833-844

Li, G., West, A.J., Densmore, A.L., Jin, Z., Zhang, F., Wang, J., Clark, M., & Hilton, R.G. (2017a). Earthquakes drive focused denudation along a tectonically active mountain front. *Earth and Planetary Science Letters, 472*, 253-265

Li, J., Xie, X., Zhao, B., Xiao, X., & Xue, B. (2022). Spatio-Temporal Processes and Characteristics of Vegetation Recovery in the Earthquake Area: A Case Study of Wenchuan, China. *Land, 11*

Li, W.-l., Huang, R.-q., Tang, C., Xu, Q., & van WESTEN, C.J.J.o.M.S. (2013). Co-seismic landslide inventory and susceptibility mapping in the 2008 Wenchuan earthquake disaster area, China*, 10*, 339-354

Li, Z., & Fang, H. (2016). Impacts of climate change on water erosion: A review. *Earth-Science Reviews, 163*, 94-117

Li, Z., Liu-Zeng, J., Almeida, R., Hubbard, J., Sun, C., & Yi, G. (2017b). Re-evaluating seismic hazard along the southern Longmen Shan, China: Insights from the 1970 Dayi and 2013 Lushan earthquakes. *Tectonophysics, 717*, 519-530

Lin, G.-W., Chen, H., Hovius, N., Horng, M.-J., Dadson, S., Meunier, P., & Lines, M. (2008). Effects of earthquake and cyclone sequencing on landsliding and fluvial sediment transfer in a mountain catchment*, 33*, 1354-1373

Lin, Y., Deng, H., Du, K., Rafay, L., Zhang, G.-s., Li, J., Chen, C., Wu, C., Lin, H., & Yu, W.J.S.o.t.T.E. (2017). Combined effects of climate, restoration measures and slope position in change in soil chemical properties and nutrient loss across lands affected by the Wenchuan Earthquake in China*, 596*, 274-283

Liu-Zeng, J., Wen, L., Oskin, M., & Zeng, L.J.G., Geophysics, Geosystems (2011). Focused modern denudation of the Longmen Shan margin, eastern Tibetan Plateau*, 12*

Liu, J., Fan, X., Tang, X., Xu, Q., Harvey, E.L., Hales, T.C., & Jin, Z. (2022). Ecosystem carbon stock loss after a mega earthquake. *Catena, 216*

Liu, S., Bliss, N., Sundquist, E., & Huntington, T.G. (2003). Modeling carbon dynamics in vegetation and soil under the impact of soil erosion and deposition*, 17*

Lloret, E., Dessert, C., Pastor, L., Lajeunesse, E., Crispi, O., Gaillardet, J., & Benedetti, M.F. (2013). Dynamic of particulate and dissolved organic carbon in small volcanic mountainous tropical watersheds. *Chemical Geology, 351*, 229-244

Lu, T., Shi, F., Sun, G., Luo, Y., Wang, Q., Wu, Y., & Wu, N. (2010). Reconstruction of the Wenchuan Earthquake-Damaged Ecosystems: Four Important Questions. *Chinese Journal of Appplied Environmental Biology, 16*, 301-304

Lu, T., Zeng, H., Luo, Y., Wang, Q., Shi, F., Sun, G., Wu, Y., & Wu, N. (2012). Monitoring vegetation recovery after China's May 2008 Wenchuan earthquake using Landsat TM time-series data: a case study in Mao County*, 27*, 955-966

Luo, Y., Keenan, T.F., & Smith, M. (2015). Predictability of the terrestrial carbon cycle*, 21*, 1737-1751

Luo, Y., Shi, Z., Lu, X., Xia, J., Liang, J., Jiang, J., Wang, Y., Smith, M.J., Jiang, L., Ahlström, A., Chen, B., Hararuk, O., Hastings, A., Hoffman, F., Medlyn, B., Niu, S.,

Rasmussen, M., Todd-Brown, K., & Wang, Y.P. (2017). Transient dynamics of terrestrial carbon storage: mathematical foundation and its applications. *Biogeosciences, 14*, 145-161

Luo, Y., Wang, X., Ouyang, Z., Lu, F., Feng, L., & Tao, J. (2020). A review of biomass equations for China's tree species. *Earth System Science Data, 12*, 21-40

Luo, Y., & Weng, E. (2011). Dynamic disequilibrium of the terrestrial carbon cycle under global change. *Trends in Ecology & Evolution, 26*, 96-104

Luo, Y.Q., Randerson, J.T., Abramowitz, G., Bacour, C., Blyth, E., Carvalhais, N., Ciais, P., Dalmonech, D., Fisher, J.B., Fisher, R., Friedlingstein, P., Hibbard, K., Hoffman, F., Huntzinger, D., Jones, C.D., Koven, C., Lawrence, D., Li, D.J., Mahecha, M., Niu, S.L., Norby, R., Piao, S.L., Qi, X., Peylin, P., Prentice, I.C., Riley, W., Reichstein, M., Schwalm, C., Wang, Y.P., Xia, J.Y., Zaehle, S., & Zhou, X.H. (2012). A framework for benchmarking land models. *Biogeosciences, 9*, 3857-3874

Madej, M.A. (2010). Redwoods, restoration, and implications for carbon budgets. *Geomorphology, 116*, 264-273

Maher, K., & Chamberlain, C.P. (2014). Hydrologic Regulation of Chemical Weathering and the Geologic Carbon Cycle*, 343*, 1502-1504

Malamud, B.D., Turcotte, D.L., Guzzetti, F., & Reichenbach, P. (2004). Landslides, earthquakes, and erosion. *Earth and Planetary Science Letters, 229*, 45-59

Manzoni, S., & Porporato, A. (2009). Soil carbon and nitrogen mineralization: Theory and models across scales. *Soil Biology and Biochemistry, 41*, 1355-1379

Marc, O., Behling, R., Andermann, C., Turowski, J.M., Illien, L., Roessner, S., & Hovius, N. (2019). Long-term erosion of the Nepal Himalayas by bedrock landsliding: the role of monsoons, earthquakes and giant landslides. *Earth Surface Dynamics, 7*, 107-128

Marc, O., & Hovius, N. (2015). Amalgamation in landslide maps: effects and automatic detection. *Natural Hazards and Earth System Sciences, 15*, 723-733

Marc, O., Hovius, N., Meunier, P., Gorum, T., & Uchida, T. (2016). A seismologically consistent expression for the total area and volume of earthquake-triggered landsliding*, 121*, 640-663

Marc, O., Hovius, N., Meunier, P., Uchida, T., & Hayashi, S. (2015). Transient changes of landslide rates after earthquakes. *Geology, 43*, 883-886

Marc, O., Stumpf, A., Malet, J.-P., Gosset, M., Uchida, T., & Chiang, S.-H. (2018a). Initial insights from a global database of rainfall-induced landslide inventories: the weak influence of slope and strong influence of total storm rainfall. *Earth Surface Dynamics, 6*, 903-922

Marc, O., Stumpf, A., Malet, J.P., Gosset, M., Uchida, T., & Chiang, S.H. (2018b). Initial insights from a global database of rainfall-induced landslide inventories: the weak influence of slope and strong influence of total storm rainfall. *Earth Surf. Dynam., 6*, 903-922

Märki, L., Lupker, M., France-Lanord, C., Lavé, J., Gallen, S., Gajurel, A.P., Haghipour, N., Leuenberger-West, F., & Eglinton, T. (2021). An unshakable carbon budget for the Himalaya. *Nature Geoscience, 14*, 745-750

Matamala, R., Jastrow, J.D., Miller, R.M., & Garten, C.T. (2008). TEMPORAL CHANGES IN C AND N STOCKS OF RESTORED PRAIRIE: IMPLICATIONS FOR C SEQUESTRATION STRATEGIES, *18*, 1470-1488

Meng, G.j., Ren, J.w., Wang, M., Gan, W.j., Wang, Q., Qiao, X.j., & Yang, Y.l.J.G., Geophysics, Geosystems (2008). Crustal deformation in western Sichuan region and implications for 12 May 2008 Ms 8.0 earthquake, *9*

Molnar, P., Anderson, R.S., & Anderson, S.P. (2007). Tectonics, fracturing of rock, and erosion, *112*

Moon, S., Chamberlain, C.P., & Hilley, G.E. (2014). New estimates of silicate weathering rates and their uncertainties in global rivers. *Geochimica Et Cosmochimica Acta, 134*, 257-274

Naus, J.J.J.o.t.A.S.A. (1969). The distribution of the logarithm of the sum of two log-normal variates, *64*, 655-659

Page, M., Trustrum, N., Brackley, H., & Baisden, T. (2004). Erosion-related soil carbon fluxes in a pastoral steepland catchment, New Zealand, *103*, 561-579

Pain, C.F., & Bowlersw, J.M. (1973). Denudation following the November 1970 earthquake at Madang, Papua New Guinea. *Z. Geomorphologie, N. F., 18*, 92-104

Pan, Y., Birdsey, R.A., Fang, J., Houghton, R., Kauppi, P.E., Kurz, W.A., Phillips, O.L., Shvidenko, A., Lewis, S.L., Canadell, J.G., Ciais, P., Jackson, R.B., Pacala, S.W., McGuire, A.D., Piao, S., Rautiainen, A., Sitch, S., & Hayes, D. (2011). A Large and Persistent Carbon Sink in the World's Forests. *Science, 333*, 988-993

Parfitt, R.L., Baisden, W.T., Ross, C.W., Rosser, B.J., Schipper, L.A., & Barry, B. (2013). Influence of erosion and deposition on carbon and nitrogen accumulation in resampled steepland soils under pasture in New Zealand. *Geoderma, 192*, 154-159

Parker, R.N., Densmore, A.L., Rosser, N.J., de Michele, M., Li, Y., Huang, R., Whadcoat, S., & Petley, D.N. (2011). Mass wasting triggered by the 2008 Wenchuan earthquake is greater than orogenic growth. *Nature Geoscience, 4*, 449-452

Parker, R.N., Rosser, N.J., Hales, T.C.J.N.H., & Discussions, E.S.S. (2017). Spatial prediction of earthquake-induced landslide probability, *2017*, 1-29

Pearce, A.J., & Watson, A.J. (1986). Effects of earthquake-induced landslides on sediment budget and transport over a 50-yr period. *Geology, 14*, 52-55

Peng, S., Ding, Y., Liu, W., & Li, Z. (2019). 1 km monthly temperature and precipitation dataset for China from 1901 to 2017. *Earth Syst. Sci. Data, 11*, 1931-1946

Petsch, S.T. (2014). 12.8 - Weathering of Organic Carbon. In H.D. Holland, & K.K. Turekian (Eds.), *Treatise on Geochemistry (Second Edition)* (pp. 217-238). Oxford: Elsevier

Phillips, O.L., Malhi, Y., Higuchi, N., Laurance, W.F., Núñez, P.V., Vásquez, R.M., Laurance, S.G., Ferreira, L.V., Stern, M., Brown, S., & Grace, J. (1998). Changes in the Carbon Balance of Tropical Forests: Evidence from Long-Term Plots, *282*, 439-442

Pierson, T.C.J.S. (1981). Dominant particle support mechanisms in debris flows at Mt Thomas, New Zealand, and implications for flow mobility, *28*, 49-60

Prach, K., & Walker, L.R. (2019). Differences between primary and secondary plant succession among biomes of the world, *107*, 510-516

Qi, S., Xu, Q., Lan, H., Zhang, B., & Liu, J.J.E.g. (2010). Spatial distribution analysis of landslides triggered by 2008.5. 12 Wenchuan Earthquake, China, *116*, 95-108

Qiu, S., Xu, M., Zheng, Y., Li, R., Wong, M.H.G., Zhang, L., Liu, L., Lai, C., & Zhang, W. (2015). Impacts of the Wenchuan earthquake on tree mortality and biomass carbon stock. *Natural Hazards, 77*, 1261-1274

Rammig, A., Fahse, L., Bugmann, H., & Bebi, P. (2006). Forest regeneration after disturbance: A modelling study for the Swiss Alps. *Forest Ecology and Management, 222*, 123-136

Ramos Scharrón, C.E., Castellanos, E.J., & Restrepo, C. (2012). The transfer of modern organic carbon by landslide activity in tropical montane ecosystems. *Journal of Geophysical Research: Biogeosciences, 117*

Rasigraf, O., & Wagner, D. (2022). Landslides: An emerging model for ecosystem and soil chronosequence research. *Earth-Science Reviews, 231*

Raymo, M.E., & Ruddiman, W.F. (1992). Tectonic forcing of late Cenozoic climate. *Nature, 359*, 117-122

Ren, D., Wang, J., Fu, R., Karoly, D.J., Hong, Y., Leslie, L.M., Fu, C., & Huang, G. (2009). Mudslide-caused ecosystem degradation following Wenchuan earthquake 2008. *Geophysical Research Letters, 36*

Restrepo, C., & Alvarez, N. (2006). Landslides and their contribution to land-cover in the mountains of Mexico and central America. *Biotropica, 38*, 446–457

Restrepo, C., Walker, L.R., Shiels, A.B., Bussmann, R., Claessens, L., Fisch, S., Lozano, P., Negi, G., Paolini, L., Poveda, G., Ramos-Scharrón, C., Richter, M., & Velázquez, E. (2009). Landsliding and Its Multiscale Influence on Mountainscapes. *BioScience, 59*, 685-698

Richardson, S.J., Peltzer, D.A., Hurst, J.M., Allen, R.B., Bellingham, P.J., Carswell, F.E., Clinton, P.W., Griffiths, A.D., Wiser, S.K., & Wright, E.F. (2009). Deadwood in New Zealand's indigenous forests. *Forest Ecology and Management, 258*, 2456-2466

Riebe, C.S., Kirchner, J.W., & Finkel, R.C. (2004). Erosional and climatic effects on long-term chemical weathering rates in granitic landscapes spanning diverse climate regimes. *Earth and Planetary Science Letters, 224*, 547-562

Rosenbloom, N.A., Harden, J.W., Neff, J.C., & Schimel, D.S. (2006). Geomorphic control of landscape carbon accumulation, *111*

Running, S.W., Nemani, R.R., Heinsch, F.A., Zhao, M., Reeves, M., & Hashimoto, H. (2004). A Continuous Satellite-Derived Measure of Global Terrestrial Primary Production. *BioScience, 54*, 547-560

Schimel, D.S. (1995). Terrestrial ecosystems and the carbon cycle, *1*, 77-91

Schlesinger, W.H., & Andrews, J.A. (2000). Soil respiration and the global carbon cycle. *Biogeochemistry, 48*, 7-20

Schomakers, J., Jien, S.H., Lee, T.Y., Huang, J.C., Hseu, Z.Y., Lin, Z.L., Lee, L.C., Hein, T., Mentler, A., & Zehetner, F. (2017). Soil and biomass carbon re-accumulation after landslide disturbances. *Geomorphology (Amst), 288*, 164-174

Schuur, E.A.G., Vogel, J.G., Crummer, K.G., Lee, H., Sickman, J.O., & Osterkamp, T.E. (2009). The effect of permafrost thaw on old carbon release and net carbon exchange from tundra. *Nature, 459*, 556-559

Schwab, M., Rieke-Zapp, D., Schneider, H., Liniger, M., & Schlunegger, F. (2008). Landsliding and sediment flux in the Central Swiss Alps: A photogrammetric study of the Schimbrig landslide, Entlebuch. *Geomorphology, 97*, 392-406

Shiels, A.B., & Walker, L.R. (2003). Bird Perches Increase Forest Seeds on Puerto Rican Landslides*, 11*, 457-465

Shiels, A.B., Walker, L.R., & Thompson, D.B. (2005). Organic matter inputs create variable resource patches on Puerto Rican landslides. *Plant Ecology, 184*, 223-236

Sierra, C.A., & Müller, M.J.E.M. (2015). A general mathematical framework for representing soil organic matter dynamics*, 85*, 505-524

Silatsa, F.B.T., Yemefack, M., Tabi, F.O., Heuvelink, G.B.M., & Leenaars, J.G.B. (2020). Assessing countrywide soil organic carbon stock using hybrid machine learning modelling and legacy soil data in Cameroon. *Geoderma, 367*

Smith, S.V., Renwick, W.H., Buddemeier, R.W., & Crossland, C.J. (2001). Budgets of soil erosion and deposition for sediments and sedimentary organic carbon across the conterminous United States*, 15*, 697-707

Smith, T.M., Cramer, W.P., Dixon, R.K., Leemans, R., Neilson, R.P., & Solomon, A.M. (1993). The Global Terrestrial Carbon Cycle. In J. Wisniewski, & R.N. Sampson (Eds.), *Terrestrial Biospheric Carbon Fluxes Quantification of Sinks and Sources of CO2* (pp. 19-37). Dordrecht: Springer Netherlands

Stone, R. (2009). Wenchuan Earthquke-A Deeply Scarred Land. *Science, 324*, 713-714

Sun, X.-f., Yuan, L.-g., Zhou, Y.-z., Shao, H.-y., Li, X.-f., & Zhong, P. (2021). Spatiotemporal change of vegetation coverage recovery and its driving factors in the Wenchuan earthquake-hit areas. *Journal of Mountain Science, 18*, 2854-2869

Sundquist, E.T., & Visser, K. (2003). 8.09 - The Geologic History of the Carbon Cycle. In H.D. Holland, & K.K. Turekian (Eds.), *Treatise on Geochemistry* (pp. 425-472). Oxford: Pergamon

Tang, C., van Asch, T.W., Chang, M., Chen, G.Q., Zhao, X.H., & Huang, X.C.J.G. (2012). Catastrophic debris flows on 13 August 2010 in the Qingping area, southwestern China: the combined effects of a strong earthquake and subsequent rainstorms*, 139*, 559-576

Tang, R., Fan, X., Scaringi, G., Xu, Q., van Westen, C.J., Ren, J., & Havenith, H.-B. (2018). Distinctive controls on the distribution of river-damming and non-damming landslides induced by the 2008 Wenchuan earthquake. *Bulletin of Engineering Geology and the Environment, 78*, 4075-4093

Tanyaş, H., van Westen, C.J., Allstadt, K.E., & Jibson, R.W. (2019). Factors controlling landslide frequency–area distributions*, 44*, 900-917

Teng, J., Yang, H., Zhang, H., & Zhang, X.J.Q.S. (2010). WENCHUAN| Ms8. 0 EARTHQUAKE| FINE VELOCITY STRUCTURES| OF THE LITHESPHERE| AND DYNAMICAL MECHANISM*, 30*, 637-651

Tong, C. (1992). Tectonic Evolution and Oil–gas-accumulating Process of the Sichuan Basin. In: Geological Publishing House, Beijing

Torres, M.A., West, A.J., Clark, K.E., Paris, G., Bouchez, J., Ponton, C., Feakins, S.J., Galy, V., & Adkins, J.F. (2016). The acid and alkalinity budgets of weathering in the Andes–Amazon system: Insights into the erosional control of global biogeochemical cycles. *Earth and Planetary Science Letters, 450*, 381-391

Torres, M.A., West, A.J., & Li, G. (2014). Sulphide oxidation and carbonate dissolution as a source of CO2 over geological timescales. *Nature, 507*, 346-349

Trustrum, N.A., & De Rose, R.C. (1988). Soil depth-age relationship of landslides on deforested hillslopes, taranaki, New Zealand. *Geomorphology, 1*, 143-160

Valagussa, A., Marc, O., Frattini, P., & Crosta, G.B. (2019). Seismic and geological controls on earthquake-induced landslide size. *Earth and Planetary Science Letters, 506*, 268-281

Velázquez, E., & Gómez-Sal, A. (2007). Environmental Control of Early Succession on a Large Landslide in a Tropical Dry Ecosystem (Casita Volcano, Nicaragua). *Biotropica, 39*, 601-609

Velázquez, E., & Gómez-Sal, A. (2008). Landslide early succession in a neotropical dry forest. *Plant Ecology, 199*, 295-308

Vindušková, O., Pánek, T., & Frouz, J. (2019). Soil C, N and P dynamics along a 13 ka chronosequence of landslides under semi-natural temperate forest. *Quaternary Science Reviews, 213*, 18-29

Walker, L., & del Moral, R. (2003). *Primary Succession and Ecosystem Rehabilitation*.

Walker, L.R., & Shiels, A.B. (2008). Post-disturbance erosion impacts carbon fluxes and plant succession on recent tropical landslides. *Plant and Soil, 313*, 205-216

Walker, L.R., Velázquez, E., & Shiels, A.B. (2009). Applying lessons from ecological succession to the restoration of landslides. *Plant and Soil, 324*, 157-168

Walker, L.R., Zarin, D.J., Fetcher, N., Myster, R.W., & Johnson, A.H. (1996). Ecosystem Development and Plant Succession on Landslides in the Caribbean. *Biotropica, 28*, 566-576

Wang, E.-q., Meng, Q.-r., & Chen, Z.-l.J.E.S.F. (2001). Early Mesozoic left-lateral movement along the Longmen Shan fault belt and its tectonic implications*, 8*, 375-384

Wang, J., Bao, C., Luo, Z., & Guo, Z. (1989). Formation and deformation of the Sichuan Basin. *Chinese Sedimentary Basins* (pp. 147-163): Elsevier Science

Wang, J., Jin, Z., Hilton, R.G., Zhang, F., Densmore, A.L., Li, G., & West, A.J. (2015). Controls on fluvial evacuation of sediment from earthquake-triggered landslides. *Geology, 43*, 115-118

Wang, J., Jin, Z., Hilton, R.G., Zhang, F., Li, G., Densmore, A.L., Gröcke, D.R., Xu, X., & West, A.J. (2016). Earthquake-triggered increase in biospheric carbon export from a mountain belt. *Geology, 44*, 471-474

Wang, Q., Wang, Z.-g., Yong, Z.-w., Zhao, K., Xiong, J.-n., Du, X.-m., & Zhao, Y. (2022). Vegetation recovery trends under dual dominance of climate change and anthropogenic factors in the severely damaged areas of the Wenchuan earthquake. *Journal of Mountain Science, 19*, 3131-3147

Wang, W., Zhao, L., Li, J., & Yao, Z.J.C.J.G. (2008a). The rupturing process of the Wenchuan, Sichuan earthquake (M 8.0)*, 51*, 1403-1410

Wang, X.-g., Zhu, B., Wang, Y., & Zheng, X.J.E.J.o.F.R. (2008b). Field measures of the contribution of root respiration to soil respiration in an alder and cypress mixed plantation by two methods: trenching method and root biomass regression method*, 127*, 285-291

Wang, X., Fan, X., Fang, C., Dai, L., Zhang, W., Zheng, H., & Xu, Q. (2024). Long-Term Landslide Evolution and Restoration After the Wenchuan Earthquake Revealed by Time-Series Remote Sensing Images*, 51*, e2023GL106422

Wang, Y., Fu, B., & Xu, P.J.P.E.S. (2012). Evaluation the impact of earthquake on ecosystem services*, 13*, 954-966

Wardle, D.A., Walker, L.R., & Bardgett, R.D. (2004). Ecosystem Properties and Forest Decline in Contrasting Long-Term Chronosequences*, 305*, 509-513

West, A.J., Lin, C.W., Lin, T.C., Hilton, R.G., Liu, S.H., Chang, C.T., Lin, K.C., Galy, A., Sparkes, R.B., & Hovius, N. (2011). Mobilization and transport of coarse woody debris to the oceans triggered by an extreme tropical storm. *Limnology and Oceanography, 56*, 77-85

Wong, K., Mason, E., Brune, S., East, M., Edmonds, M., & Zahirovic, S. (2019). Deep Carbon Cycling Over the Past 200 Million Years: A Review of Fluxes in Different Tectonic Settings*, 7*

Wu, S., Di, B., Ustin, S.L., Wong, M.S., Adhikari, B.R., Zhang, R., & Luo, M. (2023). Dynamic Characteristics of Vegetation Change Based on Reconstructed Heterogenous NDVI in Seismic Regions. *Remote Sensing, 15*

Wu, Y., Li, F., Zhang, J., Liu, Y., Li, H., Zhou, B., Shen, B., Hou, L., Xu, D., Ding, L., Chen, S., Liu, X., & Peng, J. (2024). Spatial and temporal patterns of above- and below-ground biomass over the Tibet Plateau grasslands and their sensitivity to climate change. *Science of the Total Environment, 919*, 170900

Xiao, J., Chevallier, F., Gomez, C., Guanter, L., Hicke, J.A., Huete, A.R., Ichii, K., Ni, W., Pang, Y., Rahman, A.F., Sun, G., Yuan, W., Zhang, L., & Zhang, X. (2019). Remote sensing of the terrestrial carbon cycle: A review of advances over 50 years. *Remote Sensing of Environment, 233*, 111383

Xu, C., Xu, X., Yao, X., & Dai, F.J.L. (2014). Three (nearly) complete inventories of landslides triggered by the May 12, 2008 Wenchuan Mw 7.9 earthquake of China and their spatial distribution statistical analysis*, 11*, 441-461

Xu, Q., Zeng, Y., Qian, J., & Wang, C. (2009). Study on a improved tangential angle and the corresponding landslide pre-warning criteria. *Geological Bulletin of China, 28*, 501-505

Xu, X., Wen, X.-Z., Ye, J.Q., Ma, B.Q., Chen, J., Zhou, R.J., He, H.L., Tian, Q.J., He, Y.L., Wang, Z., Sun, Z.M., Feng, X.J., Yu, G., Chen, L., Chen, G., Yu, S.E., Ran, Y., Li, X.G., Chenxia, L., & Yanfen, A. (2008). The Ms8.0 Wenchuan Earthquake Surface Ruptures and its Seismogenic Structure (in Chinese). *Seismology and Geology, 30*, 597-629

Yang, F., Fan, X., Siva Subramanian, S., Dou, X., Xiong, J., Xia, B., Yu, Z., & Xu, Q.J.L. (2021). Catastrophic debris flows triggered by the 20 August 2019 rainfall, a decade since the Wenchuan earthquake, China*, 18*, 3197-3212

Yang, J., & Huang, X. (2021). The 30 m annual land cover dataset and its dynamics in China from 1990 to 2019. *Earth System Science Data, 13*, 3907-3925

Yang, W., Qi, W., & Zhou, J. (2018). Effects of precipitation and topography on vegetation recovery at landslide sites after the 2008 Wenchuan earthquake. *Land Degradation & Development, 29*, 3355-3365

Yang, Y., Luo, Y., & Finzi, A.C. (2011). Carbon and nitrogen dynamics during forest stand development: a global synthesis. *New Phytol, 190*, 977-989

Yanites, B.J., Tucker, G.E., Hsu, H.-L., Chen, C.-c., Chen, Y.-G., & Mueller, K.J. (2011). The influence of sediment cover variability on long-term river incision rates: An example from the Peikang River, central Taiwan*, 116*

Yanites, B.J., Tucker, G.E., Mueller, K.J., & Chen, Y.-G. (2010). How rivers react to large earthquakes: Evidence from central Taiwan. *Geology, 38*, 639-642

Yoo, K., Amundson, R., Heimsath, A.M., & Dietrich, W.E. (2005). Erosion of upland hillslope soil organic carbon: Coupling field measurements with a sediment transport model*, 19*

Yoo, K., Amundson, R., Heimsath, A.M., & Dietrich, W.E. (2006). Spatial patterns of soil organic carbon on hillslopes: Integrating geomorphic processes and the biological C cycle. *Geoderma, 130*, 47-65

Yueping, Y.J.工. (2008). Researches on the geo-hazards triggered by Wenchuan earthquake, Sichuan*, 16*, 433-444

Yunus, A.P., Fan, X., Tang, X., Jie, D., Xu, Q., & Huang, R. (2020). Decadal vegetation succession from MODIS reveals the spatio-temporal evolution of post-seismic landsliding after the 2008 Wenchuan earthquake. *Remote Sensing of Environment, 236*

Zaehle, S., Sitch, S., Prentice, I.C., Liski, J., Cramer, W., Erhard, M., Hickler, T., & Smith, B. (2006). The importance of age-related decline in forest NPP for modeling regional carbon balances. *Ecol Appl, 16*, 1555-1574

Zeng, H., Lu, T., Jenkins, H., Negrón-Juárez, R., & Xu, J. (2016). Assessing Earthquake-Induced Tree Mortality in Temperate Forest Ecosystems: A Case Study from Wenchuan, China. *Remote Sensing, 8*

Zhang, G.S., Lin, Y.M., Ma, R.F., Deng, H.J., Du, K., Wu, C.Z., & Hong, W. (2015). Carbon source metabolic diversity of soil microbial community under different climate types in the area affected by Wenchuan earthquake. *Huan Jing Ke Xue, 36*, 669-677

Zhang, L., Liu, X., Li, Y., Liu, Y., Liu, Z., Lin, J., Shen, J., Tang, X., Zhang, Y., & Liang, W.J.T.L. (2012a). Emergency medical rescue efforts after a major earthquake: lessons from the 2008 Wenchuan earthquake*, 379*, 853-861

Zhang, L., Zhongkui, X., Ruifeng, Z., & YaJun, W.J.J.o.A.L. (2012b). The impact of land use change on soil organic carbon and labile organic carbon stocks in the Longzhong region of Loess Plateau*, 4*, 241-250

Zhang, P.-Z. (2008). Slip rates and recurrence intervals of the Longmen Shan active fault zone, and tectonic implications for the mechanism of the May 12 Wenchuan earthquake, 2008, Sichuan, China*, 51*, 1066-1073

Zhang, P.-Z., Shen, Z., Wang, M., Gan, W., Burgmann, R., Molnar, P., Wang, Q., Niu, Z., Sun, J., & Wu, J.J.G. (2004). Continuous deformation of the Tibetan Plateau from global positioning system data*, 32*, 809-812

Zhang, S., Zhang, L.M., & Glade, T.J.E.G. (2014). Characteristics of earthquake-and rain-induced landslides near the epicenter of Wenchuan earthquake*, 175*, 58-73

Zhang, W., Yang, G., Tu, X., & Zhang, P. (1999). Determination of forest soil water-physical properties. *China Criterion of Forest Technique*

Zhao, M., & Zhou, G.-S. (2006). Carbon Storage of Forest Vegetation in China and its Relationship with Climatic Factors. *Climatic Change, 74*, 175-189